



DIPLOMARBEIT

Numerical Analysis of an Impinging Jet in a Turbulent Flow Field

Ausgeführt am
Austrian Institute of Technology AIT
und
Institut für Festkörperphysik

unter der Anleitung von
Dipl.-Ing. Dr. Christoph Reichl
und
Univ. Doz. Roland Grössinger

durch

Michelle Böck
Untere Augartenstraße 15-17 1/20
1020 Wien

Acknowledgments

I would like to thank my mother, who gave me financial support during my academic studies.

First of all, I want to thank my supervisor Dipl.-Ing. Dr. Christoph Reichl at the Austrian Institute of Technology, who made it possible to work on my thesis in his department, for his optimism, attention and academic support. It is owing to him that I had the opportunity of attending international and national conferences. I am also thankful for his careful reading and corrections.

And I want to thank the colleagues at the Austrian Institute of Technology for creating a great working climate.

Abstract

Computational Fluid Dynamics (CFD) deals with the numerical analysis of flow phenomena. The Navier-Stokes equations, which govern the motion of a Newtonian viscous fluid, are the base of almost all CFD problems. The method of dealing with any fluid dynamics problem is to solve these equations for the appropriate boundary conditions. There are some software packages available that solve fluid flow problems, as for instance FLUENT that is used in this thesis.

The goal of this project is the investigation of flow fields and degrees of turbulence with regard to microphones which are used in cars for the purpose of hands free speaking systems. The fact that these microphones are usually positioned near the air condition outlet flow fields leads to decrease in the quality of voice recording. Hence there is a need for a better understanding of flow fields inside of vehicle interiors for the microphone producer. For the analysis of these fluid flows different setups of turbulence generators are positioned in the test wind tunnel in order to produce turbulence, so microphones can be tested under defined turbulence flow conditions which match the flow conditions in the vehicle interior.

This thesis deals with the numerical analysis of the different degrees and spectra of turbulence that are produced by different setups of turbulence generators located in the test wind tunnel. First, several steady CFD simulations are performed for each turbulence generator to investigate the characteristic of the fluid flow, and the numerically generated results for the velocity components and the turbulent kinetic energy are compared to experimental results. Unsteady CFD simulations for the quantitative analysis of the turbulent flow fields are then performed. The correlations between local velocity fluctuations and pressure fluctuations near the microphones are investigated and compared to experimental results. Among steady CFD simulations the RNG k- ϵ model compared best to experimental data, however steady solutions cannot always be delivered, transient DES have been performed to provide frequency spectra which show that prominent features of the spatial frequency behavior are well captured. The position of the shear layers, the separation and the combination of the turbulent regions can be observed easily. The comparison of the experimentally and numerically generated frequency spectra offer the possibility to find out where CFD simulations are effective and it shows that the simulation gives results approximately equivalent to the experimental results.

For the geometry and mesh generation the software tool GAMBIT is used. All CFD simulations have been performed on a Linux cluster at the Austrian Institute of Technology.

This thesis was undertaken within the 'TUNICA-Project', which is a collaboration of the Austrian Institute of Technology, an industrial partner and the Vienna University of Technology. This work was supported by the Austrian Research Promotion Agency (FFG). The experimental and numerical results of the TUNICA project have been presented at national as well as international conferences.

Zusammenfassung

Die numerische Strömungsmechanik, auf englisch Computational Fluid Dynamics (CFD) beschäftigt sich mit der numerischen Behandlung von Strömungsvorgängen. Fast jedes Strömungsphänomen kann mithilfe der Navier-Stokes Gleichungen, die das Newtonsche reibungsbehaftete Fluid beschreiben, formuliert werden. Um ein CFD Problem behandeln zu können, ist es notwendig die Navier-Stokes Gleichungen zu lösen. Es gibt verschiedene kommerzielle CFD Software Pakete, wie z.B. FLUENT, mit dem alle numerischen Simulationen in dieser Diplomarbeit durchgeführt wurden.

Ziel des TUNICA Projektes ist die Untersuchung von Strömungsfeldern und Turbulenzgraden im Bereich von Mikrofonen, die wie in diesem Fall in Fahrzeugen zum Freisprechen verwendet werden. Diese Mikrofone sind an den üblichen Montagepunkten in Fahrzeugen allerdings oft der direkten Luftströmung der Klimaanlage ausgesetzt, was die Qualität der Sprachaufnahme mindert und eine störungsfreie Kommunikation verhindert. Daher ist es wichtig die Strömungsverhältnisse im Innenraum des Fahrzeugs für den Hersteller nachvollziehbar zu machen. Für die Analyse der Strömungsfelder kommt ein Testwindkanal zum Einsatz, wobei der Turbulenzgrad der Strömung durch den Einbau von Turbulenzgeneratoren im Windkanal gezielt erhöht wird. Die Mikrofone können dann fortan unter definierten turbulenten Strömungsbedingungen untersucht werden, die den Bedingungen im Fahrzeug entsprechen.

Diese Diplomarbeit beschäftigt sich mit der Analyse der Turbulenzgrade und -spektren, die durch verschiedene Turbulenzgeneratoren in der Strömung erzeugt werden, mittels CFD Simulationen. Die Geometrie- und Netzerstellung der verschiedenen Rechengemetrien erfolgte mit dem Softwaretool GAMBIT. Zuerst werden stationäre Simulationen für jeden Turbulenzgenerator durchgeführt, um das Verhalten der turbulenten Strömung zu untersuchen. Die Ergebnisse der Geschwindigkeitskomponenten und der turbulenten kinetischen Energie aus den CFD Simulationen können mit experimentellen Ergebnissen verglichen werden. Für eine quantitative Analyse der turbulenten Strömung werden zusätzlich instationäre Simulationen durchgeführt. Die Korrelation zwischen lokalen Geschwindigkeitsfluktuationen und Druckschwankungen in Nähe der Mikrofone ist dabei von Interesse, wobei ebenfalls für einen Vergleich experimentelle Ergebnisse zur Verfügung stehen. Von den stationären Simulationen lieferte das RNG k- ϵ Modell Ergebnisse, die am besten mit den experimentell ermittelten Werten übereinstimmen. Stationäre Lösungen können jedoch nicht für jeden Turbulenzgenerator simuliert werden. Zusätzlich wurden instationäre Detached Eddy Simulationen (DES) durchgeführt. Aus der DES ergeben sich Frequenzspektren, die mit den Frequenzspektren aus dem Experiment verglichen wurden. Aus den simulierten Frequenzspektren lassen sich die Strömungscharakteristiken, wie die Position der Scherschichten oder Strömungsablösung gut ablesen. Der Vergleich der Frequenzspektren aus der Simulation mit denen aus dem Experiment zeigt in wann CFD Simulationen effektiv sind und dass die simulierten Ergebnisse in etwa den experimentellen entsprechen.

Die CFD Simulationen wurden alle an einem Linux Cluster am Austrian Institute of Technology durchgeführt.

Diese Diplomarbeit wurde im Rahmen des TUNICA Projektes, unter Zusammenarbeit des Austrian Institute of Technology, einem industriellen Partner und der Technischen Universität Wien durchgeführt. Das TUNICA Projekt wurde als Bridge Projekt von der Österreichischen Forschungsförderungsgesellschaft gefördert. Die experimentellen und numerischen Ergebnisse wurden sowohl auf nationalen als auch internationalen Fachtagungen vorgestellt und präsentiert.

Content

1 Introduction.....	1
1.1 Overview of the TUNICA Project.....	1
2 Theory of Turbulent Flow.....	2
2.1 Navier-Stokes-Equation.....	2
2.1.1 Reynolds number.....	4
2.1.2 Convection.....	6
2.1.3 Turbulent Kinetic Energy	6
2.2 Discretization.....	7
2.2.1 Discretization Methods.....	7
2.2.1.1 Finite Difference Method	7
2.2.1.2 Finite Volume Method.....	8
2.2.1.3 Finite Element Method.....	9
2.2.2 Discretization Errors.....	10
2.2.3 Consistency.....	11
2.2.4 Stability.....	12
2.2.5 Convergence.....	13
2.3 Turbulence Models.....	14
2.3.1 RANS (Reynolds-Averaged Navier-Stokes) Models.....	14
2.3.1.1 Standard k- ϵ -Model.....	16
2.3.1.2 RNG-k- ϵ -Model.....	17
2.3.1.3 k- ω -Model.....	17
2.3.1.4 Reynolds Stress Model (RSM).....	17
2.3.2 Direct Numerical Simulation (DNS).....	19
2.3.3 Large Eddy Simulation (LES) and Detached Eddy Simulation (DES).....	20
2.4 Pipe Flow.....	21
2.4.1 Laminar Pipe Flow.....	21

2.4.2 Turbulent Pipe Flow and the Law-of-the-Wall.....	22
2.5 Free Jet.....	24
3 Geometry.....	27
3.1 Geometry of Turbulence Generators.....	30
3.2 Degrees of Obstruction.....	32
4 Mesh Generation.....	34
4.1 Meshing Strategies.....	34
4.2 Meshing Process.....	36
4.3 Setting Boundary Types.....	42
5 Stationary Simulations.....	43
5.1 Boundary Conditions resulting from the Experiment.....	43
5.2 Axis-Symmetrical 2D-Simulations at TG00.....	45
5.2.1 The Selection of the Turbulence Models.....	46
5.2.2 Mesh–Dependency of the Solutions.....	48
5.3 3D-Simulations.....	56
5.4 Summary of the Results.....	59
5.4.1 Comparison of Simulation and Experiment.....	59
5.4.2 Flow Properties for the Different Turbulence Generators.....	62
6 Unsteady Simulations.....	70
6.1 Mean Velocities and Fluctuations	72
6.2 Fast Fourier Transformation	102
6.3 Spectral Analysis.....	103
6.4 Pressure Fluctuations at the Plate.....	123
7 Conclusions.....	126
8 Bibliography.....	127
9 Conference Papers.....	128

1 Introduction

1.1 Overview of the TUNICA Project

Microphones are used in vehicles for many different purposes, such as voice recognition, intercommunication and handsfree kits. First of all, they should be optimally positioned and they should adapt flexibly to the design of the vehicle. The microphone is normally set up next to the air conditioner, which decreases the quality of the voice recording and prevents interference free communication. In the course of the research project TUNICA flow fields as well as the degrees of the turbulence with regard to microphones are investigated experimentally and numerically. The aim of this research has been to make the flow fields in vehicle interiors more understandable for producers of microphones.

For the analysis of these fluid flow noises and the development of new microphones industrial partners use a wind tunnel, which has low turbulence due to its initial design. The main objective of the TUNICA project is the design and the installation of different turbulence generators in the feed of these wind tunnels, experimental surveying and numerical modeling of the stream turbulence and its influence on the microphones. Finally, a variable set of turbulence generators are adapted in the test tunnel, which produces the degrees of turbulence and its spectra on purpose. As a result, the microphones can be investigated under defined turbulence stream conditions, which match all the conditions in the vehicle.

It is essential for the production and setting up of microphones in the inside of vehicle interior to recognize flow conditions in order to offer the ideal quality of the voice recording and interference free communication. Research projects dealing with flow simulation research are important for the investigation of the interior stream of present and prospective vehicles. This method is used in order to find the ideal position for the microphone with regard to fluid engineering and in order to provide the expected degrees of turbulence for the wind tunnel. The wind channel can contribute to the fluidic optimization of microphones before they are totally finished and installed. As a result, the final products and their acoustic quality can be optimized.

2 Theory of Turbulent Flow

Most flows encountered in practice are turbulent and therefore require different treatment in comparison to laminar or non-viscous flows. Turbulence occurs as a result of instabilities of a flow. An instability occurs if a perturbation of the flow grows with time. Turbulent flows are highly unsteady, very difficult to predict in detail and always three-dimensional. The time-averaged velocity may be a function of only two coordinates, but the instantaneous field fluctuates rapidly in all three spatial dimensions. Turbulent flows contain a great deal of vorticity. Indeed vortex stretching is one of the principal mechanisms by which the intensity of turbulence is increased. The turbulence increases the rate at which conserved quantities are stirred. Stirring is a process in which parcels of fluid with differing concentrations of at least one of the conserved quantities are brought into contact. The actual mixing is accomplished by diffusion. This process is often called turbulent diffusion. As mentioned before, turbulence brings fluids of differing momentum content into contact. The reduction of the velocity gradients due to the action of viscosity reduces the kinetic energy of the flow and mixing is therefore a dissipative process. The energy is irreversibly converted into internal energy of the fluid. It has been shown in recent years that turbulent flows contain coherent structures – repeatable and essentially deterministic events that are responsible for the mixing. However, the random component of turbulent flows causes these events to differ from each other in size, strength and time interval between occurrences, making study of them very complicated. Turbulent flows fluctuate on a broad range of length and time scales. This property makes direct numerical simulation of turbulent flows very difficult.

All of these properties explained in the last paragraph are important. The effects produced by turbulence may or may not be desirable, depending on the application. Engineers need to be able to understand and predict these effects in order to achieve good designs. In some cases it is possible to control the turbulence, at least in part.

In the past, the primary approach to studying turbulent flows was experimental. Overall parameters such as the time-averaged drag or heat transfer are relatively easy to measure but as the sophistication of engineering devices increases, the levels of detail and accuracy required also increase, as does cost and the expense and difficulty of making measurements. To optimize a design it is usually necessary to understand the source of the undesired effects; this requires detailed measurements that are costly and time-consuming. Some types of measurements, for example, the fluctuating pressure within a flow are almost impossible to make at the present time. Others cannot be made with the required precision. As a result, numerical methods have an important role to play. [1, 2]

2.1 Navier-Stokes-Equation

The Navier-Stokes-Equation (2.1) is one of the most important equations in fluid mechanics since it describes the motion of a fluid. It is a vector differential equation derived from Newton's Law of Motion and by supplementation of the continuity equation. This provides a fundamental, and very general, momentum balance that is valid at all of any fluid flow.

$$\rho \frac{D\mathbf{u}}{Dt} = -\nabla p + \rho \mathbf{g} - \mu \nabla \times (\nabla \times \mathbf{u}) = -\nabla p + \rho \mathbf{g} - \mu \nabla^2 \mathbf{u} \quad \text{equation (2.1)}$$

The Navier-Stokes-Equation here is written in its vectorial form ($\mathbf{u}=(u,v,w)$) and represents therefore a system of three nonlinear second order partial differential equations. Together with the

continuity equation they form a set of four equations which is complete for incompressible Newtonian flows, i.e., in principle they are sufficient to solve for the four dependent variables p, u, v and w . Every kind of flow can be described by the Navier-Stokes-Equation by using the right initial and boundary conditions. The proper boundary conditions for the velocity on a rigid boundary are

$$u_n = u_t = 0 \quad \text{equation (2.2)}$$

where u_n is the normal component of the velocity relative to the solid boundary, and u_t is its tangential component. These conditions are also termed the *no-penetration* ($u_n = 0$) and *no-slip* ($u_t = 0$) *viscous boundary conditions*. When the region occupied by the fluid is not closed, i.e., the fluid is not completely confined, additional conditions are still required on some surfaces which completely enclose the domain of the solution. These may represent some real physical surfaces or they may be chosen arbitrarily, provided the velocity on them is known. The pressure which is also a dependent variable, requires boundary conditions too.

The form containing $\nabla \times (\nabla \times \mathbf{u})$ is a standard vectorial form for the Navier-Stokes equations. The other form derives from taking $\nabla \times (\nabla \times \mathbf{u})$ and using the equation of continuity, $\nabla \cdot \mathbf{u} = 0$ for incompressible flows. [3]

For the physical interpretation of the Navier-Stokes equation we divide equation 2.1 and express the vectorial equation system as follows

$$\underbrace{\frac{\partial \mathbf{u}}{\partial t}}_{\substack{\text{local} \\ \text{accel}}} + \underbrace{(\mathbf{u} \cdot \nabla) \mathbf{u}}_{\substack{\text{convective} \\ \text{accel}}} = \underbrace{\frac{-1}{\rho} \nabla p}_{\text{pressure forces}} + \underbrace{\nu \Delta \mathbf{u}}_{\text{viscous forces}} + \underbrace{\frac{1}{\rho} \mathbf{f}}_{\text{body forces}} \quad \text{equation (2.3)}$$

Here, ν is the *kinematic viscosity*, the ratio of viscosity μ to density ρ , and \mathbf{f} represents other body forces. It is worthwhile to consider the Navier-Stokes equation term-by-term and ascribe specific physical meaning to each of these terms. This understanding is important for simplifying of the equations to treat specific physical flow situations. By knowing the physics represented by these terms and what physics is not included in a problem, it is easy to determine what terms can be omitted from the equation to simplify the analysis. The characterization of the terms is carried out in equation 2.3. The left-hand side of this equation is the substantial derivative of the velocity \mathbf{u} and these terms are often called the 'inertial terms' in the context of the Navier-Stokes equations, and they contain of two main contributions: local acceleration and convective acceleration. They can be viewed as time-rate of change of momentum per unit mass. The first term on the right-hand side of equation 2.3 represents normal surface forces due to pressure, 'pressure forces', but in the present form this is actually a force per unit mass as it must be to be consistent with the time rate of change of momentum per unit mass on the left-hand side. To understand the behavior of solutions to the Navier-Stokes equations it is essential to thoroughly treat the unique phenomena arising from the viscous terms. These terms are:

$$\nu \Delta \mathbf{u} = \nu (u_{xx} + u_{yy} + u_{zz}) \quad \text{equation (2.4)}$$

Viscosity arises at the molecular level, and the terms given above are associated with molecular transport (i.e., diffusion) of momentum. In general, second derivative terms in a differential equation are usually associated with diffusion, and in both physical and mathematical contexts this represents a smearing, or smoothing, or mixing process. Diffusive action of the viscosity dissipates mechanical energy, ultimately converting it to thermal energy. In turn, this results in entropy increases and loss of usable energy. Thus, we see that the viscous terms in the momentum equations

render them non-conservative, and appreciable pressure, shearing or body forces must be applied continuously to preserve the fluid motion. [4]

2.1.1 Reynolds number

The Reynolds number Re is a dimensionless parameter and one of the most important parameters in all fluid dynamics. The Reynolds number is named after Osborne Reynolds who proposed it in 1883. This parameter gives qualitative information about the flow field, whether it is laminar or turbulent. It is defined as the ratio of the inertial forces ($U\rho$) to the viscous forces (μ/L). U , L , μ and ρ are the reference values for velocity, length, density and dynamic viscosity.

$$Re = \frac{(\text{inertial force})}{(\text{viscous force})} = \frac{(\rho UL)}{\mu} \quad \text{equation (2.5)}$$

And in terms of kinematic viscosity $\nu = (\mu/\rho)$ the Reynolds number is given by

$$Re = \frac{(UL)}{\nu} \quad \text{equation (2.6)}$$

One of the main efforts in theoretical analysis of fluid flow is to predict the changes in the qualitative nature of the flow as Re increases. If Re is large the diffusive terms (viscous force terms) will be small, hence the behavior of the flow will be dominated by the inertial forces. At high Reynolds numbers flows tend to be turbulent. [5, 4]

The importance of the Reynolds number can be demonstrated by regarding the *Reynolds Experiment*.

Consider the experimental apparatus shown in Fig.2.1. It consists of a small tube inserted inside a large transparent pipe. The inner tube has a small diameter and its opening is located far from the bend, i.e., L_B is sufficiently long to guarantee fully developed flow. The fluid in the inner tube is the same as that in the outer pipe, and they have the same ρ and μ . However the inner fluid is dyed while the outer one is clear. In all experiments the velocities of the two fluids are adjusted so as to have a little shear strain between them as possible.

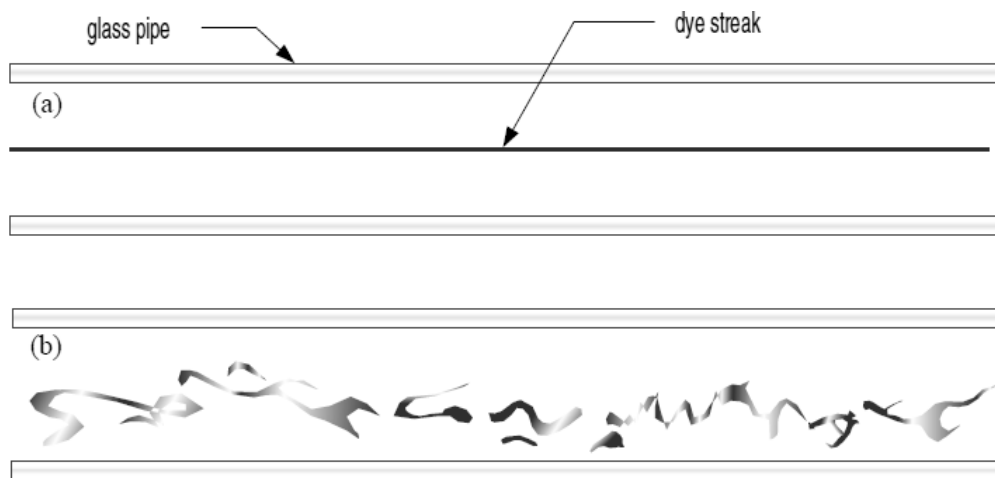


Figure 2.1.: Reynolds Experiment using water in a pipe to study the transition to turbulence, (a) low-speed flow, (b) high-speed flow [4]

As the experiment proceeds, a dyed stream cylinder is seen to form downstream from the opening of the inner tube. The stream tube which makes the envelope of this stream cylinder is well defined,

and the dye is restricted to the inside of this stream tube. The dye begins to spread out by molecular diffusion only far downstream.

The experiment is repeated for various fluids and for various velocities and all these can be summarized using the Reynolds number as the single parameter involved. It is found that the description given above fits flows whose Reynolds number, calculated using the pipe diameter D as the characteristic length, is below a certain numerical value, namely,

$$Re_D = \frac{VD}{\nu} < 2000 \quad \text{equation (2.7)}$$

where V is the average velocity in the pipe, i.e., the flowrate per unit cross-sectional area. Above this Reynolds number the envelope of the dyed stream tube is not clearly defined. The dye is seen to mix with the outer fluid right from the opening of the inner tube. The laminar character of the flow is lost and the flow becomes turbulent.

One finds out that the momentum and continuity equations, with time-independent solutions for $Re < 2000$, do not have such time-independent solutions for $Re > 2000$. Although the boundary conditions remain time-independent, the resulting flow persists to be time-dependent, non-periodic and non-decaying. The transition to turbulence is illustrated in Figure 2.2.:

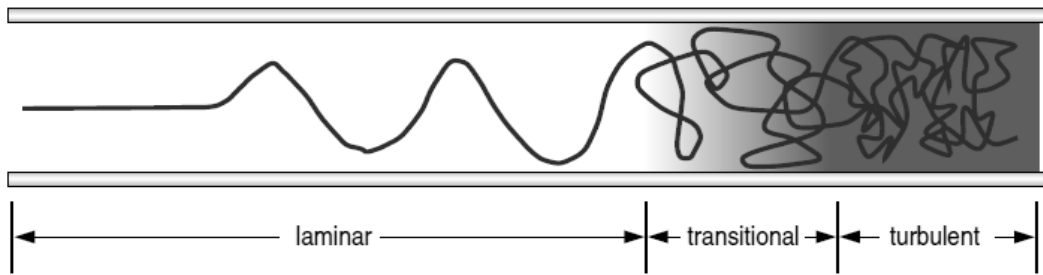


Figure 2.2.: Transition to turbulence in spatially-evolving flow [4]

If one was to plot the velocity of the fluid at a given point in the pipe, a pattern similar to that of Figure 2.3. would result. As seen, there are small rapid velocity fluctuations about some average value. This average value may or may not depend on time. The velocity then is a superposition of an average velocity \bar{u} and a velocity fluctuation u' ,

$$u = \bar{u} + u' \quad \text{equation (2.8)}$$

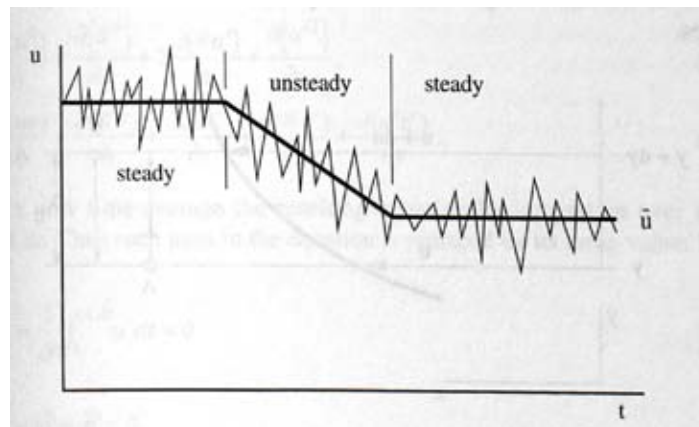


Figure 2.3.: Velocity in turbulent flow [6]

Similar relations may be written for the other velocity components as well as for other properties, such as the pressure, the temperature, etc.:

$$p = \bar{p} + p' \quad , \quad T = \bar{T} + T' \quad . \text{ equation (2.9)}$$

The average quantities are defined according to the form

$$\bar{q} = \frac{1}{\Delta t} \int_t^{t+\Delta t} q \, dt = \frac{1}{\Delta t} \int_t^{t+\Delta t} (\bar{q} + q') \, dt \quad \text{equation (2.10)}$$

and

$$\bar{q}' = \frac{1}{\Delta t} \int_t^{t+\Delta t} q' \, dt = 0 \quad \text{equation (2.11)}$$

i.e., the time average of the fluctuation vanishes. [3]

2.1.2 Convection

Convection is one of the major modes of mass and heat transfer. There exist two types of convection, forced convection and natural convection. Convection occurs when a system becomes unstable and therefore begins to mix by the movement of mass. The onset of convection is characterized by the Rayleigh number Ra , a dimensionless parameter.

$$Ra = \frac{(g \Delta \rho L^3)}{(\rho_0 \nu \kappa)} \quad \text{equation (2.12)}$$

Where g is the acceleration of gravity, $\Delta \rho$ is the density variation within the domain, ρ_0 is a reference density and κ is the *thermal diffusivity*. Buoyancy-driven or natural convection is that density variations interacting with gravity produces a body force. That may modify the flow considerably and may be the principal driving force in the flow. The relative importance of forced convection to buoyancy effects is measured by the ratio of the Rayleigh and Reynolds numbers. If $Re/Ra > 10^4$, the effects of natural convection may be ignored. In a zero-gravity environment exist no buoyancy forces and therefore natural convection processes are not possible. In forced convection the heat-mass transfer is due to movement in the fluid that is caused by many other forces, such as a pump. [1]

2.1.3 Turbulent Kinetic Energy

The turbulent kinetic energy k is one of the most important variables to study the turbulence of a flow. As demonstrated above the velocity components and pressure are split into a mean and fluctuating component:

$$p = \bar{p} + p' \quad , \quad u = \bar{u} + u' \quad \text{equation (2.13)}$$

Introducing this concept to the Navier-Stokes equation, one gets the Reynolds-averaged Navier-Stokes equations, which is demonstrated in section 2.3.1.. The terms that involve the products of the fluctuating velocities act as turbulent stresses, also called the Reynolds stresses, on the mean velocity components. The Reynolds averaged Navier-Stokes equation for a stationary, incompressible flow of a Newtonian fluid can be written as:

$$\rho \frac{\partial \overline{u_j u_i}}{\partial x_j} = \rho \overline{f_i} + \frac{\partial}{\partial x_j} \left[-\overline{p} \delta_{ij} + \mu \left(\frac{\partial \overline{u_i}}{\partial x_j} + \frac{\partial \overline{u_j}}{\partial x_i} \right) - \rho \overline{u_i u_j} \right] \quad \text{equation (2.14)}$$

As it is explained later, it is general not possible to derive governing equations for the Reynolds stresses, because of the closure problem. Hence several turbulence models have been introduced, that are described in sections 2.3.1.1-2.3.1.3. Since in laminar flows, energy dissipation and transport of mass, momentum, and energy normal to the streamlines are mediated by viscosity, it is natural to assume that the effect of turbulence can be represented as an increased viscosity. This leads to the eddy-viscosity model for the Reynolds stresses. The Reynolds stresses are calculated from

$$-\overline{u_i u_j} = \nu_t \left(\frac{\partial \overline{u_i}}{\partial x_j} + \frac{\partial \overline{u_j}}{\partial x_i} \right) - \frac{2}{3} k \delta_{ij} \quad \text{equation (2.15)}$$

where k is the turbulent kinetic energy:

$$k = \frac{1}{2} \overline{u_i u_i} = \frac{1}{2} (\overline{u_x u_x} + \overline{u_y u_y} + \overline{u_z u_z}) \quad \text{equation (2.16)}$$

and ν_t is the eddy-viscosity. [6, 1]

2.2 Discretization

2.2.1 Discretization Methods

After selecting the mathematical method, i.e. the set of partial differential or integro-differential equations governing a complex fluid dynamics problem the solution process requires the introduction of a suitable discretization method. Discretization means that the differential equations are approximated by a system of algebraic equations for the variables at some set of discrete locations in space and time. Several methods have been developed and are currently in use. Most important approaches are finite differences (FD), finite volume (FV) and finite element (FE) methods. In this section the basic ideas of these discretization methods will be presented. [6, 1]

2.2.1.1 Finite Difference Method

The finite difference method (FD) is the the oldest method for numerical solution of PDE's, believed to have been introduced by Euler in the 18th century. It is also the easiest method to use for simple geometries. The starting point is the conservation equation in differential form. The solution domain is covered by a grid. At each grid point, the differential equation is approximated by replacing the partial derivatives by approximations in terms of the nodal values of the functions. The result is one algebraic equation per grid node, in which the variable value at that and a certain number of neighbor nodes appear as unknowns. [1]

Taylor series expansion or polynomial fitting is used to obtain approximations to the first and second derivatives of the variables with respect to the coordinates. When necessary, these methods are also used to obtain variable values at locations other than grid nodes (interpolation). [1]

On structured grids, the FD method is very simple and effective. It is especially easy to obtain higher-order schemes on regular grids. The disadvantage of FD methods is that the conservation is not enforced unless special care is taken. Also, the restriction to simple geometries is a significant disadvantage in complex flows. [1]

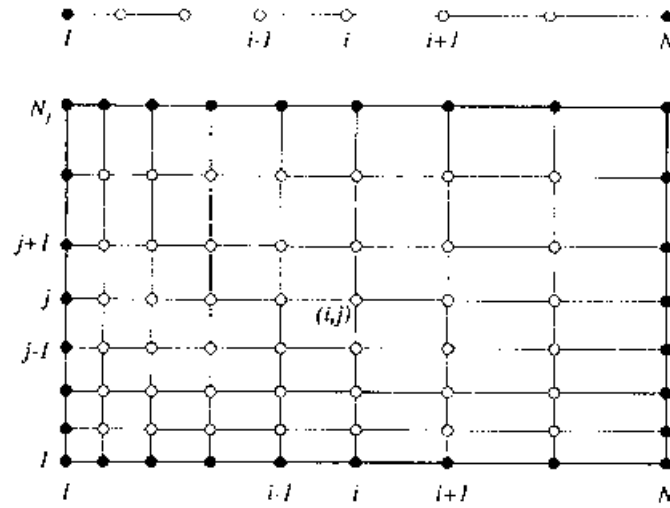


Figure 2.4.: An example of a 1D (above) and 2D (below) Cartesian grid for FD methods (full symbols denote boundary nodes and open symbols denote computational nodes) [1]

2.2.1.2 Finite Volume Method

The FV method uses the integral form of the conservation equations as its starting point. The solution domain is subdivided into a finite number of contiguous control volumes (CVs), and the conservation equations are applied to each CV. At the centroid of each CV lies a computational node at which the variable values are to be calculated. Interpolation is used to express variable values at the CV surface in terms of the nodal (CV-center) values. Surface and volume integrals are approximated using suitable quadrature formulas. As a result, one obtains an algebraic equation for each CV, in which a number of neighbor nodal values appear. [1]

The FV method can accommodate any type of grid, so it is suitable for complex geometries. The grid defines only the control volume boundaries and need not be related to a coordinate system. The method is conservative by construction, so long as surface integrals (which represent convective and diffusive fluxes) are the same for the CVs sharing the boundary. [1]

The FV approach is perhaps the simplest to understand and to program. All terms that need be approximated have physical meaning which is why it is popular with engineers. [1]

The disadvantage of FV methods compared to FD schemes is that methods of order higher than second are more difficult to develop in 3D. This is due to the fact that the FV approach requires three levels of approximation: interpolation, differentiation and integration. [1]

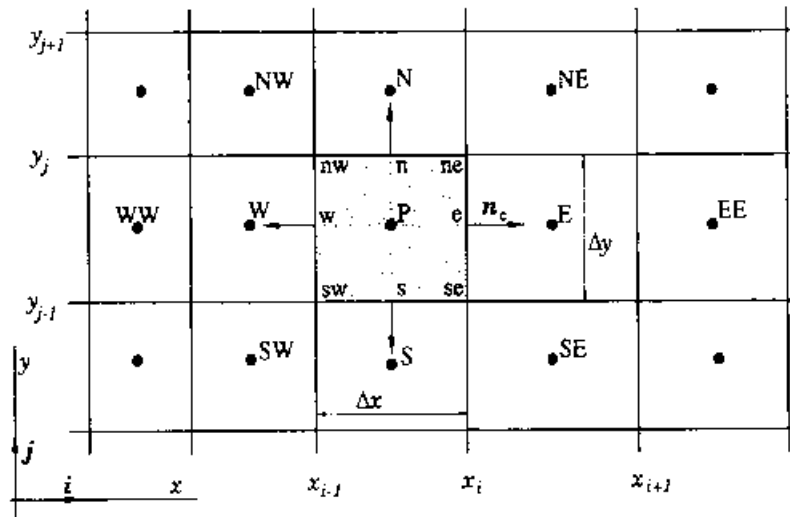


Figure 2.5.: A typical CV and the notation used for a Cartesian 2D grid [1]

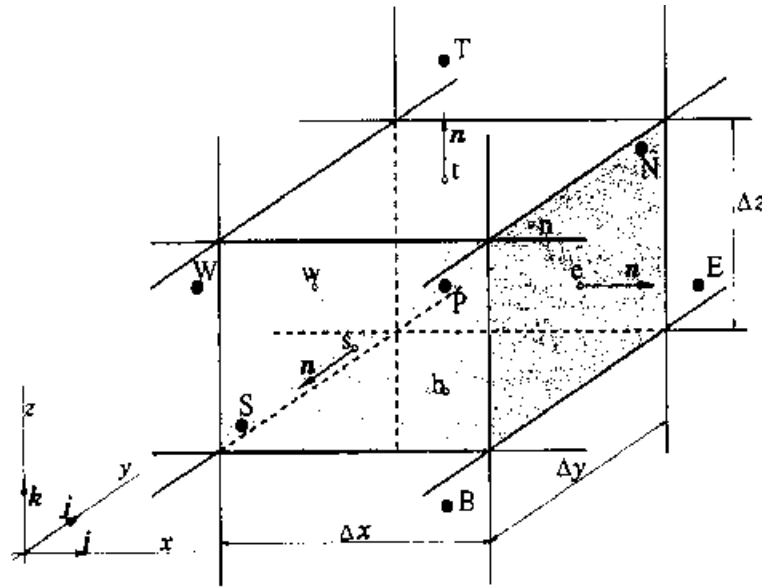


Figure 2.6.: A typical CV and the notation used for a Cartesian 3D grid [1]

2.2.1.3 Finite Element Method

The FE method is similar to the FV method in many ways. The domain is broken into a set of discrete volumes or finite elements that are generally unstructured; in 2D, they are usually triangle or quadrilaterals, while in 3D tetrahedra or hexahedra are most often used. The distinguishing feature of FE methods is that the equations are multiplied by a *weight function* before they are integrated over the entire domain. In the simplest FE methods, the solution is approximated by a linear shape function within each element in a way that guarantees continuity of the solution across element boundaries. Such a function can be constructed from its values at the corners of the elements. The weight function is usually of the same form. [1]

This approximation is then substituted into the weighted integral of the conservation law and the equations to be solved are derived by requiring the derivative of the integral with respect to each

nodal value to be zero; this corresponds to selecting the best solution within the set of allowed functions (the one with minimum residual). The result is a set of non-linear algebraic equations.[1]

An important advantage of finite element methods is the ability to deal with arbitrary geometries. The grids are easily refined; each element is simply subdivided. Finite element methods are relatively easy to analyze mathematically and can be shown to have optimality properties for certain types of equations. The principal drawback, which is shared by any methods that uses unstructured grids, is that the matrices of the linearized equations are not as well structured as those for regular grids making it more difficult to find efficient solution methods. [1]

2.2.2 Discretization Errors

Discretization errors are defined as the difference between the exact solution of the conservation equations and the exact solution of the algebraic system of equations obtained by discretizing the differential equations.

Since the discretized equations represent approximations to the differential equation, the exact solution of the latter, which we shall denote by Φ , does not satisfy the differential equation. The imbalance, which is due to truncation of the Taylor series, is called truncation error. For a grid with a reference spacing h , the truncation error τ_h is defined as:

$$L(\Phi) = L_h(\Phi) + \tau_h = 0 \quad \text{equation (2.17)}$$

where L is a symbolic operator representing the differential equation and L_h is a symbolic operator representing the algebraic equation system obtained by discretization on grid h , which is given by Eq. (2.18).

$$A\Phi = Q \quad \text{equation (2.18)}$$

A is the square sparse coefficient matrix, Φ is a vector containing the variable values at the grid nodes of h and Q contains all the terms which do not contain unknown variable values.

The exact solution of the discretized equations on grid h , Φ_h , satisfies the following equation:

$$L_h(\Phi_h) = (A\Phi - Q)_h = 0. \quad \text{equation (2.19)}$$

It differs from the exact solution of the partial differential equation by the discretization error, ϵ_h^d , i.e.:

$$\Phi = \Phi_h + \epsilon_h^d \quad \text{equation (2.20)}$$

From Eqs. (2.17) and (2.19) one can show that the following relation holds for linear problems:

$$L_h(\epsilon_h^d) = -\tau_h. \quad \text{equation (2.21)}$$

This equation states that the truncation error acts as a source of the discretization error, which is convected and diffused by the operator L_h . Exact analysis is not possible for non-linear equations, but we expect similar behavior; in any case, if the error is small enough, we can locally linearize about the exact solution and what we will say in this section is valid. Information about the magnitude and distribution of the truncation error can be used as a guide for grid refinement and can help achieve the goal of having the same level of the discretization error everywhere in the solution domain. However, as the exact solution Φ is not known, the truncation error cannot be

calculated exactly. An approximation to it may be obtained by using a solution from another (finer or coarser) grid. The estimate of the truncation error thus obtained is not always accurate but it serves the purpose of pointing to regions that have large errors and need finer grids. For sufficiently fine grids, the truncation error (and the discretization error as well) is proportional to the leading term in the Taylor series:

$$\epsilon_h^d \approx \alpha h^p + H \quad \text{equation (2.22)}$$

where H stands for higher-order terms and α depends on the derivatives at the given point but is independent of h . The discretization error can be estimated from the difference between solutions obtained on systematically refined (or coarsened) grids. Since the exact solution may be expressed as (see eq. (2.20)):

$$\Phi = \Phi_h + \alpha h^p + H = \Phi_{2h} + \alpha (2h)^p + H \quad \text{equation (2.23)}$$

the exponent p , which is the order of the scheme, may be estimated p as follows:

$$p = \frac{\log \left(\frac{\Phi_{2h} - \Phi_{4h}}{\Phi_h - \Phi_{2h}} \right)}{\log 2} \quad \text{equation (2.24)}$$

From Eq. (2.22) it also follows that the discretization error on grid h can be approximated by:

$$\epsilon_h^d \approx \frac{\Phi_h - \Phi_{2h}}{2^p - 1} \quad \text{equation (2.25)}$$

If the ratio of the grid sizes on successive grids is not two, the factor 2 in the last two equations needs to be replaced by that ratio.

When solutions on several grids are available, one can obtain an approximation of Φ which is more accurate than the solution Φ_h on the finest grid by adding the error estimate (2.25) to Φ_h ; this method is known as Richardson extrapolation. It is simple and, when the convergence is monotonic, accurate. When a number of solutions are available, the process can be repeated to improve the accuracy further.

It is shown in the paragraphs shown above that it is the rate at which the error is reduced when the grid is refined that matters, not the formal order of the scheme as defined by the leading term in the truncation error. Equation (2.24) takes this into account and returns the correct exponent p . [1]

2.2.3 Consistency

The discretization should become exact as the grid spacing tends to zero. The difference between the discretized equation and the exact one is called the *truncation error*. It is usually estimated by replacing the nodal values in the discrete approximation by a Taylor series expansion about a single point. As a result one recovers the original differential equation plus a remainder, which represents the truncation error. For a method to be *consistent*, the truncation error must become zero when the mesh spacing $\Delta t \rightarrow 0$ and/or $\Delta x_i \rightarrow 0$. The truncation error is usually proportional to a power of the grid spacing Δx_i and/or the time step Δt . If the most important term is proportional to $(\Delta x)^n$ or $(\Delta t)^n$ we call the method an n th-order approximation; $n > 0$ is required for consistency. Ideally, all terms should be discretized with approximations of the same order of

accuracy; however, some terms (eg. convective terms in high Reynolds number flows or diffusive terms in low Reynolds number flows) may be dominant in a particular flow and it may be reasonable to treat them with more accuracy than the others. Some discretization methods lead to truncation errors which are functions of the ratio of Δx_i to Δt or vice versa. In such a case the consistency requirement is only conditionally fulfilled: Δx_i and Δt must be reduced in a way that allows the appropriate ratio to go to zero. Even if the approximations are consistent, it does not necessarily mean that the solution of the discretized equation system will become the exact solution of the differential equation in the limit of small step size. For this to happen, the solution method has to be stable; which is defined below. [1]

2.2.4 Stability

A numerical solution method is said to be stable if it does not magnify the errors that appear in the course of numerical solution process. For temporal problems, stability guarantees that the method produces a bounded solution whenever the solution of the exact equation is bounded. For iterative methods a stable is one that does not diverge. Stability can be difficult to investigate, especially when boundary conditions and non-linearities are present. For this reason, it is common to investigate the stability of a method for linear problems with constant coefficients without boundary conditions. Experience shows that the results obtained in this way can often be applied to more complex problems but there are notable exceptions. The most widely used approach to studying stability of numerical schemes is the *von Neumann's method*. We shall describe it briefly for one scheme in the next paragraphs.

The von Neumann's method is based on the Fourier decomposition of the error. The discrete Fourier-series for the initial condition at the time $n=0$ in the interval of $x \in [0,1]$ can be stated as:

$$\xi_j^0 = \sum_{m=1}^J a_m e^{i m \pi (j \Delta x)} = \sum_{m=1}^J a_m e^{i \theta_m j} \quad , \text{ for } j = 1, 2, 3, \dots, J \text{ equation (2.26)}$$

while $\theta_m = m \pi \Delta x \in \mathbb{R}$ and $a_m \in \mathbb{C}$. The space is defined by $j \Delta x$, the wave number by $k = m \pi$ and the wave length is given by $\lambda = 2 \pi / k = 2 / m$.

for linear partial differential equations, only the temporal Fourier-series are needed. Since the modes are linear independent from each other, working with one mode is sufficient for the method. The general solution of the different equation is given by superposition. For the temporal expansion of ξ_j the *separation ansatz*

$$\xi_j^n = (G)^n \xi_j^0 = a (G)^n e^{i \theta j} \quad \text{equation (2.27)}$$

is used. $G \in \mathbb{C}$ is the separated time-dependency of the spatial mode of interest and represents the *enhancement factor* G at one time step:

$$G = \frac{\xi_j^{n+1}}{\xi_j^n} \quad . \text{ equation (2.28)}$$

The amplitude of the mode is amplified about the factor $(G)^n$ after n time steps. The enhancement factor G certainly depends on the wave number (θ respectively) and some other parameters.

The separation-ansatz should be implemented in the discretized differential equation of interest in order to checking the stability of the used discretization. Since it is necessary that the discretization scheme should be stable the error must not grow which leads to the condition for the enhancement factor:

$$|G| \leq 1 \quad . \text{ equation (2.29)}$$

[7]

When solving complicated, non-linear and coupled equations with complicated boundary conditions, there are few stability results so we may have to rely on experience and intuition. Many solutions schemes require that the time step be smaller than a certain limit or that under relaxation be used. [1]

2.2.5 Convergence

A numerical method is said to be convergent if the solution of the discretized equations tends to the exact solution of the differential equation as the grid spacing tends to zero. For linear initial value problems, the *Lax equivalence theorem* states that “given a properly posed linear initial value problem and a finite difference approximation to it that satisfies the consistency condition, stability is the necessary and sufficient condition for convergence”. Obviously, a consistent scheme is useless unless the solution method converges.

For non-linear problems which are strongly influenced by boundary conditions, the stability and convergence of a method are difficult to demonstrate. Therefore convergence is usually checked using numerical experiments, i.e., repeating the calculation on a series of successively refined grids. If the method is stable and if all approximations used in the discretization process are consistent, we usually find that the solution does converge to a *grid-independent solution*. For sufficiently small grid sizes, the rate of convergence is governed by the order of principal truncation error component. This allows us to estimate the error in the solution. [1]

2.3 Turbulence Models

All numerical methods that are described in the following sections require the solution of some form the conservation equation for mass, momentum, energy, or chemical species. The major difficulty is that turbulent flows contain variations on a much wider range of length and time scales than laminar flows. So, even though they are similar to the laminar flow equations, the equations describing turbulent flows are usually more difficult and expensive to solve. [1]

2.3.1 RANS (Reynolds-Averaged Navier-Stokes) Models

Engineers are normally interested in knowing just a few quantitative properties of a turbulent flow, such as the average force on a body, the degree of mixing between two incoming streams of fluid, or the amount of a substance that has reacted.

In Reynolds-averaged approaches to turbulence, all of the unsteadiness is averaged out, i.e. all unsteadiness is regarded as part of the turbulence. On averaging, the non-linearity of the Navier-Stokes equations gives rise to terms that must be modeled. The complexity of turbulence make it unlikely that any single Reynolds-averaged model will be able to represent all turbulent flows, so turbulence models should be regarded as engineering approximations rather than scientific laws.

When the flow becomes turbulent every variable can be written as the sum of a time-averaged value and a fluctuating value, i.e.

$$\Phi(x_i, t) = \bar{\Phi}(x_i) + \Phi'(x_i, t) \quad \text{equation (2.30)}$$

$$\text{where } \bar{\Phi}(x_i) = \lim_{T \rightarrow \infty} \frac{1}{T} \int_0^T \Phi(x_i, t) dt \quad \text{equation (2.31)}$$

Here t is the time and T is the averaging interval. This interval must be large compared to the typical time scale of the fluctuations; thus, we are interested in the limit of $T \rightarrow \infty$. If T is large enough, $\bar{\Phi}$ does not depend on the time at which the averaging is started. If the flow is unsteady, time averaging cannot be used and it must be replaced by ensemble averaging. This concept is illustrated in Figure 2.7..

$$\bar{\Phi}(x_i, t) = \lim_{N \rightarrow \infty} \frac{1}{N} \sum_{n=1}^N \Phi(x_i, t) \quad \text{equation (2.32)}$$

where N is the number of members of the ensemble and must be large enough to eliminate the effects of the fluctuations. This type of averaging can be applied to any flow. We use the term *Reynolds averaging* to refer to any of these averaging processes; applying Reynolds-averaging on the Navier-Stokes equations yields the Reynolds-averaged Navier-Stokes (RANS) equations.

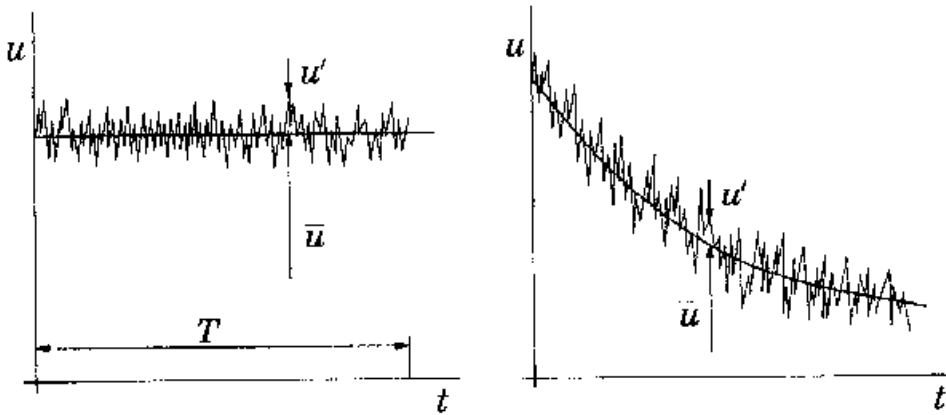


Figure 2.7.: Time averaging for a statistically steady flow (left) and ensemble averaging for an unsteady flow (right) [1]

From Eq. (2.31), it follows that $\overline{\Phi'} = 0$. Thus, averaging any linear term in the conservation equations simply gives the identical term for the averaged quantity. From a quadratic nonlinear term we get two terms, the product of the average and a covariance:

$$\overline{u_i \Phi} = \overline{(\bar{u}_i + u'_i)(\bar{\Phi} + \Phi')} = \bar{u}_i \bar{\Phi} + \overline{u'_i \Phi'} \quad \text{equation (2.33)}$$

The last term is zero only if the two quantities are uncorrelated; this is rarely the case in turbulent flows and, as a result, the conservation equations contain terms such as $\overline{\rho u'_i u'_j}$, called the *Reynolds stresses*, and $\overline{\rho u'_i \Phi'}$, known as the *turbulent scalar flux*, among others. These cannot be represented uniquely in terms of the mean quantities.

The averaged continuity and momentum equations can, for incompressible flows without body forces, be written in tensor notation and Cartesian coordinates as:

$$\frac{\partial(\rho \bar{u}_i)}{\partial x_i} = 0 \quad \text{equation (2.34)}$$

$$\frac{\partial(\rho \bar{u}_i)}{\partial t} + \frac{\partial}{\partial x_j} (\rho \bar{u}_i \bar{u}_j + \overline{u'_i u'_j}) = -\frac{\partial \bar{p}}{\partial x_i} + \frac{\partial \bar{\tau}_{ij}}{\partial x_j}, \quad \text{equation (2.35)}$$

where the $\bar{\tau}_{ij}$ are the mean viscous stress tensor components:

$$\bar{\tau}_{ij} = \mu \left(\frac{\partial \bar{u}_i}{\partial x_j} + \frac{\partial \bar{u}_j}{\partial x_i} \right) \quad \text{equation (2.36)}$$

Finally the equation for the mean of a scalar quantity can be written:

$$\frac{\partial(\rho \bar{\Phi})}{\partial t} + \frac{\partial}{\partial x_j} (\rho \bar{u}_j \bar{\Phi} + \overline{u'_j \Phi'}) = \frac{\partial}{\partial x_i} \left(\Gamma \frac{\partial \bar{\Phi}}{\partial x_j} \right) \quad \text{equation (2.37)}$$

The occurrence of pressure of the Reynolds stresses and turbulent scalar flux in the conservation equations means that the latter are not closed, that is to say, they contain more variables than there are equations. Closure requires use of some approximations, which usually take the form of

prescribing the Reynolds stress tensor and turbulent scalar fluxes in terms of the mean quantities. It is possible to derive a closed set of exact equations. To close the equations we must introduce turbulence models. The widely used turbulence models are introduced in the next paragraphs. [1]

2.3.1.1 Standard k- ϵ -Model

The Two-Equation, k- ϵ -Model calculates the turbulent viscosity using the ansatz:

$$\mu_t = \rho C_\mu \frac{k^2}{\epsilon} \quad , \quad C_\mu = 0.09 \quad . \text{ equation (2.38)}$$

The model assumes that the turbulent viscosity, $\mu_t = \rho \nu_t$, is related to the turbulent kinetic energy, k , and the dissipation rate of turbulent kinetic energy per unit volume, ϵ , where

$$\epsilon = \mu \left(\frac{\partial \overline{u_i}}{\partial x_k} \right)^2 \quad \text{equation (2.39)}$$

and C_μ is an empirical constant determined from experiments. This model is equivalent to a specification of a length scale

$$l_t = C_D \frac{k^{3/2}}{\epsilon} \quad \text{equation (2.40)}$$

and a time scale

$$\tau_t = C_t \frac{k}{\epsilon} \quad \text{equation (2.41)}$$

where both k and ϵ are determined by semi-empirical turbulent transport equations. The equations for k and ϵ are modeled as

$$\frac{Dk}{Dt} = \frac{1}{\rho} \frac{\partial}{\partial x_l} \left[\frac{\mu_t}{\sigma_k} \frac{\partial k}{\partial x_l} \right] + \frac{\mu_t}{\rho} \left(\frac{\partial U_i}{\partial x_l} + \frac{\partial U_l}{\partial x_i} \right) \frac{\partial U_i}{\partial x_l} - \epsilon \quad \text{equation (2.42)}$$

$$\frac{D\epsilon}{Dt} = \frac{1}{\rho} \frac{\partial}{\partial x_l} \left[\frac{\mu_t}{\sigma_\epsilon} \frac{\partial \epsilon}{\partial x_l} \right] + \frac{C_1 \mu_t}{\rho} \frac{\epsilon}{k} \left(\frac{\partial U_i}{\partial x_l} + \frac{\partial U_l}{\partial x_i} \right) \frac{\partial U_i}{\partial x_l} - \frac{C_2 \epsilon^2}{k} \quad \text{equation (2.43)}$$

where the constants are chosen to be

$$C_1 = 1.44 \quad , \quad C_2 = 1.92 \quad , \quad \sigma_k = 1.0 \quad \text{and} \quad \sigma_\epsilon = 1.3 \quad \text{equation (2.44)}$$

The equation for k is derived in a straightforward fashion from the Reynolds stress equations, but the ϵ equation has empirical roots. In fact, the lack of physical interpretation of the ϵ equation may lead to its downfall as more complicated flows are attempted. Also, the model as currently formulated does not predict accurately the transition and viscous layers near the wall. In order to treat these regions, wall functions or additional low Reynolds number modeling must be added to both the k and the ϵ equations. Both of these near-wall, corrections continue to undergo extensive study and revision. The k- ϵ -model is only valid for high-Reynolds number flows. The k- ϵ model is the most widely applicable model of the existing models, but with considerable deficiencies. [8, 6]

2.3.1.2 RNG- k - ε -Model

The RNG- k - ε -model was developed using Renormalization group methods by *Yakhot et al.* to renormalize the Navier-Stokes equations, to account for the effects of smaller scales of motion. The RNG- k - ε -model brings improvements in contrast to the Standard- k - ε -Model. The RNG approach, which is a mathematical technique yields an additional term in the epsilon equation which attempts to account for the different scales of motion through changes to the production term. Hence, it is suitable for low Reynolds number flows than the Standard k - ε -model. The effects near the boundaries are better calculated by using the RNG k - ε -Model in contrast to the Standard- k - ε -Model and the effect of swirls is included in this mathematical method. These features make the RNG k - ε -Model more accurate and reliable for a wider class of flows. [9]

2.3.1.3 k - ω -Model

Another two-equation model is the k - ω model by *Wilcox*. One equation formulates the turbulent kinetic energy k and the second equation describes the variable ω – defined as dissipation per turbulent kinetic energy. The k - ω model uses the kinetic energy equation from the proceeding section, but it is modified:

$$\rho \frac{\partial k}{\partial t} + \rho U_j \frac{\partial k}{\partial x_j} = \tau_{ij} \frac{\partial U_i}{\partial x_j} - \beta^* \rho k \omega + \frac{\partial}{\partial x_j} \left[(\mu + \sigma^* \mu_t) \frac{\partial k}{\partial x_j} \right] \quad \text{equation (2.45)}$$

The equation for the specific dissipation rate ω is given by Wilcox as:

$$\rho \frac{\partial \omega}{\partial t} + \rho U_j \frac{\partial \omega}{\partial x_j} = \alpha \frac{\omega}{k} \tau_{ij} \frac{\partial U_i}{\partial x_j} - \beta \rho \omega^2 + \frac{\partial}{\partial x_j} \left[(\mu + \sigma \mu_t) \frac{\partial \omega}{\partial x_j} \right] \quad \text{equation (2.46)}$$

In this model the eddy-viscosity is expressed as:

$$\mu_t = \rho \frac{k}{\omega} \quad \text{equation (2.47)}$$

The closure coefficients are different from those of the k - ε -model:

$$\alpha = \frac{5}{9} \quad , \quad \beta = \frac{3}{40} \quad , \quad \beta^* = \frac{9}{100} \quad , \quad \sigma^* = \sigma = \frac{1}{2} \quad \text{equation (2.48)}$$

The model performs best at low to medium Reynolds numbers. [10]

2.3.1.4 Reynolds Stress Model (RSM)

The most complex models in common use today are Reynolds stress models which are based on dynamic equations for the Reynolds stress tensor $\tau_{ij} = \rho \overline{u_i' u_j'}$ itself. These equations can be derived from the Navier-Stokes equations and are given as:

$$\frac{\partial \tau_{ij}}{\partial t} + \frac{\partial \overline{u_k} \tau_{ij}}{\partial x_k} = - \left(\tau_{ik} \frac{\partial \overline{u_j}}{\partial x_k} + \tau_{jk} \frac{\partial \overline{u_i}}{\partial x_k} \right) + \rho \epsilon_{ij} - \Pi_{ij} + \frac{\partial}{\partial x_k} \left(\nu \frac{\partial \tau_{ij}}{\partial x_k} + C_{ijk} \right) \quad \text{equation (2.49)}$$

The left hand side is always exact. The first two terms of the right hand side are the production terms and require no approximation or modeling. The following term is defined as:

$$\rho \epsilon_{ij} = 2\mu \overline{\frac{\partial u'_i}{\partial x_k} \frac{\partial u'_j}{\partial x_k}} \quad \text{equation (2.50)}$$

which is the dissipation tensor. The following term:

$$\Pi_{ij} = p' \overline{\left(\frac{\partial u'_i}{\partial x_k} + \frac{\partial u'_j}{\partial x_k} \right)} \quad \text{equation (2.51)}$$

is often called the pressure-strain term. It redistributes turbulent kinetic energy among the components of the Reynolds stress tensor but does not change the total kinetic energy. The last term is:

$$C_{ijk} = \rho \overline{u'_i u'_j u'_k} + \overline{p' u'_i} \delta_{ik} + \overline{p' u'_j} \delta_{ik} \quad \text{equation (2.52)}$$

and is often called the turbulent diffusion.

The dissipation, pressure-strain, and turbulent diffusion terms cannot be computed exactly in terms of the other terms in the equations and therefore must be modeled. The simplest and most common model for the dissipation term treats it as isotropic, i.e., instead of a tensor a scalar domain- the dissipation rate ϵ , that is used in the proceeding sections - is calculated:

$$\epsilon_{ij} = \frac{2}{3} \epsilon \delta_{ij} \quad \text{equation (2.53)}$$

This means that an equation for the dissipation must be solved along with the Reynolds stress equations. Typically, this equation is taken to formulate the dissipation, ϵ , in the k - ϵ -model.

In three dimensions, Reynolds stress models require the solution of seven partial differential equations in addition to the equations for the mean flow (six components for the Reynolds stress tensor – since it is symmetric - and one equation for ϵ). Still more equations are needed when scalar quantities need to be predicted. These equations are solved in a manner similar to that for the k - ϵ equations. The only additional issue is that when the Reynolds-averaged Navier-Stokes equations are solved together with a Reynolds stress model they are even stiffer than those obtained with the k - ϵ equations and even more care is required in their solution and the calculations usually converge more slowly.

While there is no doubt that Reynolds stress models have greater potential to represent turbulent flow phenomena more correctly than the two-equation models, their success so far has been moderate. Excellent results have been obtained for some flows in which k - ϵ models perform badly (e.g., swirling flows, flows with stagnation points or lines, flows with strong curvature and with separation from curved surfaces, etc.); however, in some flows their performance is hardly better at all. There is a lot of current research in this field, and new models are often proposed. Which model is best for which kind of flow (none is expected to be good for all flows) is not yet clear, partly due to the fact that in many attempts to answer this question numerical errors were too large to allow clear conclusions to be reached. [1]

2.3.2 Direct Numerical Simulation (DNS)

A direct numerical simulation is a simulation in which the Navier-Stokes equations are solved without using averaging or approximation other than numerical discretization whose errors can be estimated and controlled. In such simulations, all of the motions contained in the flow are resolved. The computed flow field obtained is equivalent to a short-duration laboratory experiment.

In a direct numerical simulation, in order to assure that all of the significant structures of turbulence have been captured, the domain on which the computation is performed must be at least as large as the physical domain to be considered or the largest turbulent eddy. A useful measure of the latter scale is the integral scale of turbulence L which is essentially the distance over which the fluctuating of the viscosity remains correlated. Thus, each linear dimension of the domain must be at least a few times the integral scale. A valid simulation must also capture all of the kinetic energy dissipation. This occurs on the smallest scales, the ones on which viscosity is active, so the size of the grid must be no larger than a viscosity determined scale, called the *Kolmogoroff scale*, η .

Since the grid points that can be used in a computation is limited by the proceeding speed and memory of the machine on which it is carried out direct numerical simulation is possible only for flows at relatively low Reynolds numbers and in geometrically simple domains. On present machines, it is possible to make direct numerical simulations of homogeneous flows at turbulent Reynolds numbers up to a few hundred. At the low end of the range of Reynolds numbers the DNS is for engineers a useful method in some cases.

The results of a DNS contain very detailed information about the flow. This can be very useful but, on the one hand, it is far more information than any engineer needs and, on the other, DNS is too expensive to be employed very often and cannot be used as a design tool. One must then ask what DNS can be used for. With it, one can obtain detailed information about the velocity, pressure, and any other variable of interest at a large number of grid points. These results may be regarded as the equivalent of experimental data and can be used to produce statistical information or to create a 'numerical flow visualization'. From the latter, one can learn a great deal about the coherent structures that exist in the flow. DNS makes it possible to investigate certain effects accurately. This wealth of information can then be used to develop a qualitative understanding of the physics of the flow or to construct a quantitative model, which will allow other, similar, flows to be computed. One can thus conclude that the major role that DNS can fill is as a research tool. [1]

2.3.3 Large Eddy Simulation (LES) and Detached Eddy Simulation (DES)

The *Large Eddy Simulation (LES)* is a popular technique for the simulation of turbulent flows. As we have noted, turbulent flows contain a wide range of length and time scales; the range of eddy sizes that might be found in a flow is shown schematically in Fig. 2.8.

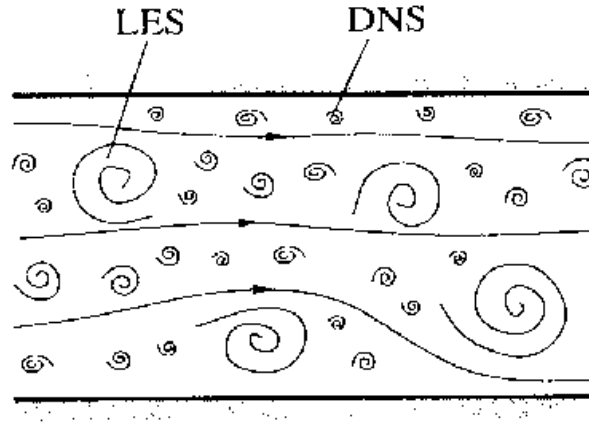


Figure 2.8. Schematic representation of turbulent motion [1]

The large scale motions are generally much more energetic than the small scale ones; their large size and strength make them by far the most effective transporters of the conserved properties. The small scales are usually much weaker and provide little transport of these properties. A simulation which treats the large eddies more exactly than the small ones may make sense; large eddy simulation is just such an approach. Large eddy simulations are three dimensional, time dependent and expensive but much less costly than DNS of the same flow. In general, because it is more accurate, DNS is the preferred method whenever it is feasible. LES is the preferred method for flows in which the Reynolds number is too high or the geometry is too complex to allow application of DNS.

A velocity field that contains only the large scale components of the total field is needed for the LES approximation. This is best produced by filtering the velocity field; in this approach, the large or resolved scale field, the one to be simulated, is essentially a local average of the complete field. A one-dimensional notation is used; the generalization to three dimensions is straightforward. The filtered velocity is defined by:

$$\bar{u}_i(x) = \int G(x, x') u_i(x') dx' \quad \text{equation (2.54)}$$

where $G(x, x')$, the filter kernel, is a localized function. Filter kernels which have been applied in LES include a Gaussian, a box filter (a simple local average) and a cutoff (a filter which eliminates all Fourier coefficients belonging to wave numbers above a cutoff). Every filter has a length scale associated with it, Δ . Roughly, eddies of size larger than Δ are large eddies while those smaller than Δ are small eddies, the ones that need to be modeled.

When the Navier-Stokes equations with constant density (incompressible flow) are filtered, one obtains a set of equations very similar to the RANS equations:

$$\frac{\partial(\rho \bar{u}_i)}{\partial t} + \frac{\partial(\rho \bar{u}_i \bar{u}_j)}{\partial x_j} = -\frac{\partial \bar{p}}{\partial x_i} + \frac{\partial}{\partial x_j} \left[\mu \left(\frac{\partial \bar{u}_i}{\partial x_j} + \frac{\partial \bar{u}_j}{\partial x_i} \right) \right] \quad \text{equation (2.55)}$$

Since the continuity equation is linear, filtering does not change it:

$$\frac{\partial(\rho \bar{u}_i)}{\partial x_i} = 0 \quad \text{equation (2.56).}$$

[1]

The *detached eddy simulation (DES)* is a very new hybrid technique, that is introduced by *Travin et al.* (2000) and already included in commercialized CFD-codes. This simulation uses a RANS-method in the adjacent boundary layers, while the LES is used to resolve the shear flow which results from flow separation. Since near-wall regions do not need to be resolved in detail, the DES can be applied for high Reynolds number flow. Admittedly the coupling of these regions and their boundary conditions meet to problems. Since very good results have been achieved by applying the DES to many applications (mainly to the prediction of aerodynamic noises), also disappointing results are published. [11]

2.4 Pipe Flow

Flow phenomena in round pipes are a subject of interest for technical applications as well as for scientific research. Pipes a very suitable tool for fundamental experiments, since many phenomena can be observed and documented without great complexities and the Navier-Stokes equations can be solved exactly. These research findings can be applied on similar problems in fluid mechanics.

2.4.1 Laminar Pipe Flow

A classic problem is the steady laminar flow of a Newtonian fluid through a very long pipe of radius R , as shown in Figure 2.9. (a). Let x be the axial coordinate.

For a location far downstream of the entrance, the flow will be *fully-developed*, that is, the axial velocity $u=u(r)$ in the plane velocities $v=w=0$. Then continuity is satisfied identically and the momentum equation reduces to

$$\frac{\mu}{r} \frac{\partial}{\partial r} \left(r \frac{\partial u}{\partial r} \right) = \frac{\partial p}{\partial x} = \text{constant} \quad \text{equation (2.57)}$$

subject to the no-slip condition $u(R) = 0$

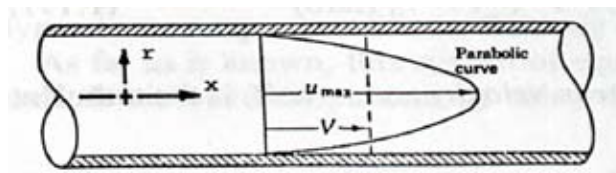


Figure 2.9.: velocity-profile of a fully-developed laminar pipe flow [6]

The solution is the Poiseuille paraboloid distribution:

$$u = u_{\max} \left(1 - \frac{r^2}{R^2} \right) \quad \text{equation (2.58)}$$

where

$$u_{max} = \frac{R^2}{4\mu} \left(-\frac{dp}{dx} \right) \quad \text{equation (2.59)}$$

The average velocity V can be computed from the volume flow

$$V = \frac{Q}{A}, \quad Q = \int u dA \quad \text{equation (2.60)}$$

After combining the two equations one yields the laminar solution:

$$V = \frac{1}{2} u_{max} = \frac{R^2}{8\mu} \left(-\frac{dp}{dx} \right) \quad \text{equation (2.61)}$$

The pressure drop through a pipe of length L can be derived from equation and one gets the pressure gradient as follows:

$$-\frac{dp}{dx} = \frac{\Delta p}{L} = 8\mu Q / (\pi R^4) = 8\mu V / R^2 \quad \text{equation (2.62)}$$

That means that the drop in pressure is proportional to the velocity. The pipe Reynolds number is defined as

$$Re_D = \frac{\rho V D}{\mu} \quad \text{equation (2.63)}$$

Pressure drop and velocity distribution can be computed easily for fully-developed laminar pipe flow, but the results are only valid up to Reynolds numbers $Re_D = 2000$, after which the flow gets unstable undergoes a transition to turbulence. [6]

2.4.2 Turbulent Pipe Flow and the Law-of-the-Wall

The analysis of turbulent pipe is simplified by the fact that the mean velocity profile is correlated over the complete range of Reynolds numbers by a simple formula called the *Law-of-the-Wall*. Both axial velocity U and distance y from the wall are non dimensionalized by wall shear stresses, density, and viscosity

$$u^+ = \frac{U}{u_*} \quad \text{the dimensionless velocity,} \quad u_* = \left(\frac{\tau_w}{\rho} \right)^{1/2} \quad \text{equation (2.64)}$$

$$y^+ = \frac{\rho u_* y}{\mu} \quad \text{the dimensionless distance from the wall equation (2.65)}$$

where $y = R - r$ for pipe flow. R is the radius of the pipe. For smooth wall flow with a negligible pressure gradient, turbulent velocity data forms a nearly unique curve $u^+(y^+)$, as shown in Figure 2.10. Except very near the wall and in the center of the pipe, the data is well approximated by a logarithmic law

$$u^+ = \frac{1}{\kappa} \ln(y^+) + 5.0, \quad \kappa = 0.41 \quad \text{equation (2.66)}$$

This correlation of constants was developed in the 1930's by L. Prandtl and by T. von Karman; the constant κ is now called the Karman's constant and is sensitive to wall or external flow conditions. Note in Figure 2.10., the viscous sublayer very near the wall ($y^+ \leq 5$), where $u^+ = y^+$ and turbulence effects on the profile are completely damped out. [6]

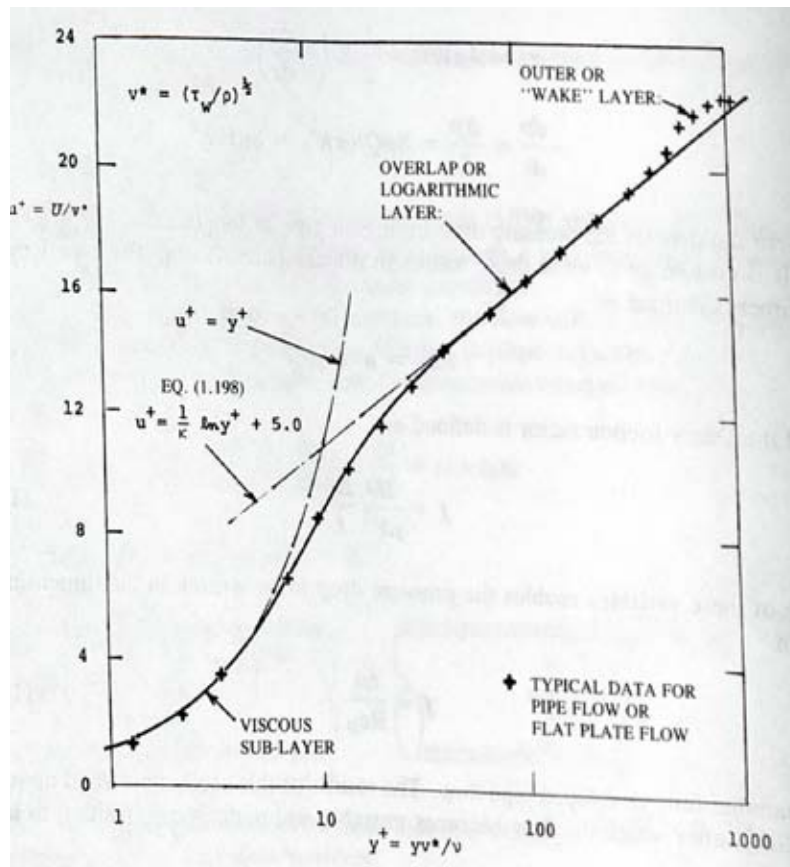


Figure 2.10.: The law-of-the-wall for turbulent mean flow past a smooth, impermeable surface with modest pressure gradient [6]

A more elaborate treatment divides the flow in a pipe into a laminar sublayer near the wall, a turbulent core and a buffer layer in between. The velocity profile obtained is given in the form of three equations, one for each region. It is known as the universal profile and it holds for the whole cross section of the pipe.

For the laminar sublayer, which extends from the wall to $y^+ = 5$, the profile is linear:

$$u^+ = y^+ \quad , \quad 0 \leq y^+ < 5 \quad \text{equation (2.67)}$$

For the buffer layer the profile is given by

$$u^+ = 5.0 \ln(y^+) + 3.5 \quad , \quad 5 \leq y^+ < 30 \quad \text{equation (2.68)}$$

while for the turbulent core Prandtl's simple expression still applies,

$$u^+ = 2.5 \ln(y^+) + 5.5 \quad , \quad y^+ \geq 30 \quad \text{equation (2.69)}$$

The universal profile given by equations (2.67.), (2.68.) and (2.69) applies to turbulent flows in smooth pipes. It is particularly useful in the analysis of heat and mass transfer to walls in turbulent conduit flows, where the processes depend strongly on the flow field details near the wall. In some cases the use of the profile, ignoring the laminar sublayer and the buffer zone, yields also good results. [3]

2.5 Free Jet

The mixing of a free jet and its vicinity is of great importance for practical and theoretical reasons. If an air jet resigns from a blind, as pictured in Figure 2.11., ram pressure profiles are enlarging sideways and the original exit speed is only available in the center.

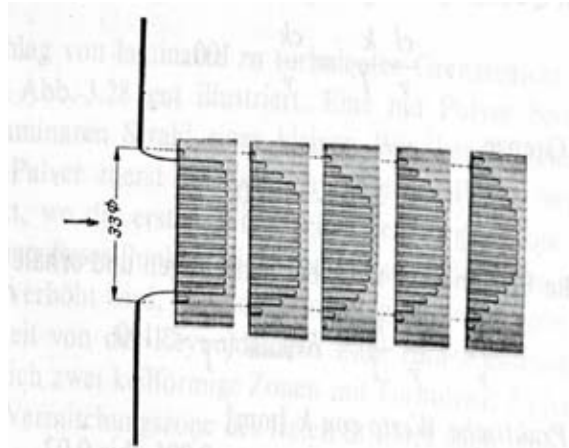


Figure 2.11.: Development of ram pressure profiles [12]

A schematic overview is given in Figure 2.11.. Afterwards the jet spreads straight-lined, while a steadily decreasing part of the jet still moves with the original injector exit speed in the jet's center. This area is called the *core* of the jet. It has the form of a cone and is 4 to 4,74 times the length of the jet's diameter. The propagation of the jet also has the form of a cone whereas the total momentum is preserved. Air particles are swept along from the outside so that the amount of air in the jet direction is increasing. The development of a free jet is documented in figure 2.12. While the inside cone angle δ_i of the development of the core is clearly defined, another question arises: How should the outside angle δ_a be determined?

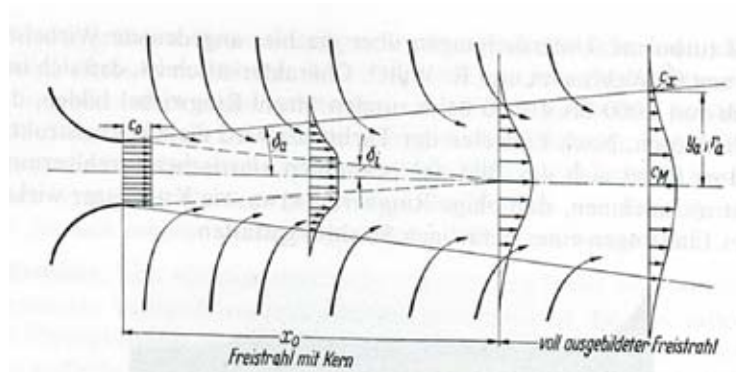


Figure 2.12.: Development of a free jet [12]

The speed profile moves diffusely ad infinitum and this represents another difficulty. In this case it is necessary to define that point as a barrier, where the speed matches a special part of the speed in the jet's center, such as 0.5 0.05 etc. In the inside of the jet there is a small overpressure, which is about $\frac{1}{2}$ % of the ram pressure. Furthermore, the overpressure results from the impact of the

impulse of the streaming air, which streams in from outside. This impulse is always constant due to the same pressure. This is an especially beautiful result of Prandtl's turbulence theory because the theoretical calculation of this case has succeeded and has been affirmed completely. The account, that the mixing path in the mixing zone is constant and proportional to its particular width, was responsible for its success. However, the ratio of mixing path/width of the mixing zone is taken from experimental results. [12]

Despite extensive research, there exists still some unclarity regarding the turbulence in the core jet. In the course of all experiments, scientists have mostly worked with air of great speed and high Reynolds number, that streamed out of an injector. As a result, impacts of the turbulence's character of the core were not observed. In a transition zone of smaller Reynolds numbers it seems that there is such an influence. In the area of air conditioning of rooms, scientists have proved such an influence. It has been found out that laminar streams penetrate greater distances than turbulent streams. These differences of the depth of impression are observed in the order of 1:3. Therefore scientists should take account this influence by introducing a factor m . Depending on the turbulence, the angle δ_i of the core is bigger or smaller. This means $\tan(2\delta_i) = d/x_0 = m$.

In connection with a freeblowing stream another useful and important phenomena will be described. There exists a difference between a freeblowing and suction process in a closed room. This is a problem especially in connection with air ventilation. In order to illustrate these differences, one observes the following experiment. If one tries to aspirate the fumes of cigarettes which have already been blown out of the mouth, it will not work. During the suction process, air particles stream in from all sides, as pictured in Figure 2.13. A suction of purged air will not occur. [12]

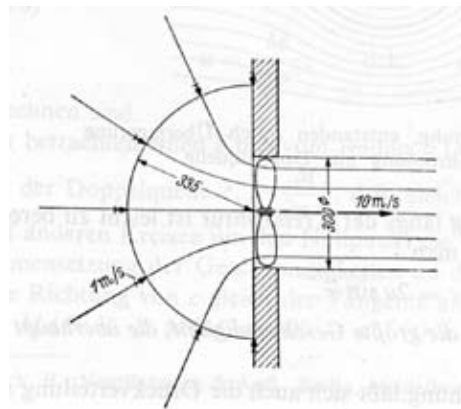


Figure 2.13.: air particles stream in from all sides [12]

The extension of a stream through micro strainers. While accelerated streams can make any contractions possible, they can just reach moderate grades of deceleration. The possible cross-section extension is limited by the angles which may lead to the development of turbulent mixing. Values from 10° to 14° are surely within reach. If higher cross-section extensions are needed, they are most likely to be reached with the help of micro strainers. Figure 2.14 shows the fluid flow of a stream with three micro strainers, which are put in series. The result is that the fluid flow is spreading immediately to the fourfold cross-section. The flow of the fluid becomes more and more constant, the more micro strainers are used. Several wide-mashed micro strainers work better than one small-meshed micro strainer. However, it is clear that this sudden delay can only be explained with a huge loss of energy. [12] The deceleration and the stream extension of a fluid flow is also

observed in the simulations that are performed in this thesis. Turbulence generators that are built of blades, spikes and rods are positioned in the pipe outlet to create a turbulent flow field. This is described in detail in the following chapter. [12]

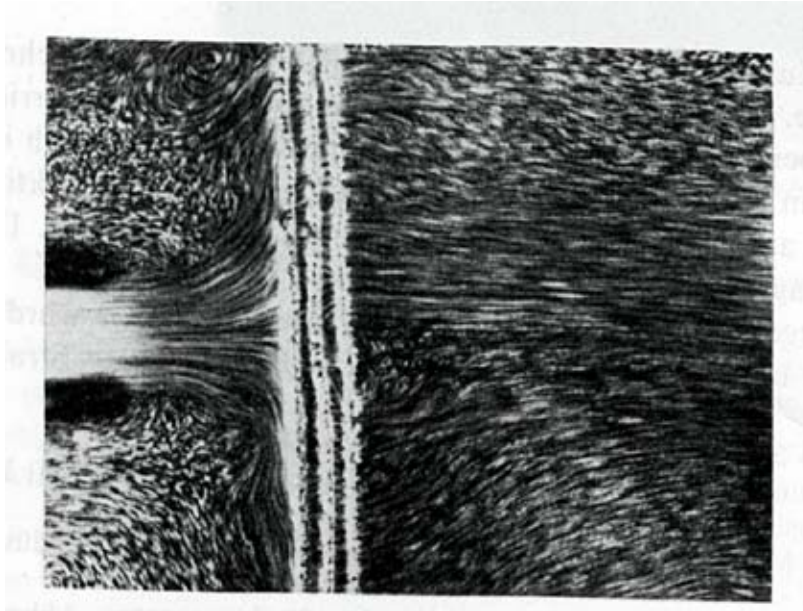


Figure 2.14.: Stream extension after passing a microstrainer [12]

3 Geometry

The geometry for the CFD simulation is designed on the basis of the experimental setup. Some simplifications are needed, as for building a mesh that guarantees a good mesh quality or for controlling the number of cells in the mesh. An increased number of cells also leads to increased calculation times. The whole geometry is designed with the geometry- and meshing- tool GAMBIT. In general GAMBIT is a preprocessor for CFD analysis. The calculation geometry is rebuilt for each turbulence generator which leads to eleven different setups. Figure 3.1 shows the graphical user interface of the software tool GAMBIT.

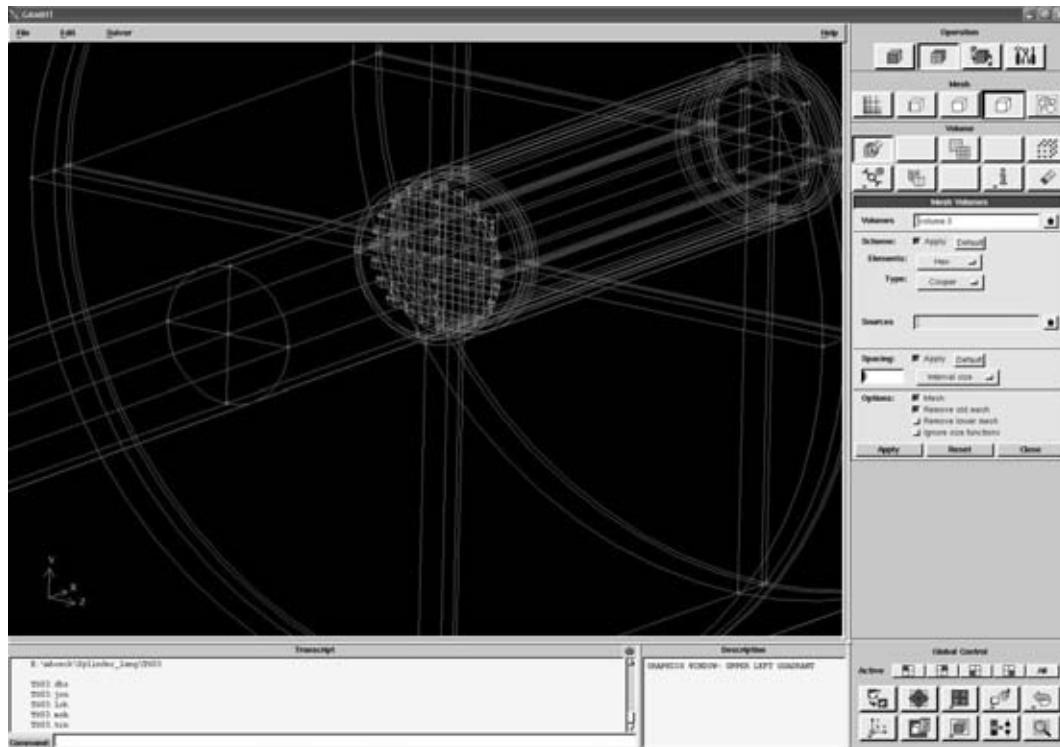


Figure 3.1.: GAMBIT graphical user interface

The geometric definition of the calculation volume is given in Figure 3.2.

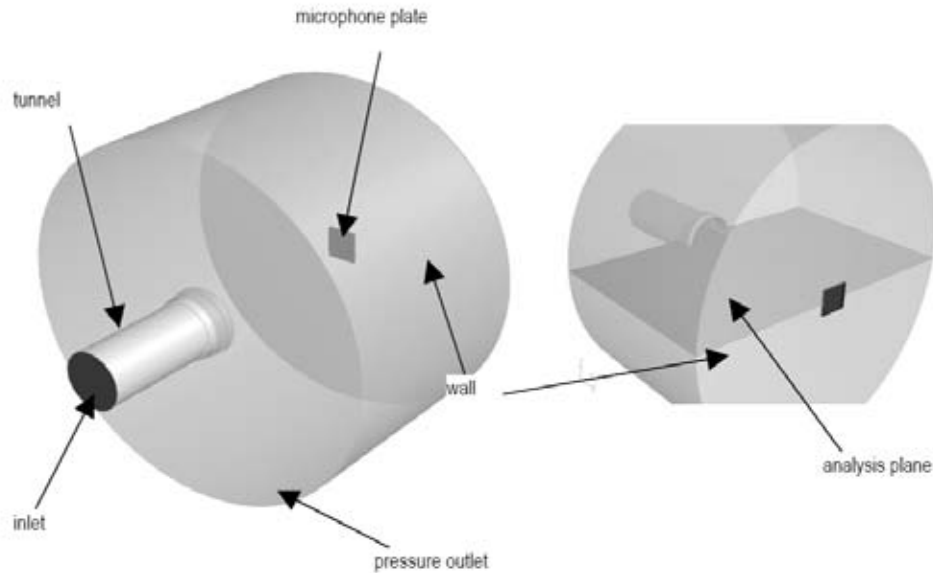


Figure 3.2.: Geometry for the CFD Simulation

The process that is going to be simulated is explained in the following paragraph. A circular pipe flow leaves the cylindrical tube and the generated separating jet impinges on a wall which is 550 millimeters distant from the pipe outlet. Since it is the aim of this work to investigate the characteristics of turbulence, different sets of turbulence generators consisting of rods, cubes and spikes are used. These turbulence generators are all positioned at the pipe outlet.

Twelve different evaluation lines L01-L12 are defined in the area between the pipe outlet and the plate. The x-coordinates positions of the evaluation lines in the analysis plane are summarized in Figure 3.3., 3.4. and Figure 3.5. below.

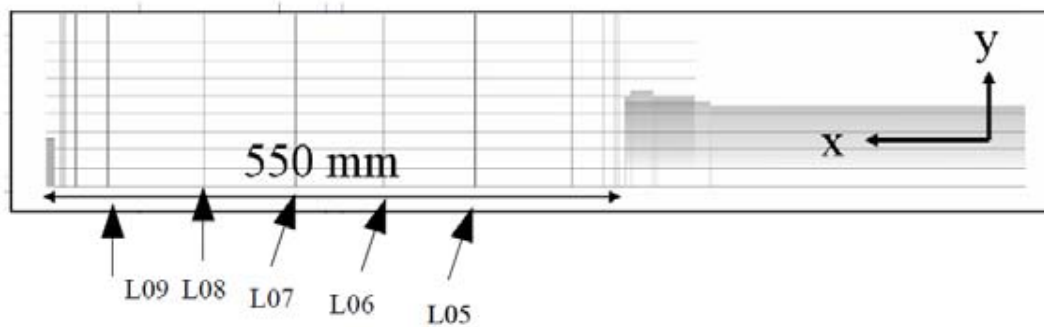


Figure 3.3.: Evaluation lines L01-L12 in the analysis plane

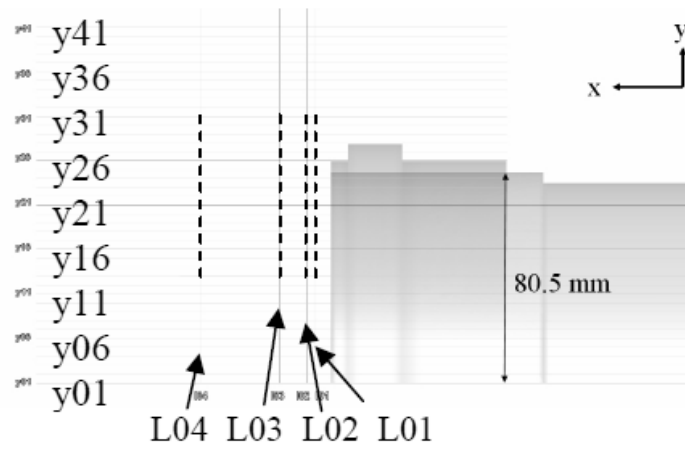


Figure 3.4.: Lines L01-L04 in detail

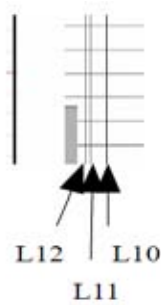


Figure 3.5.: Lines L10-L12 in detail

The x-coordinates positions of the evaluation lines in the analysis plane are given by table 3.1.

Line-name	Position on the x-axis [mm]
L01v	6.00
L02v	9.40
L03v	19.59
L04v	50.17
L05v	141.90
L06v	229.26
L07v	312.74
L08v	400.10
L09v	491.83
L10v	522.41
L11v	532.60
L12v	536.00

Table 3.1.: x-coordinates

3.1 Geometry of Turbulence Generators

Different turbulence generators are positioned in the pipe outlet as described in the proceeding section to create different turbulent flow fields. These turbulence generators TG00-TG10 built of spikes, rods and blades, are illustrated in the following figures. The TG00 is the only pipe section without any obstruction.



Figure 3.6.: TG00



Figure 3.7.: TG01



Figure 3.8.: TG02



Figure 3.9.: TG03



Figure 3.10: TG04



Figure 3.11.: TG05



Figure 3.12.: TG06



Figure 3.13.: TG07



Figure 3.14.: TG08



Figure 3.15.: TG09



Figure 3.16.: TG10

3.2 Degrees of Obstruction

The installation of spikes, rods and blades in the pipe outlet has a great impact on the flow field. The turbulence generators change the form and area of the cross-section at the pipe outlet, which influences the characteristics of the pipe flow leaving the outlet to different pressure gradients Δp . Additionally the fan speed is influenced by the pressure drop inside the pipe. The pass-through surface area of the pipe's cross-section is pictured in the following figures.



Figure 3.17.: TG01



Figure 3.18.: TG02

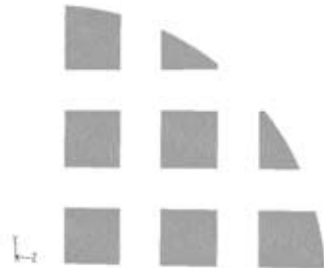


Figure 3.19.: TG03



Figure 3.20.: TG04

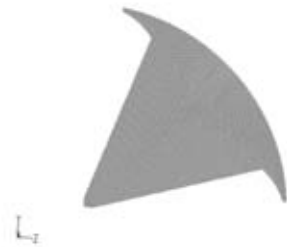
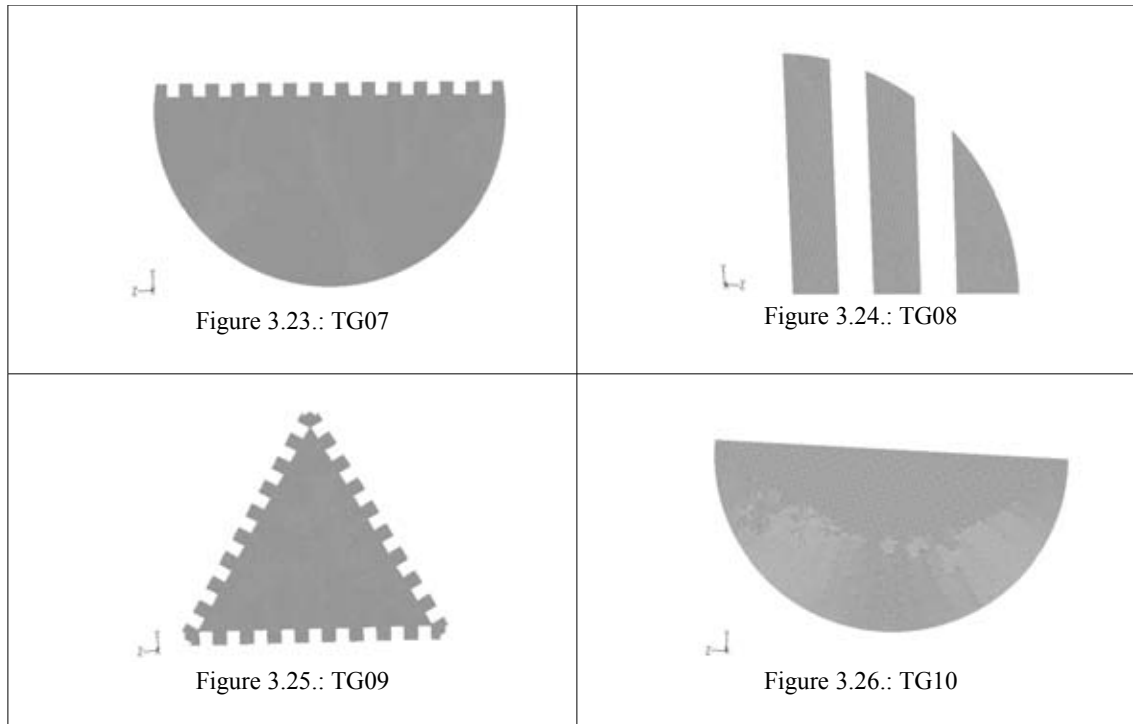


Figure 3.21: TG05



Figure 3.22.: TG06



The surface area of the pass-through surface for each turbulence generator is listed in table 3.2. Additionally, the size of the obstructed areas and their percentage on the total cross-section for different geometries can be seen in the following table:

turbulence generator	area of the pass-through surface [mm ²]	obstructed surface area [mm ²]	degree of obstruction [%]
TG00	20 459	-	-
TG01	12 116	8 343	40.78
TG02	12 929	7 830	38.27
TG03	7 731	12 728	62.21
TG04	7 172	13 287	64.94
TG05	13 193	7 266	35.51
TG06	15 010	5 449	26.64
TG07	11 803	8 656	42.31
TG08	12 061	8 398	41.05
TG09	5 579	14 880	72.73
TG10	10 504	9 955	48.66

Table 3.2.: degrees of obstruction for each turbulence generator

4 Mesh Generation

All geometries used for simulations in this thesis are meshed with the CFD preprocessing-software GAMBIT. The user interface of the mesh generation software with a meshed geometry can be seen from Figure 4.1. Since eleven different geometry setups have been created, each one of those needs to be meshed separately.

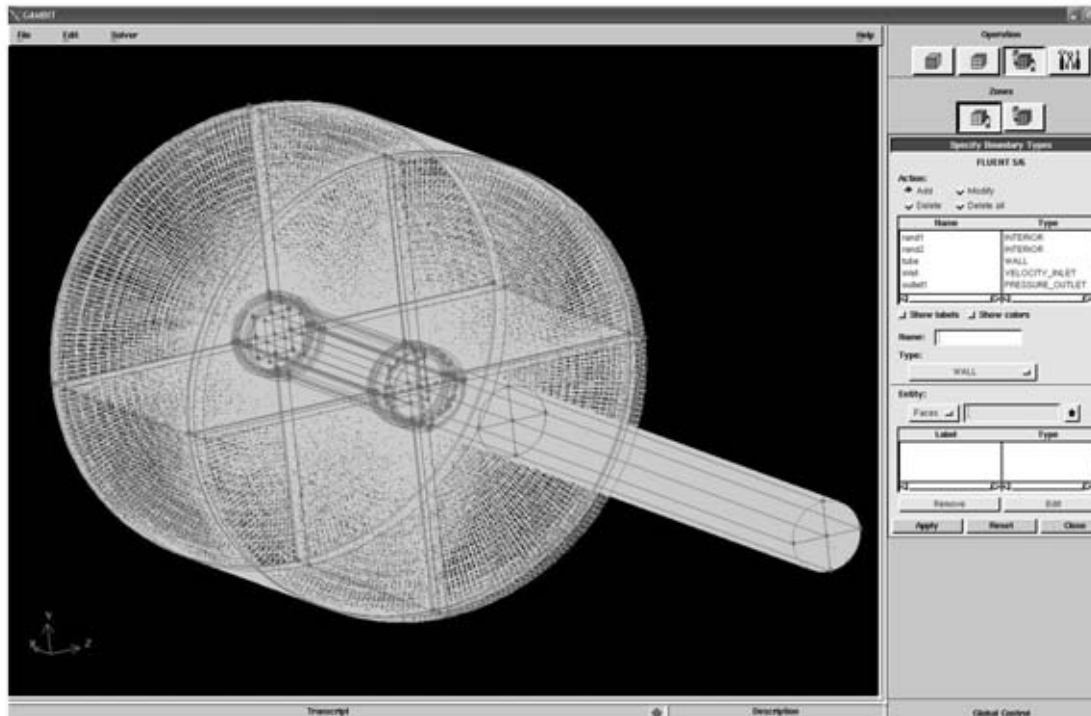


Figure 4.1.: software interface of GAMBIT for mesh generation

4.1 Meshing Strategies

For discretization the flow domains have to be split in smaller subdomains made up of geometric figures like tetrahedra or hexahedra in 3D and quadrilaterals and triangles in 2D respectively. The partial differential equations describing the flow are then discretized and solved inside each of these subdomains. The subdomains are often called elements or cells, and the collection of all elements or cells is called a mesh or grid. Mesh generation is the process of obtaining an appropriate mesh in the flow domain. It is essential that the grid is fitted to the size and form of the geometry. The mesh quality can have a great impact on the accuracy of the solutions resulting from the computational analysis. Grid refinement on the boundaries is achieved by increasing the number of cells, which may lead to a better resolution of smaller eddy structures in the flow. The drawback of achieving high numbers of cells is the increasing calculation time. For industrial applications particularly long calculation times of some weeks are not desired. Thus a compromise between the number of cells and the accuracy of the calculation must be found. The meshes in this thesis consist of four to six million elements.

Primarily the geometry has to be clean and connected before one starts the meshing process. As mentioned in the proceeding paragraph the quality of the grid is basically important for the accuracy

of the computational analysis. It is very important to reproduce the physical phenomena in the flow correctly. The quality of a grid [6] is defined by basic metric measures. These metric measures include cell aspect ratios, lengths, angles, and sizes. It also includes variations of these items as we go to their neighbors. This is just the smoothness in the distribution of these properties. In the case of structured grids, good geometric quality is seen as smooth variations in cell properties with angles that are nearly perpendicular. In case of unstructured grids, quality is seen as smoothness together with nearly equilateral triangles in 2D or similarly contrived tetrahedra in 3D. For unstructured paving (quadrilaterals) and plastering (hexahedrals) it is smoothness and orthogonality. Examples of a structured (regular) and one unstructured grid are given in Figures 4.2. and 4.3. [1].

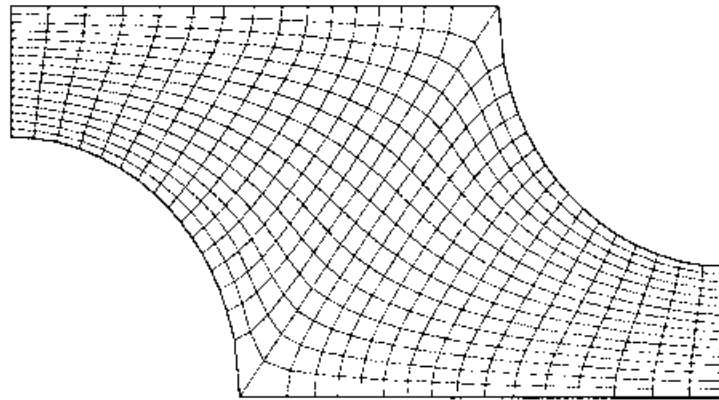


Figure 4.2.: Example of a 2D, structured, non-orthogonal grid [1]

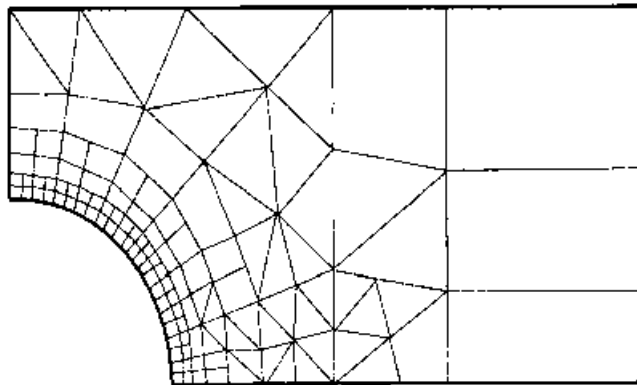


Figure 4.3.: Example of a 2D unstructured grid [1]

Strong acute and obtuse angles in the elements should be avoided, otherwise numerical problems cannot be excluded. Two examples of undesirable distortions of control volumes are depicted in Figure 4.4. In one case, the upper face of a regular hexahedral CV is rotated around its normal, warping the adjacent faces. In the other case, the top face is sheared in its own plane. Both features are undesirable and should be avoided at all if possible.

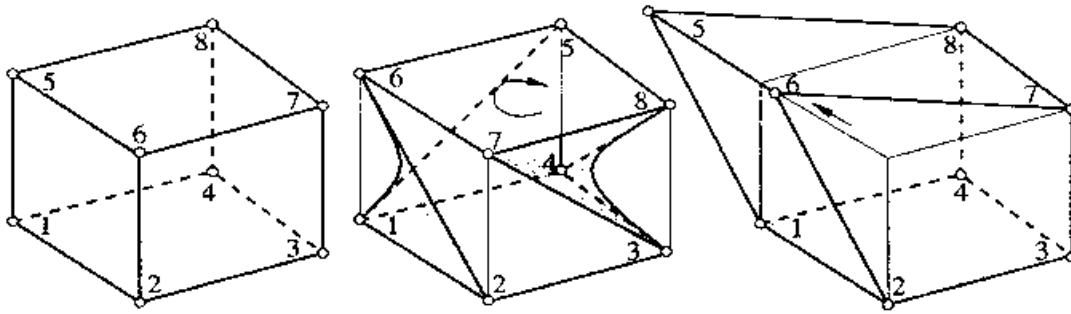


Figure 4.4.: An example of poor grid quality due to warping (middle) and distortion (right) [1]

4.2 Meshing Process

This section will explain the special meshing strategy for the geometry, as pictured in Figure 3.2. with the different turbulence generators (Figures 3.4. - 3.14.) located in the pipe outlet. As shown in Figure 3.1 and 4.1. the whole domain is cut into quarters in the direction of the y- and z-axis. Furthermore the geometry is cut into slices. By separating the originally entire volume into quarter slices it gets easier to achieve a mesh with good quality. To simplify the description of this meshing process the final grid is pictured in Figure 4.5..

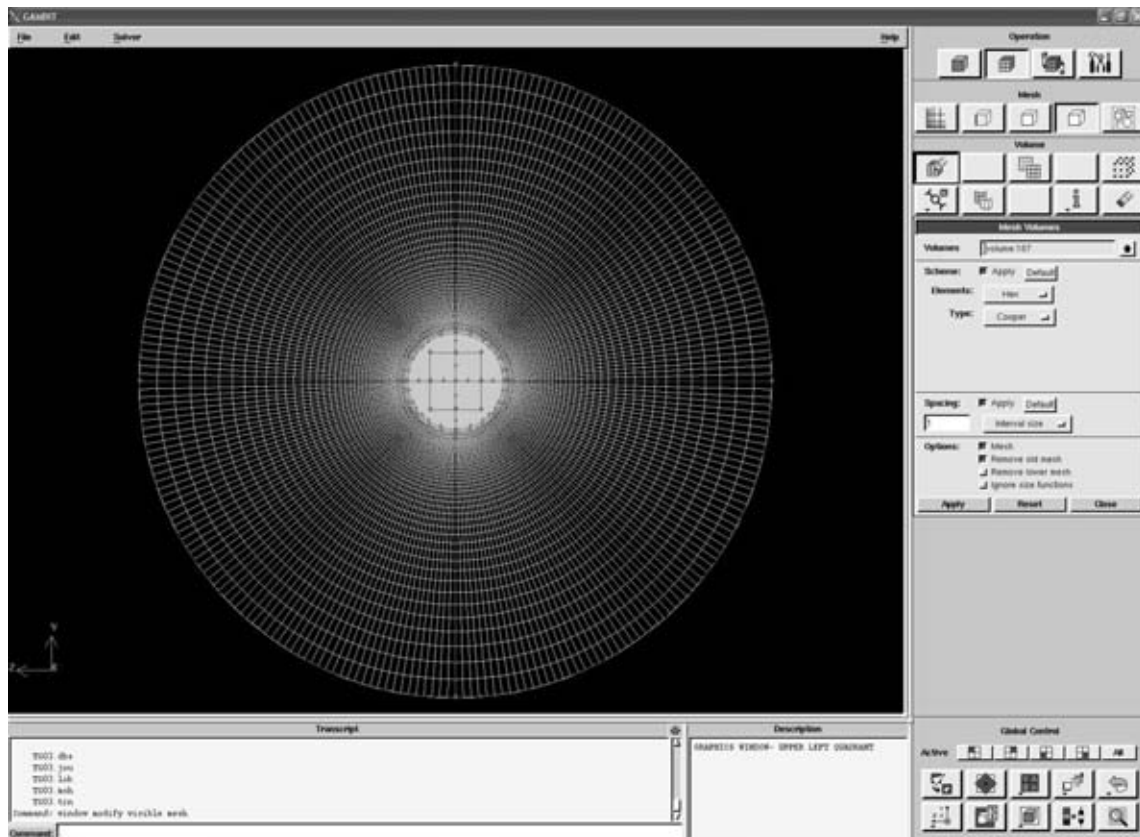


Figure 4.5.: Final mesh in the y-z-plane

One can see that the grid is much finer in the center, where the pipe is located. The details of the grid can be seen in Figure 4.6.

As soon the geometry is clean and connected one can start the meshing process. Grids are created on the faces for the beginning, at which the cross-section of the pipe and the regions close the pipe wall have a more refined grid than the outer regions. Since the characteristics of the pipe flow and its behavior after leaving the outlet are the matter of interest this meshing scheme makes sense. GAMBIT provides many options for the parameters that specify the face meshing scheme [13]. These parameters are the *Elements parameter* and the *Type parameter*. The *Elements parameter* defines the shape(s) of the elements that are used to mesh the face, while the *Type parameter* defines the pattern of mesh elements on the face. The cross-section of the pipe is meshed with the *Quad Pave* meshing scheme. The *Quad-Map* scheme is used for meshing the exterior faces. The *Elements parameter Quad* specifies that the mesh includes only quadrilateral mesh elements. Enabling the *Type parameter Map* creates a regular, structured grid of mesh elements on the face, while the parameter *Pave* creates an unstructured grid of mesh elements. Another important step in mesh generation is to create *boundary layers*. Boundary layers define the spacing of mesh node rows in regions immediately adjacent to edges and/or faces. They are used primarily to control mesh density and, thereby, to control the amount of information available from the computational model in specific regions of interest. This problem now consists of a pipe through which flows a viscous fluid, air. Under normal circumstances, it is likely that the fluid velocity gradients are large in the region immediately adjacent to the pipe wall and small near the center of the pipe. By attaching a boundary layer to the face that represents the pipe wall, the mesh density near the wall can be increased and the density near the center of the cylinder can be decreased, thereby obtaining sufficient information to characterize the gradients in both regions while minimizing the total number of mesh nodes in the model. The grid near the pipe wall refined by creating boundary layers is pictured in Figure 4.7.

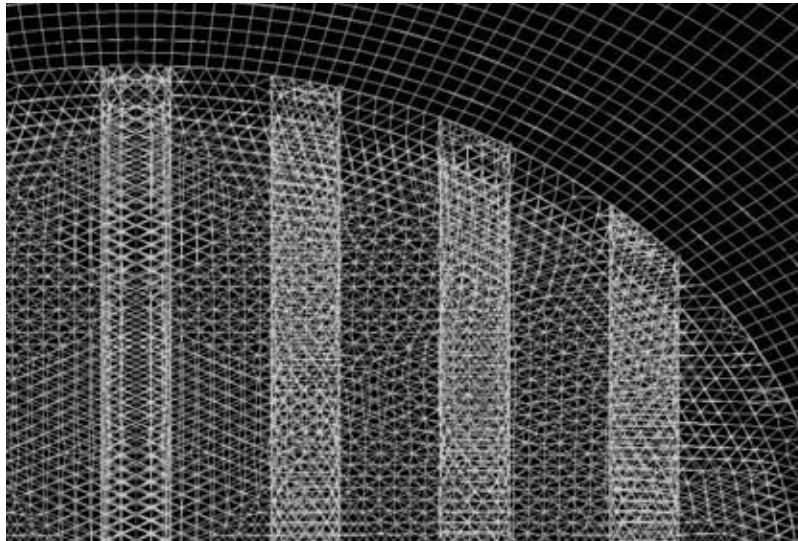


Figure 4.6.: Generated mesh in detail near the pipe center

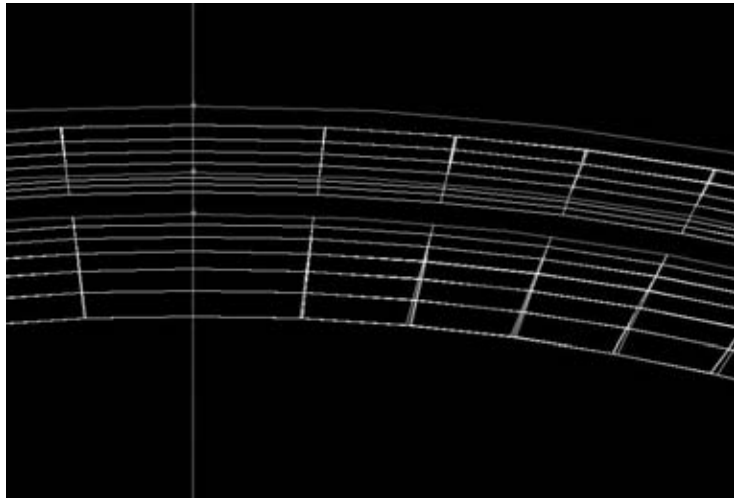


Figure 4.7.: Boundary layer near the boundaries

After having meshed all faces which are located along the x-axis and parallel to each other, the meshing process can be finished by creating the volume mesh. By meshing a volume one creates mesh nodes throughout the selected volume according to the currently specified meshing parameters. One has to specify the volume(s) to be meshed, the meshing scheme and the mesh node spacing. The meshing scheme is defined by two parameters. The *Elements* parameter defines the shape(s) of the elements that are used to mesh the volume. The *Type* parameter defines the meshing algorithm and, therefore, the overall pattern of mesh elements in the volume.

The *Element* option *Hex/Wedge* which specifies that the mesh is built primarily of hexahedral mesh elements but includes wedge elements where appropriate. By looking more closely at the face meshes in Figure 4.5. it is realized that the face meshes match. This is a very important factor for using the *Cooper* meshing scheme for the generation of a volume mesh. The *Cooper* meshing type sweeps the mesh node patterns of specified "source" faces through the volume. Hence applying the *Cooper* meshing scheme to a volume this volume gets treated as consisting of one or more logical cylinders each of which is composed of two end caps and a barrel. Faces that comprise the caps of such cylinders are called "source" faces; faces that comprise the barrels of the cylinders are called "non-source" faces. This strategy is depicted in Figure 4.8.

In general, the *Cooper* meshing scheme can be only applied to volumes which meet the following two criteria. The volume should consist of at least one face that is neither mappable nor submappable. Moreover the volume can also consist of faces that are all mappable or submappable, but the vertex types are specified that the volume cannot be divided into mappable subvolumes. Faces that meet either of these two criteria outlined above, as well as those that are logically parallel to such faces, constitute source faces for the volume and the end caps of the corresponding logical cylinder.

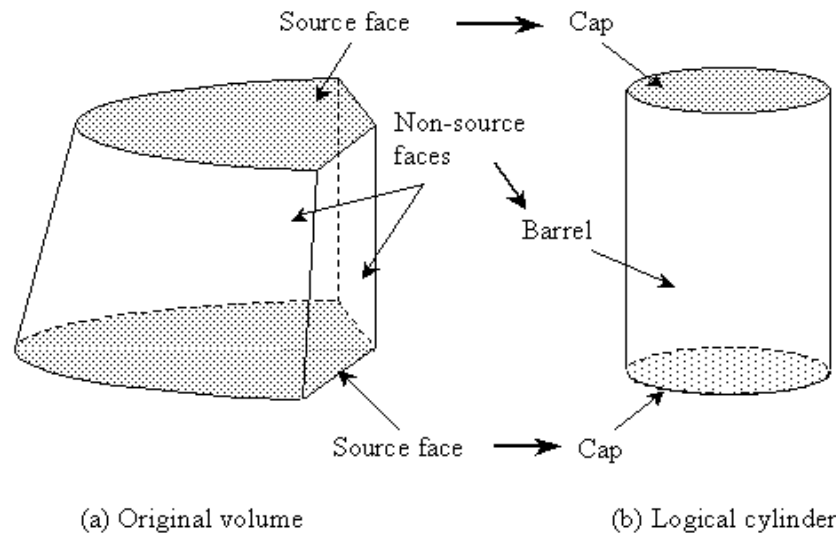


Figure 4.8.: Cooper volume meshing scheme [14]

This strategy as explained in this section is basically applied to all eleven geometries. The geometry set-ups which include the turbulence generators TG01-TG10 cannot be meshed with the Cooper meshing scheme. Hence this volumes that include spikes, rods or blades are meshed by selecting the *Tet/Hybrid Element* option and the *TGrid Type* option. One example of a geometry that includes the turbulence generators is given in Figure 4.9.:

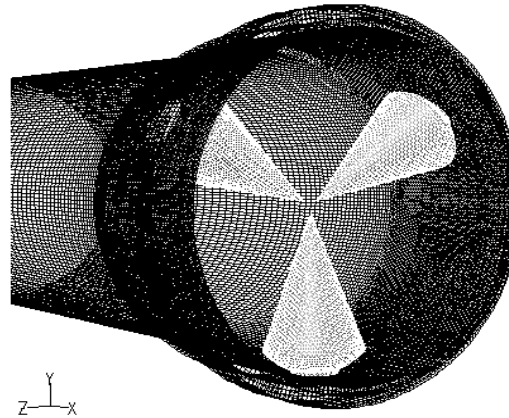


Figure 4.9.: meshed geometry of a turbulence generator

The *Tet/Hybrid Element* option specifies that the mesh is composed primarily of tetrahedral mesh elements but may include hexahedral, pyramidal, and wedge elements where they may be appropriate. By applying the *TGrid* meshing scheme to a volume, GAMBIT creates a mesh that consists primarily of tetrahedral mesh elements but which may also contain elements that possess other shapes. If one meshes one or more faces of the volume by means of a *Quad* or *Quad/Tri* scheme before applying the *TGrid* volume meshing scheme to a volume, GAMBIT creates hexahedral, pyramidal, and/or wedge elements where appropriate in proximity to the previously meshed faces. [13] This strategy of meshing the faces in the cross-sections in a *Quad* scheme before the volume mesh is generated is chosen for all volumes that include the turbulence generators. Hence the Cooper meshing scheme can be applied in the adjacent volumes.

When the meshing process is finished, one has to check the grid quality, which is a very important factor for the subsequent computational analysis. Executing this mesh volume check in GAMBIT displays a tabular output, as pictured in Table 4.1. The tabular output represents the statistical distribution of element mesh quality values. [13]

From value	To value	Count in range	% of total count (1238354)
0	0.1	1005697	81.21
0.1	0.2	165010	13.32
0.2	0.3	58614	4.73
0.3	0.4	7506	0.61
0.4	0.5	1527	0.12
0.5	0.6	0	0.00
0.6	0.7	0	0.00
0.7	0.8	0	0.00
0.8	0.9	0	0.00
0.9	1	0	0.00
0	1	1238354	100.00

Table 4.1.: Check Volume Meshes tabular output

In addition to the tabular output shown in Table 4.1, the Check Volume Meshes command displays the minimum and maximum values of element quality for the set of specified volumes, thus:

```
Measured minimum value: 0.000133551
Measured maximum value: 0.48541
```

Table 4.2.: minimum and maximum value of cell quality

The meshing process is then successfully finished when the grid quality is good. Only then the mesh can be exported for the subsequent CFD-applications. One complete meshed geometry is pictured in Figure 4.10.:

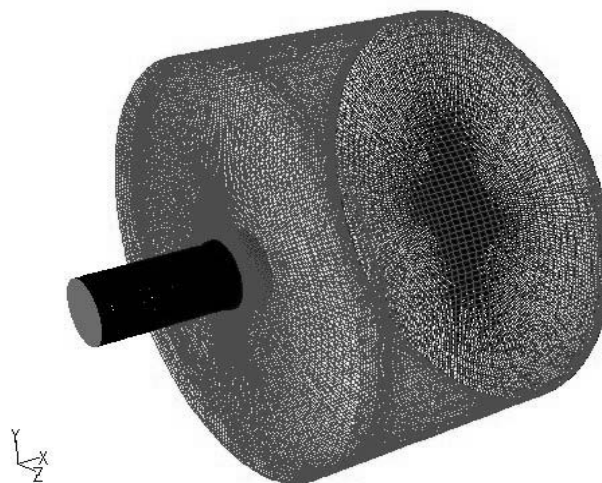


Figure 4.10.: completed volume mesh

The following table 4.3. gives an overview of the numbers of cells in the grid for each turbulence generator.

Turbulence Generator	Number of Cells
TG00	$4.95 * 10^6$
TG01	$5.54 * 10^6$
TG02	$5.59 * 10^6$
TG03	$5.57 * 10^6$
TG04	$5.52 * 10^6$
TG05	$5.49 * 10^6$
TG06	$5.42 * 10^6$
TG07	$5.85 * 10^6$
TG08	$5.56 * 10^6$
TG09	$5.22 * 10^6$
TG10	$5.62 * 10^6$

Table 4.3.: Overview of the characteristics for each turbulence generator

4.3 Setting Boundary Types

Before the mesh-file can be exported for the subsequent CFD-analysis, the boundary type specifications have to be set. Boundary-type specifications define the physical and operational characteristics of the model at its boundaries. The following Figure 4.11. gives an overview of the various zones and their type specifications in the volume.

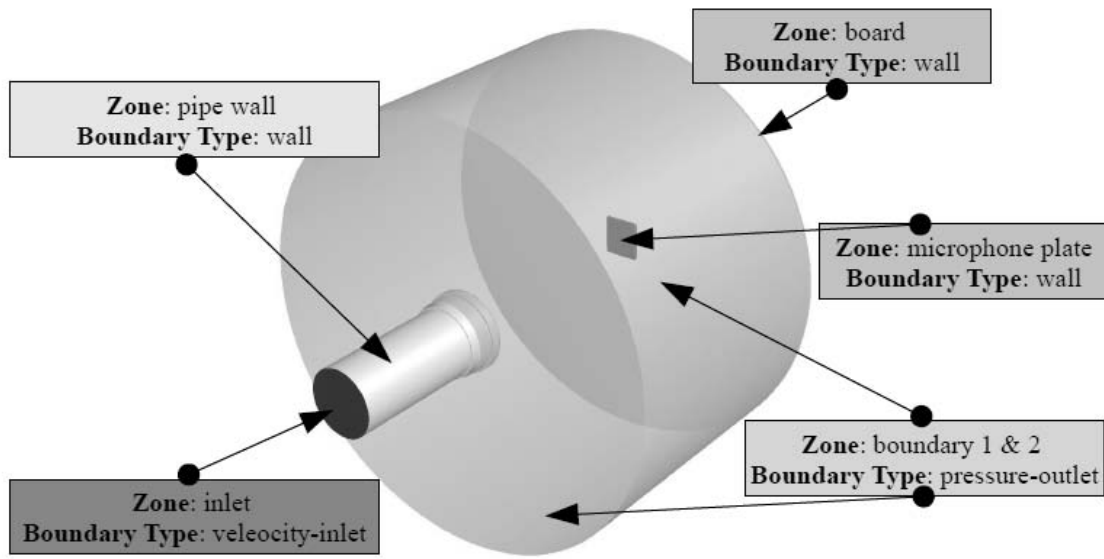


Figure 4.11...: Boundary-Type specification

After saving the final GAMBIT file, the mesh-file for FLUENT can be exported to start the computational analysis.

5 Stationary Simulations

For the numerical simulations the commercial CFD-software FLUENT is used.

A complicated CFD problem involving turbulence can be solved by splitting the grid. At this point *parallel computing* comes into play. The simultaneous use of more than one processor to execute a program is defined as parallel computing. [14] The computational analysis matter is performed on a Cluster at AIT (Austrian Institute of Technology), where the numerical simulation are performed on a set of computers that are interconnected through a cluster. Figure 5.1. gives an example of a FLUENT user-interface while working a node of this network.

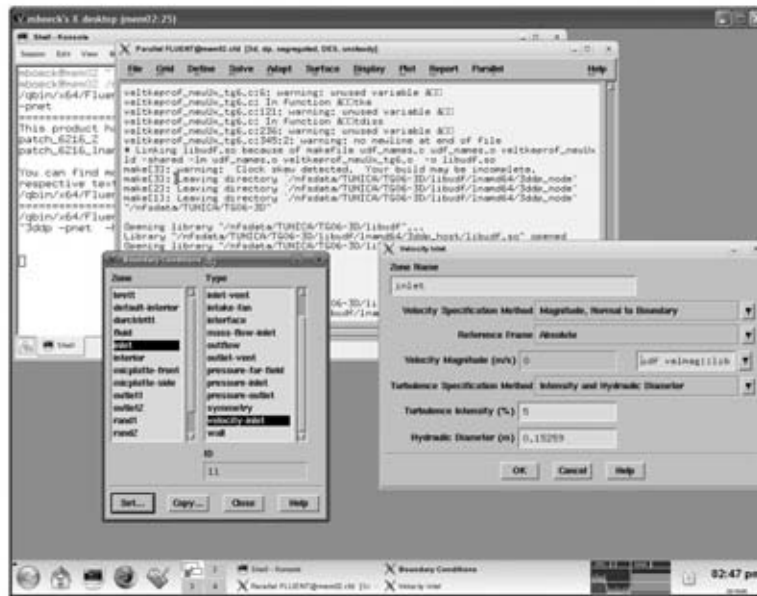


Figure 5.1.: FLUENT user interface

5.1 Boundary Conditions resulting from the Experiment

As mentioned in the Introduction the second thesis of the TUNICA project deals with the experimental investigation of this problem. The data taken from the results of the experimental analysis are the base for the ansatz of the initial conditions at the velocity inlet of the geometry. These initial conditions are individually set for each geometry set-up.

Since FLUENT has the option of importing *user-defined-functions (UDF)* the values taken from the experiment are used to define a function profile for the velocity-inlet. It is necessary for the CFD-simulations to specify values for the variables at the inlet. Usually the conditions at each type of boundary zone are defined as constant values, but they can be defined also as profile functions. This gives us the opportunity of optimizing the simulation, since it is possible to compare the results from the numerical calculation with the experiment. If necessary the boundary conditions can be adapted to the experimental results [14].

For the stationary CFD simulations the $k-\varepsilon$ model and $RNG\ k-\varepsilon$ model are used, which are described in 2.3.1., and therefore we have to specify the values of the turbulence variables k and ε at the inlet. The values for the turbulent kinetic energy, the velocity magnitude and the velocities in x-direction

are given by the experiment. The values of the dissipation rate can be calculated by using the following formula:

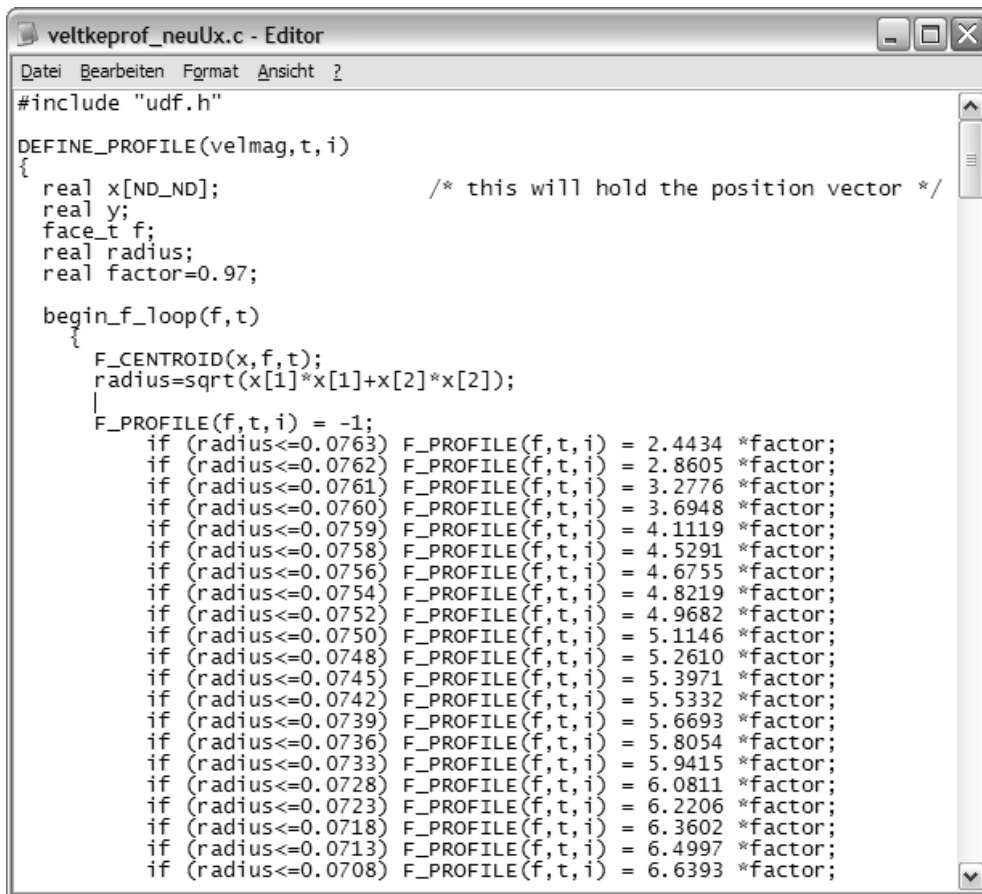
$$\epsilon = C_\mu^{3/4} k^{3/2} \frac{1}{l} \quad \text{equation (5.1)}$$

where C_μ is an empirical constant for turbulence models which has usually the value of 0.09 for k - ϵ models or 0.085 for RNG k - ϵ models, and l is defined as the turbulent length scale:

$$l = 0.07 L$$

where L is the characteristic length. For these simulations L has the value of the pipe diameter.

So the UDF specifies the values for x-velocity, turbulent kinetic energy and the turbulence dissipation rate at the inlet. The values are specified for each variable in equally spaced radius intervals. One extract of one of the eleven UDFs is given below. All UDFs are written in C.



```

veltkeprof_neuUx.c - Editor
Datei Bearbeiten Format Ansicht ?
#include "udf.h"

DEFINE_PROFILE(velmag,t,i)
{
    real x[ND_ND];          /* this will hold the position vector */
    real y;
    face_t f;
    real radius;
    real factor=0.97;

    begin_f_loop(f,t)
    {
        F_CENTROID(x,f,t);
        radius=sqrt(x[1]*x[1]+x[2]*x[2]);
        F_PROFILE(f,t,i) = -1;
        if (radius<=0.0763) F_PROFILE(f,t,i) = 2.4434 *factor;
        if (radius<=0.0762) F_PROFILE(f,t,i) = 2.8605 *factor;
        if (radius<=0.0761) F_PROFILE(f,t,i) = 3.2776 *factor;
        if (radius<=0.0760) F_PROFILE(f,t,i) = 3.6948 *factor;
        if (radius<=0.0759) F_PROFILE(f,t,i) = 4.1119 *factor;
        if (radius<=0.0758) F_PROFILE(f,t,i) = 4.5291 *factor;
        if (radius<=0.0756) F_PROFILE(f,t,i) = 4.6755 *factor;
        if (radius<=0.0754) F_PROFILE(f,t,i) = 4.8219 *factor;
        if (radius<=0.0752) F_PROFILE(f,t,i) = 4.9682 *factor;
        if (radius<=0.0750) F_PROFILE(f,t,i) = 5.1146 *factor;
        if (radius<=0.0748) F_PROFILE(f,t,i) = 5.2610 *factor;
        if (radius<=0.0745) F_PROFILE(f,t,i) = 5.3971 *factor;
        if (radius<=0.0742) F_PROFILE(f,t,i) = 5.5332 *factor;
        if (radius<=0.0739) F_PROFILE(f,t,i) = 5.6693 *factor;
        if (radius<=0.0736) F_PROFILE(f,t,i) = 5.8054 *factor;
        if (radius<=0.0733) F_PROFILE(f,t,i) = 5.9415 *factor;
        if (radius<=0.0728) F_PROFILE(f,t,i) = 6.0811 *factor;
        if (radius<=0.0723) F_PROFILE(f,t,i) = 6.2206 *factor;
        if (radius<=0.0718) F_PROFILE(f,t,i) = 6.3602 *factor;
        if (radius<=0.0713) F_PROFILE(f,t,i) = 6.4997 *factor;
        if (radius<=0.0708) F_PROFILE(f,t,i) = 6.6393 *factor;
    }
}

```

5.2 Axis-Symmetrical 2D-Simulations at TG00

Since the geometry for the turbulence generator TG00 is axis-symmetrical, a 2D mesh can be created. This provides the opportunity to study the characteristics of the turbulent flow after a short calculation time because the number of cells in the 2D grid is much smaller than in the 3D grid. It is also the matter of interest in which way the solution is dependent on the grid.

Hence three different meshes are created to answer this question. These face meshes are all regular and meshed with the face meshing scheme *Map*. The first grid consists of 29 915 cells, the second of 110 105 and the third of 442 075. Furthermore more cells are added by using the boundary adaption function in FLUENT, which allows to mark and then refine cells in the proximity of the selected boundary zones. The ability to refine the grid near one or more boundary zones is provided because important fluid interactions often occur in these regions, such as the development of strong velocity gradients in the boundary layer near a wall [Fluent User's Guide]. This refinement at the boundary zones board and pipe wall leads to an increased number of cells. After the boundary adaption the first grid consists of 216 153, the second of 295 532 and the third of 625 018 cells. Numerical simulations are also performed on these refined grids.

The details of all six grids are pictured in the following figures:

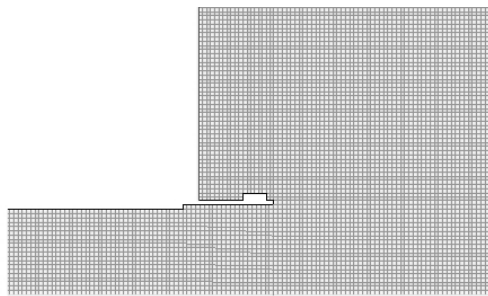


Figure 5.2.: First Grid (regular) in detail

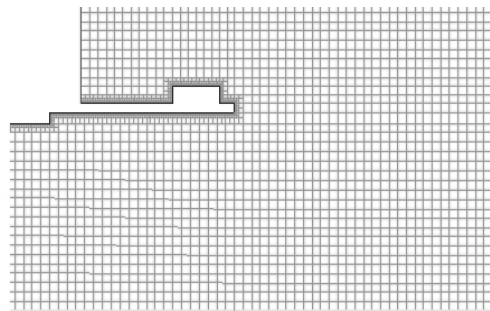


Figure 5.3.: First Grid refined in detail

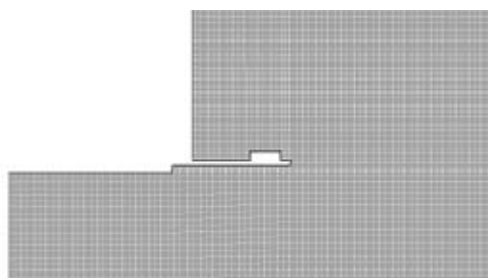


Figure 5.4.: Second Grid (regular) in detail

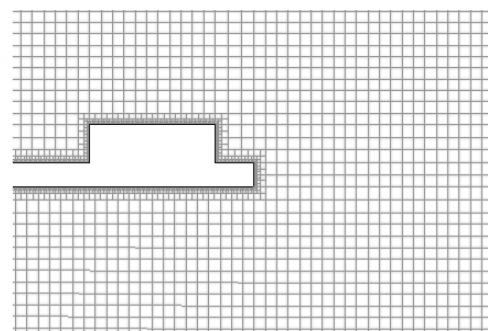


Figure 5.5.: Second Grid refined in detail

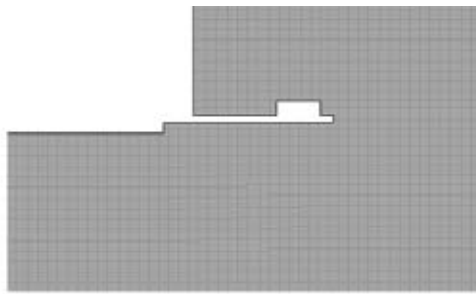


Figure 5.6.: Third Grid (regular) in detail

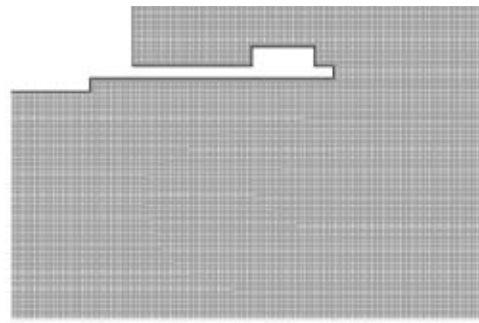


Figure 5.7.: Third Grid refined in detail

5.2.1 The Selection of the Turbulence Models

The grids are imported in the 2D FLUENT solver. After checking and scaling the grid one can define the properties of the numerical problem. The three important categories that are to define are *Models*, *Materials* and *Boundary Conditions* which specify the flow. Then the *Solution Parameters* can be set. The settings in FLUENT for the simulations, using the K-Epsilon model without the *Enhanced Wall Treatment* option are summarized in the following table 5.1. Summarizing all grids and two different variations of FLUENT settings six CFD-simulations are performed.

Solver	
Solver	segregated
Formulation	implicit
Space	2D
Time	steady
Viscous Model	
Model	k- ϵ model
k- ϵ model	RNG
Near-Wall Treatment	Standard Wall Functions
Materials	
Name:	air
Boundary Conditions	
Inlet:	velocity inlet
Velocity Specification Method	Magnitude, normal to boundary
Velocity [m/s]	UDF
Turbulence Specification Method	K and Epsilon
Turbulence Kinetic Energy	UDF
Turbulence Dissipation Rate	UDF
Outlet 1 & 2:	pressure outlet
Gauge Pressure [Pa]	0
Backflow Direction	normal to boundary
Backflow Turbulence Intensity [%]	0

Backflow Turbulence Length Scale [m]	1
Solution Controls	
Discretization	
Pressure	Second Order
Momentum	Second Order Upwind
Turbulence Kinetic Energy	Second Order Upwind
Turbulence Dissipation Rate	Second Order Upwind
Solution Initialization	
Gauge Pressure [Pa]	0
X-Velocity [m/s]	0
Y-Velocity [m/s]	0
Turbulence Kinetic Energy	0.001
Turbulence Dissipation Rate	0.01

Table 5.1.: Settings in FLUENT

An overview of the variations on the settings for the different grids is given below by table 5.2.. They differ from each other, whether the Enhanced Wall Treatment or the Standard Wall Functions option is enabled.

	Regular Grid	Refined Grid
k-ϵ Model	RNG	RNG
Near Wall Treatment	Standard Wall Functions	Enhanced Wall Treatment

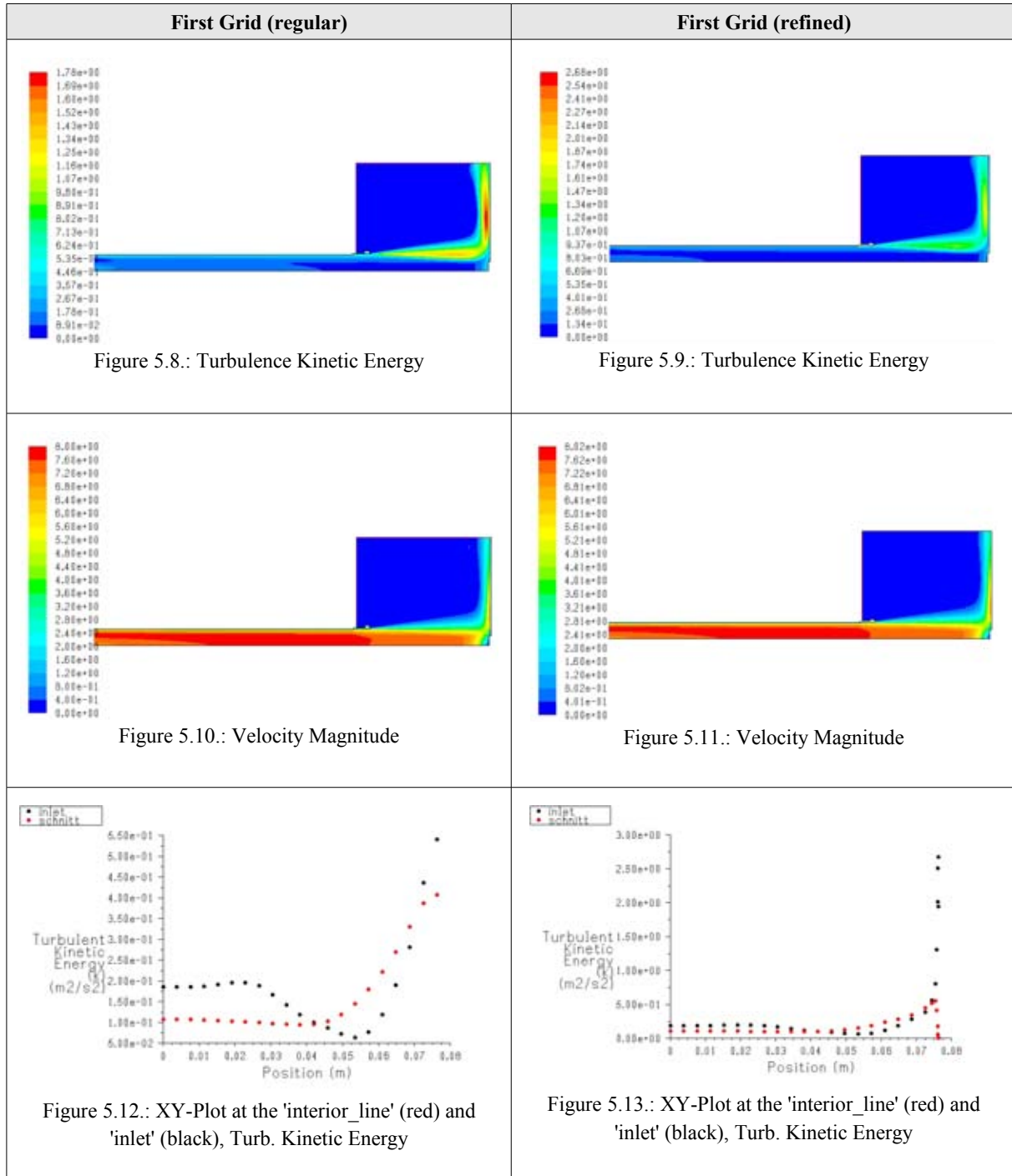
Table 5.2.: Differences between the FLUENT settings

Since this differentiation is applied to all grids, twelve CFD-simulations have to be performed.

5.2.2 Mesh–Dependency of the Solutions

This chapter deals with the interpretation of the solutions of the computational analysis.

The solutions for the regular and refined grid are all summarized in the following figures. The results of the computational analysis using the RNG k - ϵ Model for the regular meshes are confronted with the refined meshes, to investigate the mesh-dependency of the solutions. It should be mentioned that the representations of the solutions do not all have the same scaling. Furthermore the 'interior_line' is called 'schnitt' in the related figures.



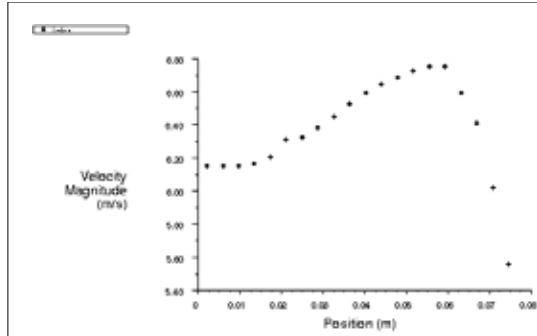


Figure 5.14.: XY-Plot at the inlet, Velocity Magnitude

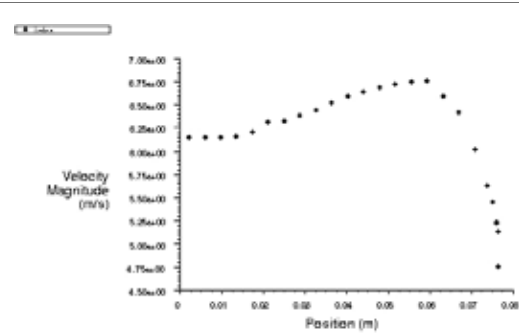


Figure 5.15.: XY-Plot at the inlet, Velocity Magnitude

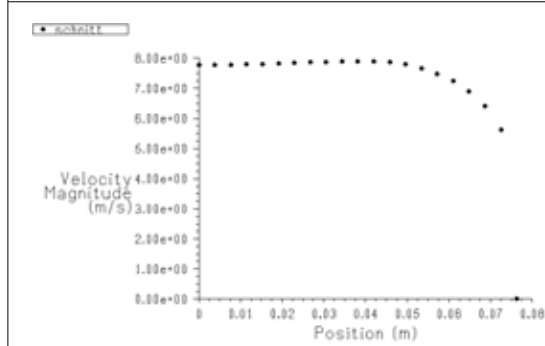


Figure 5.16.: XY-Plot at the 'interior_line', Velocity Magnitude

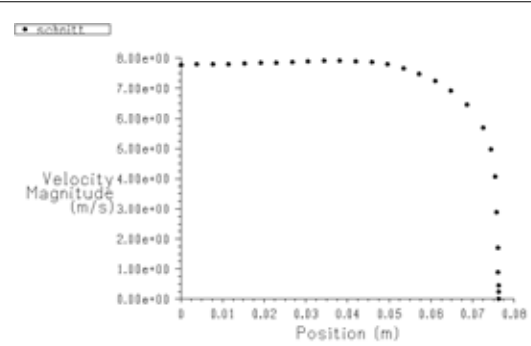


Figure 5.17.: XY-Plot at the 'interior_line', Velocity Magnitude

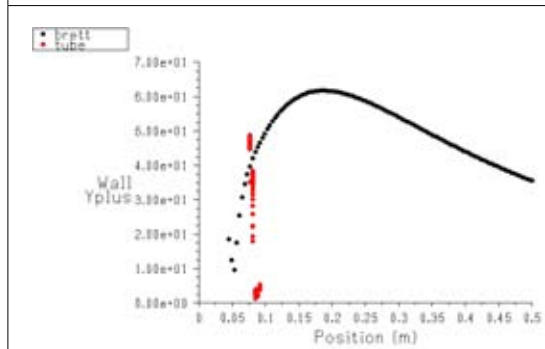


Figure 5.18.: XY-Plot of Yplus along the board (black)

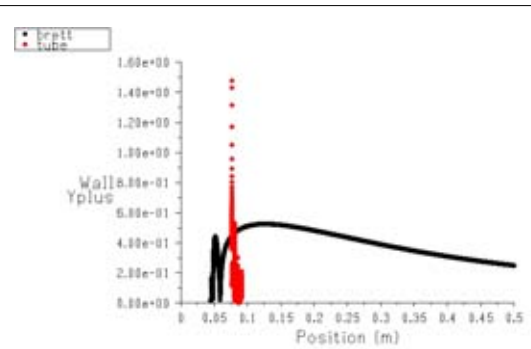


Figure 5.19.: XY-Plot of Yplus along the board (black)

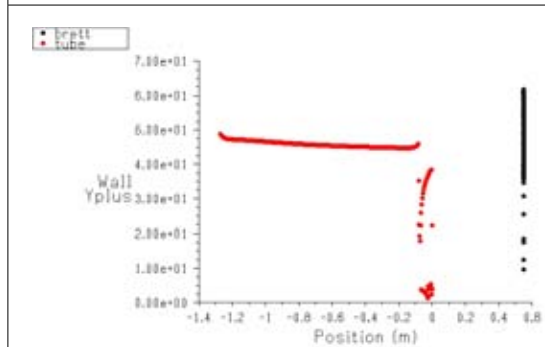


Figure 5.20.: XY-Plot of Yplus along the pipe wall (red)

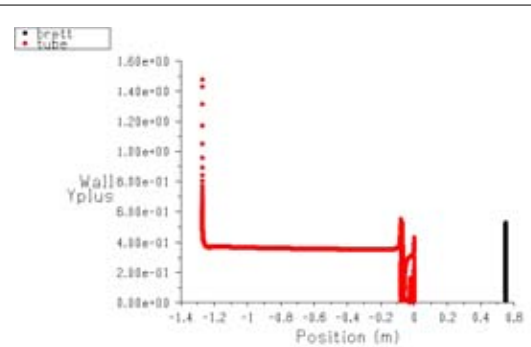


Figure 5.21.: XY-Plot of Yplus along the pipe wall (red)

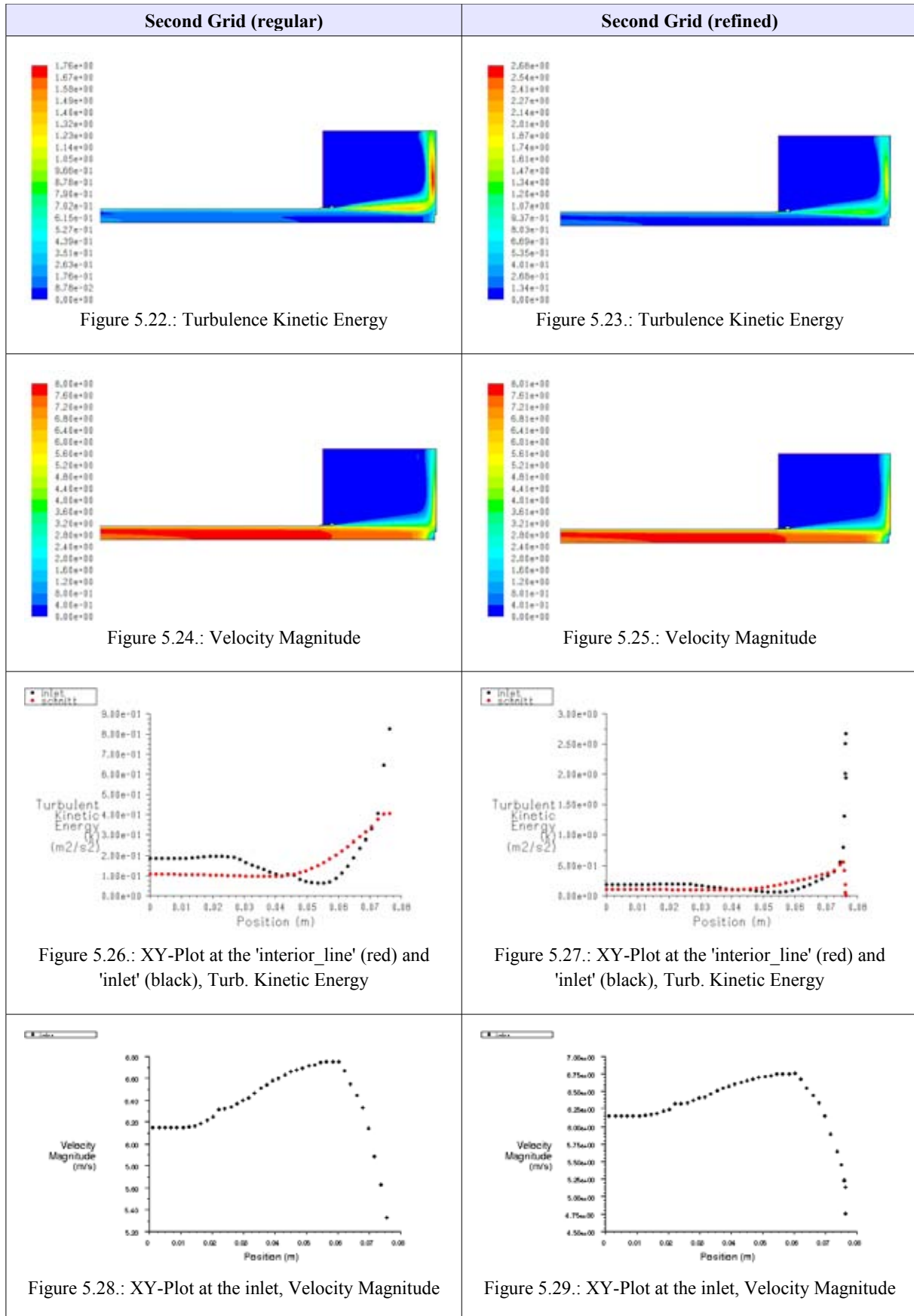
The solutions for the simulations on the first grid using the RNG k- ϵ model show that the contours of the turbulent kinetic energy for the regular and refined grid do not strongly differ from each other which can be observed in the Figures 5.8. and 5.9. The contours of the velocity magnitude for the two grids do not differ from each other either (s. Fig. 5.10., 5.11.). The color scaling is positioned at the left-hand side of the figures.

Figures 5.12-5.17 show in which way the velocity and turbulence profiles change during the propagation through the tube. The 'inlet' defines the velocity or turbulence profile at the inlet of the pipe. 'Interior_line', called as 'schnitt' in the figures, is positioned 127.25 mm distant from the velocity inlet. By comparing the values of the variables at this two positions the change of these variables in a turbulent pipe flow can be seen. The profiles are not dependent on the mesh. The values of the variables are nearly the same, only the shape of the profiles are a bit different, caused by the higher number of grid points in the refined grid.

According to the analysis of the y^+ value it is possible to find out, if the grid in near wall regions is suitable for the chosen turbulence model and the chosen option for near wall treatment. Here turbulence has a great impact of the behavior of the flow and its quantities. Therefore turbulence quantities should be resolved appropriately to guarantee a high accuracy of the numerical simulation. So numerical results for turbulent flows are more dependent on the grid than those for laminar flows. The near wall meshed is then checked by plotting the y^+ values at the boundary regions 'tube', the pipe wall and 'brett', the board (s. Fig. 4.11.). These checks are plotted by Figures 5.18-5.20.

The Fig. 5.18. and 5.20. show the y^+ values in the two near wall regions. Since standard wall functions are used the law-of-the-wall is valid for values of $y^+ \geq 30$ [chapter 2.4.2, 3]. The y^+ values for the board (s. Fig. 5.18.) match this conditions apart from a small deviation near the zero point. The y^+ values along the pipe wall (s. Fig. 5.20.) also satisfy the law.

Due to the law-of-the-wall the y^+ values should satisfy $0 \leq y^+ < 5$, when the enhanced wall treatment option is chosen. It can be seen from Figures 5.19. and 5.21. the grid fulfills this condition over the whole range.



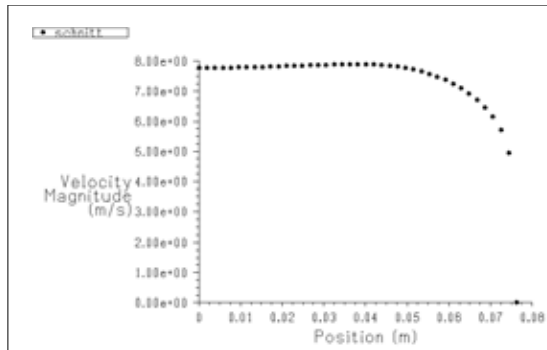


Figure 5.30.: XY-Plot at the 'interior_line', Velocity Magnitude

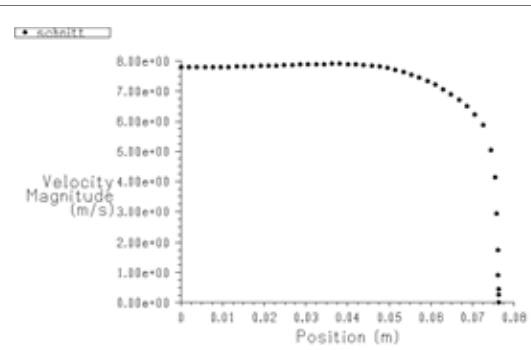


Figure 5.31.: XY-Plot at the 'interior_line', Velocity Magnitude

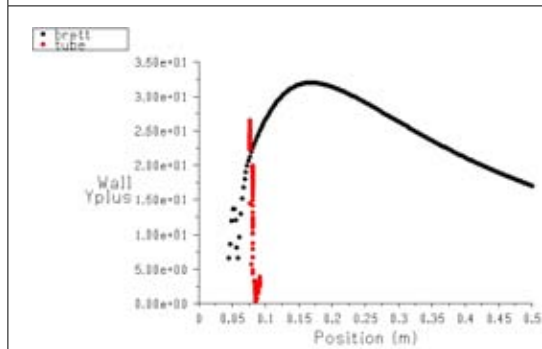


Figure 5.32.: XY-Plot of Yplus along the board (black)

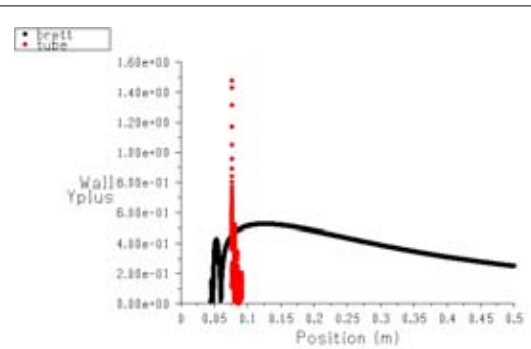


Figure 5.33.: XY-Plot of Yplus along the board (black)

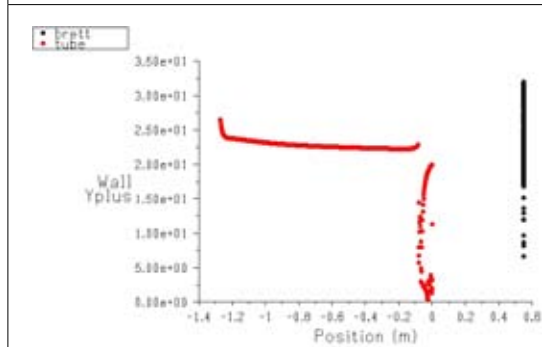


Figure 5.34.: XY-Plot of Yplus along the pipe wall (red)

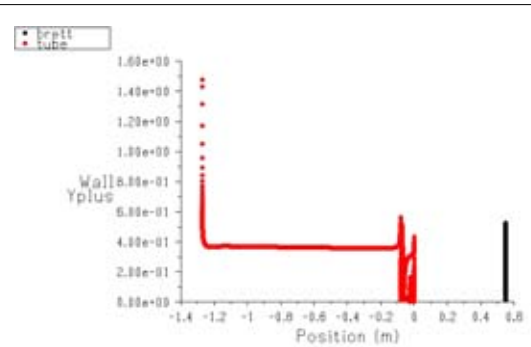


Figure 5.35.: XY-Plot of Yplus along the pipe wall (red)

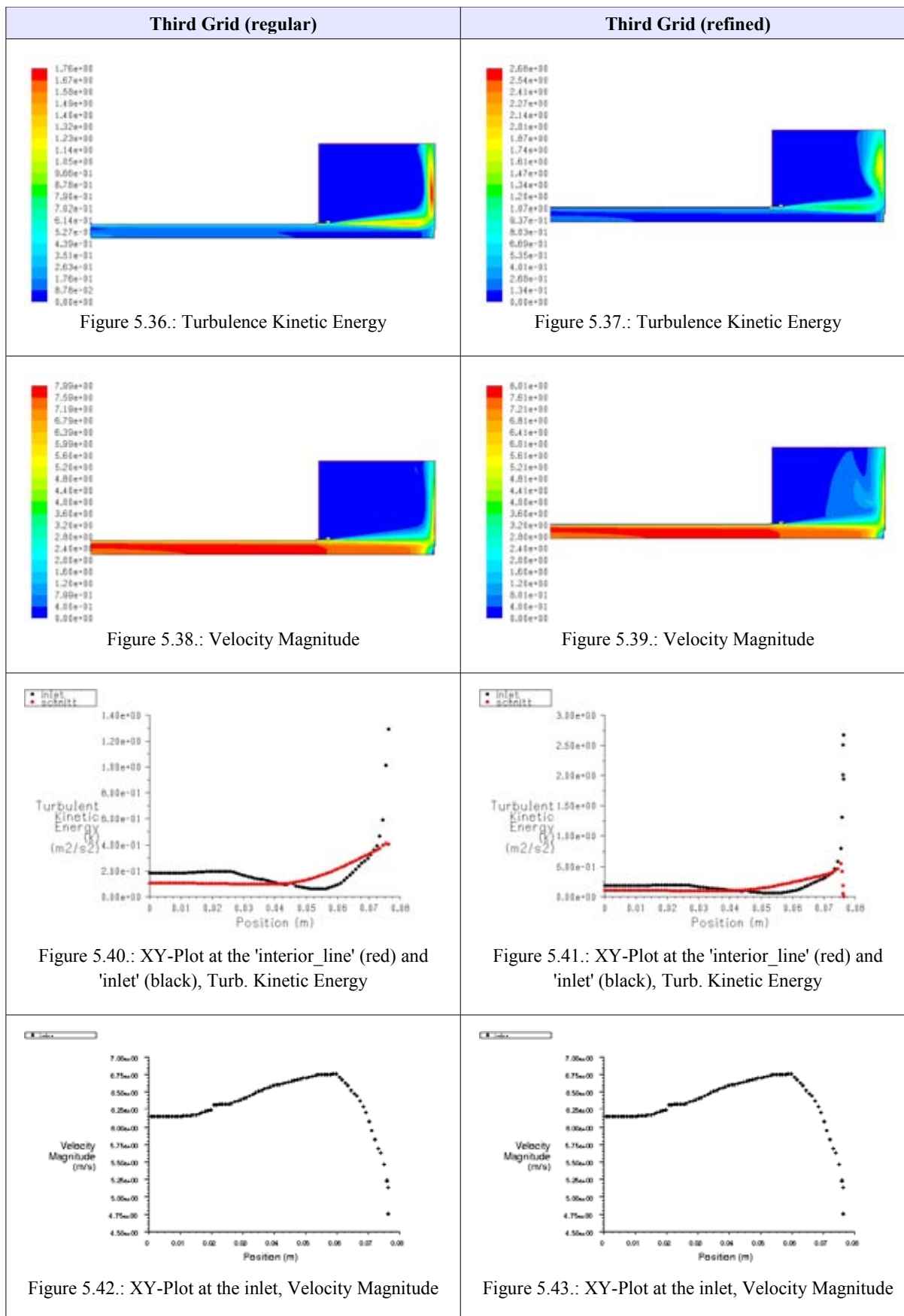
The results of the computational analysis using the RNG k- ϵ model on the second grid do not show strong differences in the contours of the turbulent kinetic energy for different mesh resolutions. The contours of the velocity magnitude are not grid dependent as well which can be seen from the Figures 5.22. – 5.25.

The figures from 5.26. to 5.31. show in which way the velocity and turbulence profiles change during the propagation through the tube. One can see that the profiles are not dependent on the mesh. The values of the variables are nearly the same, only the shape of the profiles are a bit different, caused by the higher number of grid points in the refined grid.

The y^+ values in the two near wall regions can be taken from Fig. 5.32. - 5.35. Since standard wall functions are used, the law-of-the-wall is valid for values of $y^+ \geq 30$ [chapter 2.4.2, 3]. Most y^+ values for the board (s. Fig. 5.32.) do not match this conditions, the

values range from 20 to 25. The y^+ values along the pipe wall (s. Fig. 5.34.) do not satisfy the law either.

Due to the law-of-the-wall the y^+ values should be $0 \leq y^+ < 5$, when the enhanced wall treatment option is chosen. It can be seen from Figures 5.33. and 5.35. the grid fulfills the condition.



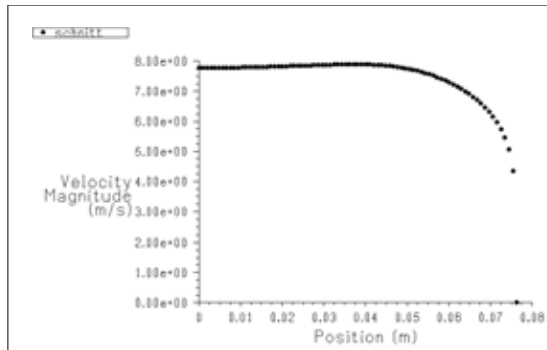


Figure 5.44.: XY-Plot at the 'interior_line', Velocity Magnitude

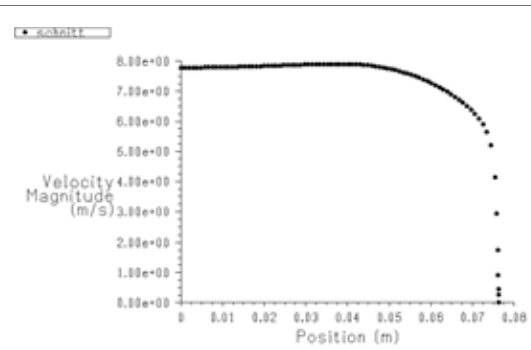


Figure 5.45.: XY-Plot at the 'interior_line', Velocity Magnitude

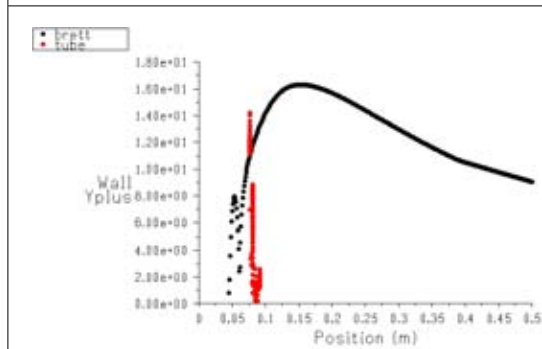


Figure 5.46.: XY-Plot of Yplus along the board (black)

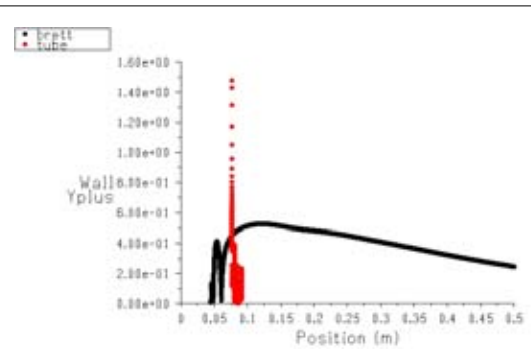


Figure 5.47.: XY-Plot of Yplus along the board (black)

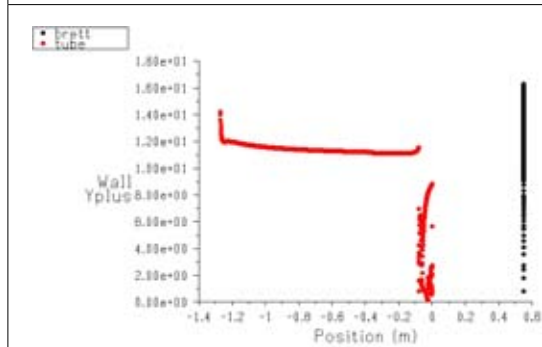


Figure 5.48.: XY-Plot of Yplus along the pipe wall (red)

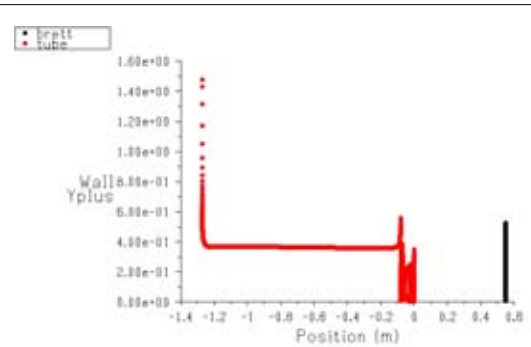


Figure 5.49.: XY-Plot of Yplus along the pipe wall (red)

The results of the computational analysis using the RNG k- ϵ model on the third grid are all summarized in Figures 5.36-5.49.

The contours of the turbulent kinetic energy and the velocity magnitude as well are not dependent on the grid which can be seen from the Figures 5.36. – 5.39.

The figures from 5.40. to 5.45. show in which way the velocity and turbulence profiles change during the propagation through the tube. One can see that the profiles are not dependent on the mesh. The values of the variables are nearly the same, only the shape of the profiles can be a bit different, caused by the higher number of grid points in the refined grid.

The y^+ values in the two near wall regions can be taken from Fig. 5.46. - 5.49. Since standard wall functions are used, the law-of-the-wall is valid for values of $y^+ \geq 30$ [chapter 2.4.2, 3]. Most y^+ values for the board (s. Fig. 5.46.) do not match this conditions, the highest values which are reached are from 8 to 17. The y^+ values along the pipe wall (s. Fig. 5.48.) do not satisfy the law either.

Due to the law-of-the-wall the y^+ values should be $0 \leq y^+ < 5$, when the enhanced wall treatment option is chosen. It can be seen from Figures 5.47. and 5.49. that the grid fulfills the condition.

By summarizing the results of the stationary 2D simulations there is almost no grid dependency of the kinematic variables. Thus the first grid can be used. According to the analysis of the y^+ values either the first grid using the standard wall functions or the refined first grid can be used. The refined grid with a better resolution in near wall regions would be better according to the analysis of the y^+ values. Numerical simulations on the refined grid are too expensive because of the higher number of grid cells, which may lead to longer calculation times. By using the regular first grid some geometric features might not be perfectly modeled, but numerical solutions can be generated very quickly. Therefore the use of finer mesh sizes is prohibitive in terms of the total cell number, when one starts with 3D simulations. This fact is accounted for the 3D simulations.

5.3 3D-Simulations

The computational analysis for the volumes including different types of turbulence generators have been performed on a hybrid mesh consisting of tetrahedral cells in the region of the turbulence generators and a prismatic/hexahedral mesh in the up- and downstream area. The details of mesh generation and the properties of the generated grids are described in chapter 4.2.

The flow propagates through the pipe and turbulence is generated by using different sets of turbulence generators which are positioned in the pipe outlet. The different types of turbulence generators have been introduced in section 3.1. The turbulent flow field downstream of the pipe outlet is analyzed in the analysis plane. The turbulent jet then impinges on the opposite circular area of the cylinder, which is defined as a hard wall.

Steady CFD calculations using the standard k - ϵ model and the RNG k - ϵ model are performed for all geometries. The FLUENT settings for the numerical simulations using the Standard - and RNG k - ϵ model are summarized in the following tables.

Solver	
Solver	segregated
Formulation	implicit
Space	3D
Time	steady
Viscous Model	
Model	k- ϵ model
k- ϵ model	Standard
Near-Wall Treatment	Standard Wall Functions
Materials	
Name:	air
Boundary Conditions	
Inlet:	velocity inlet
Velocity Specification Method	Magnitude, normal to boundary
Velocity [m/s]	UDF
Turbulence Specification Method	K and Epsilon
Turbulence Kinetic Energy	UDF
Turbulence Dissipation Rate	UDF
Outlet 1 & 2:	pressure outlet
Gauge Pressure [Pa]	0
Backflow Direction	normal to boundary
Backflow Turbulence Intensity [%]	0
Backflow Turbulence Length Scale [m]	1
Solution Controls	
Discretization	
Pressure	Second Order
Momentum	Second Order Upwind
Turbulence Kinetic Energy	Second Order Upwind
Turbulence Dissipation Rate	Second Order Upwind
Solution Initialization	
Gauge Pressure [Pa]	0
X-Velocity [m/s]	0
Y-Velocity [m/s]	0
Z-Velocity [m/s]	0
Turbulence Kinetic Energy	0. 001
Turbulence Dissipation Rate	0. 01
Parallel Partitioning	
Method	Cartesian X-Coordinate
Number	4

Table 5.3.: Settings in FLUENT for the steady k- ϵ simulations

Solver	
Solver	segregated
Formulation	implicit
Space	3D
Time	steady
Viscous Model	
Model	k- ϵ model
k- ϵ model	RNG
Near-Wall Treatment	Standard Wall Functions
Materials	
Name:	air
Boundary Conditions	
Inlet:	velocity inlet
Velocity Specification Method	Magnitude, normal to boundary
Velocity [m/s]	UDF
Turbulence Specification Method	K and Epsilon
Turbulence Kinetic Energy	UDF
Turbulence Dissipation Rate	UDF
Outlet 1 & 2:	pressure outlet
Gauge Pressure [Pa]	0
Backflow Direction	normal to boundary
Backflow Turbulence Intensity [%]	0
Backflow Turbulence Length Scale [m]	1
Solution Controls	
Discretization	
Pressure	Second Order
Momentum	Second Order Upwind
Turbulence Kinetic Energy	Second Order Upwind
Turbulence Dissipation Rate	Second Order Upwind
Solution Initialization	
Gauge Pressure [Pa]	0
X-Velocity [m/s]	0
Y-Velocity [m/s]	0
Z-Velocity [m/s]	0
Turbulence Kinetic Energy	0. 001
Turbulence Dissipation Rate	0. 01
Parallel Partitioning	
Method	Cartesian X-Coordinate
Number	4

Table 5.4.: Settings in FLUENT for the steady RNG k- ϵ simulations

5.4 Summary of the Results

The solutions of the numerical simulations are evaluated on the one hand along the post processing lines L01-L12 (s. chap. 3) and on the other hand on the analysis plane.

The values of the velocity and the turbulent kinetic energy can be plotted along each evaluation line. These plots can be generated both for the experimental and the numerical results, which provides the possibility of comparing experiment and numerical simulation. The results of these evaluations are summarized in chapter 5.4.1

The behavior of the turbulent flow can be easily illustrated by displaying the contours of the turbulent kinetic energy and the velocity magnitude on the analysis plane. Further explanations are in chapter 5.4.2.

5.4.1 Comparison of Simulation and Experiment

The values for the flow properties along each evaluation line are plotted in MATLAB. These plots compare the results of the experimental and both numerical analyses along each line. This will show, if the simulation match the experiment in the entire flow domain. The post processing lines are positioned that they can give information about the regions of interest in the flow domain. Many of them are positioned near the pipe outlet and the plate where the jet impinges. A few are positioned at the half distance from the pipe outlet and the plate, as it is explained in chapter 3 (s. Fig. 3.2. - 3.4.).

The comparison of the simulation with the experiment for the x-velocity, y-velocity and the turbulent kinetic energy is given in the following Figures 5.50. - 5.52., where the color black represents the experimental results, red the results of the standard k- ϵ and blue of the RNG k- ϵ simulation. This comparison is done with the experimental and numerical results with the geometry that includes TG00 which does not have a turbulence generator. Further information about the experimental setup and experimental data can be found on the Master Thesis by Wolfgang Tilser.

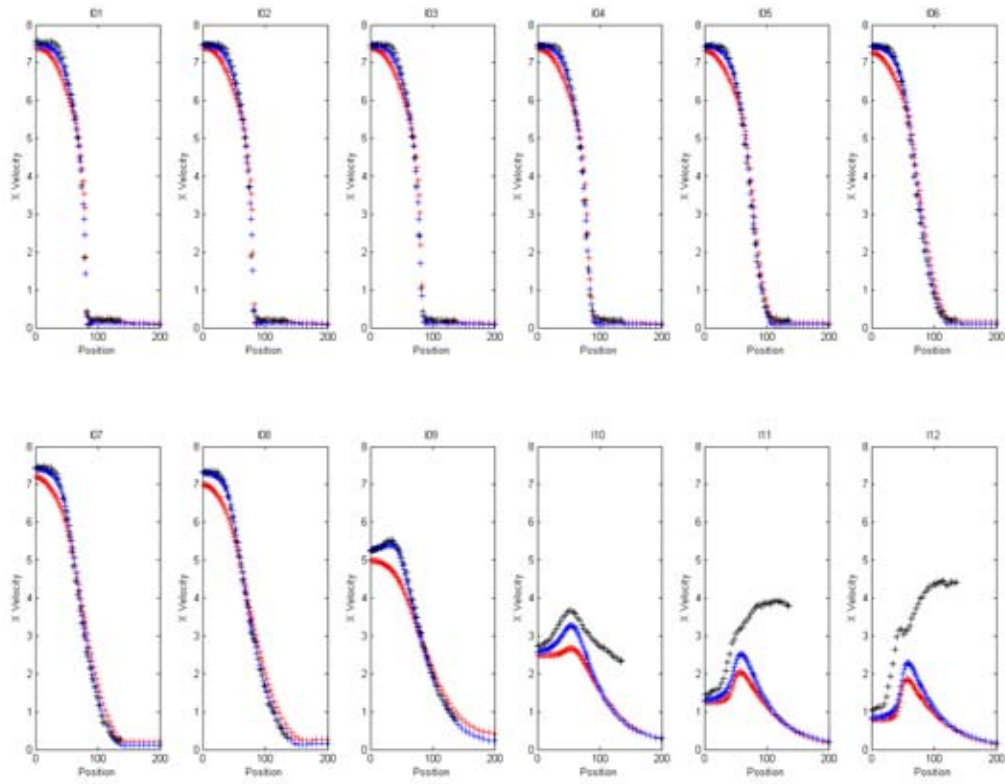


Figure 5.50.: Evaluation of the x-velocity [m/s] along the lines

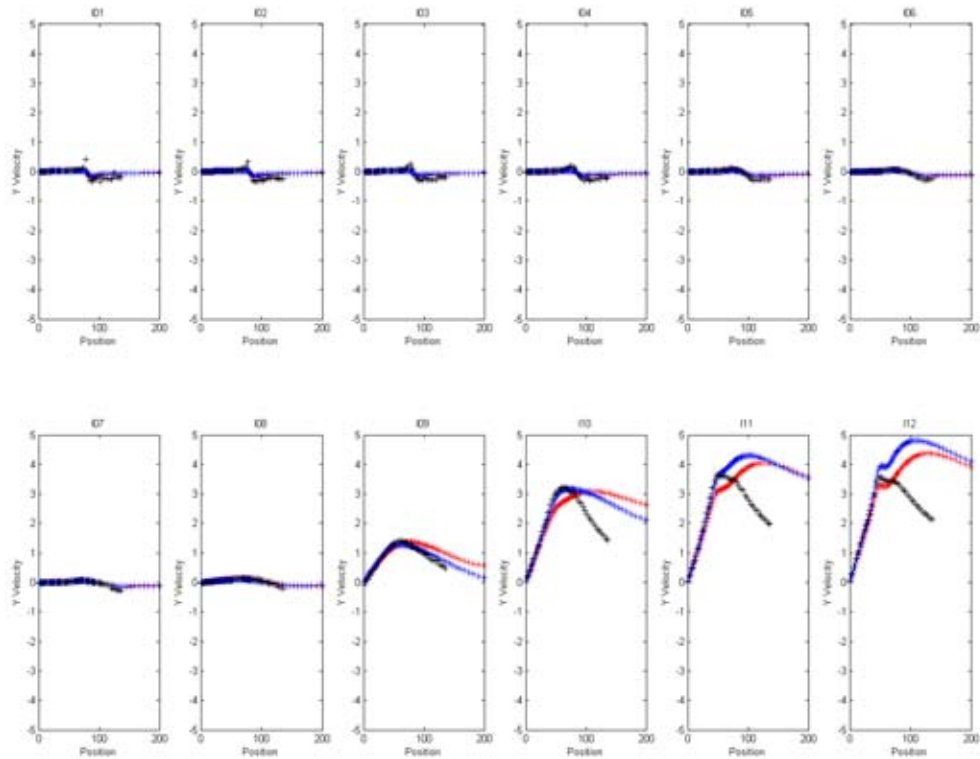


Figure 5.51.: Evaluation of the y-velocity [m/s] along the lines

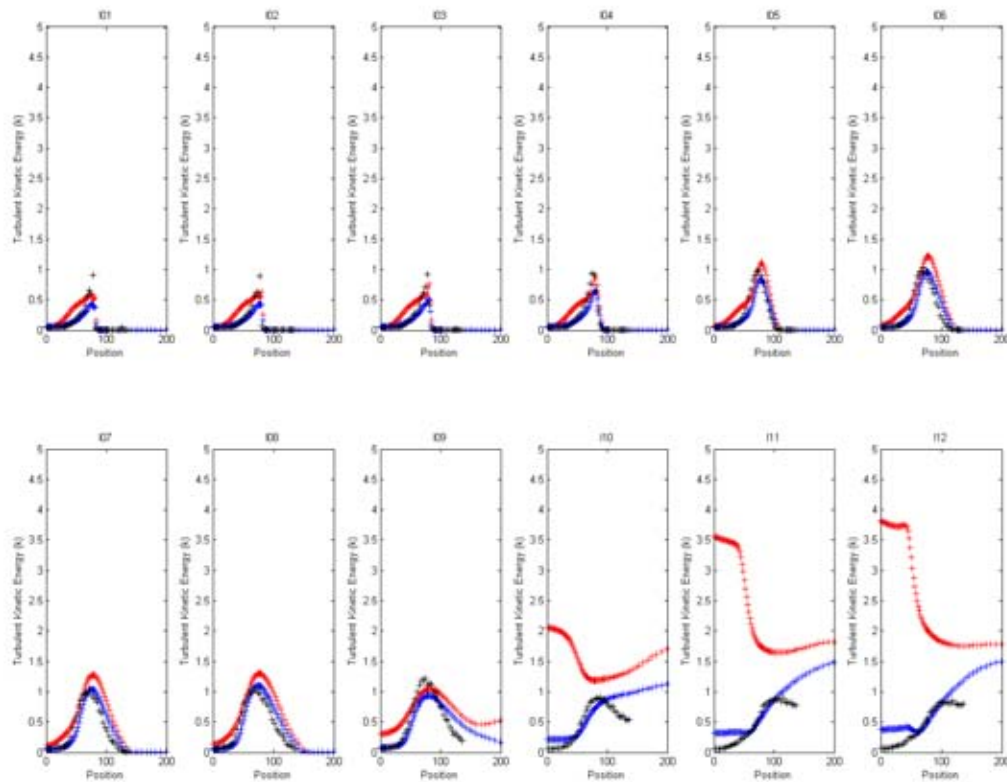


Figure 5.52.: Evaluation of the turbulent kinetic energy [m^2/s^2] along the lines

The comparison for each property leads to the conclusions that both turbulence models match the behavior of the flow in the region reaching from line L01 to L09. A short overview of the positions of the post processing lines in the flow domain is given in Figure 5.53. The plots for L10 – L12 show, that the RNG k - ϵ model is more applicable in near-wall regions than the standard k - ϵ model.

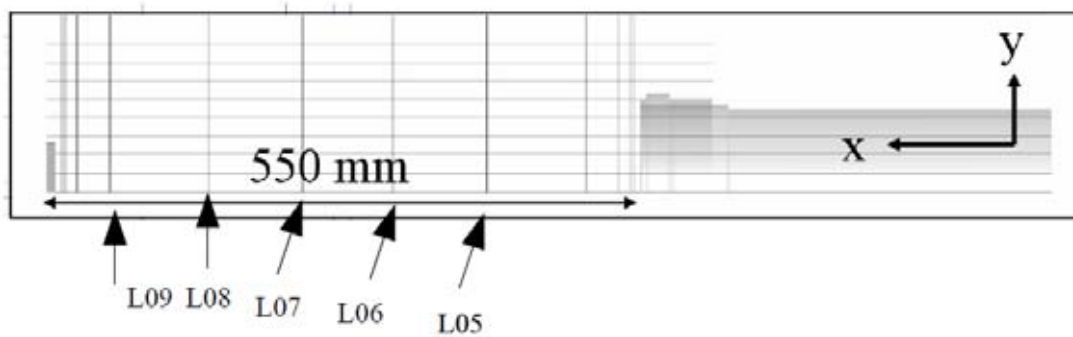


Figure 5.53.: Definition of the post processing lines in the flow domain

5.4.2 Flow Properties for the Different Turbulence Generators

Since the RNG k- ϵ model compared to the experiment is the better turbulence model, the simulations the geometries including the other turbulence generators are performed by use of the RNG k- ϵ model. So the following figures show the solution of the steady RNG k- ϵ simulations.

The contours of the turbulent kinetic energy and the velocity magnitude are all evaluated on the analysis plane. The behavior of the turbulent flow is then illustrated for each turbulence generator which makes it is easy to investigate the impact of each turbulence generator on the pipe flow.

Contours of the velocity magnitude [m/s]:

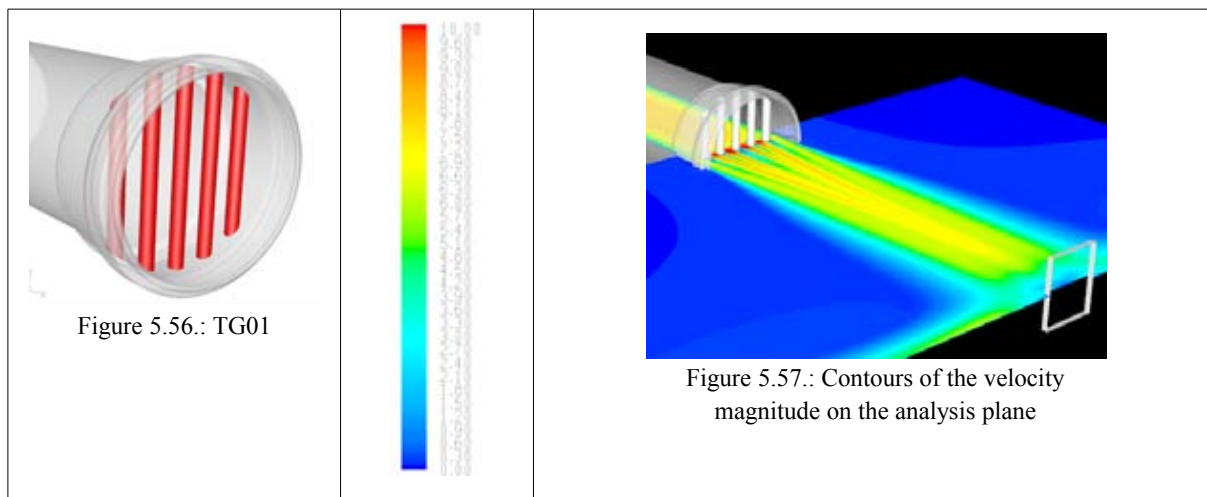
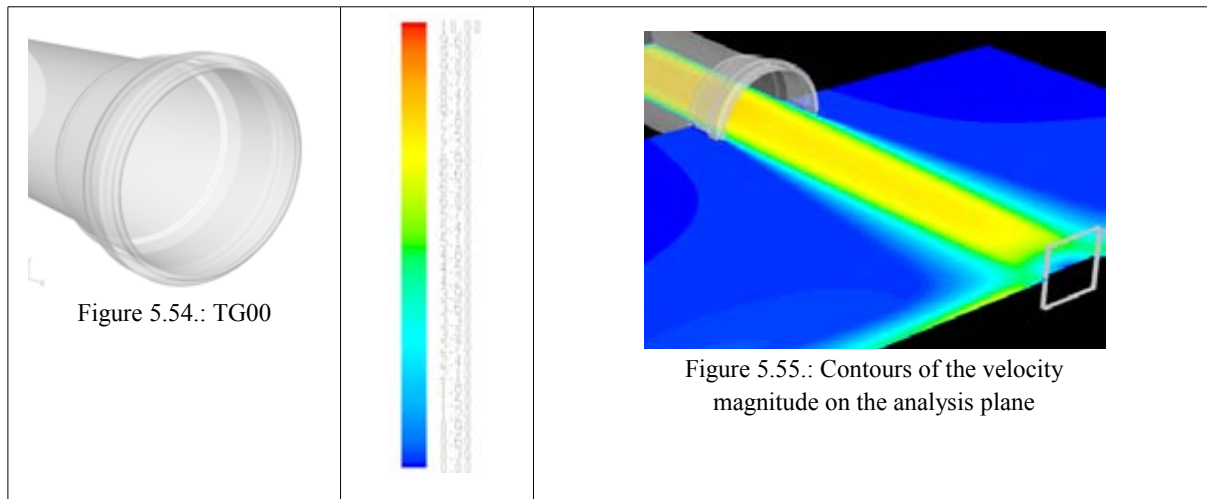




Figure 5.58.: TG02

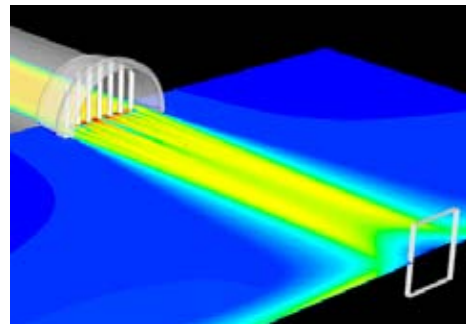


Figure 5.59.: Contours of the velocity magnitude on the analysis plane



Figure 5.60.: TG03

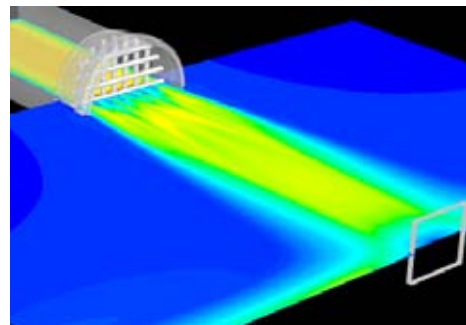


Figure 5.61.: Contours of the velocity magnitude on the analysis plane

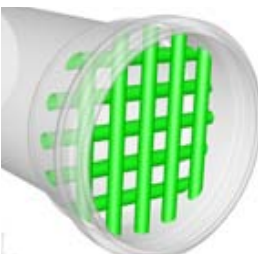


Figure 5.62.: TG04

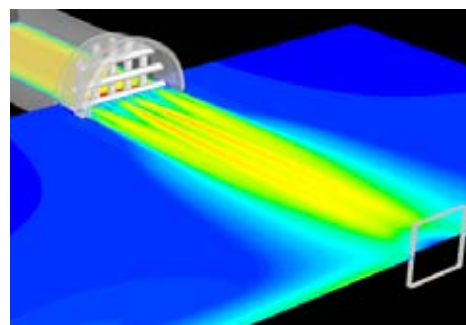


Figure 5.63.: Contours of the velocity magnitude on the analysis plane



Figure 5.64.: TG05

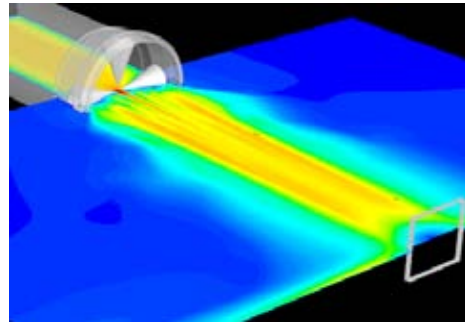


Figure 5.65.: Contours of the velocity magnitude on the analysis plane



Figure 5.66.: TG06

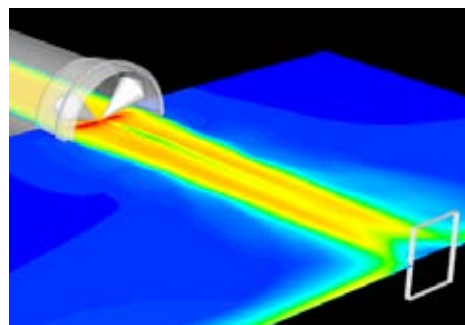


Figure 5.67.: Contours of the velocity magnitude on the analysis plane



Figure 5.68.: TG07

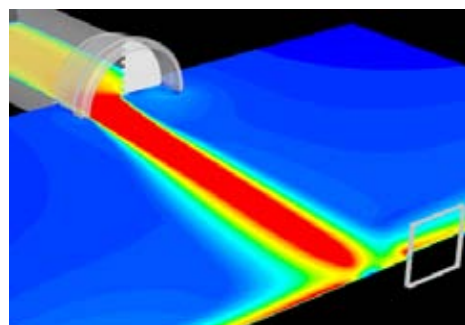


Figure 5.69.: Contours of the velocity magnitude on the analysis plane



Figure 5.70.: TG08

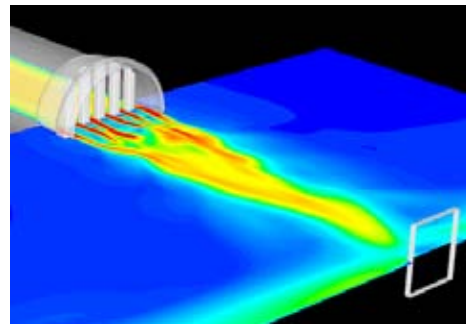


Figure 5.71.: Contours of the velocity magnitude on the analysis plane



Figure 5.72.: TG09

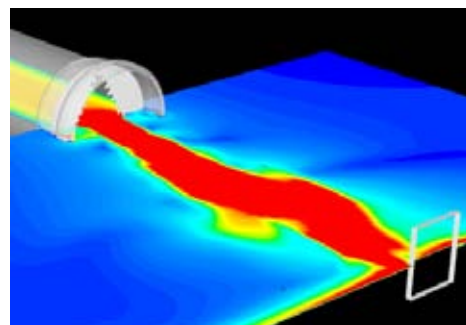


Figure 5.73.: Contours of the velocity magnitude on the analysis plane



Figure 5.74.: TG10

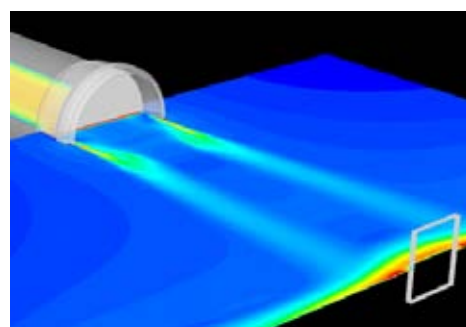
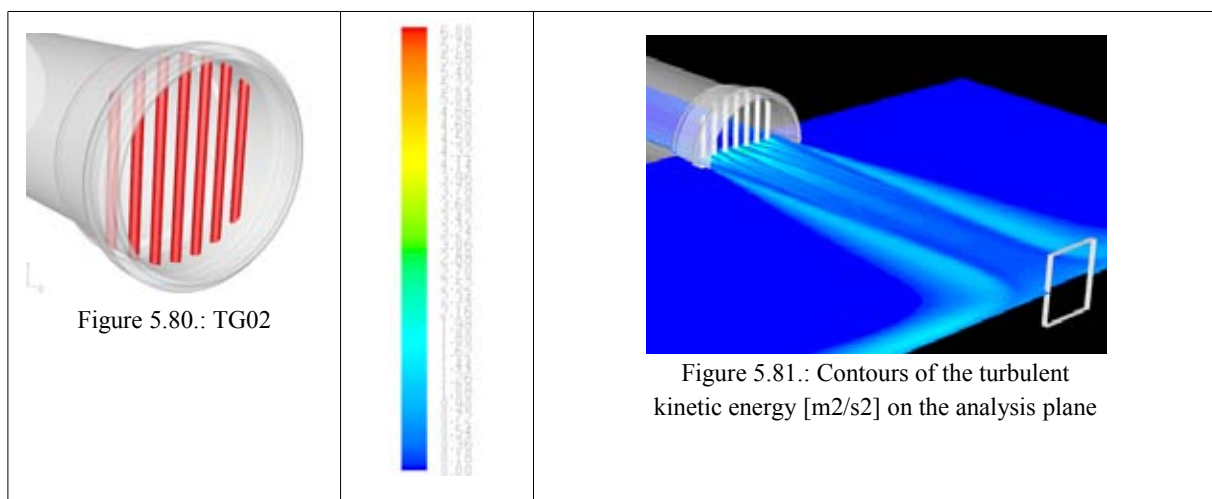
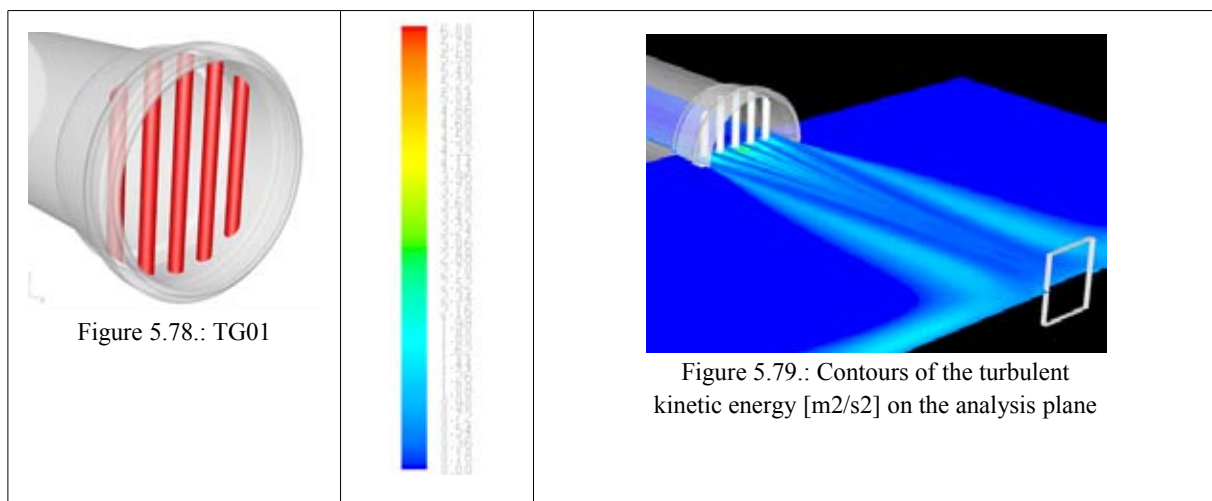
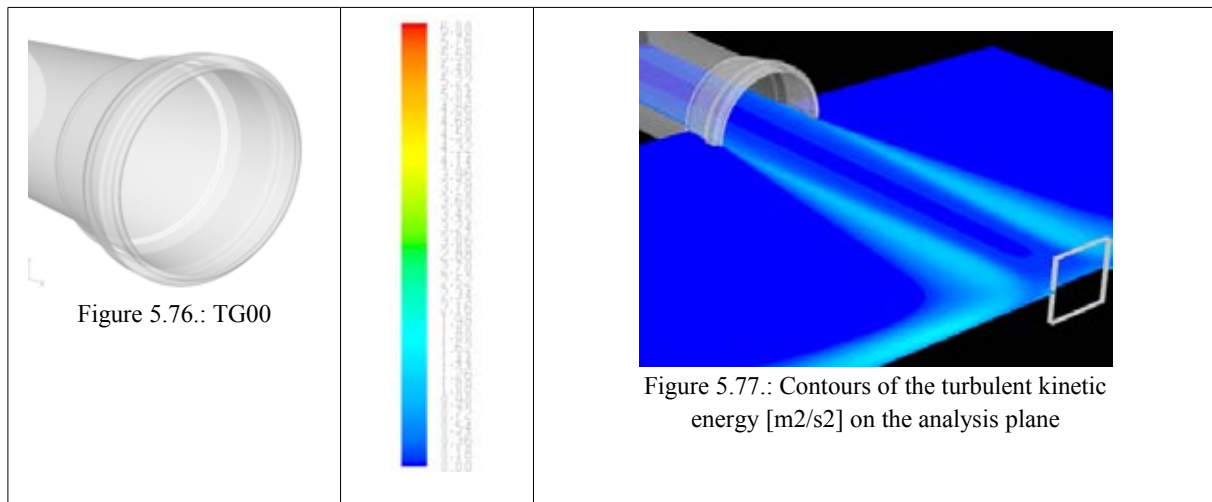


Figure 5.75.: Contours of the velocity magnitude on the analysis plane

Contours of the turbulent kinetic energy [m^2/s^2]:

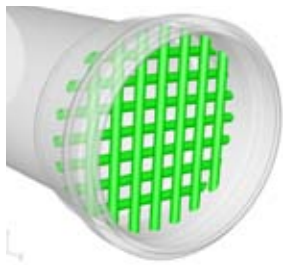


Figure 5.82.: TG03

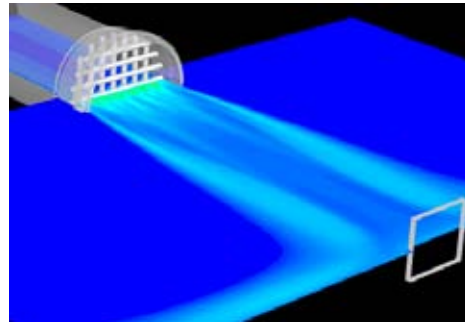
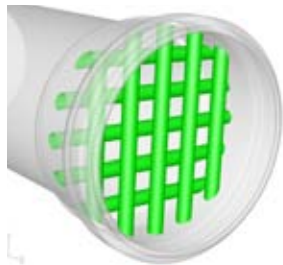
Figure 5.83.: Contours of the turbulent kinetic energy [m²/s²] on the analysis plane

Figure 5.84.: TG04

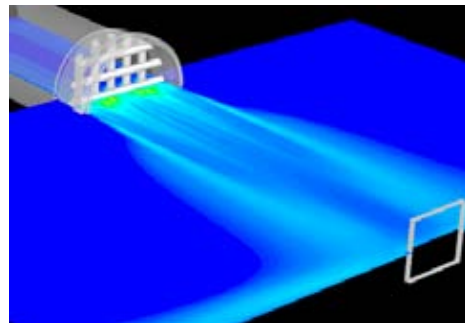
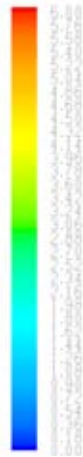
Figure 5.85.: Contours of the turbulent kinetic energy [m²/s²] on the analysis plane

Figure 5.86.: TG05

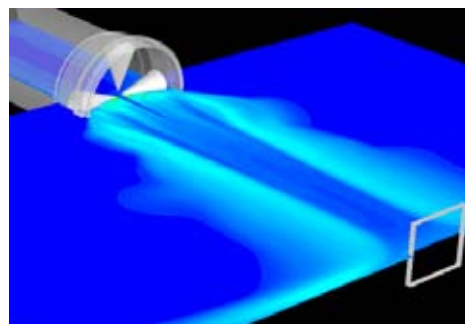
Figure 5.87.: Contours of the turbulent kinetic energy [m²/s²] on the analysis plane



Figure 5.88.: TG06

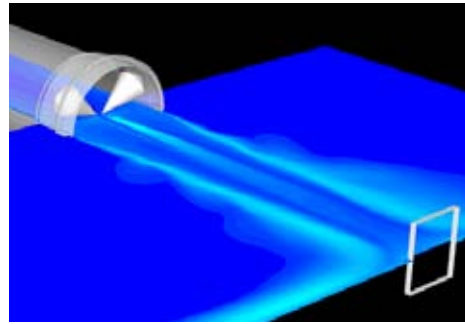


Figure 5.89.: Contours of the turbulent kinetic energy [m2/s2] on the analysis plane



Figure 5.90.: TG07

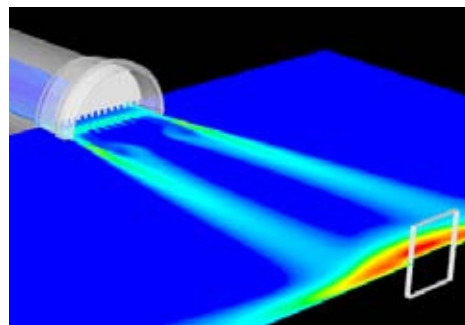


Figure 5.91.: Contours of the turbulent kinetic energy [m2/s2] on the analysis plane



Figure 5.92.: TG08

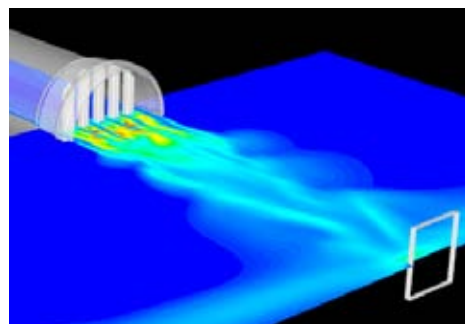
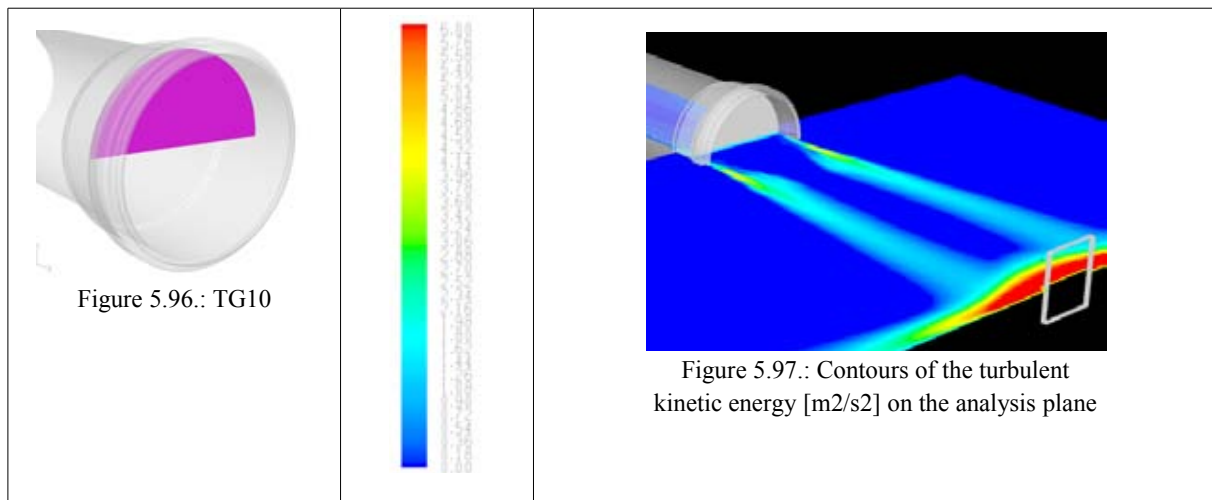
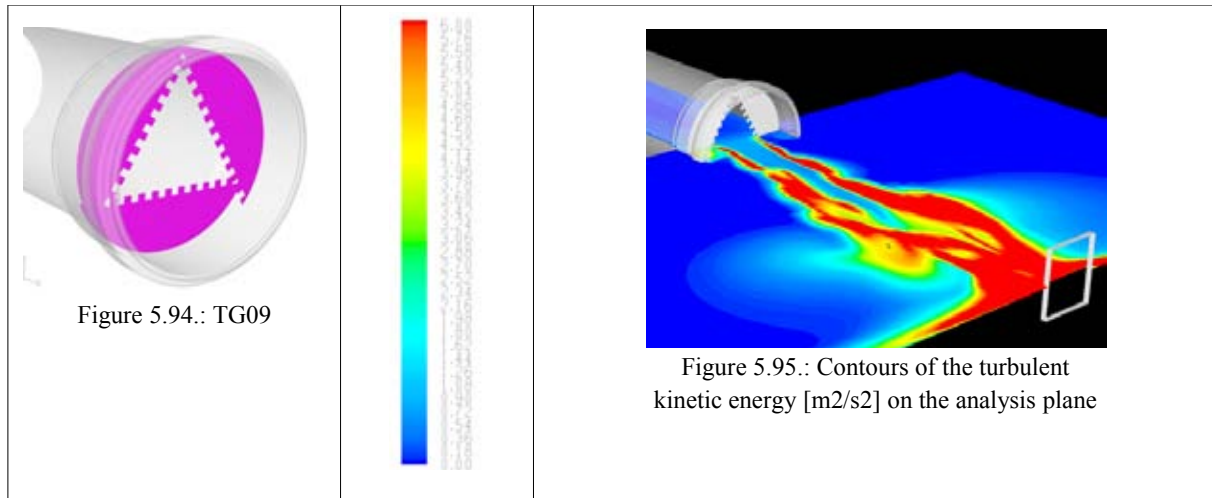


Figure 5.93.: Contours of the turbulent kinetic energy [m2/s2] on the analysis plane



The ability to produce turbulence of each turbulence generator can be observed in the Figures 5.94. – 5.97. Steady CFD simulations leading to acceptable low numerical residuals cannot be achieved for all types of turbulence generators. Turbulence generators built of blades cause very high fluctuating flow fields. Examples of the oscillating behavior of turbulent flow fields are given in Figures 5.73. and 5.95. Turbulent flows like them cannot be captured by using steady solvers. Therefore the average of transient computations have to be calculated for these turbulence generators. [15, 16]

Transient CFD simulations (DES) will be employed to provide frequency spectra for further comparison with the experimental data. Furthermore, this offers the opportunity to investigate the correlation between simulated local velocity fluctuations and pressure fluctuations at the wall. [15, 16]

Details of the unsteady CFD simulations using the Detached Eddy Simulation and their results are documented and evaluated in the following chapters.

6 Unsteady Simulations

CFD simulations are performed for the different turbulence generators using the Detached Eddy Simulation (DES). The Settings for the numerical calculations in FLUENT are summarized in the following table.

Solver	
Solver	segregated
Formulation	implicit
Space	3D
Time	unsteady
Unsteady Formulation	2 nd Order Implicit
Viscous Model	
Model	Detached Eddy Simulation
Spalart-Allmaras Option	Vorticity-Based Production
Materials	
Name:	air
Boundary Conditions	
Inlet:	velocity inlet
Velocity Specification Method	Magnitude, normal to boundary
Velocity [m/s]	UDF
Turbulence Specification Method	Intensity and Hydraulic Diameter
Turbulence Intensity [%]	5
Hydraulic Diameter [m]	0.15259
Outlet 1 & 2:	pressure outlet
Gauge Pressure [Pa]	0
Backflow Direction	normal to boundary
Turbulence Specification Method	Intensity and Length Scale
Backflow Turbulence Intensity [%]	0
Backflow Turbulence Length Scale [m]	1
Solution Controls	
Discretization	
Pressure	Second Order
Momentum	Bounded Central Difference
Modified Turbulent Viscosity	Bounded Central Difference
Solution Initialization	
Gauge Pressure [Pa]	0
X-Velocity [m/s]	0
Y-Velocity [m/s]	0
Z-Velocity [m/s]	0
Modified Turbulent Viscosity [m ² /s]	0. 1
Reference Frame	Relative to Cell Zone

Iteration	
Time Step Size [s]	0.0001
Time Stepping Method	fixed
Options	Data Sampling for Time Statistics
Max. Iteration per Time Step	10
Reporting Interval	1
UDF Profile Update Interval	1
Parallel Partitioning	
Method	Cartesian X-Coordinate
Number	4

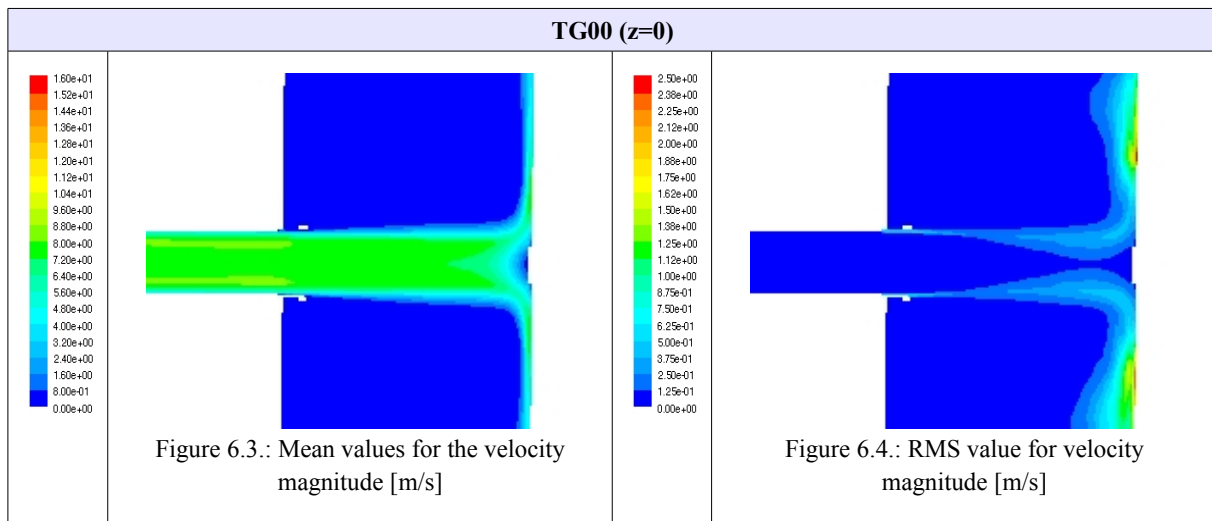
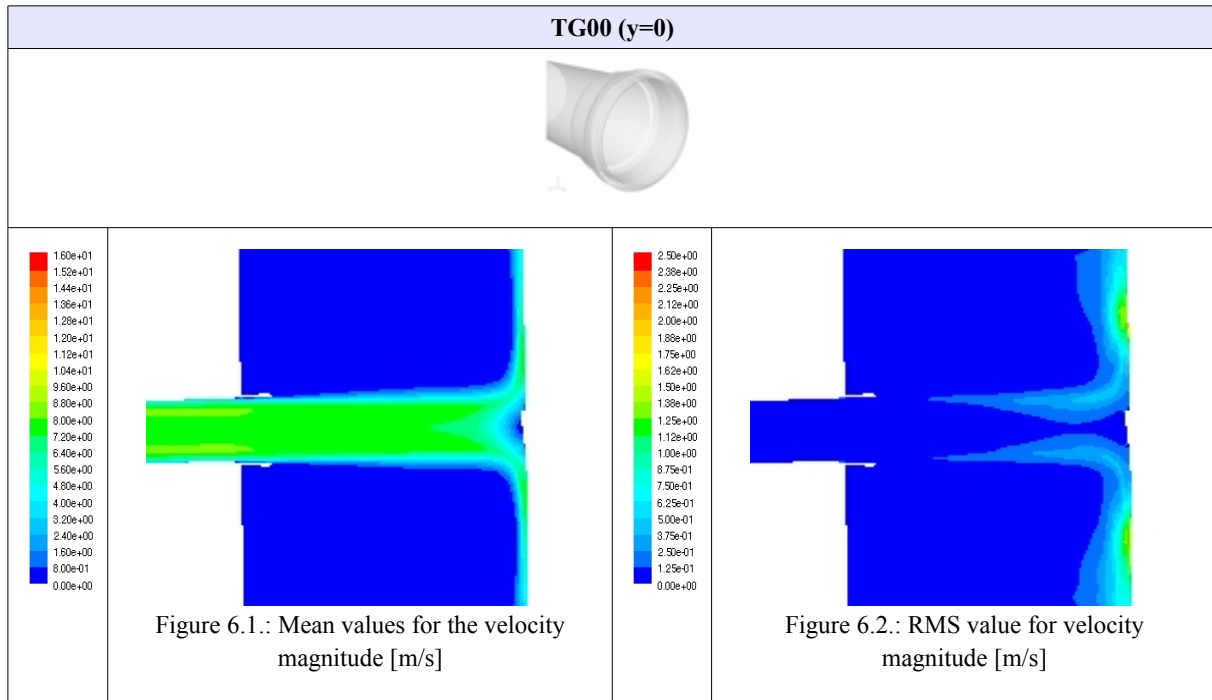
Table 6.1.: Settings in FLUENT for DES

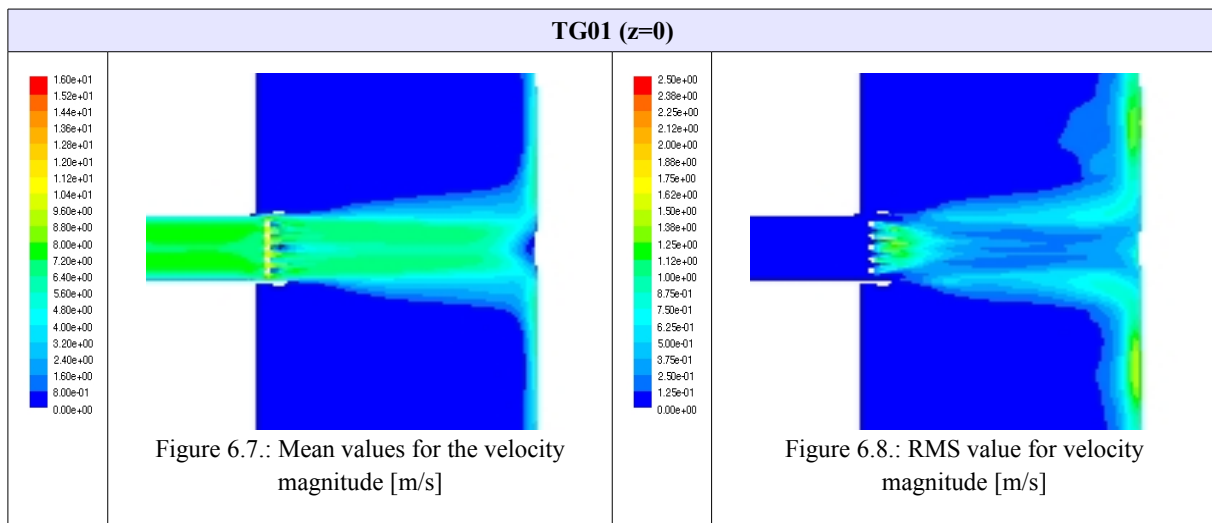
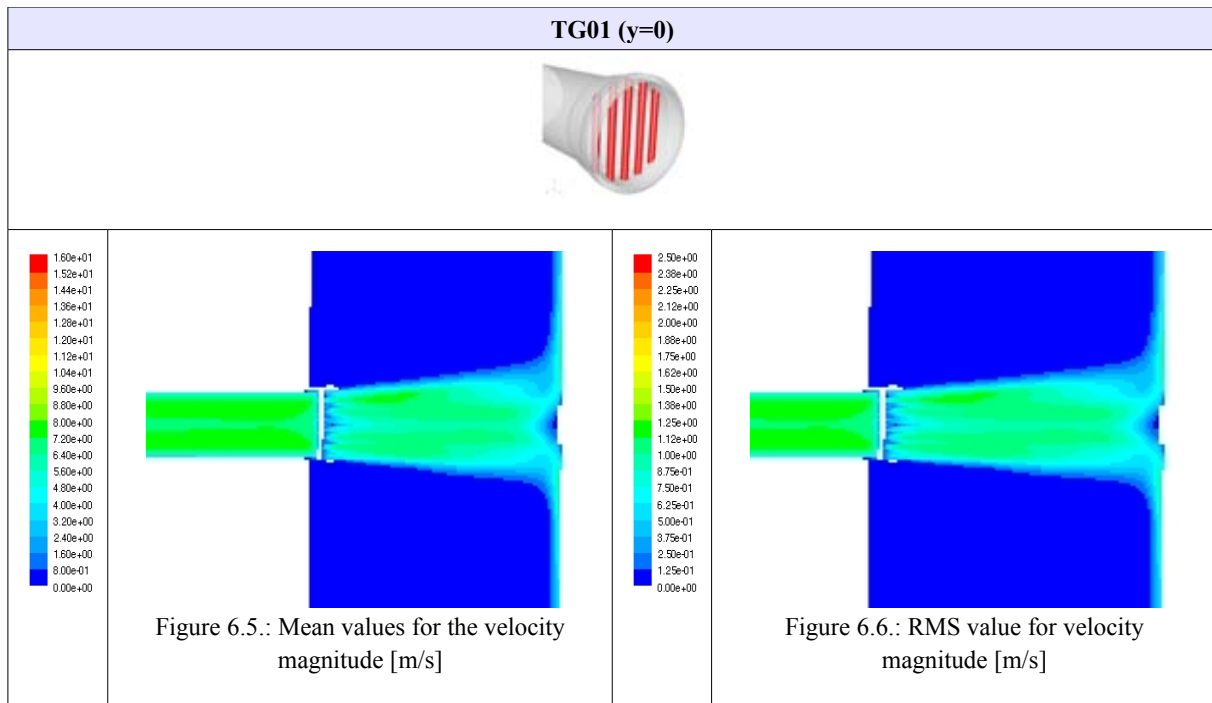
The results of the unsteady CFD calculations are the base for the extraction of fluctuating velocity and pressure time series. Using a time step of $100\mu\text{s}$ around 5000 time steps for the CFD simulations are necessary to reach quasi-static behavior of the flow field. An additional amount of 5000 time steps are calculated and recorded to perform the steps for the spectral analysis. The spectral evaluation of the data is performed using Fourier Transformation and analyzed in 1/3 terz band representations. [16, 17] The simulations have been performed for each turbulence generator, except for TG03 which has been omitted out of its similarity to TG04.

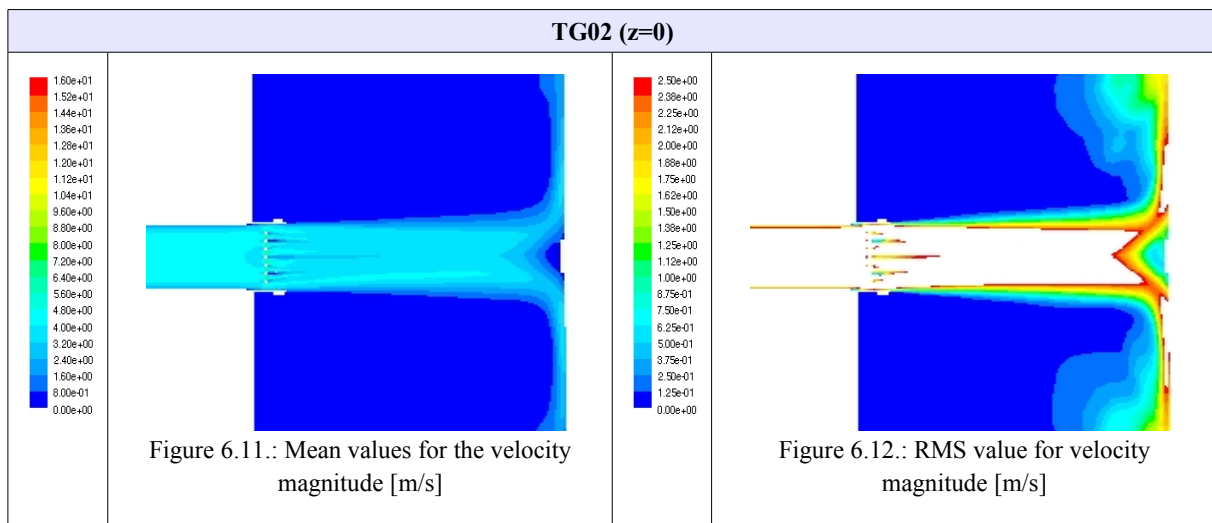
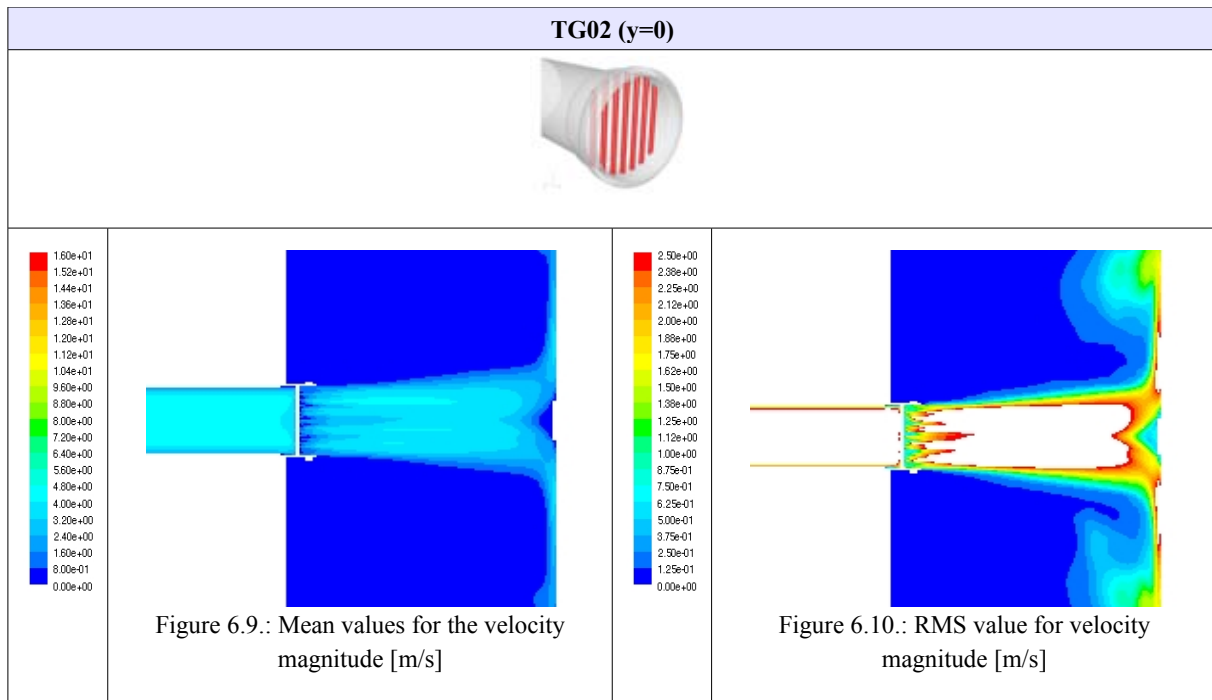
6.1 Mean Velocities and Fluctuations

The following figures show the mean and RMS values of the velocity magnitude [m/s] for the different turbulence generators on the planes $y=0$ and $z=0$. An overview of the calculation volume is given in figure 3.2. In some figures are white regions which represent RMS values that are beyond the range.

Mean values (left) and RSM (right) for the velocity magnitude [m/s]:







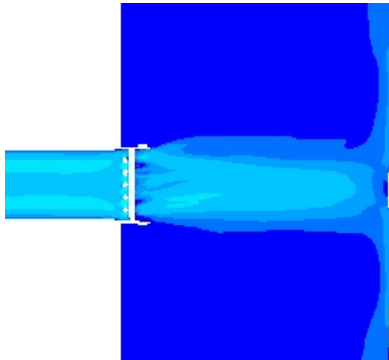
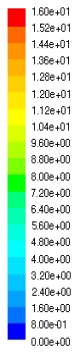
TG04 ($y=0$)

Figure 6.13.: Mean values for the velocity magnitude [m/s]

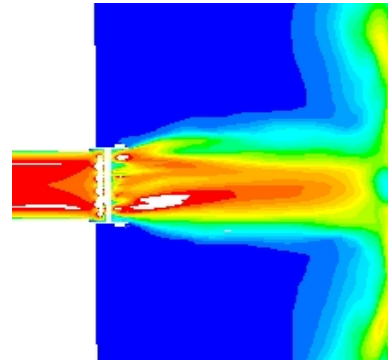


Figure 6.14.: RMS value for velocity magnitude [m/s]

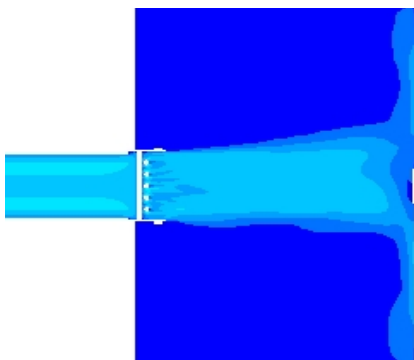
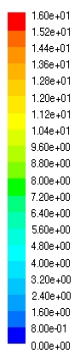
TG04 ($z=0$)

Figure 6.15.: Mean values for the velocity magnitude [m/s]

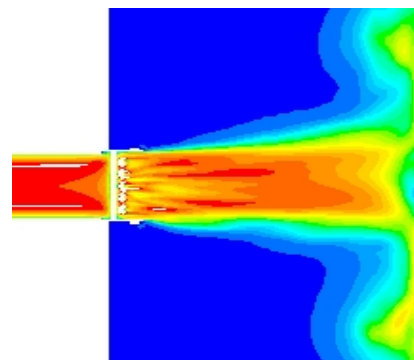
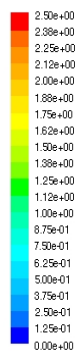
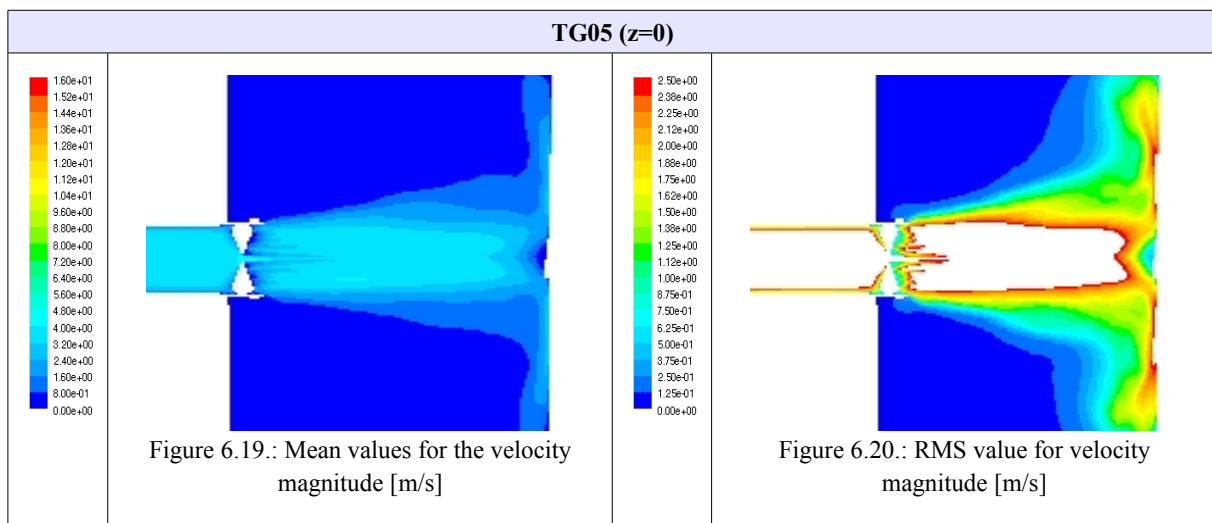
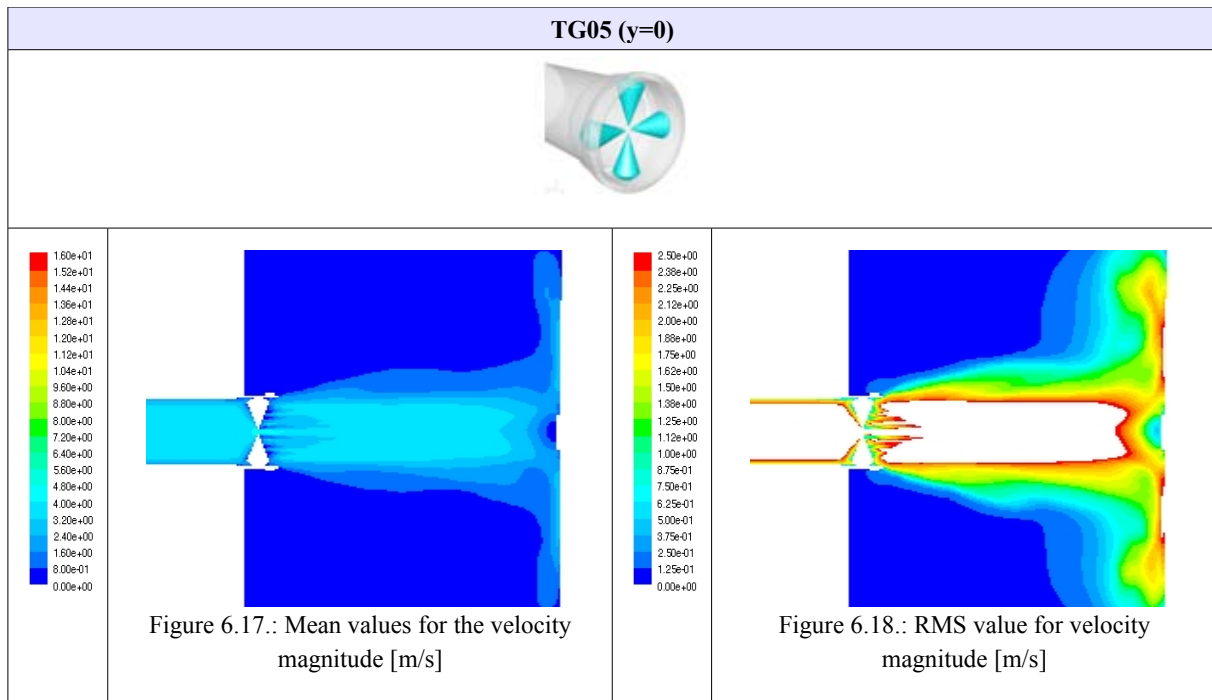
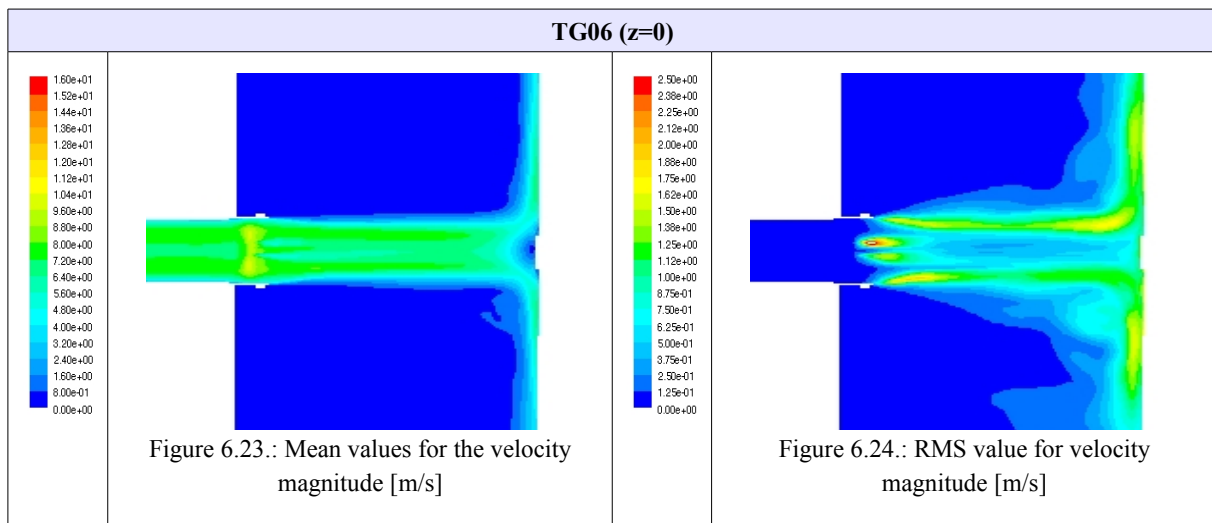
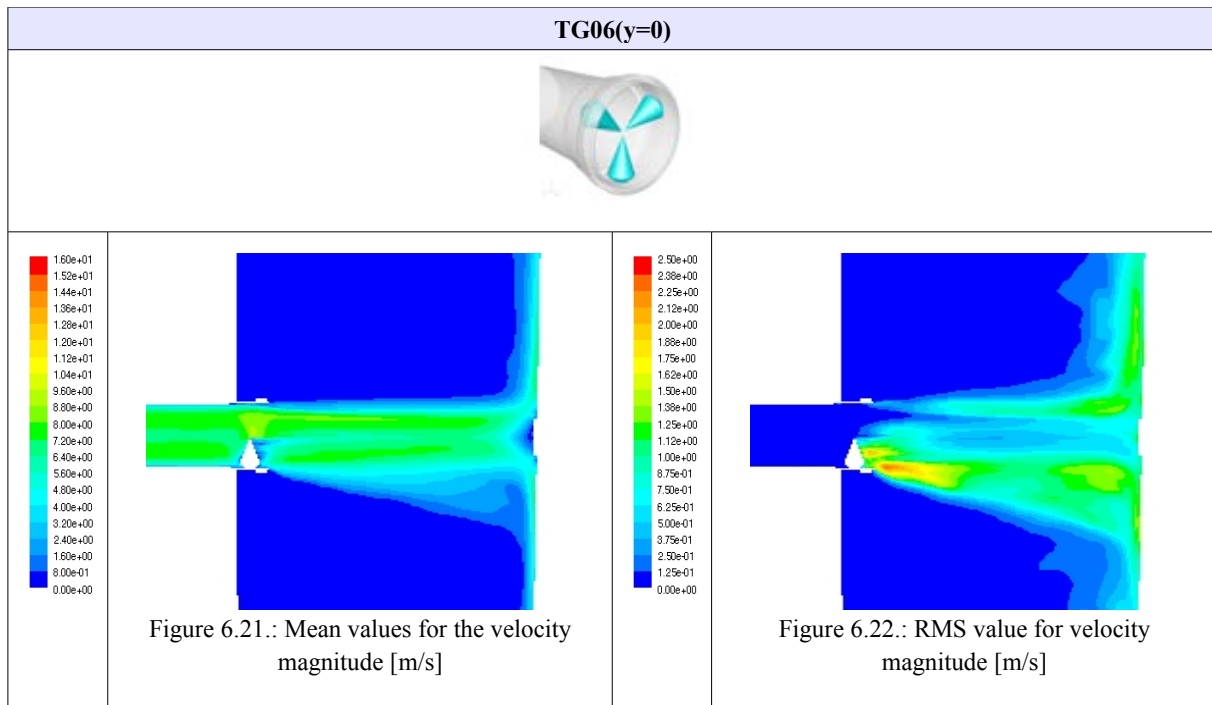
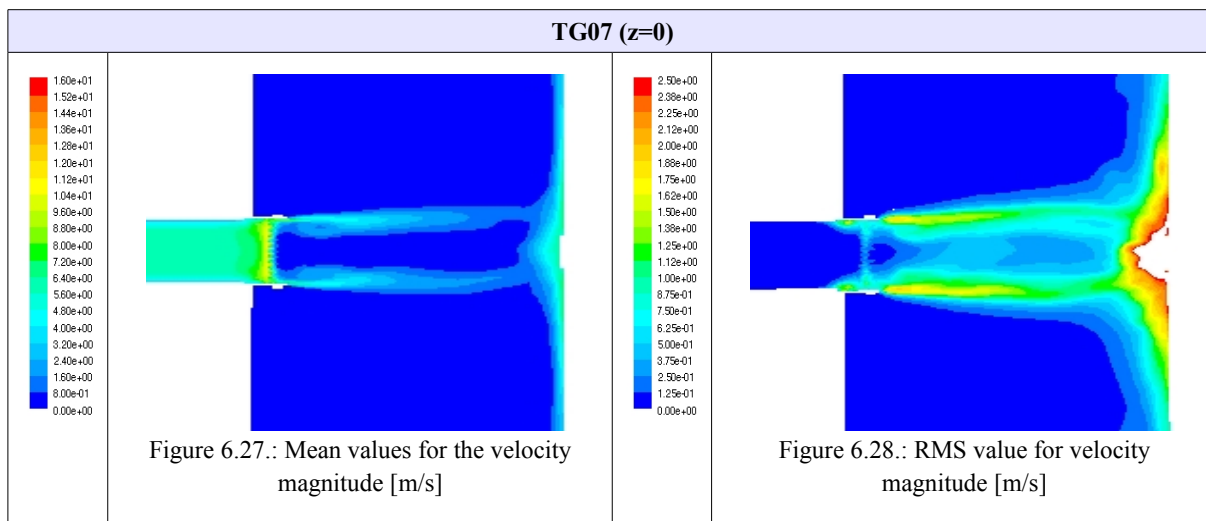
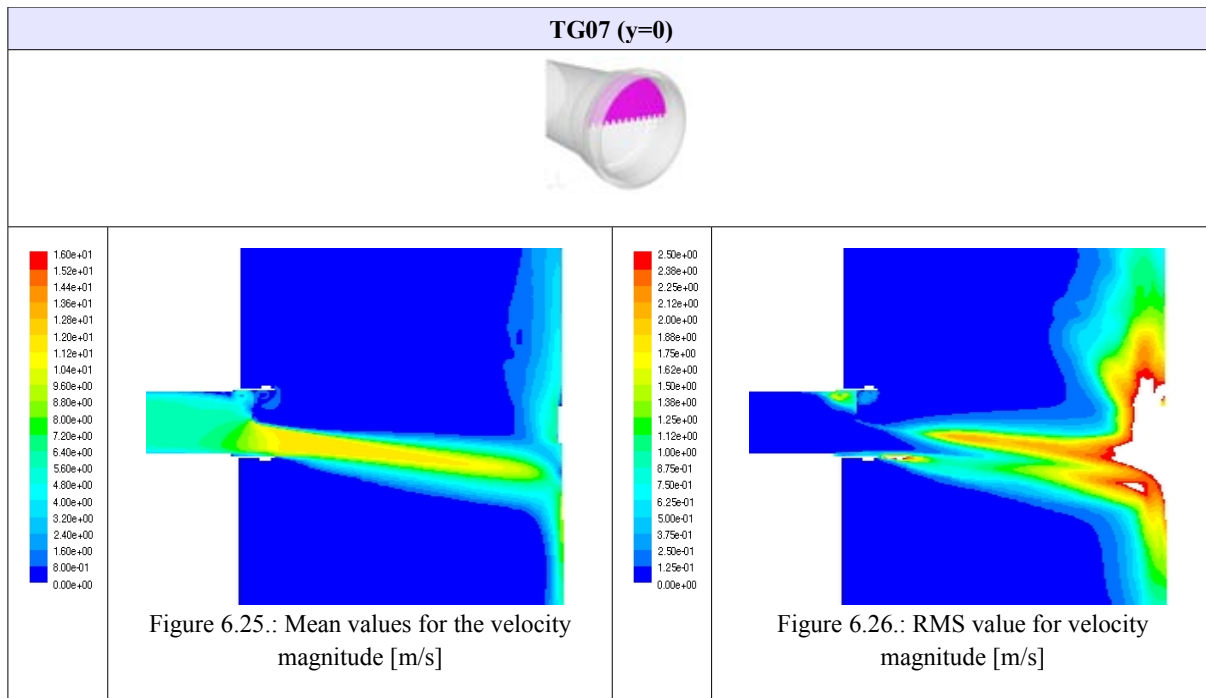
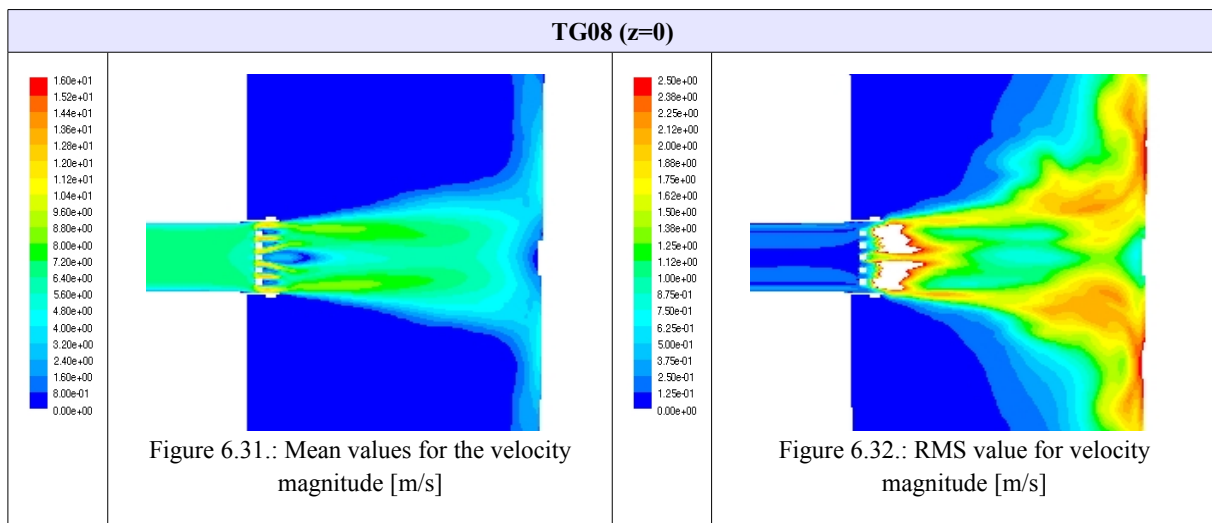
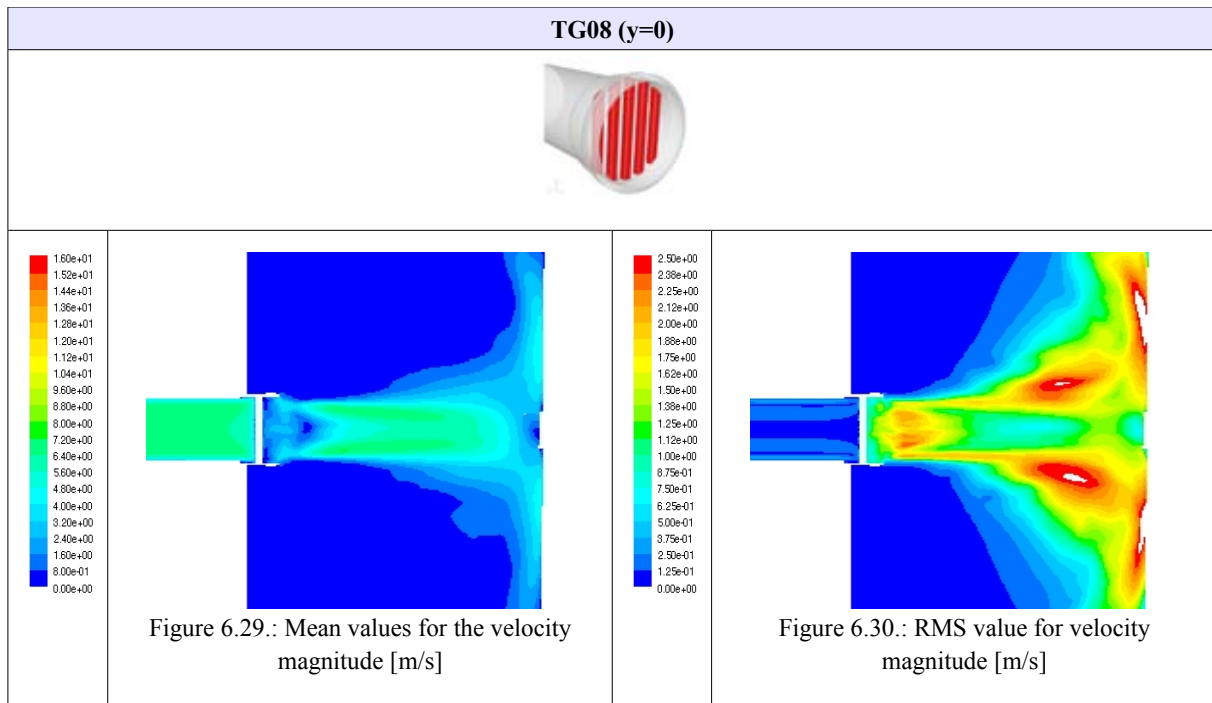


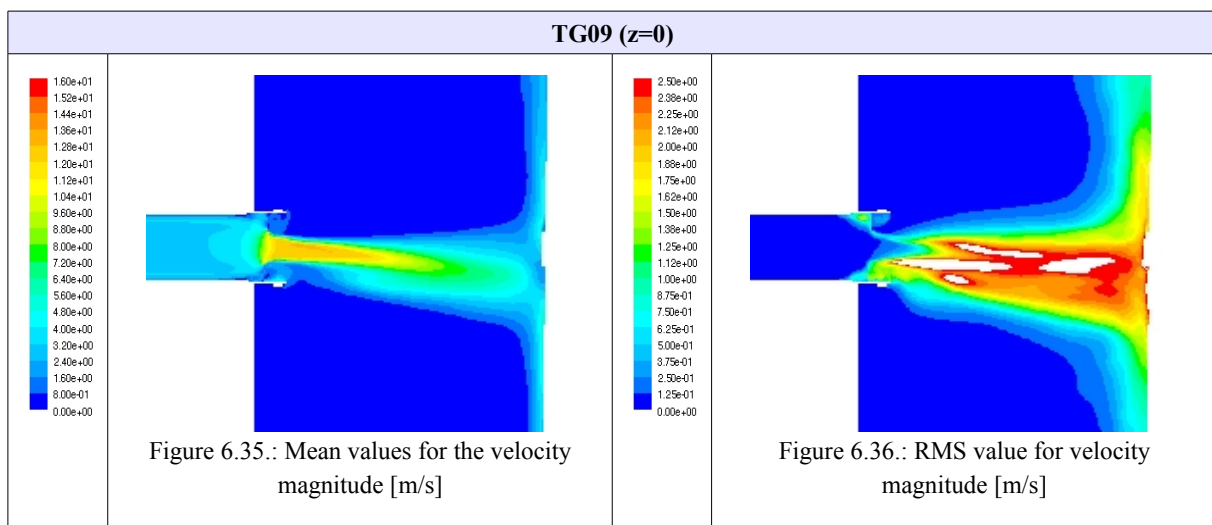
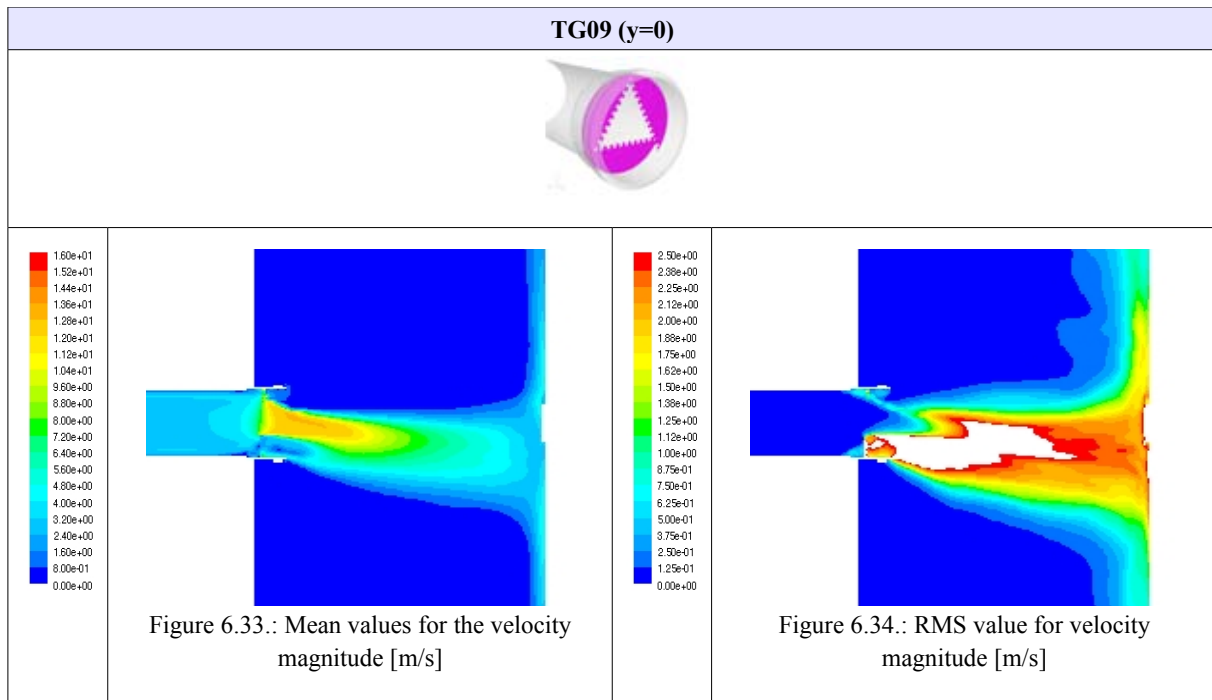
Figure 6.16.: RMS value for velocity magnitude [m/s]

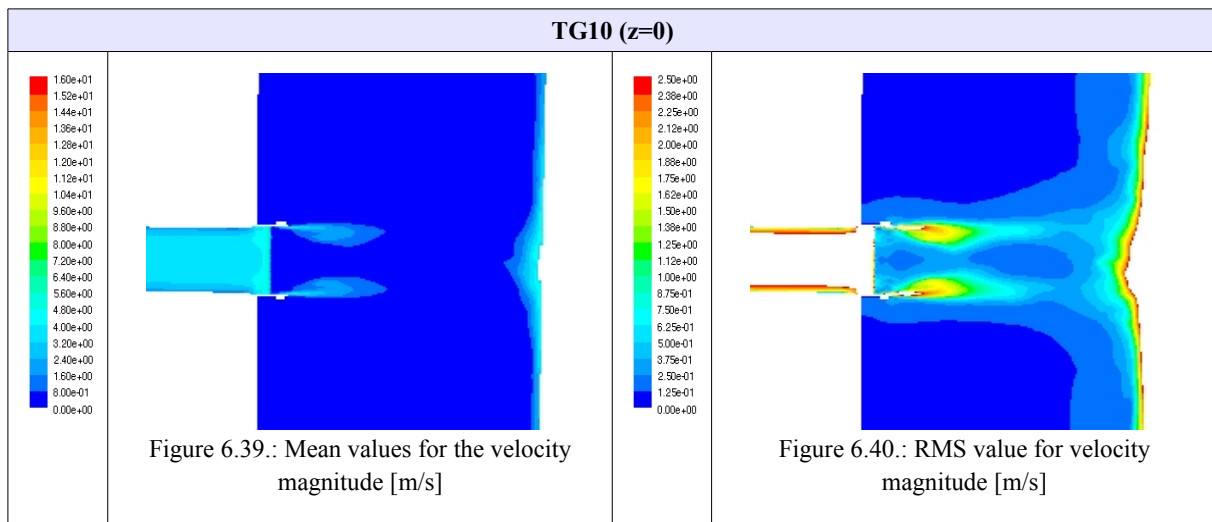
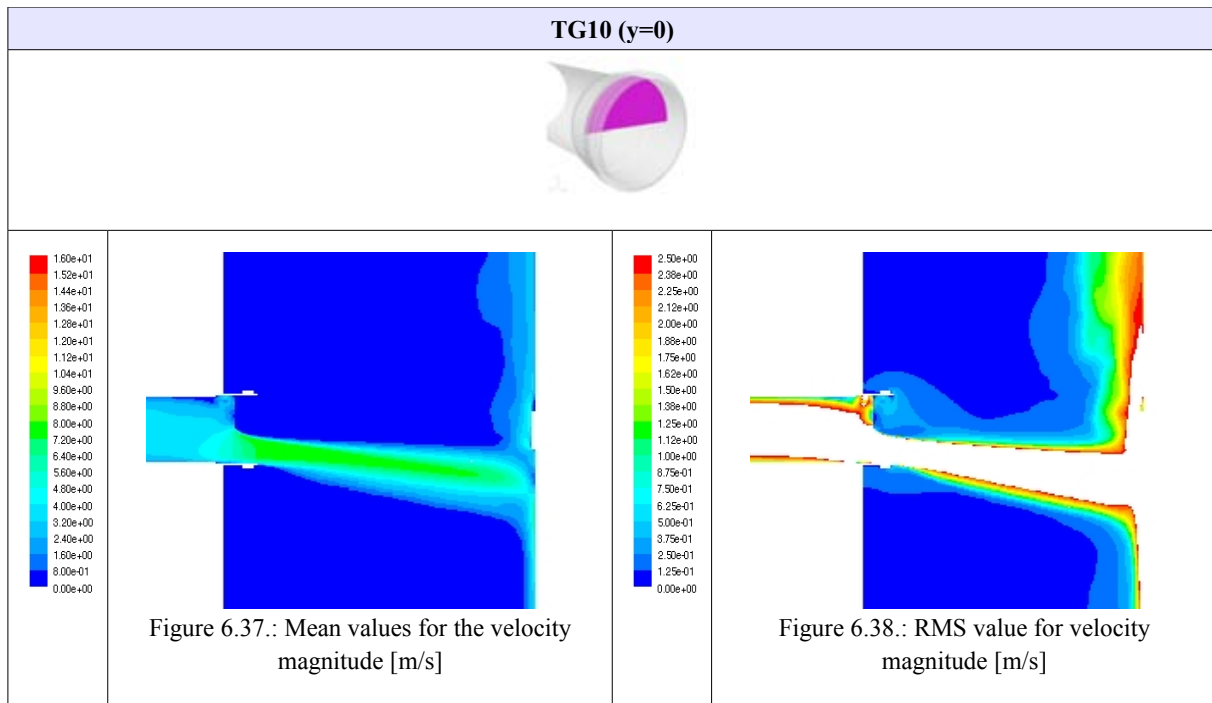






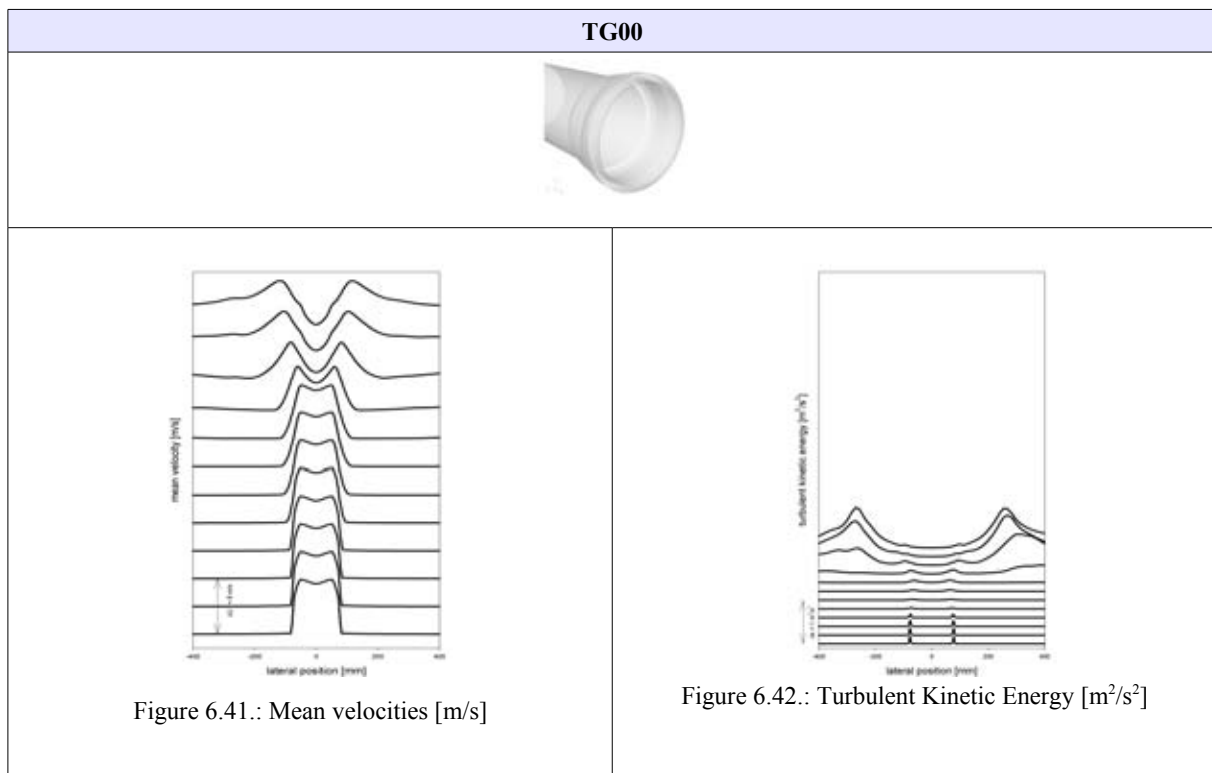






The mean values of the velocity magnitude on the planes $y=0$ and $z=0$ for each turbulence generator are given in a profile representation. These profiles show the results of the CFD simulation at the post-processing lines L01-L12. The lines are separated and shifted by 4 m/s which helps to observe the change of the velocity magnitude in the turbulent flow. The profile representations of the turbulent kinetic energy for the different turbulence generators using DES for the computational analysis are given also in the following figures. The turbulent kinetic energy $k = \frac{1}{2} \overline{u_i u_i} = \frac{1}{2} (\overline{u_x u_x} + \overline{u_y u_y} + \overline{u_z u_z})$ is calculated from the values of all three velocity variations (x, y, z) . The different lines are separated and shifted by a value of $0.2 \text{ m}^2/\text{s}^2$.

These profiles are given in the Fig. 6.41. - 6.78. which are all generated in the graphing software SigmaPlot .



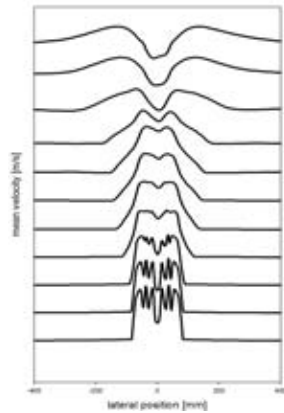
TG01 ($z=0$)

Figure 6.43.: Mean velocities [m/s]

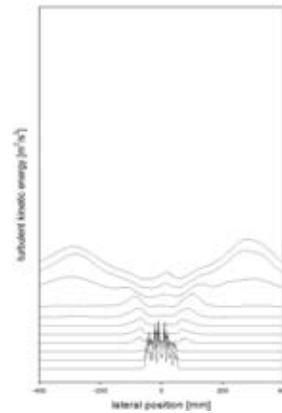
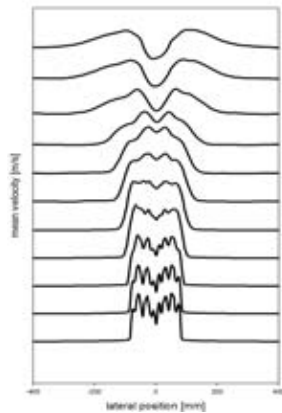
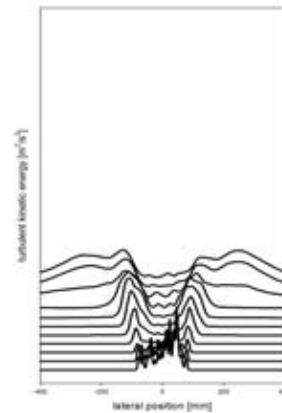
Figure 6.44.: Turbulent Kinetic Energy [m²/s²]TG01 ($y=0$)

Figure 6.45.: Mean velocities [m/s]

Figure 6.46.: Turbulent Kinetic Energy [m²/s²]

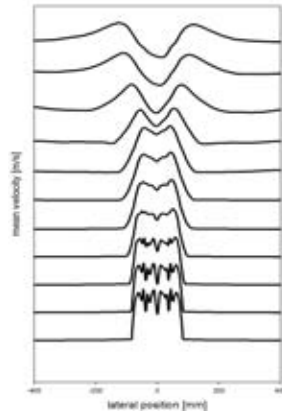
TG02 ($z=0$)

Figure 6.47.: Mean velocities [m/s]

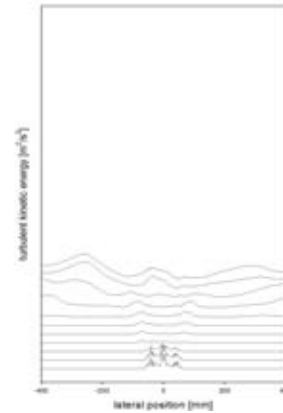
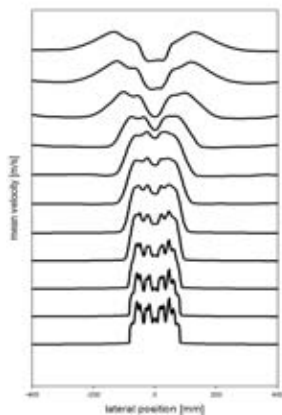
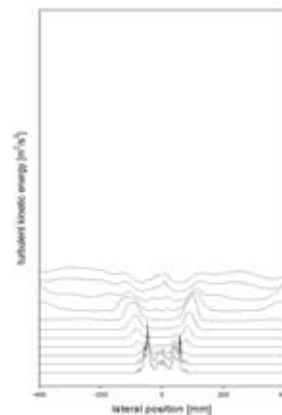
Figure 6.48.: Turbulent Kinetic Energy [m^2/s^2]TG02 ($y=0$)

Figure 6.49.: Mean velocities [m/s]

Figure 6.50.: Turbulent Kinetic Energy [m^2/s^2]

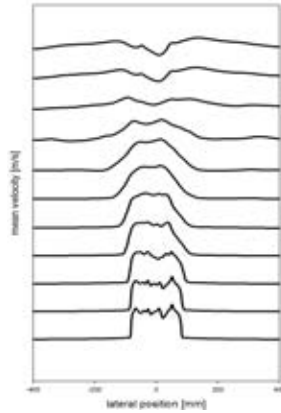
TG04 ($z=0$)

Figure 6.51.: Mean velocities [m/s]

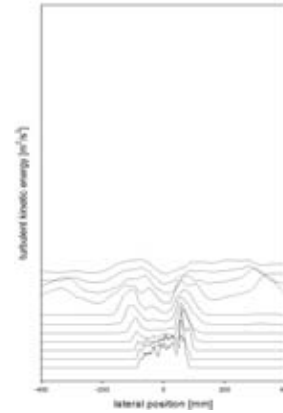
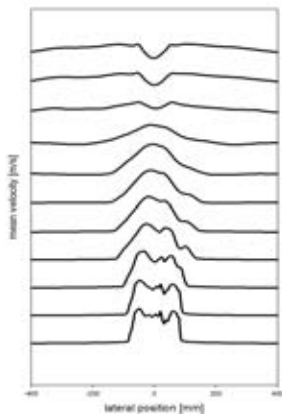
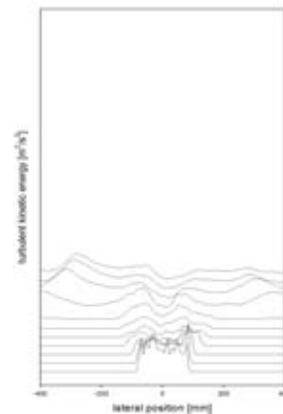
Figure 6.52.: Turbulent Kinetic Energy [m^2/s^2]TG04 ($y=0$)

Figure 6.53.: Mean velocities [m/s]

Figure 6.54.: Turbulent Kinetic Energy [m^2/s^2]

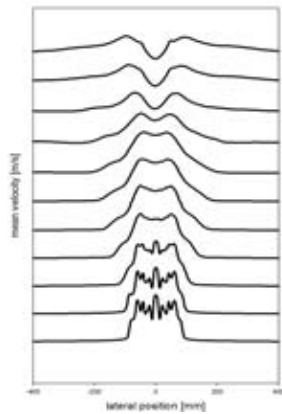
TG05 ($z=0$)

Figure 6.55.: Mean velocities [m/s]

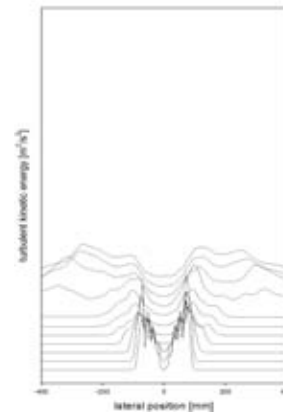


Figure 6.56.: Turbulent Kinetic Energy [m²/s²]

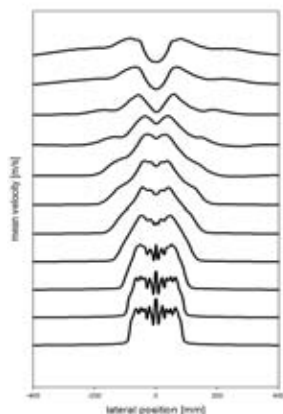
TG05 ($y=0$)

Figure 6.57.: Mean velocities [m/s]

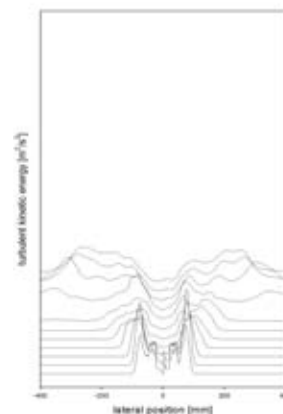


Figure 6.58.: Turbulent Kinetic Energy [m²/s²]

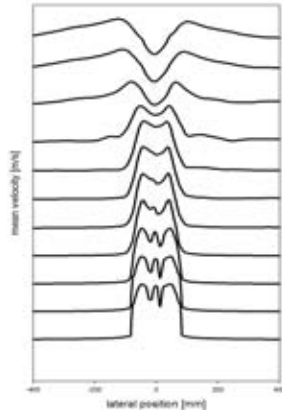
TG06 ($z=0$)

Figure 6.59.: Mean velocities [m/s]

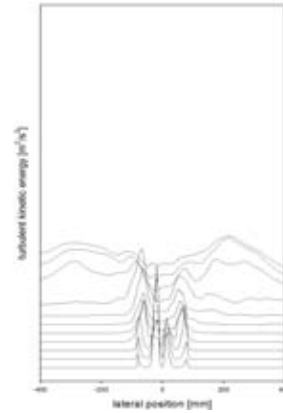
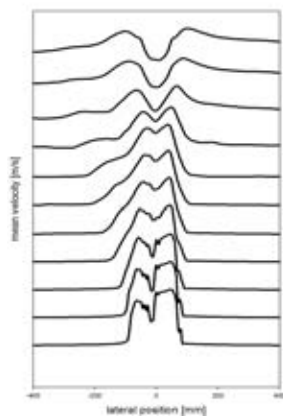
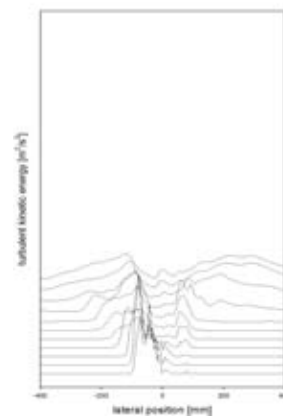
Figure 6.60.: Turbulent Kinetic Energy [m^2/s^2]TG06 ($y=0$)

Figure 6.61.: Mean velocities [m/s]

Figure 6.62.: Turbulent Kinetic Energy [m^2/s^2]

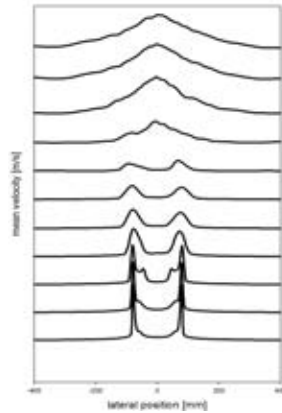
TG07 ($z=0$)

Figure 6.63.: Mean velocities [m/s]

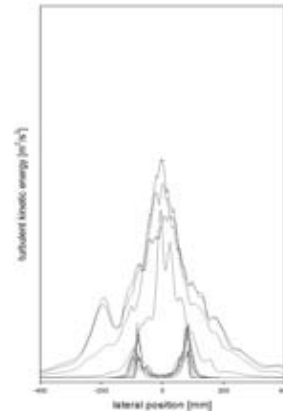
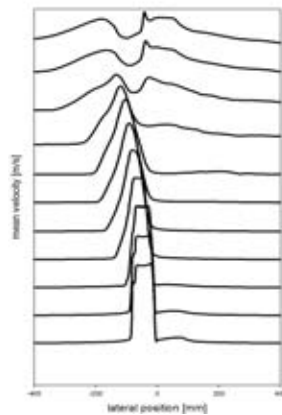
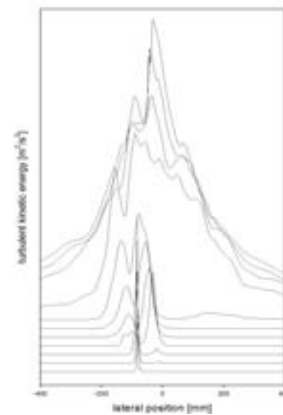
Figure 6.64.: Turbulent Kinetic Energy [m^2/s^2]TG07 ($y=0$)

Figure 6.65.: Mean velocities [m/s]

Figure 6.66.: Turbulent Kinetic Energy [m^2/s^2]

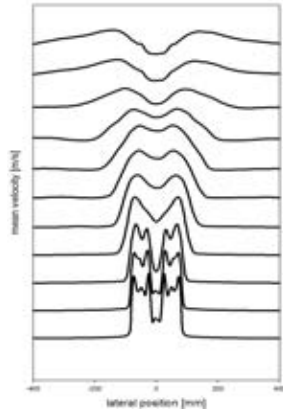
TG08 ($z=0$)

Figure 6.67.: Mean velocities [m/s]

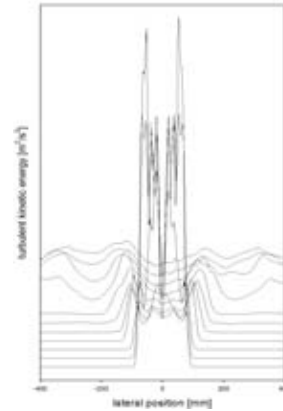
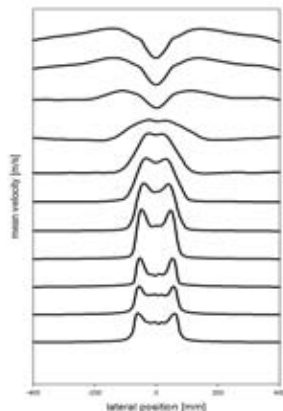
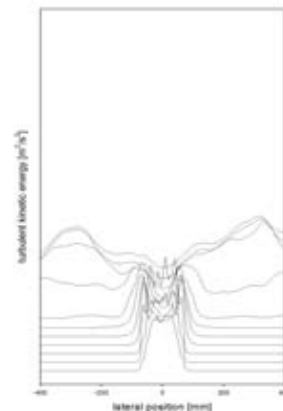
Figure 6.68.: Turbulent Kinetic Energy [m²/s²]TG08 ($y=0$)

Figure 6.69.: Mean velocities [m/s]

Figure 6.70.: Turbulent Kinetic Energy [m²/s²]

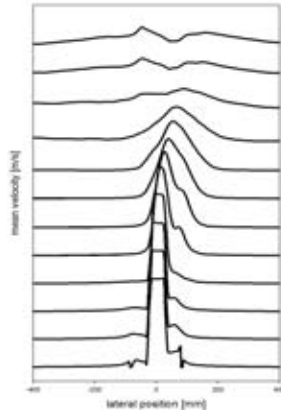
TG09 ($z=0$)

Figure 6.71.: Mean velocities [m/s]

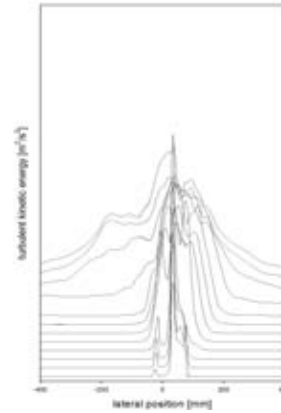
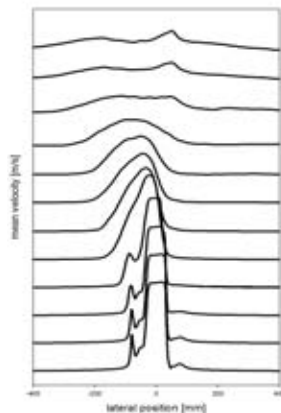
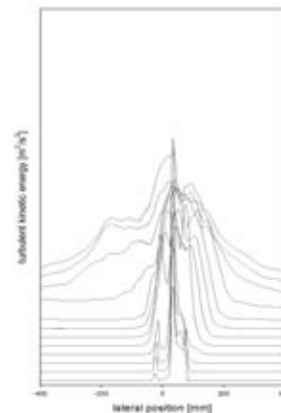
Figure 6.72.: Turbulent Kinetic Energy [m^2/s^2]TG09 ($y=0$)

Figure 6.73.: Mean velocities [m/s]

Figure 6.74.: Turbulent Kinetic Energy [m^2/s^2]

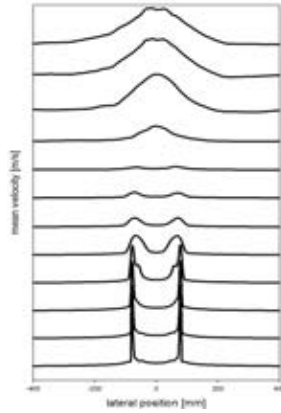
TG10 ($z=0$)

Figure 6.75.: Mean velocities [m/s]

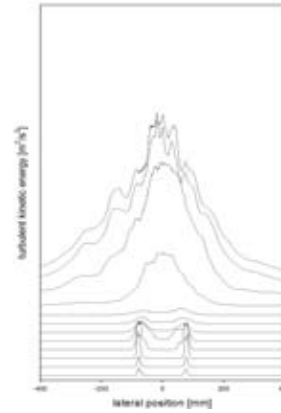
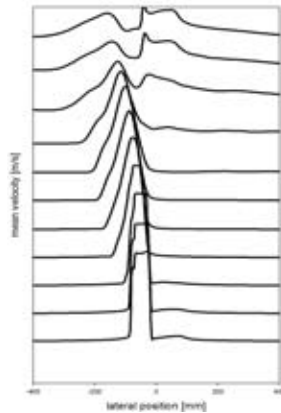
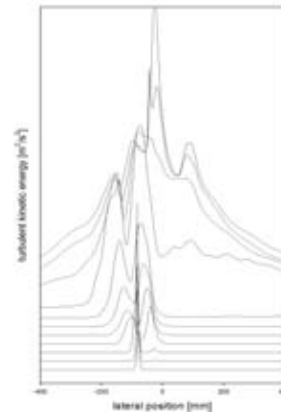
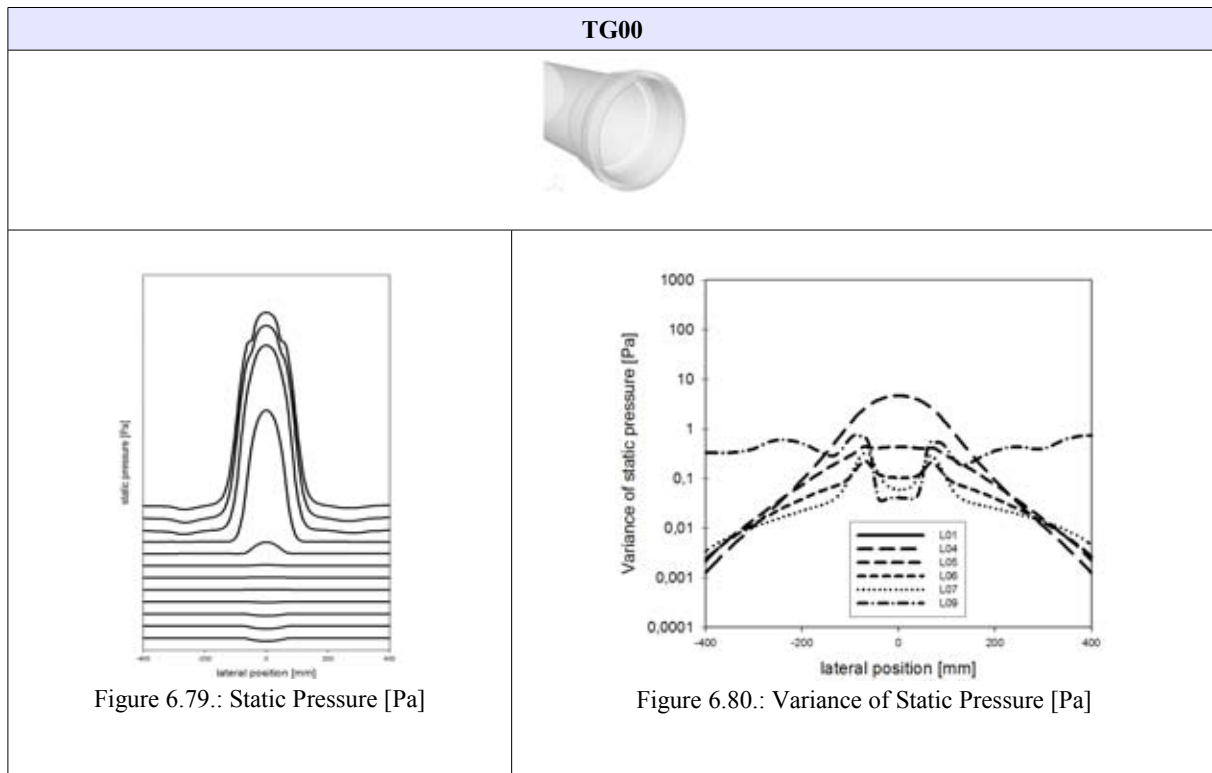
Figure 6.76.: Turbulent Kinetic Energy [m^2/s^2]**TG10 ($y=0$)**

Figure 6.77.: Mean velocities [m/s]

Figure 6.78.: Turbulent Kinetic Energy [m^2/s^2]

Pressure fluctuations have been recorded on the evaluation lines during the transient DES. The profile representations in the planes $y=0$ and $z=0$ for the mean value (left) of static pressure are given at the evaluation lines L01-L12 which are shifted by the value of 2 Pa. The RSM (right) value of static pressure is given at 6 selected evaluation lines L01, L04, L05, L06, L07 and L09 from top to bottom. The y-axis for the RMS of static pressure is given in a logarithmic representation.



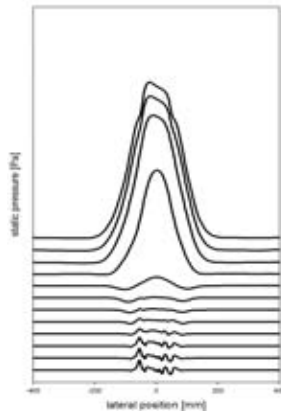
TG01 ($y=0$)

Figure 6.81.: Static Pressure [Pa]

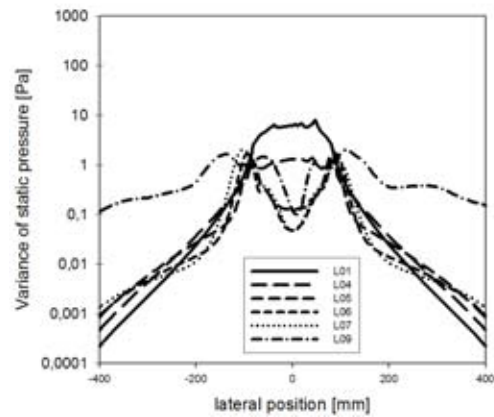


Figure 6.82.: Variance of static pressure [Pa]

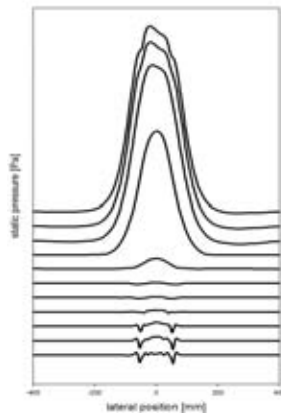
TG01 ($z=0$)

Figure 6.83.: Static Pressure [Pa]

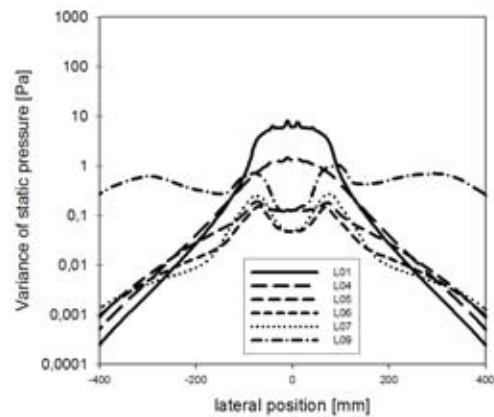


Figure 6.84.: Variance of static pressure [Pa]

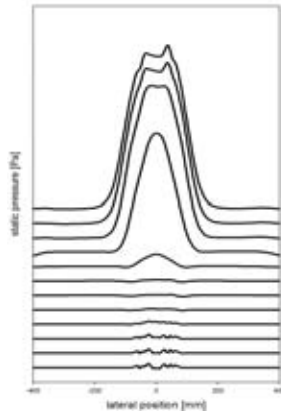
TG02 ($y=0$)

Figure 6.85.: Static Pressure [Pa]

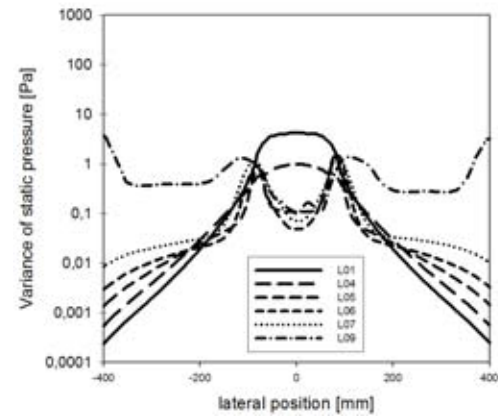


Figure 6.86.: Variance of static pressure [Pa]

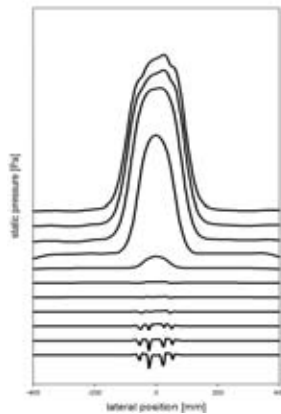
TG02 ($z=0$)

Figure 6.87.: Static Pressure [Pa]

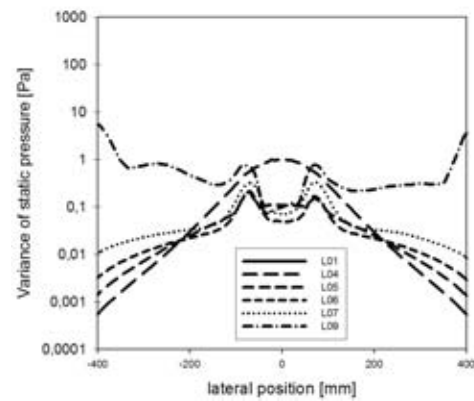


Figure 6.88.: Variance of static pressure [Pa]

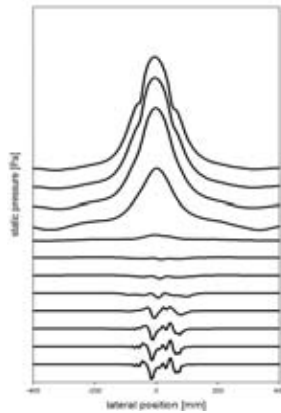
TG04 ($y=0$)

Figure 6.89.: Static Pressure [Pa]

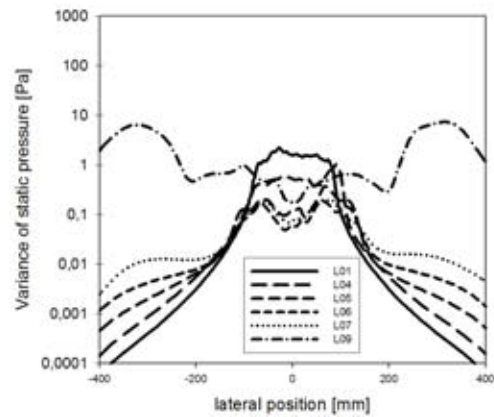


Figure 6.90.: Variance of static pressure [Pa]

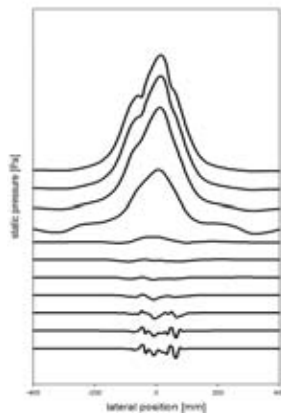
TG04 ($z=0$)

Figure 6.91.: Static Pressure [Pa]

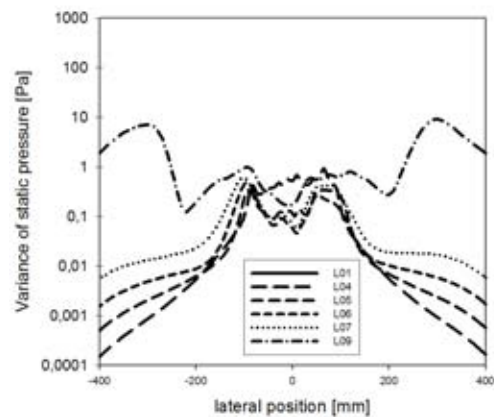


Figure 6.92.: Variance of static pressure [Pa]

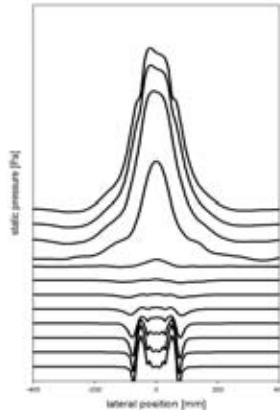
TG05 ($y=0$)

Figure 6.93.: Static Pressure [Pa]

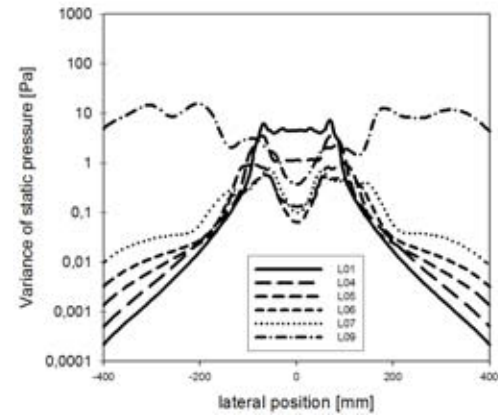


Figure 6.94.: Variance of static pressure [Pa]

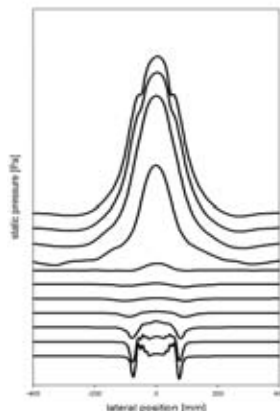
TG05 ($z=0$)

Figure 6.95.: Static Pressure [Pa]

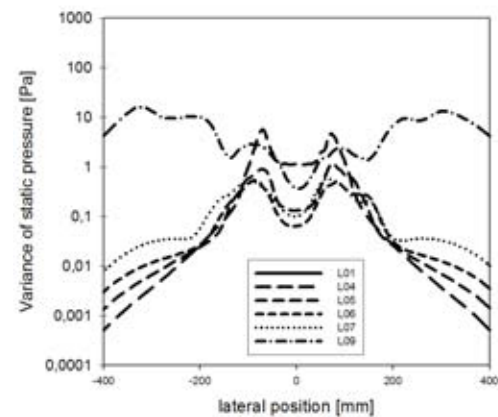


Figure 6.96.: Variance of static pressure [Pa]

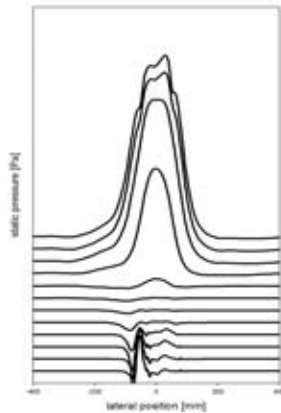
TG06 ($y=0$)

Figure 6.97.: Static Pressure [Pa]

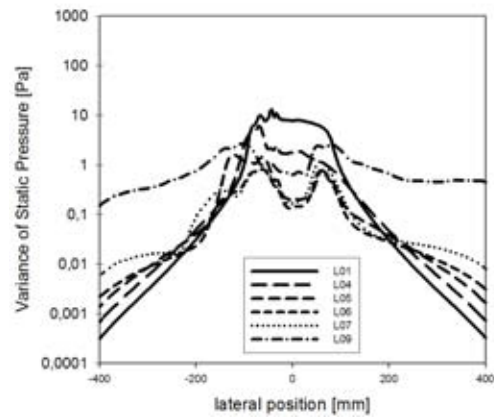


Figure 6.98.: Variance of static pressure [Pa]

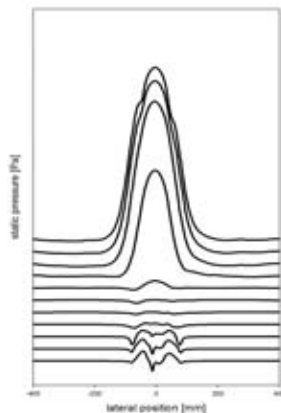
TG06 ($z=0$)

Figure 6.99.: Static Pressure [Pa]

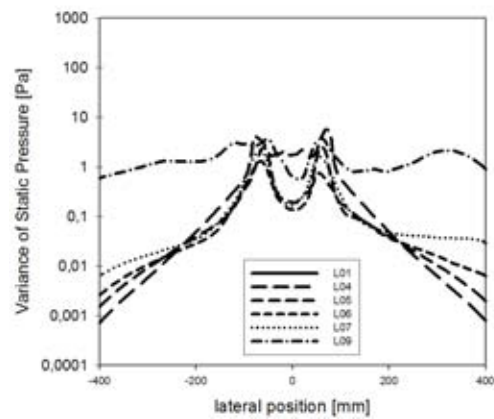


Figure 6.100.: Variance of static pressure [Pa]

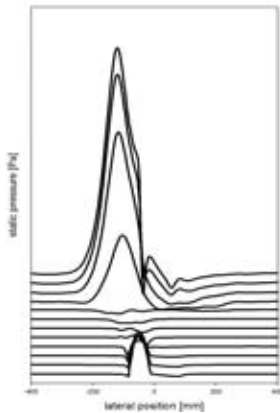
TG07 ($y=0$)

Figure 6.101.: Static Pressure [Pa]

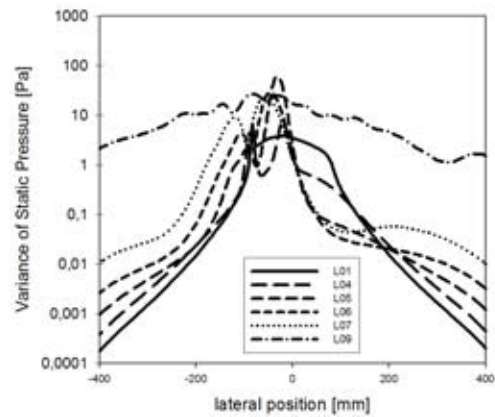


Figure 6.102.: Variance of static pressure [Pa]

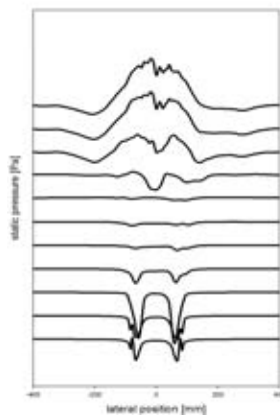
TG07 ($z=0$)

Figure 6.103.: Static Pressure [Pa]

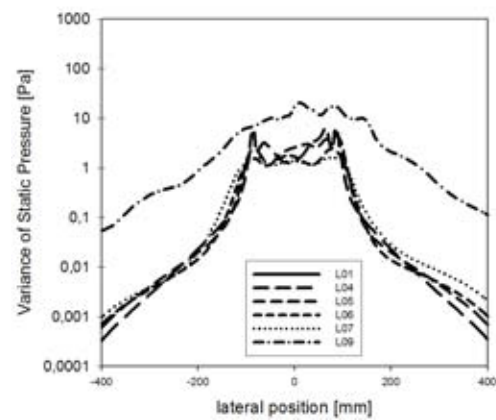


Figure 6.104.: Variance of static pressure [Pa]

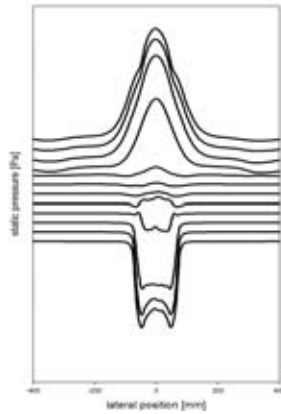
TG08 ($y=0$)

Figure 6.105.: Static Pressure [Pa]

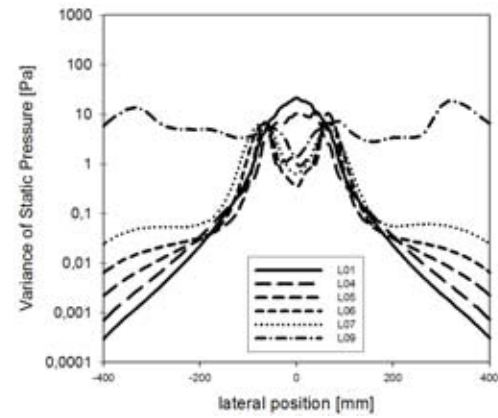


Figure 6.106.: Variance of static pressure [Pa]

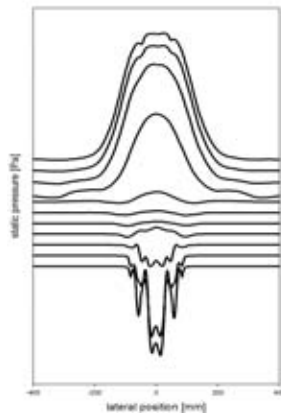
TG08 ($z=0$)

Figure 6.107.: Static Pressure [Pa]

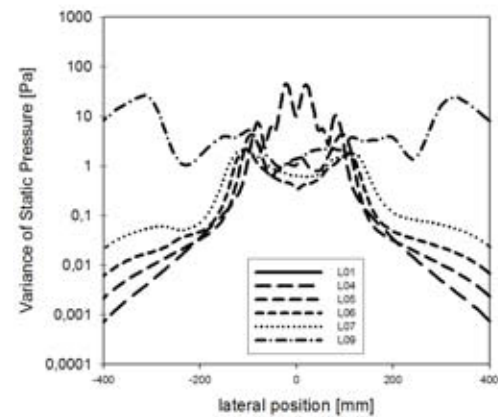


Figure 6.108.: Variance of static pressure [Pa]

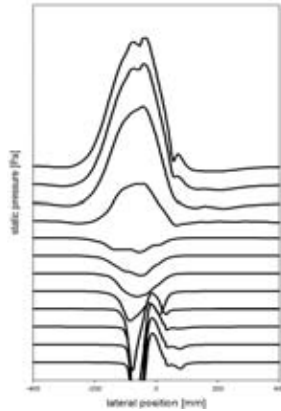
TG09 ($y=0$)

Figure 6.109.: Static Pressure [Pa]

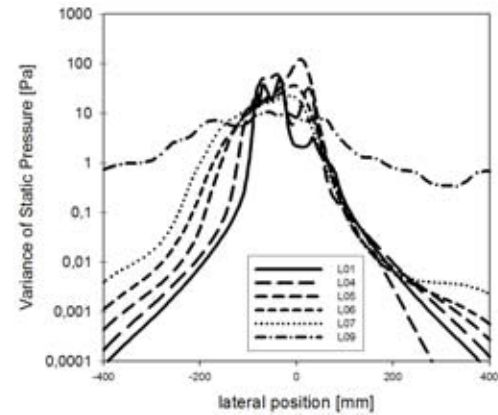


Figure 6.110.: Variance of static pressure [Pa]

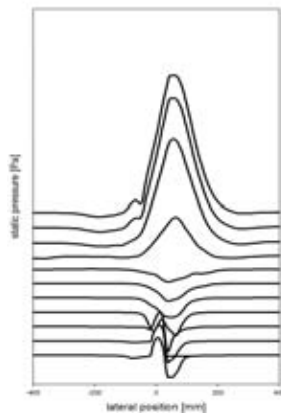
TG09 ($z=0$)

Figure 6.111.: Static Pressure [Pa]

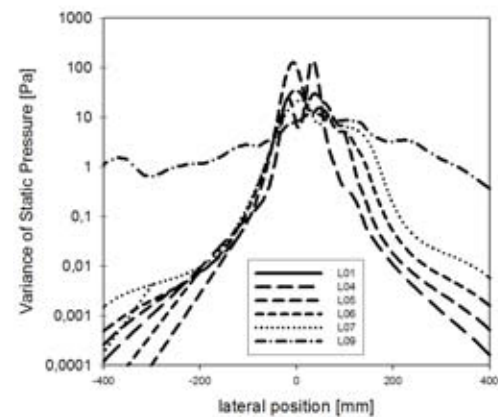


Figure 6.112.: Variance of static pressure [Pa]

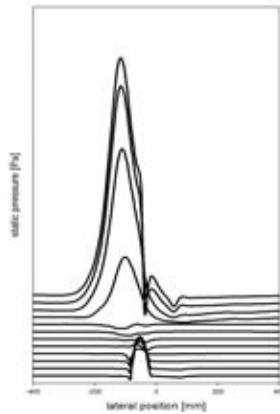
TG10 ($y=0$)

Figure 6.113.: Static Pressure [Pa]

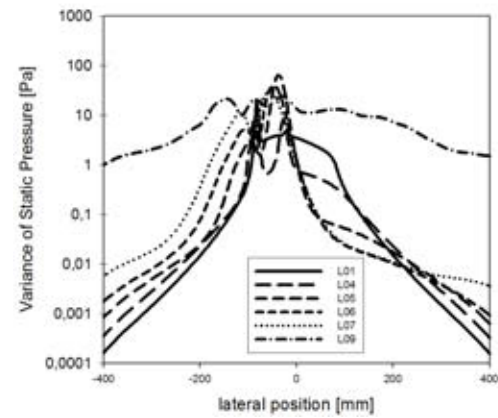


Figure 6.114.: Variance of static pressure [Pa]

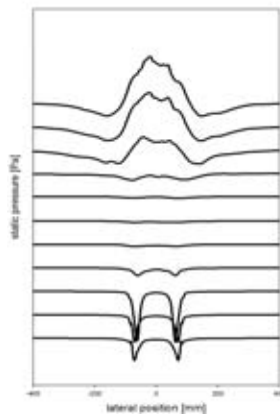
TG10 ($z=0$)

Figure 6.115.: Static Pressure [Pa]

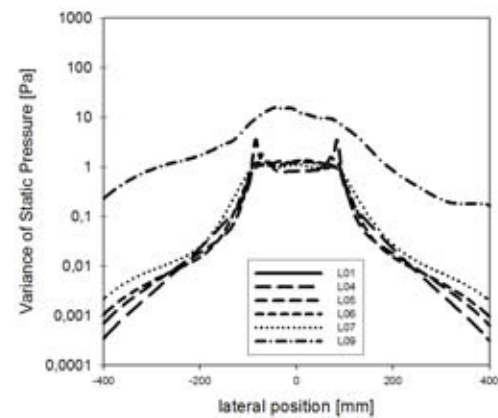


Figure 6.116.: Variance of static pressure [Pa]

6.2 Fast Fourier Transformation

Spectral Methods are important in some applications, as the simulation of turbulence. Hence they are briefly described here.

The *Fast Fourier-Transformation (FFT)* is based on the *Discrete Fourier-Transformation (DFT)*. Spectral Methods use periodic functions which can be represented by discrete Fourier-series:

$$u_j = u(x_j) = \sum_{k=-K}^K \hat{u}_k e^{ikx_j} \quad \text{equation (6.1)}$$

where $x_j = j \Delta x$, $j = 1, 2, \dots, N$ and $x_j = 2\pi j/N$. Equation (6.1) can be inverted by using

$$\hat{u}_k = \hat{u}(x_k) = \frac{1}{N} \sum_{m=1}^N u_m e^{-ikx_m} \quad \text{equation (6.2)}$$

where $k = -K, \dots, K$.

In many situations, there is a considerable advantage of implementing equation (6.1) by FFT. Data are shuffled into a bit-reversed order and appropriate phase factors are introduced. The Fast Fourier Transformation reduces successively the original Fourier Transformations at N points to Fourier Transformations each with the half number of points ($N \rightarrow N/2 \rightarrow N/4$). This splitting is going to be continued till only one trivial Fourier Transformation for one single point remains.

The savings in computational time are substantial, since only $N \cdot \ln(N)$ operations are required for an N -point transformation as opposed to N^2 operations for the DFT.

To take advantage of the FFT, N must not be a prime number. The highest acceleration of the computational efforts can be achieved by choosing N to the power of 2:

$$N = 2^p, p \in \mathbb{N} \quad [6, 7]$$

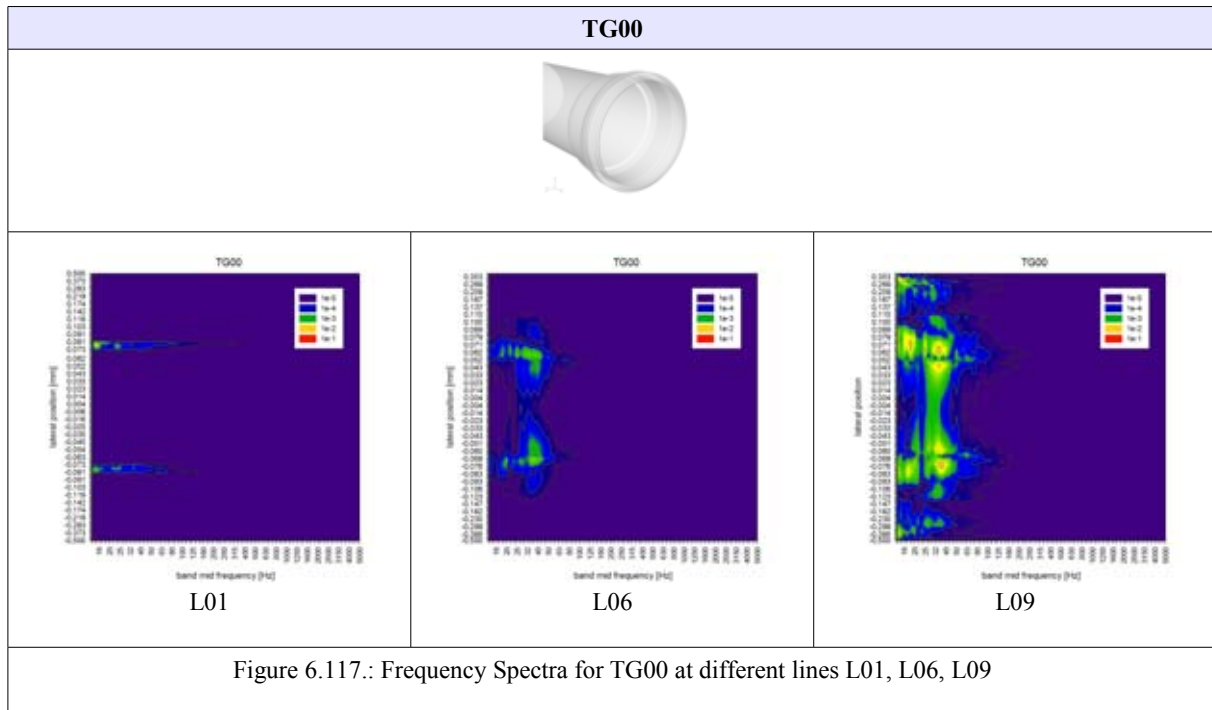
6.3 Spectral Analysis

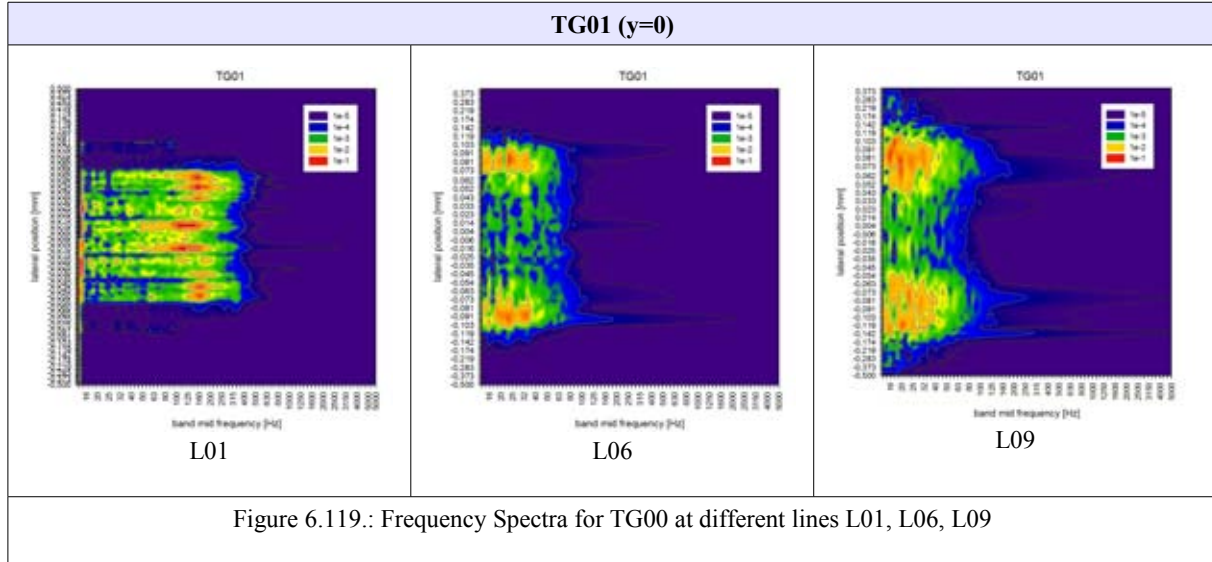
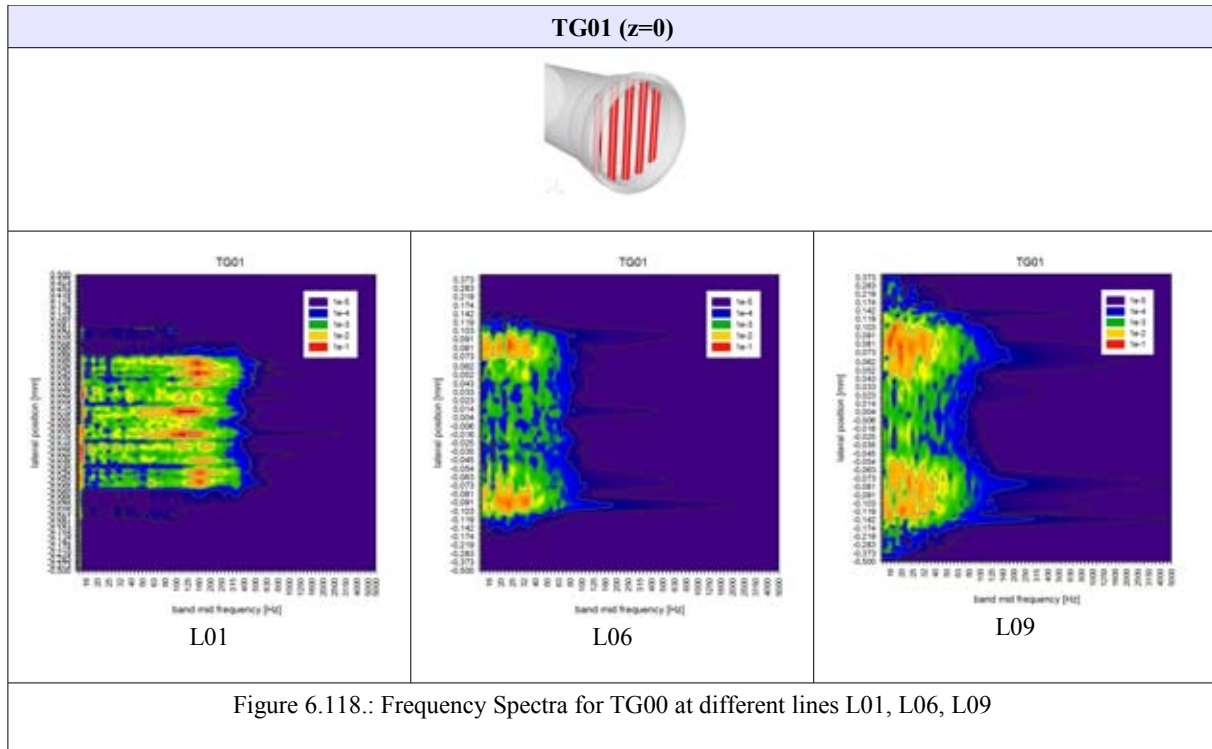
This chapter gives detailed information about the simulation post-processing and shows the FFT spectra

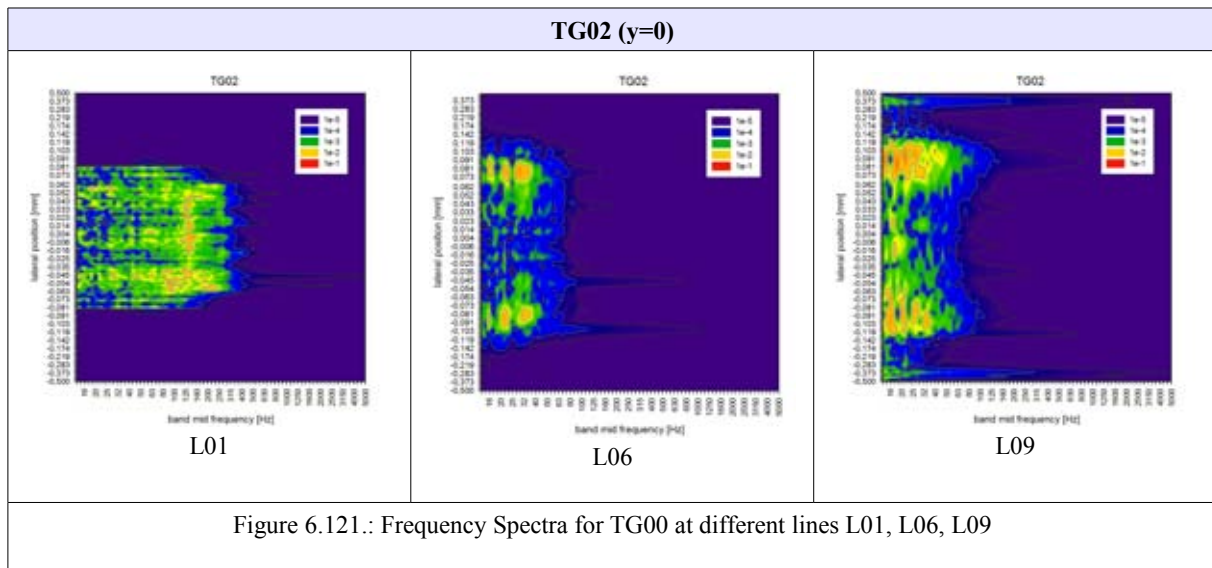
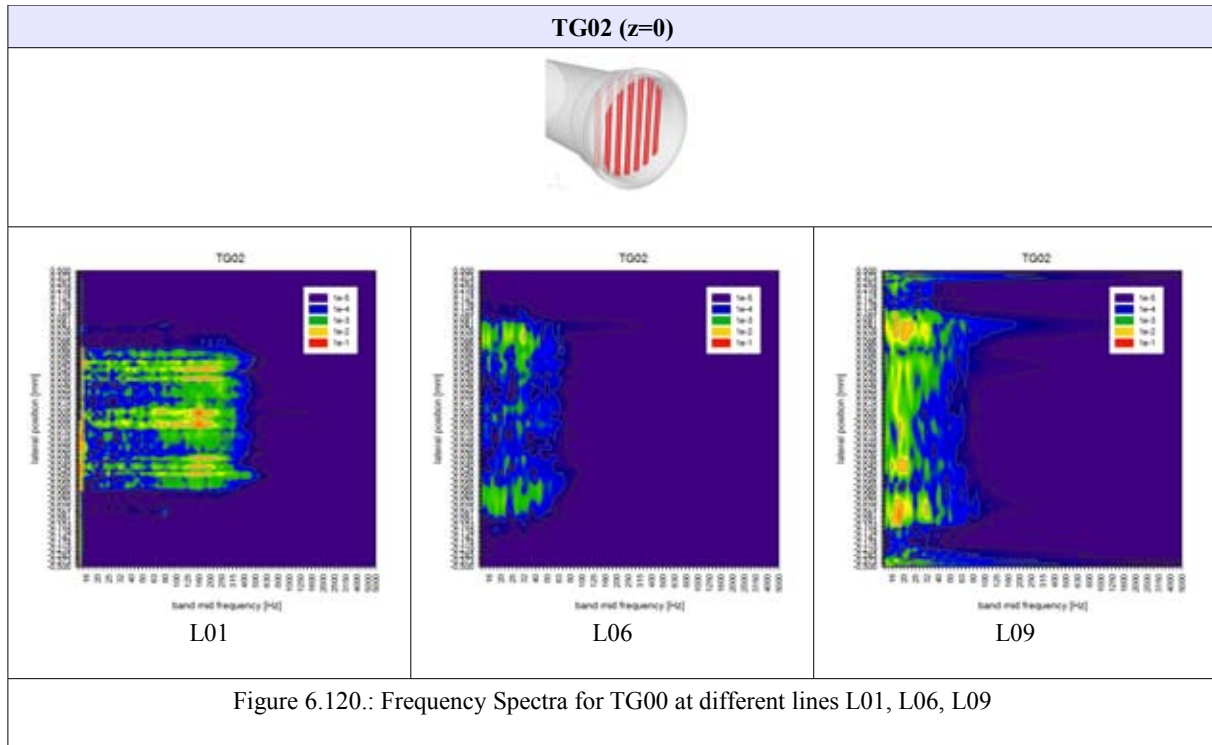
With the purpose of a spectral analysis, data for the x-, y-, z-velocities and the transient static pressure have been recorded on twelve evaluation lines (L01 – L12) for about 5000 time steps after the simulation has reached a quasi-periodic state.

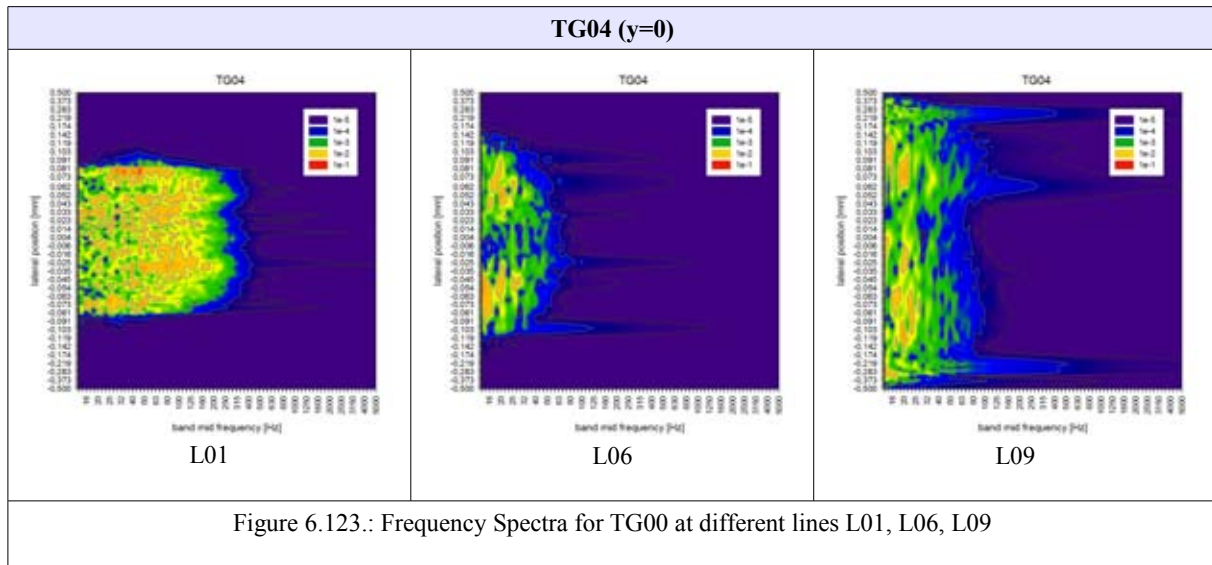
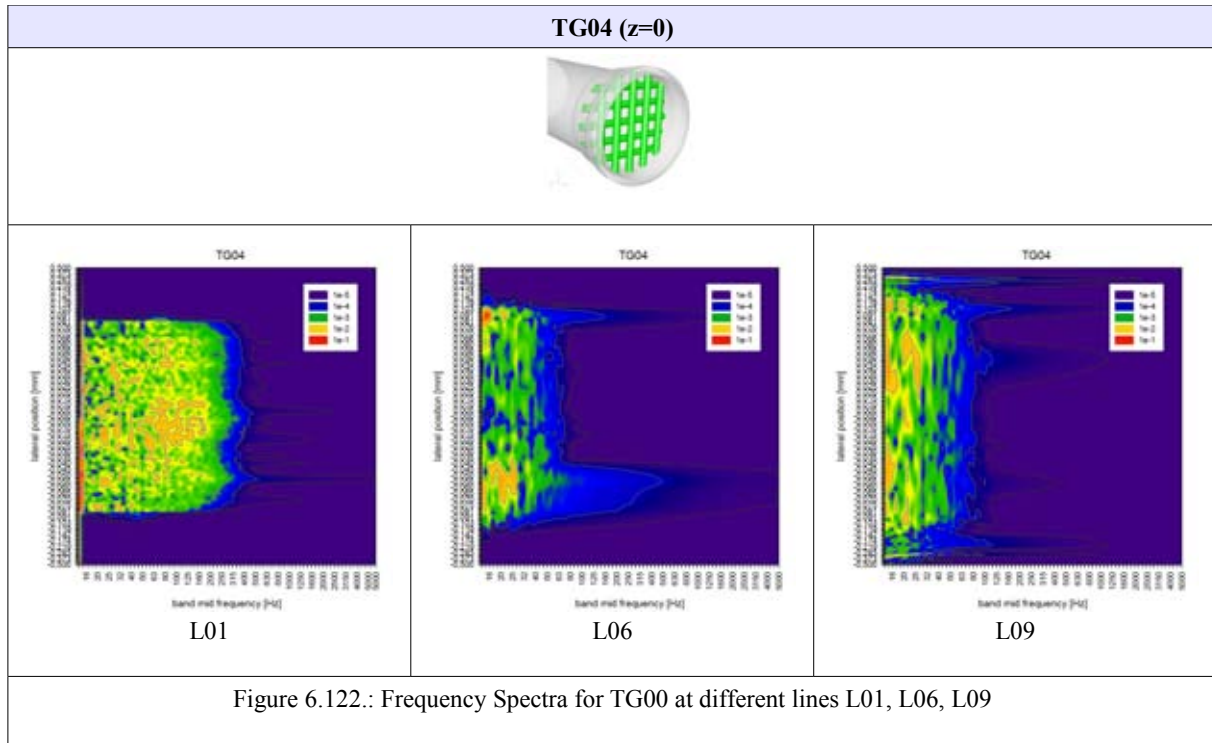
Velocity Fluctuations:

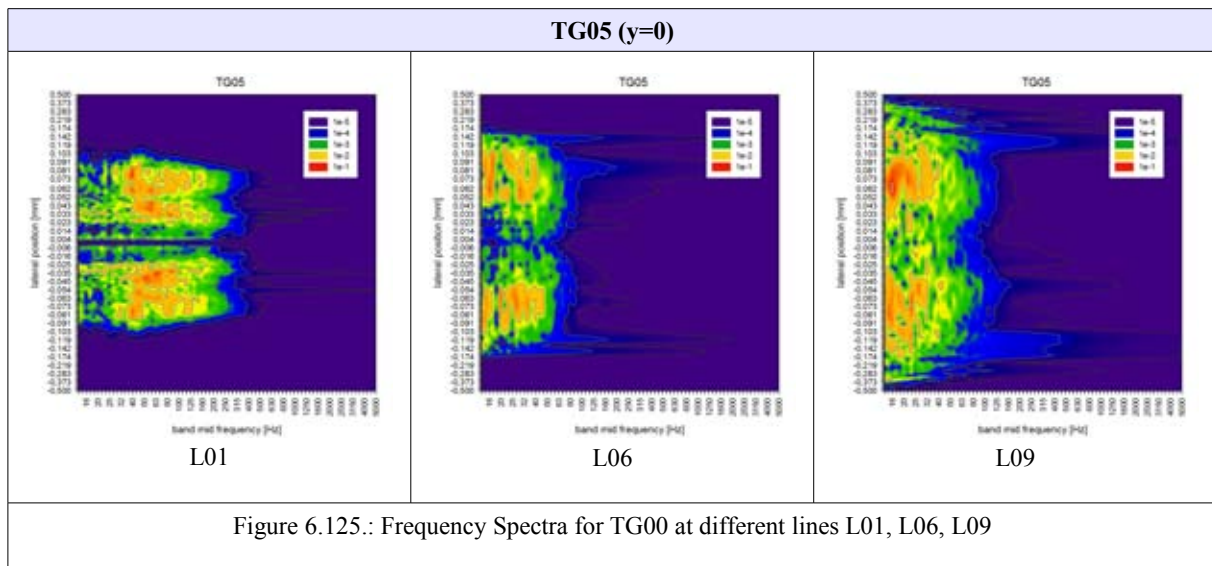
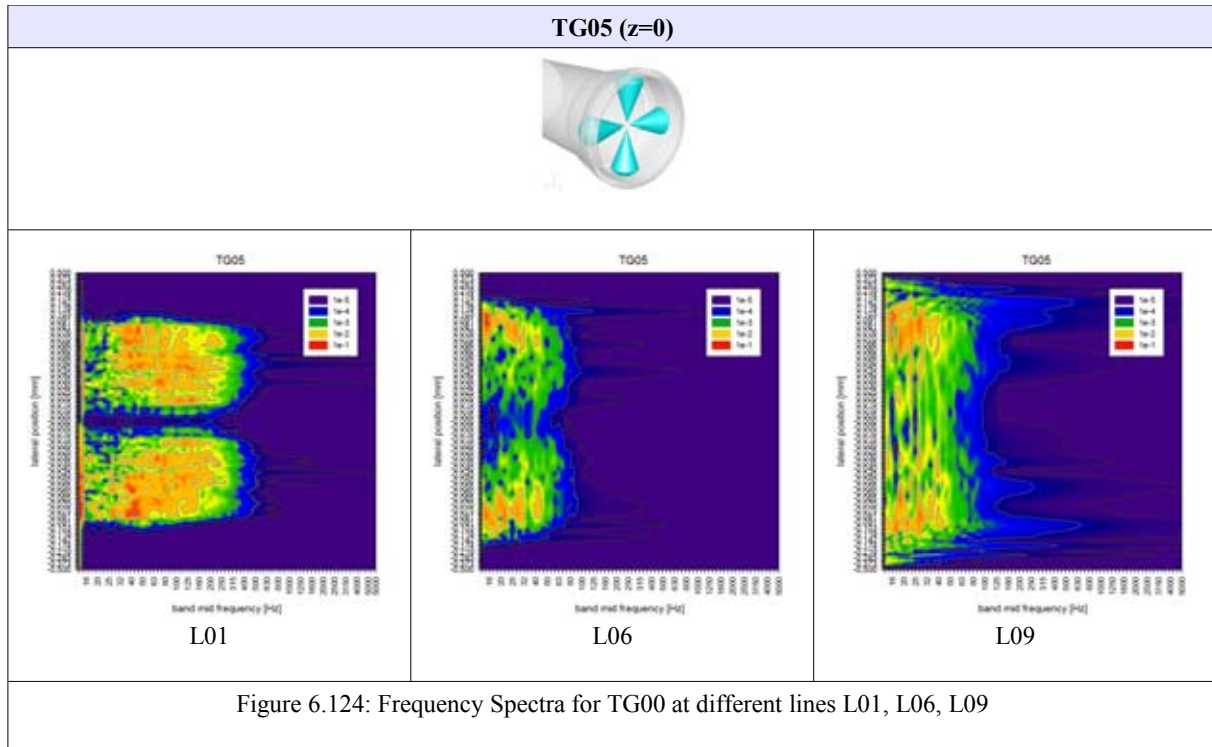
Figures 6.117. - 6.135. show the spectral normalized, absolute squared value of the variance of the mean velocity, which is multiplied by a factor of two to account for the positive frequency space. The FFT signals are displayed in a logarithmic scale (logarithmic y-axis) with a reference value set to $1 \text{ m}^2/\text{s}^2$. By integrating over the frequency space one yields the corresponding turbulent kinetic energy. The frequency spectra at different evaluation lines, which are described in detail in chapter 3, are displayed, as follows. The colors represent the order of the band mid frequency. While the area with the highest frequencies is red-colored, the area with the lowest band mid frequency is dark-blue colored.

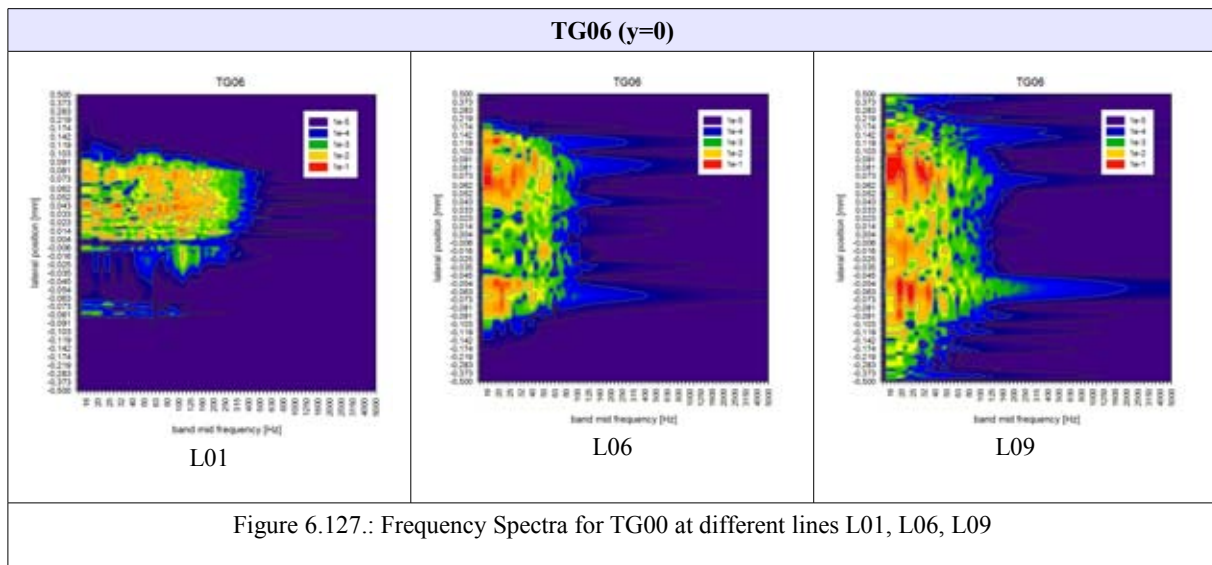
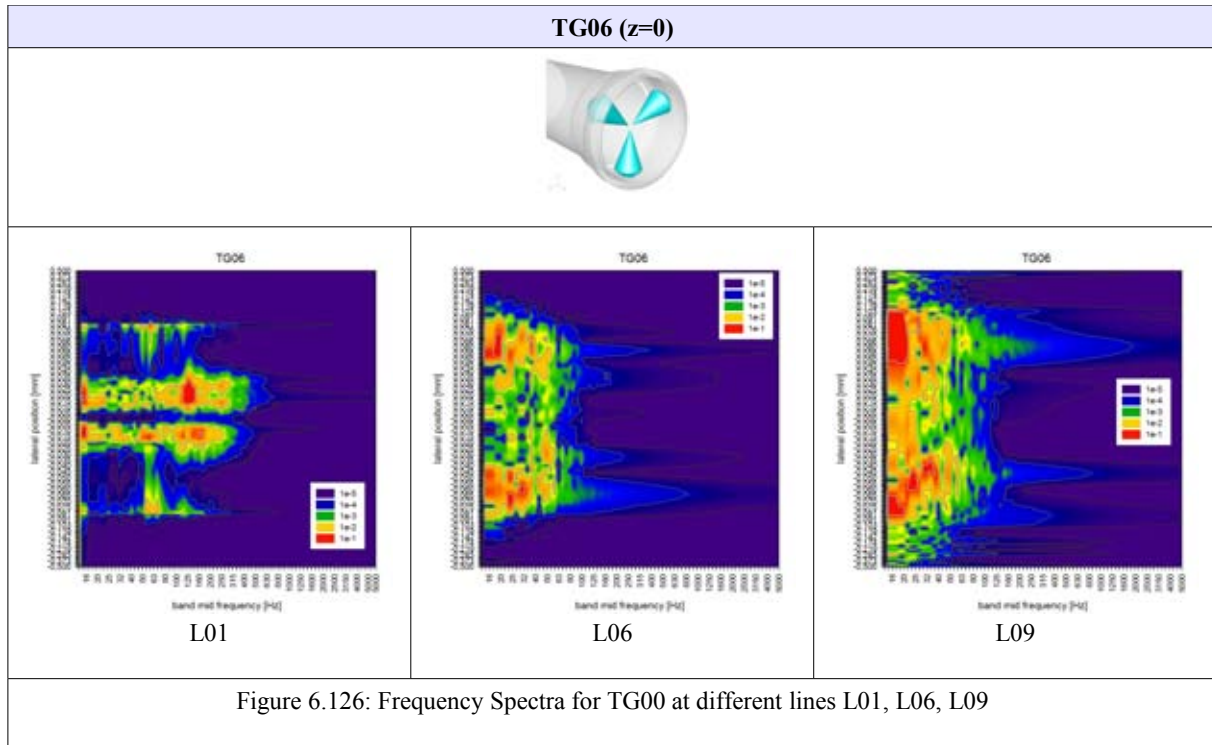


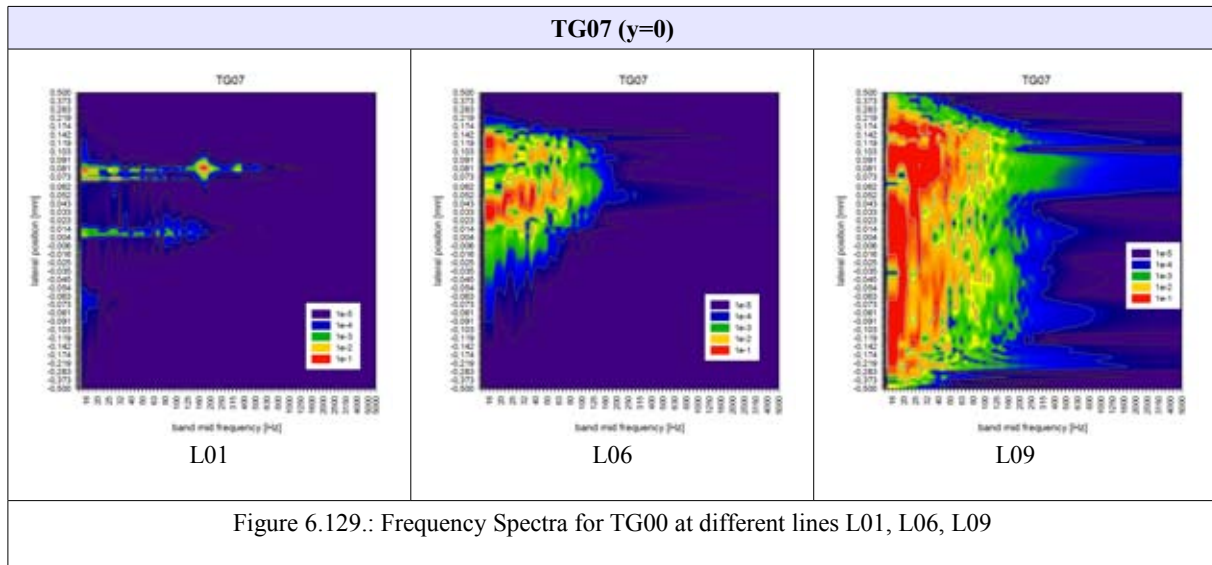
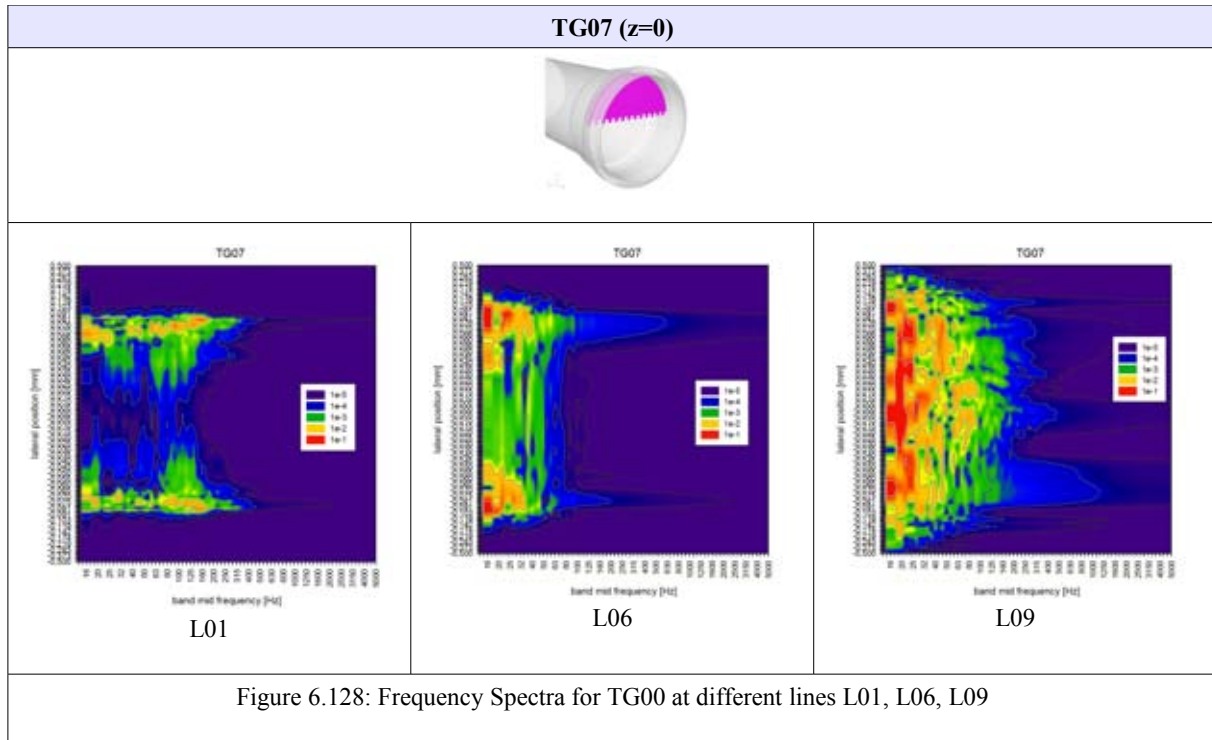


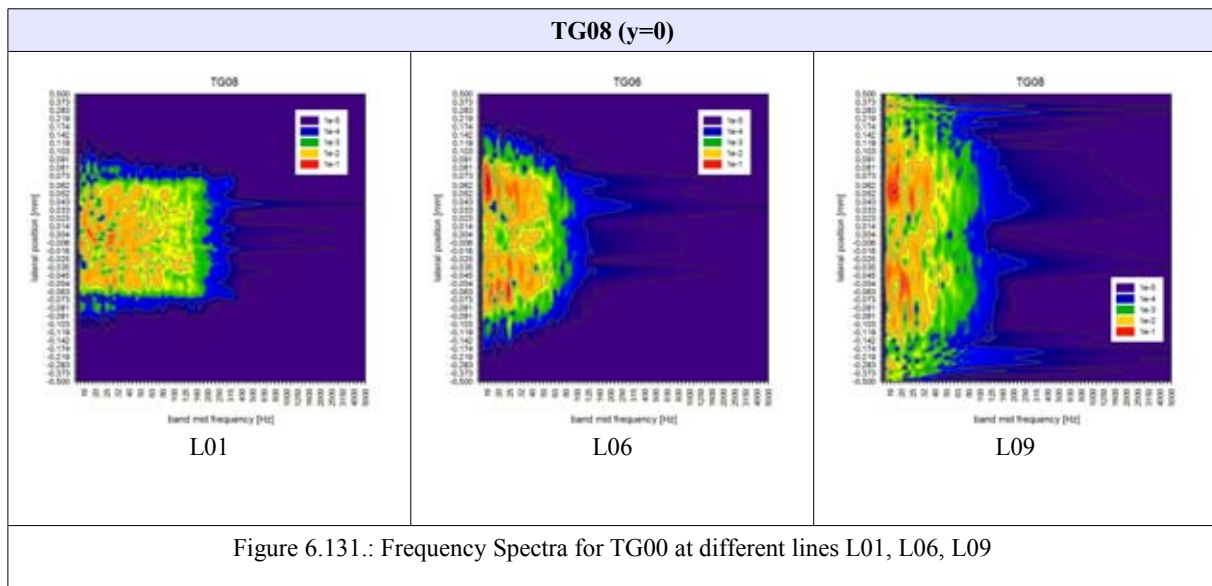
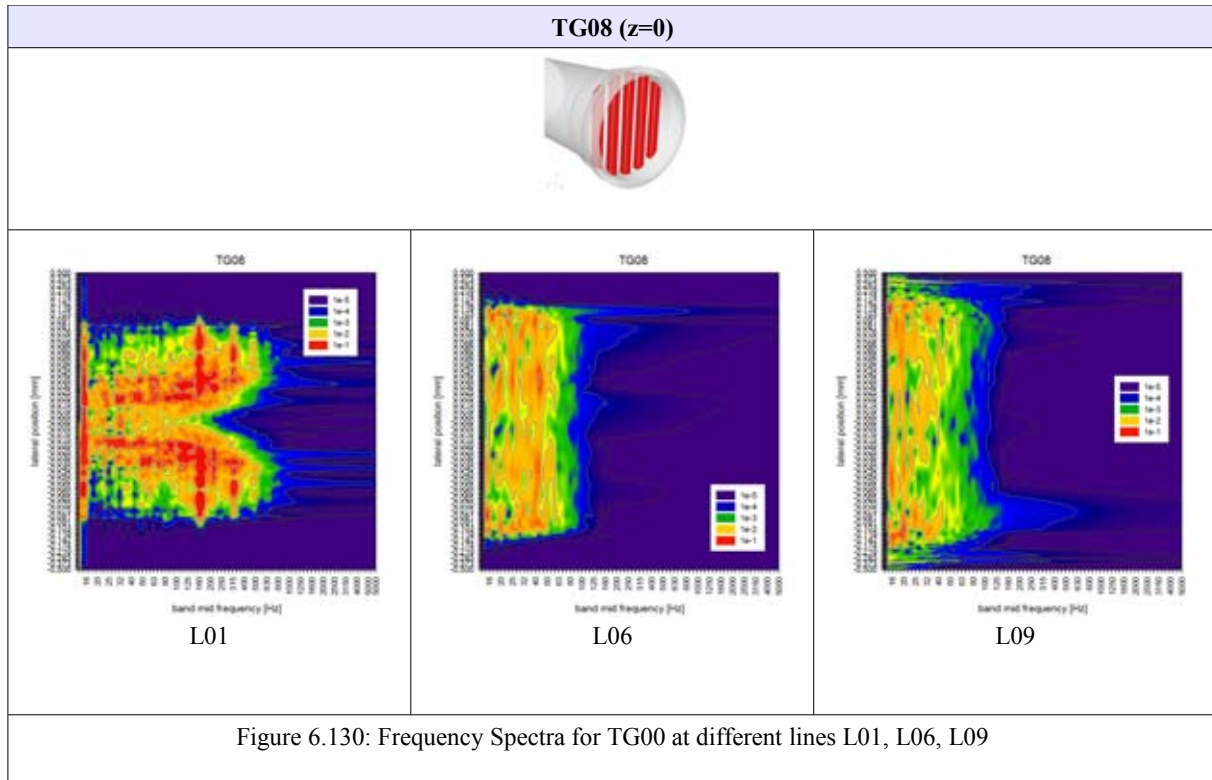


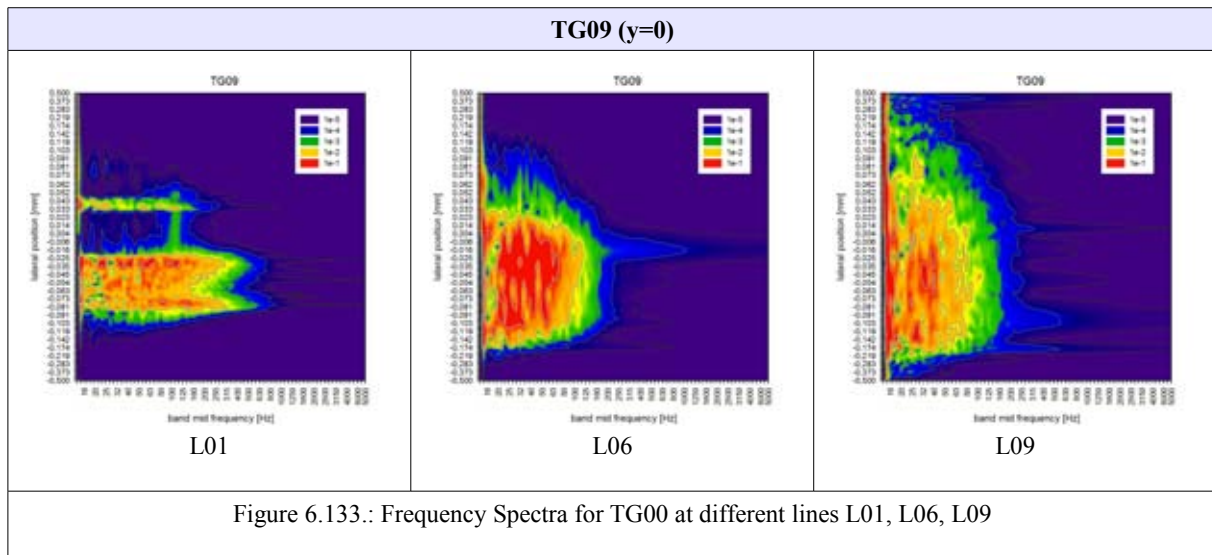
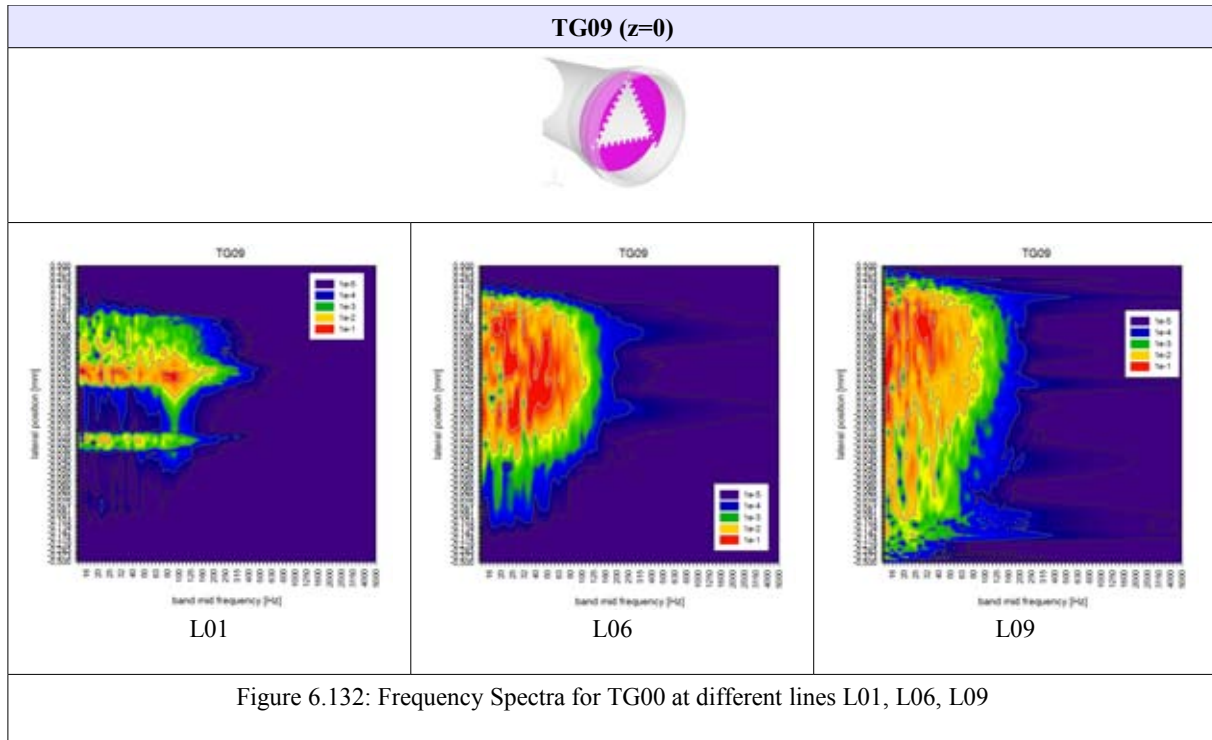


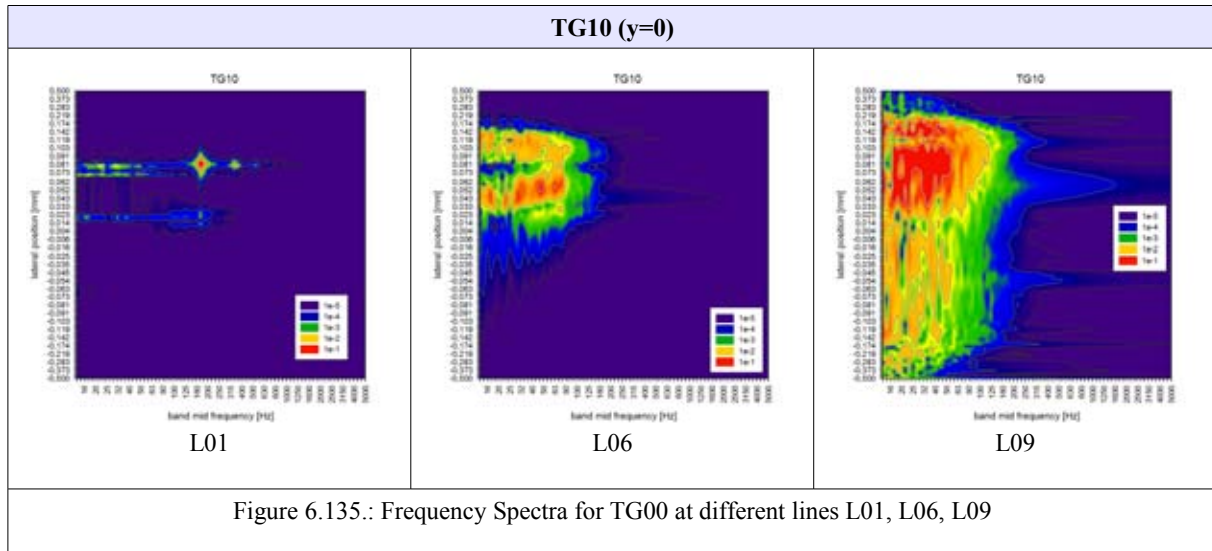
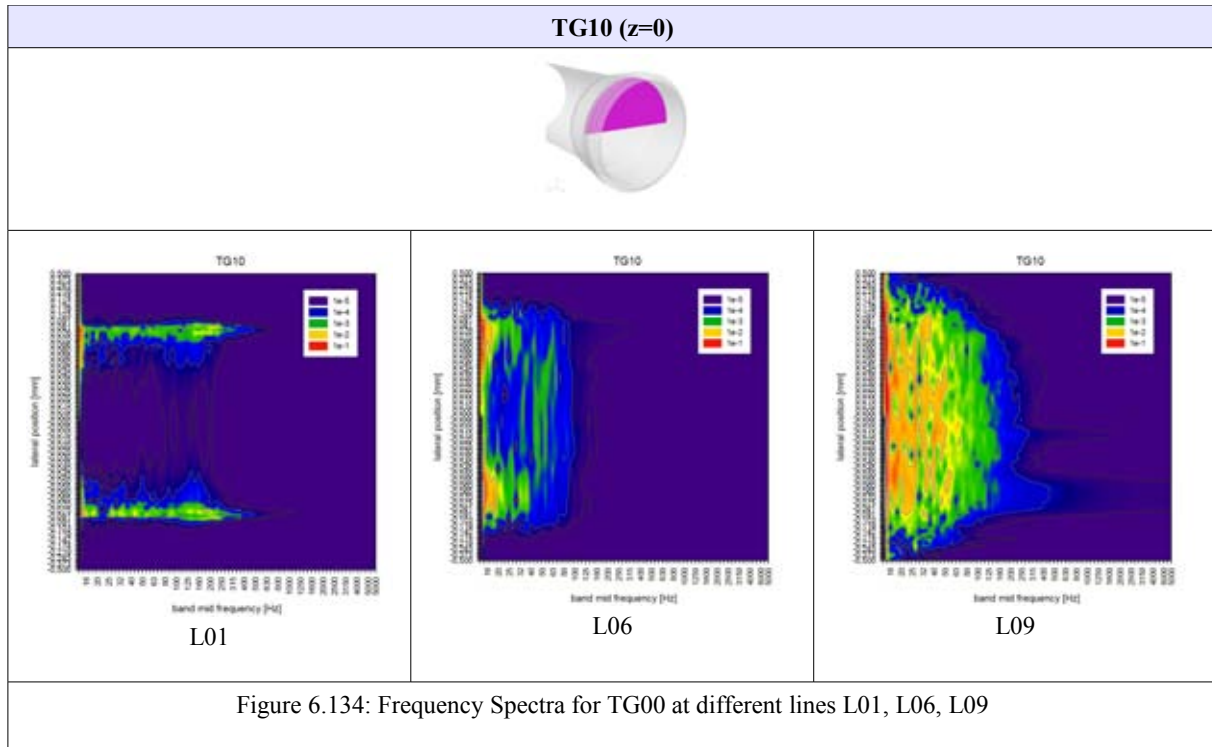






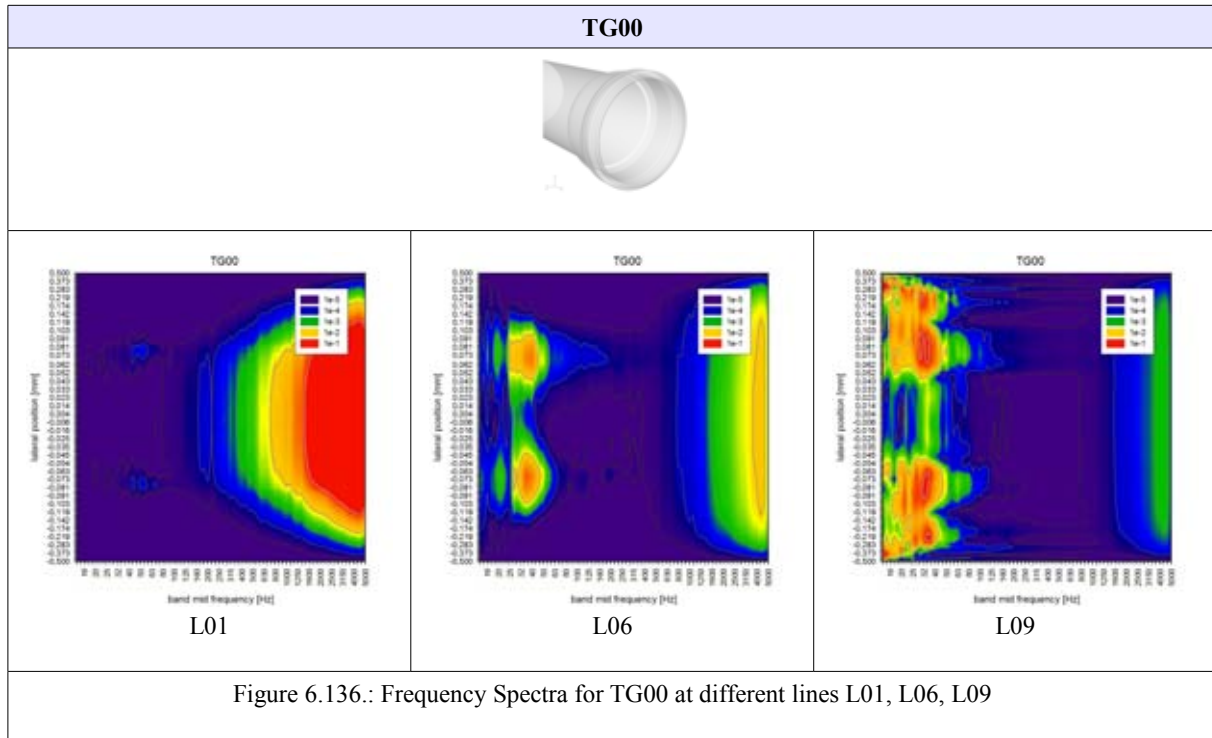


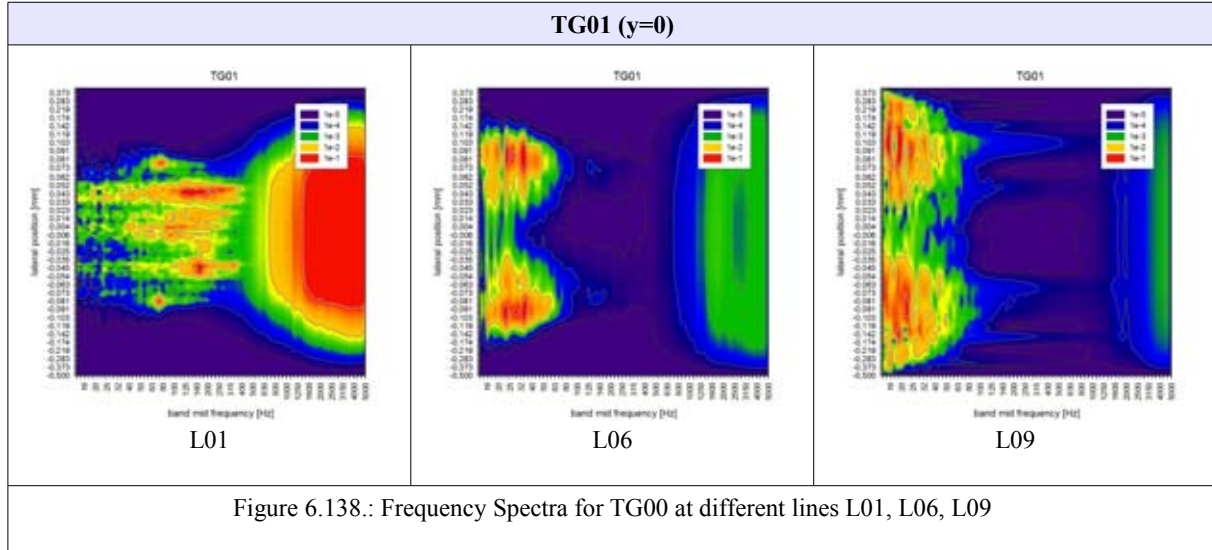
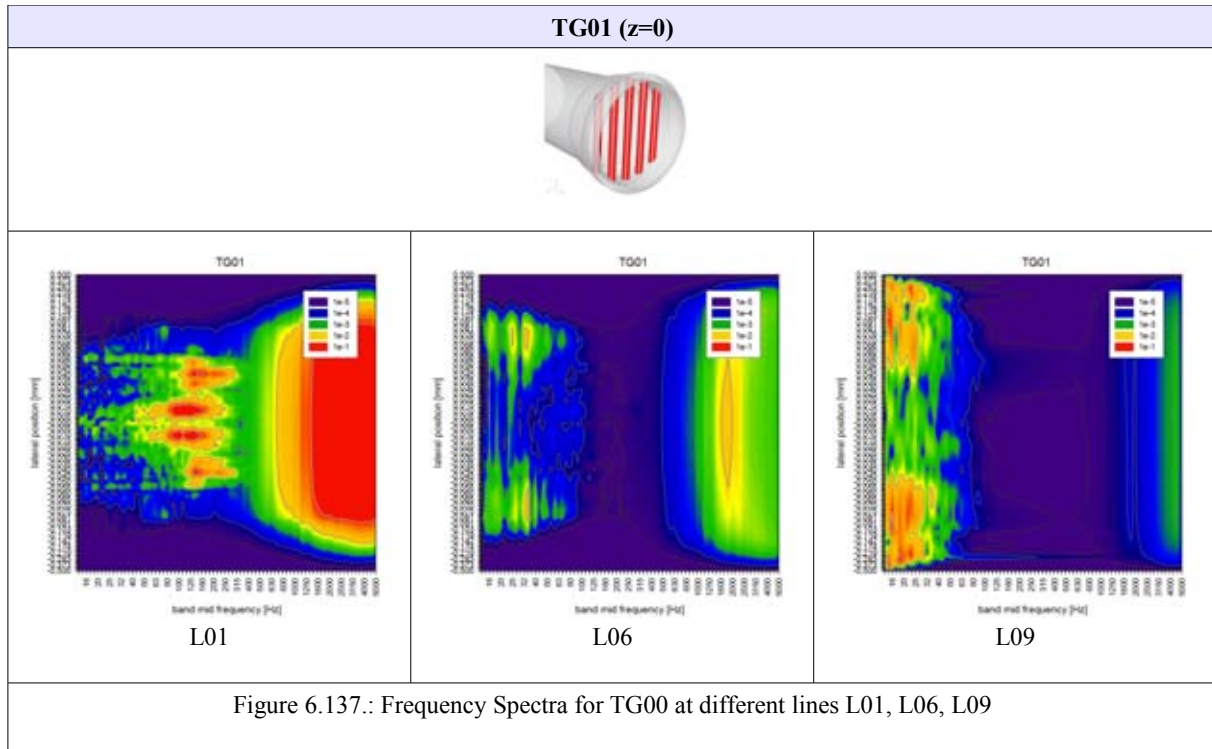


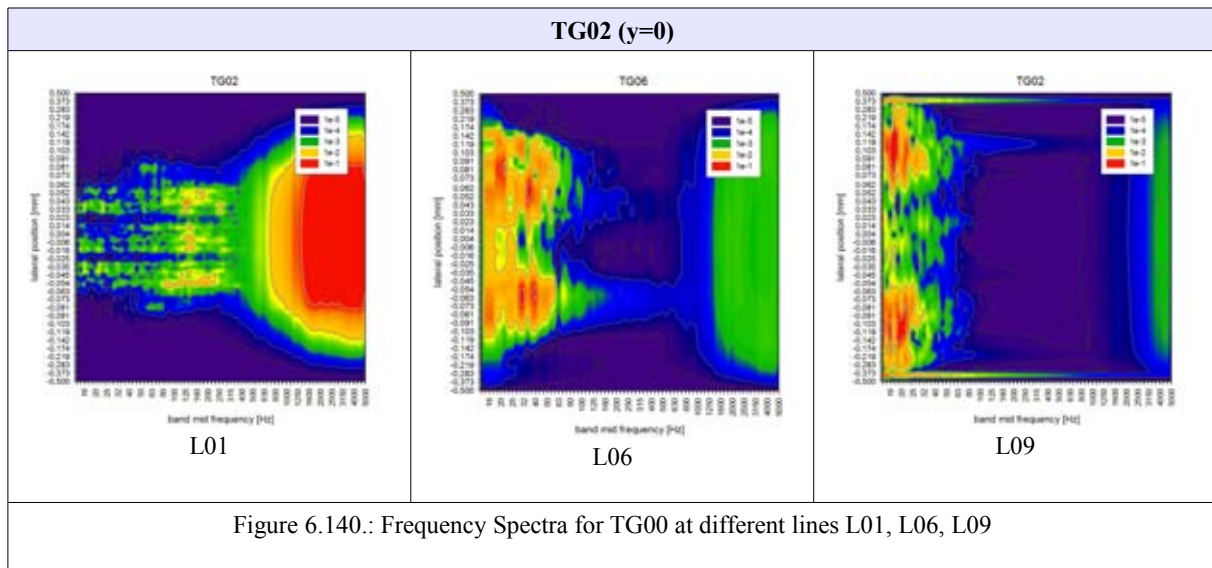
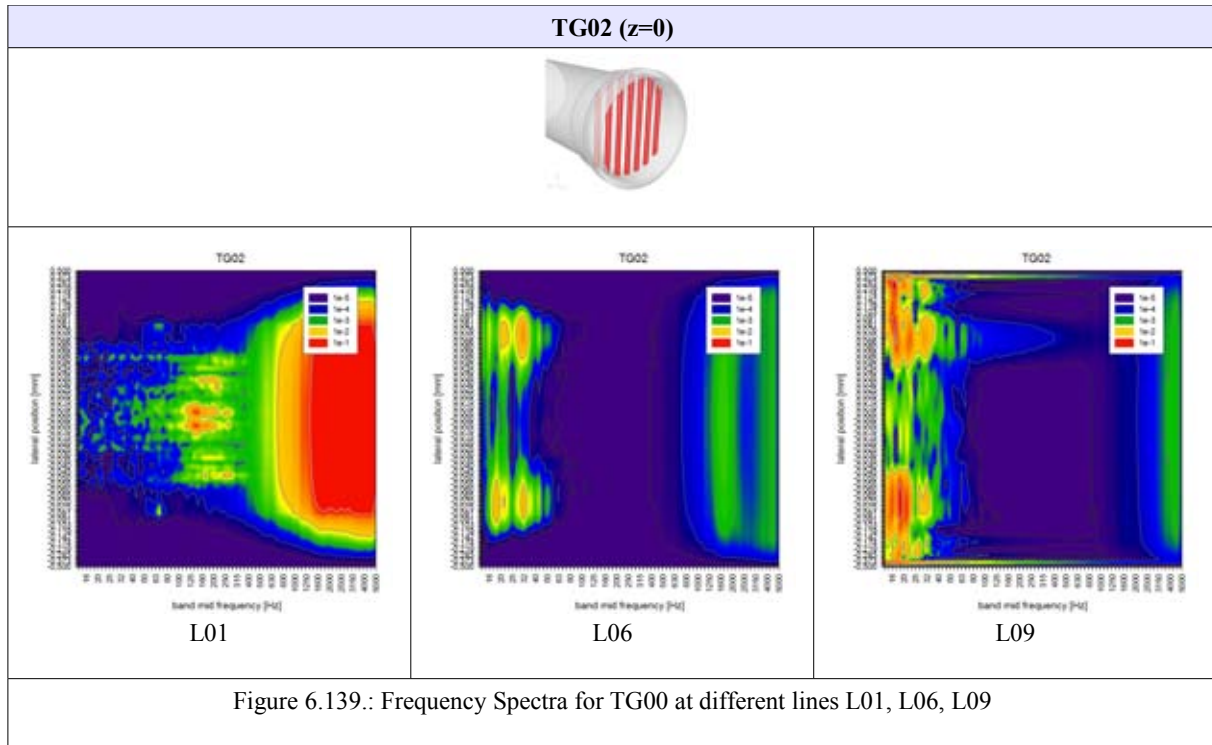


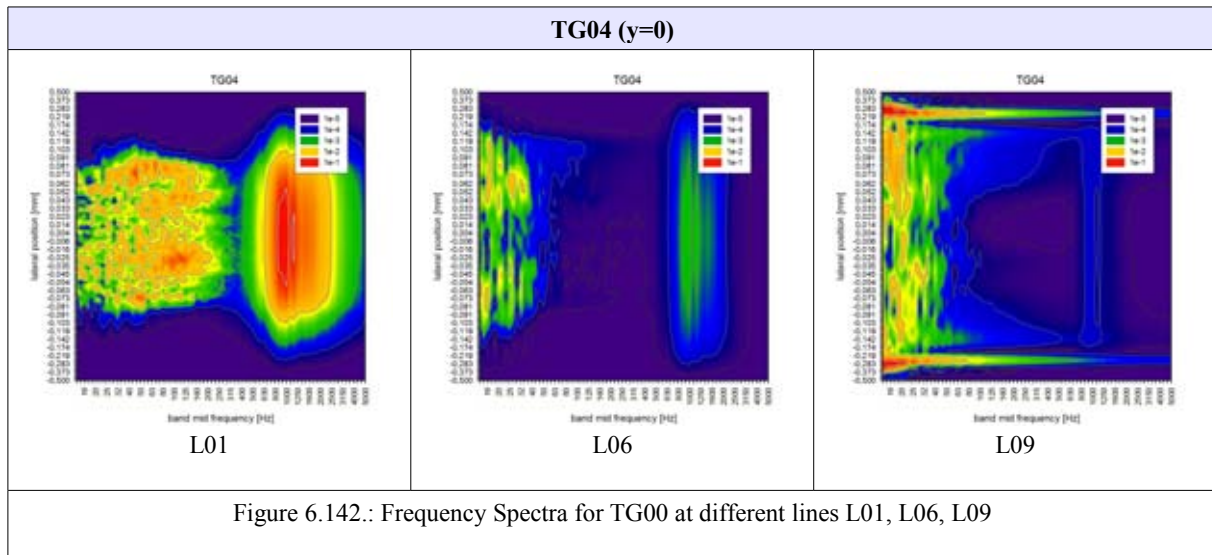
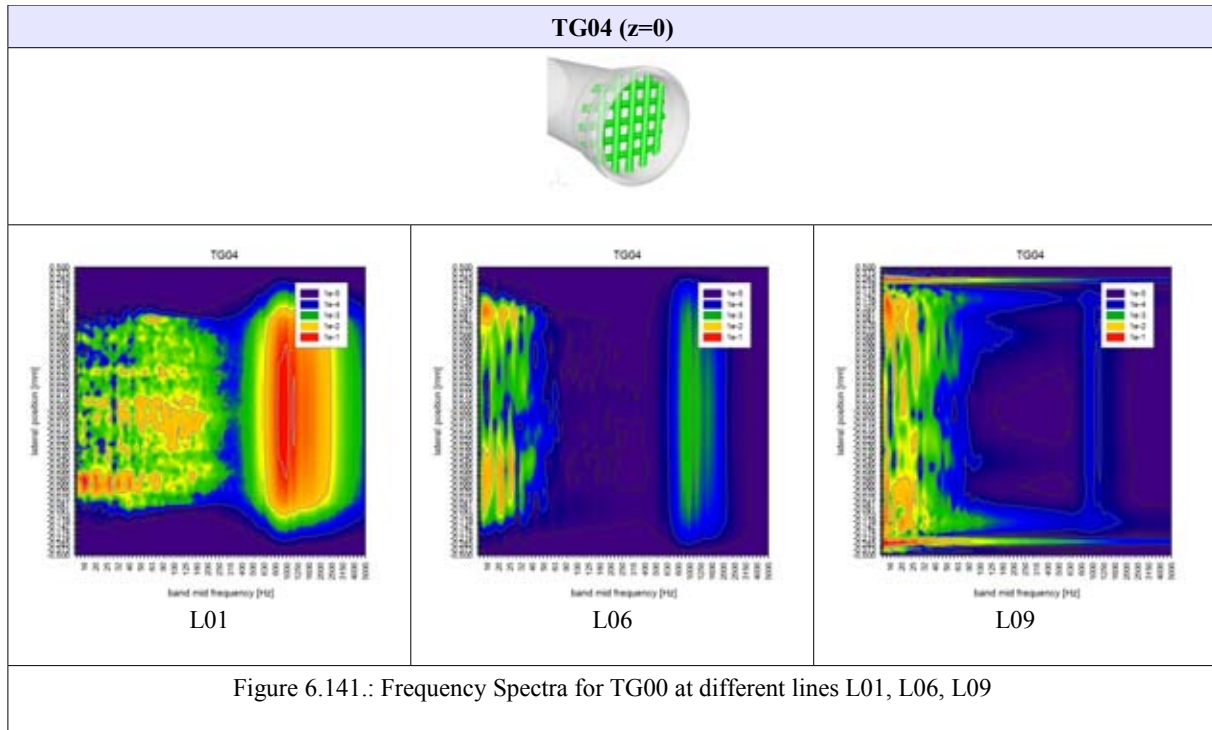
Pressure Fluctuations:

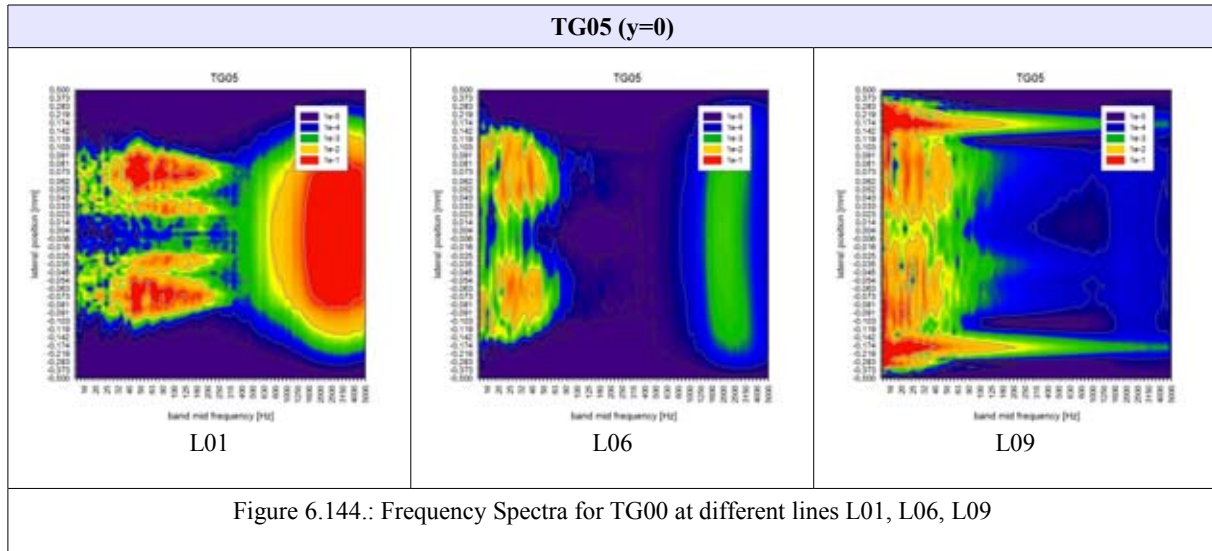
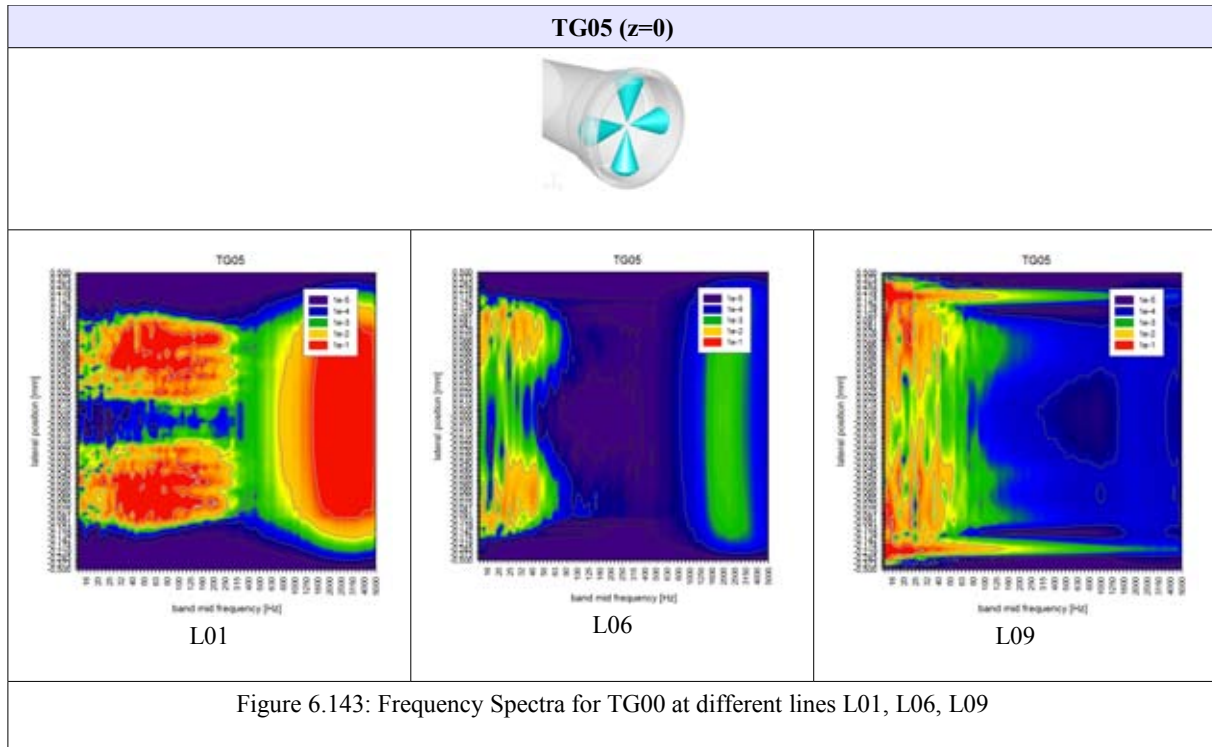
Fig. 6.136 – 6.154. show the spectral normalized, absolute squared value of the variance of the static pressure, which is multiplied by a factor of two to account for the positive frequency space. FFT signals are displayed in a logarithmic scale with a reference value set to $1 \text{ m}^2/\text{s}^2$.

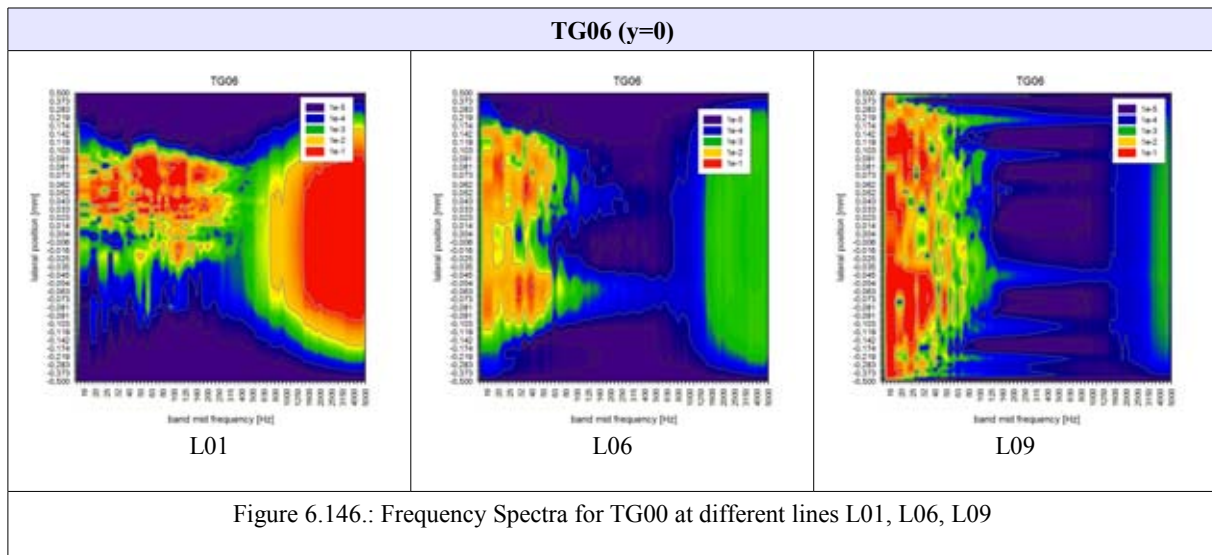
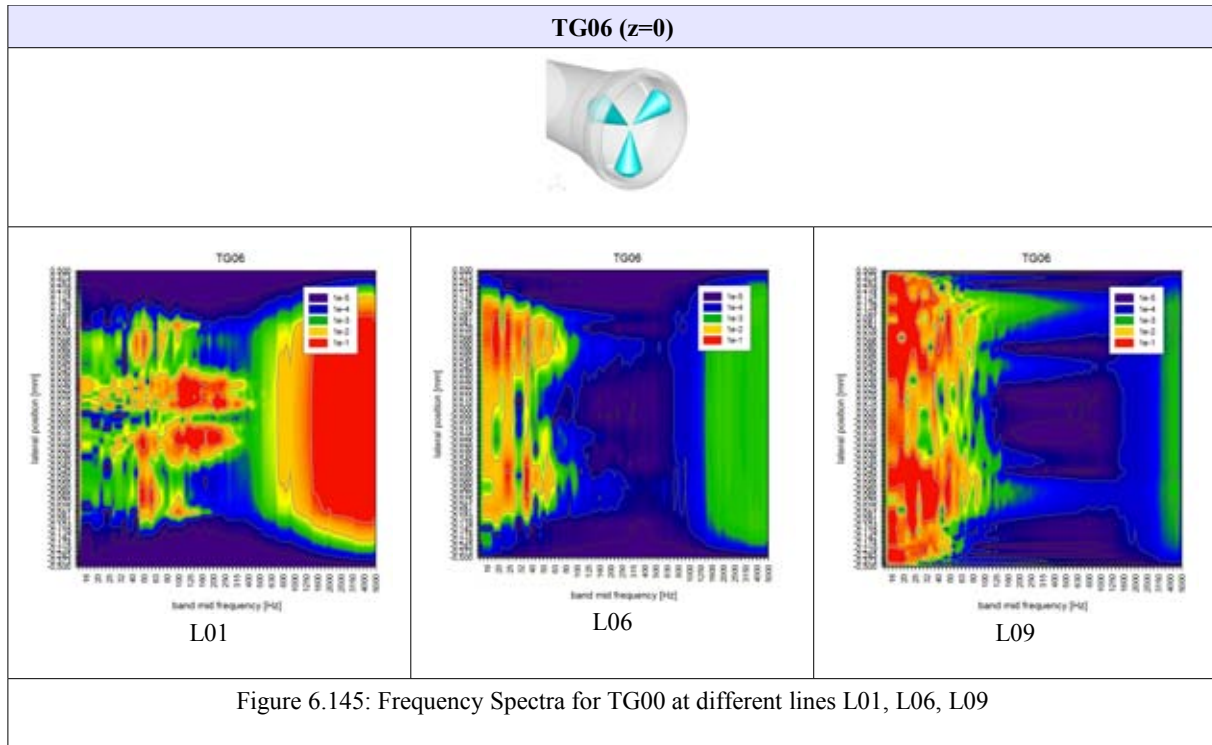


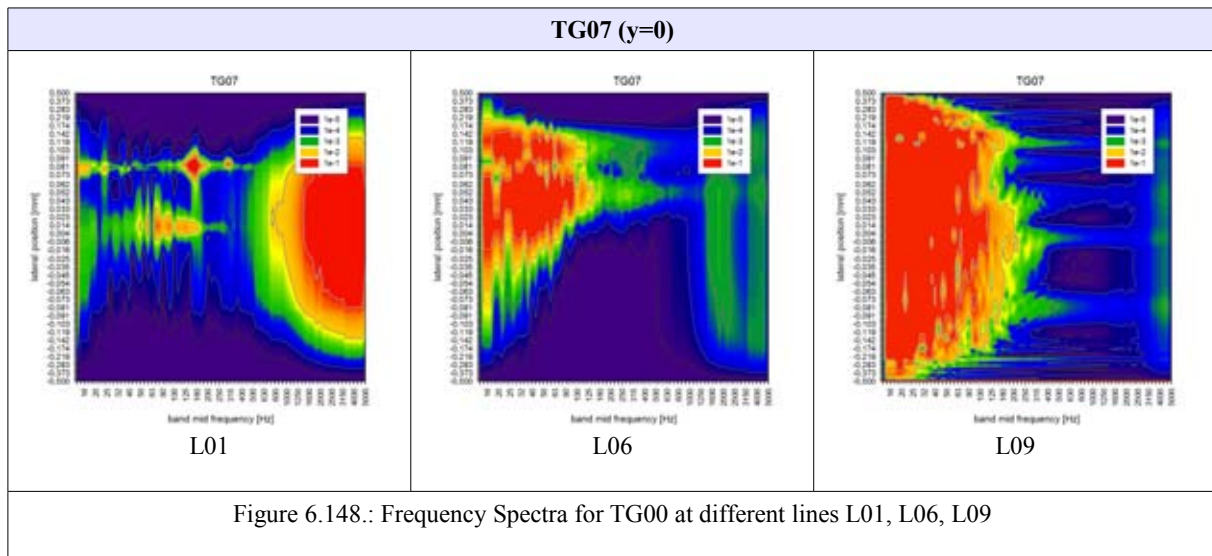
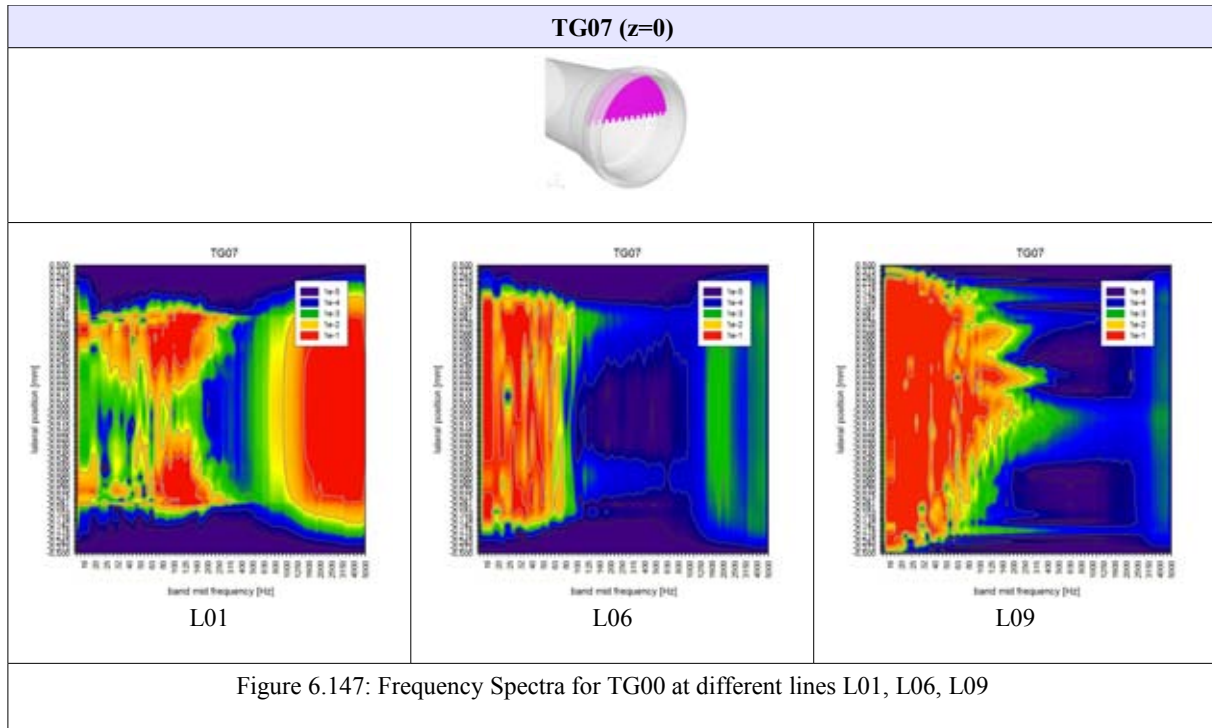


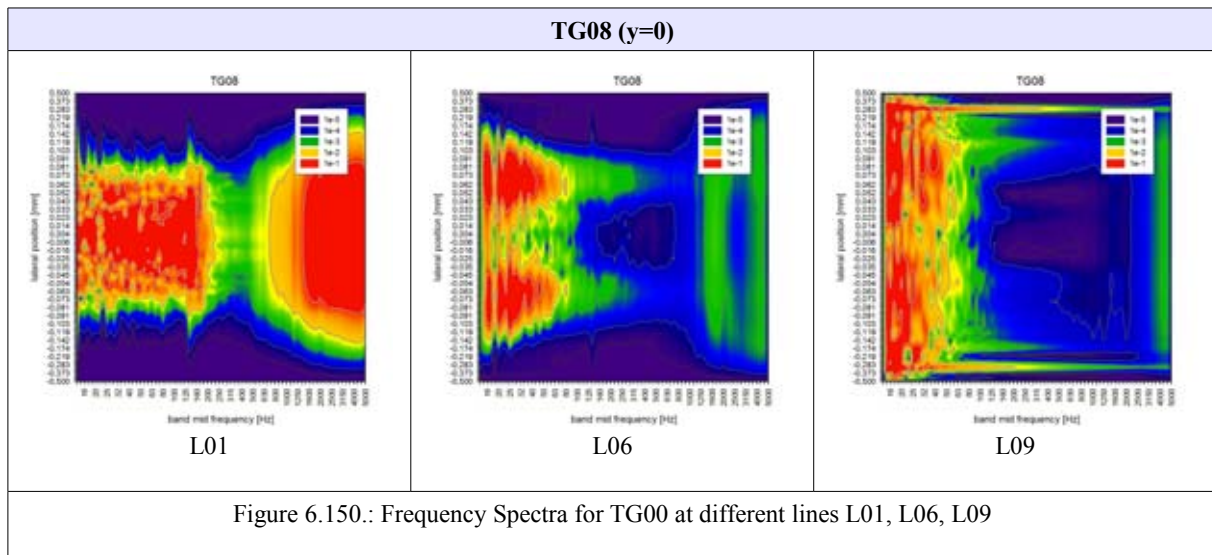
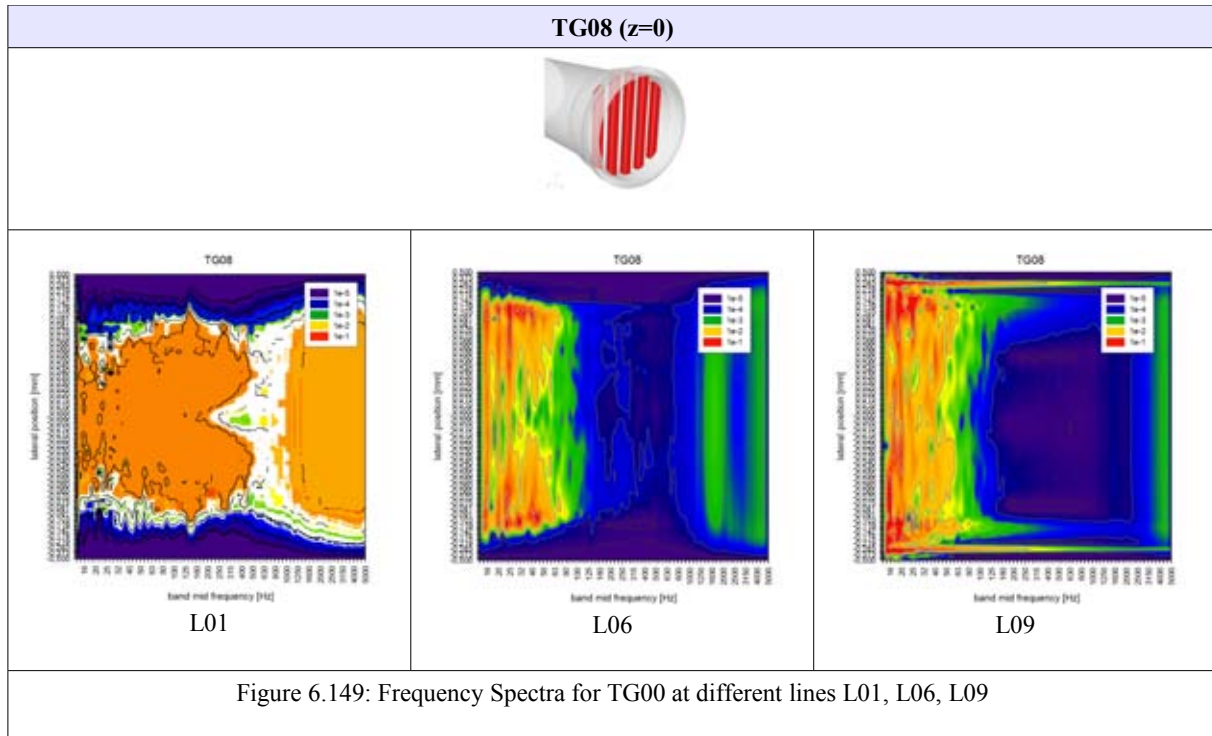


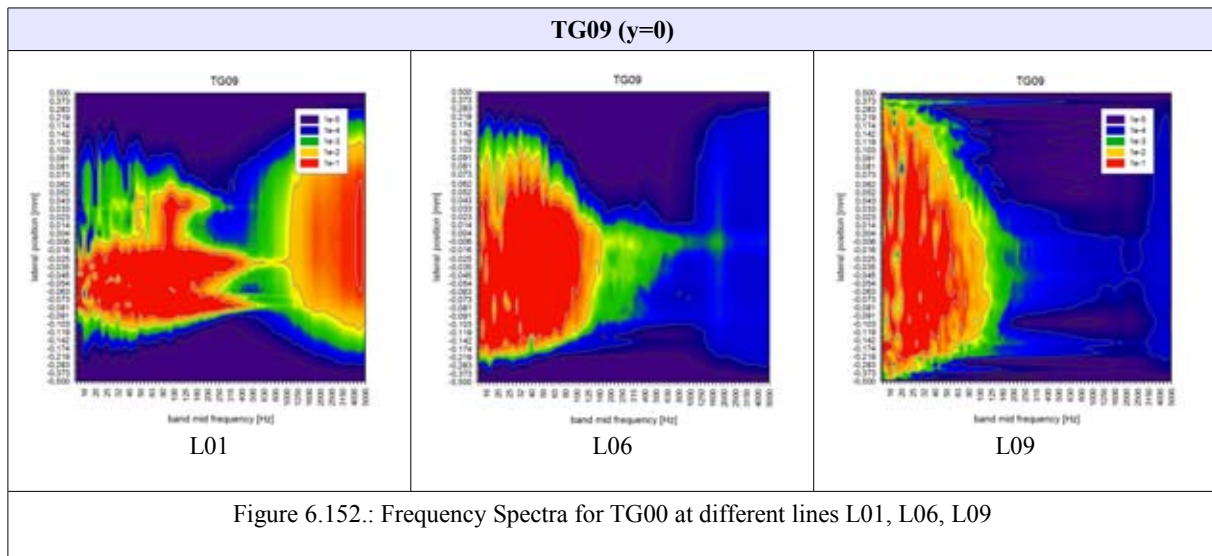
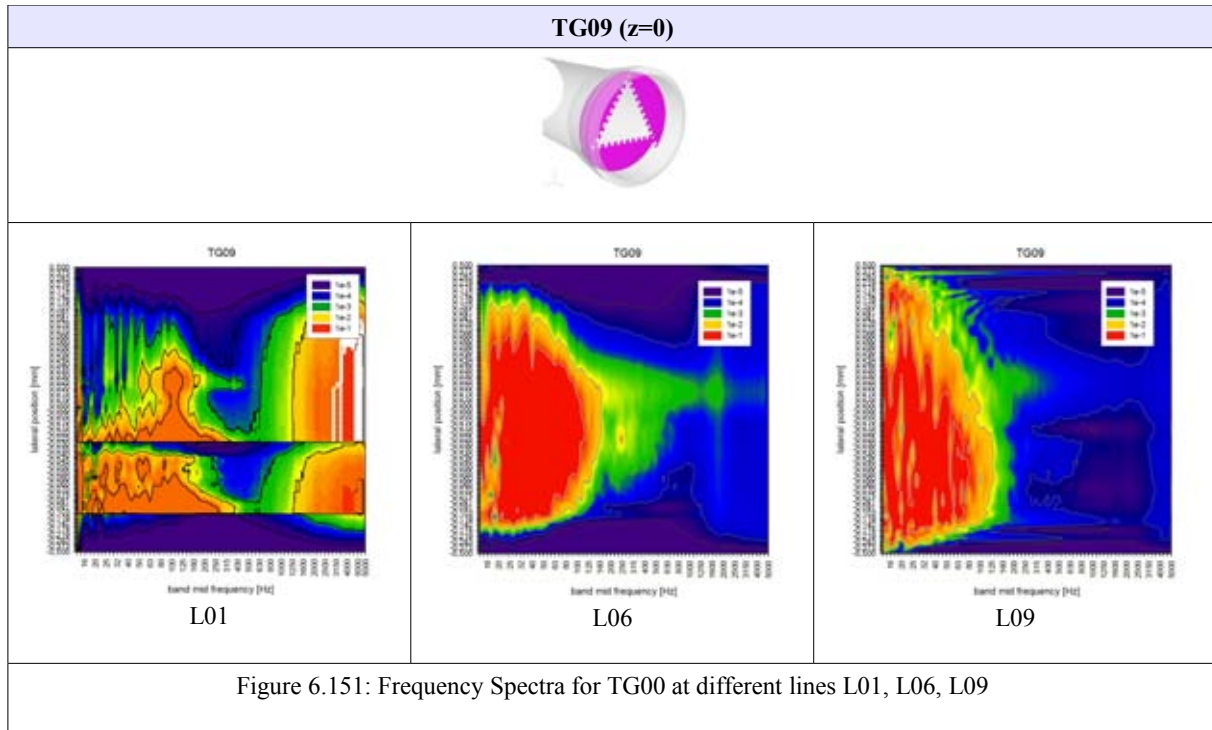


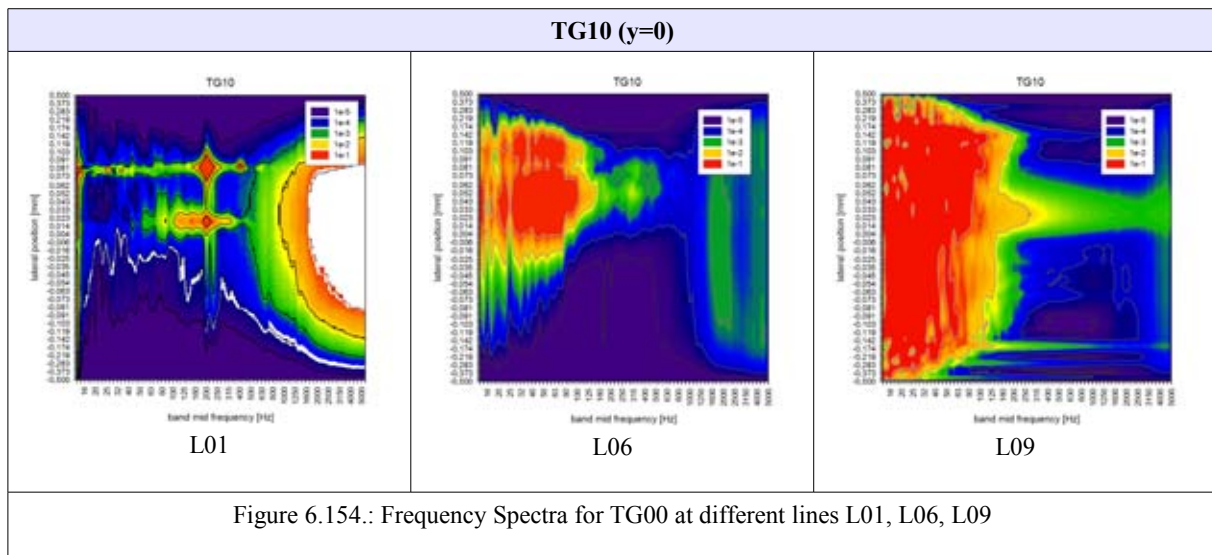
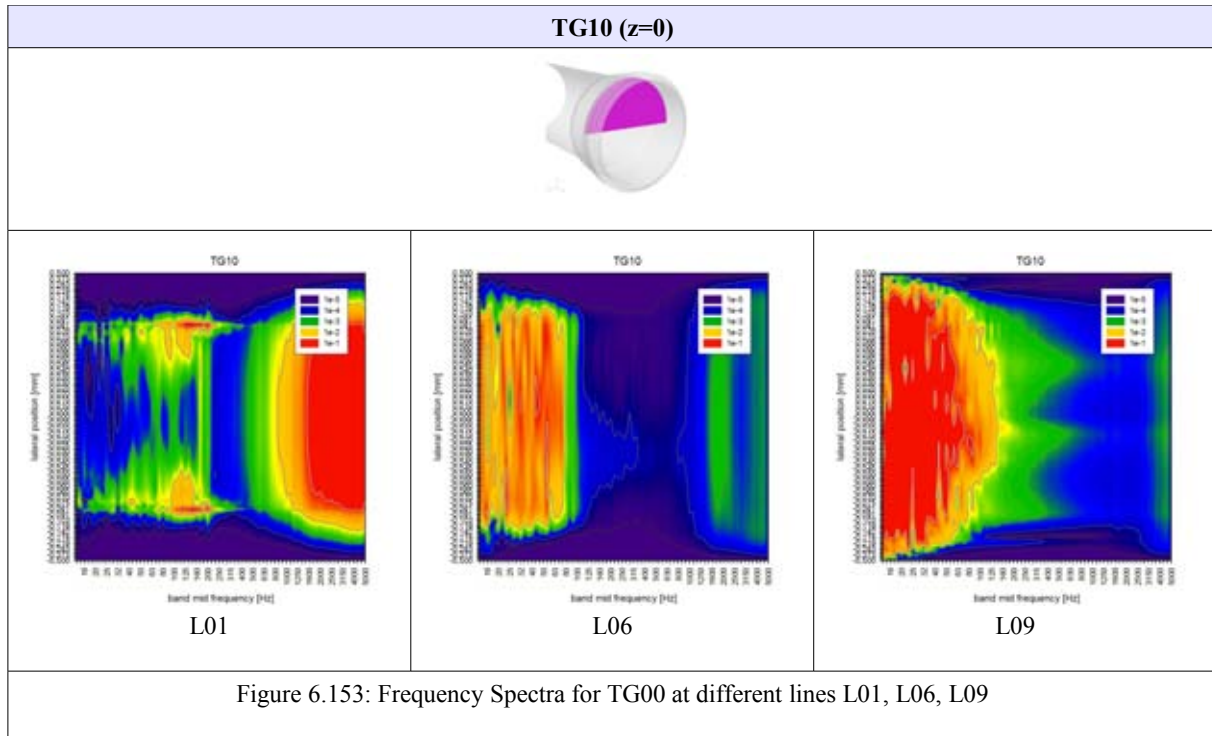












6.4 Pressure Fluctuations at the Plate

Pressure fluctuations are recorded at several points at the center of the microphone plate during the Detached Eddy Simulation. These data are collected for each simulated turbulence generator. The frequency spectra of the pressure fluctuations at those specific points can be compared to the frequency spectra of the microphones from the experimental analysis. The following figure (Fig. 6.155.) represents the comparison of the frequency spectra of one microphone MIC 12 for the different turbulence generators. The experimental signals are recorded at the center of the plate where the jet impinges on the microphone plate. The off-axis signal represents the acoustic signal of the fan. The wall is positioned at a distance of 550mm downstream the tube outlet. The gray area represents the the maximal signal of the acoustic offset measurement for the different turbulence generators. The experimental part of the TUNICA-project was done by Wolfgang Tilser in course of his Master Thesis at the AIT.

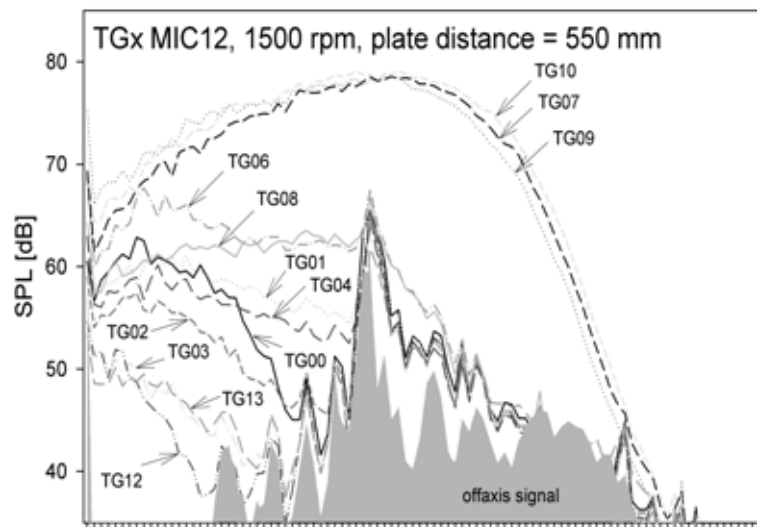


Figure 6.155.: Summary of the frequency spectra of the microphone MIC12 for the different turbulence generators [15, 16, 17, 18]

The comparison of the frequency spectra of the simulated pressure fluctuations for the different turbulence generators is given in Figure 6.156.

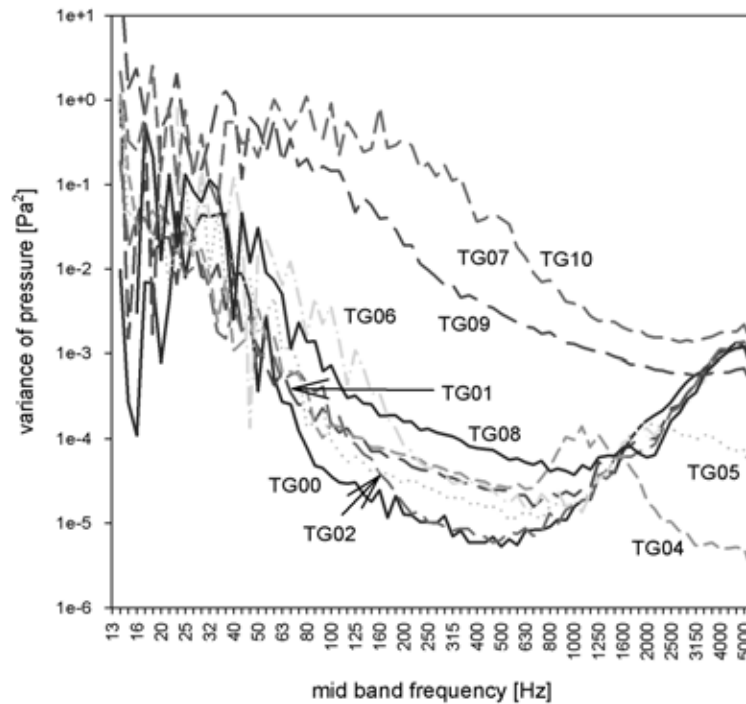


Figure 6.156.: Comparison of the simulated frequency spectra [17, 18]

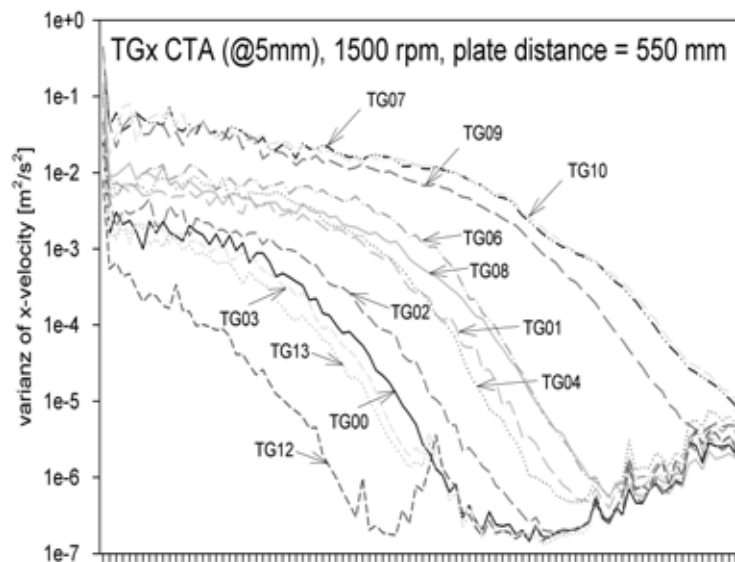


Figure 6.157.: Frequency spectra of the CTA signals [17, 18]

All turbulence generators are represented in figures 3.4. - 3.14. The experimental as well the computational analysis of the frequency spectra show that TG10 and TG07 reach the highest and broadest spectra. By comparing Figure 6.155. and Figure 6.155. one sees the correlations of velocity with pressure fluctuations. The turbulence generators which cause high velocity fluctuations do also lead to high pressure fluctuations. The spectra of the other turbulence generators show similar behavior for the experimental and computational counter parts. The simulation results drop at lower frequency values than the experimental results do, which can be related to insufficient mesh resolution in the propagation region. Due to the minimum cell side

length of 1 mm at the turbulence generating surfaces and a mean value of around 5 mm cell side length in the turbulent area, higher frequencies cannot be propagated well.

These results have been presented at several conferences, and further information can be taken from the publications. [17,18]

7 Conclusions

Flow phenomena can be solved quickly by means of steady CFD simulations. In case of laminar flow they can provide reliable results. Turbulent flows can be hard to solve by stationary CFD simulations if the flow is unsteady, but they can give trends about the global behavior of the flow. The inherent transient flow patterns cannot be captured by steady solvers. The RNG k- ϵ model compared best to the experimental data. Differences in the models are most pronounced in the stagnation area of the impinging jet at the wall. For some turbulence generators that are built of blades, a steady solution cannot be achieved. The characteristics and the values of the variables of interest of these turbulent flows can be investigated by performing unsteady CFD simulations. Transient CFD calculations using the detached eddy simulation are performed to provide frequency spectra which can be compared to the experimental data. Moreover, the correlation between simulated local velocity and pressure fluctuations at the wall can be investigated. [15, 16]

Grid quality has a great impact on the success and accuracy of the computational analysis of flow phenomena. The grid resolution at the boundaries of the flow domain is important for the modulation of eddies and turbulence. By checking the y^+ values in near wall regions in respect to the *law-of-the-wall* it is possible to fit the number and size of cells to the demands of the flow and geometry.

The acoustic effects of the different turbulence generators can be compared by performing unsteady DES CFD-simulations. The general behavior of the DES simulated spectra of the pressure fluctuations for the different turbulence generators coincide with the experimental frequency spectra recorded with the microphone signals concerning broadness and level. However the simulation results under-predict their experimental counterparts with regards to the lower frequency values. From the velocity spectra in figures 6.115 – 6.136. it can be seen that prominent features of the spatial frequency behavior are well captured. The position of the shear layers, the separation and the combination of the turbulent regions can be observed easily. The comparison of the experimentally and numerically generated frequency spectra offer the possibility to find out where CFD simulations are effective and gives results approximately equivalent to the experimental results. However, the representation of all details of the spectra is limited. This can be attributed to the constraints of the computing power and cell size. Using a cell number of around five million and the fact that one time step takes approximately six minutes, leads to calculation times of 40 days on four CPUs of a 3.2 GHz Linux cluster. Due to the minimum cell side length of 1 mm at the turbulence generating surfaces and a mean value of around 5 mm cell side length in the turbulent area, higher frequencies cannot be propagated well, which can be seen in the lower frequency content of the numerical based spectra compared to the experimental data.

To overcome present limitations different mesh strategies and the implementation of stronger fluctuating boundary conditions would be needed. [17,18]

8 Bibliography

- [1] Joel H. Ferziger and Milovan Peric, *Computational Methods for Fluid Dynamics*. Springer-Verlag 2002
- [2] Robert G. Deissler, *Turbulent fluid motion*. Taylor & Francis 1998
- [3] David Pnueli, Chaim Gutfinger, *Fluid mechanics*. Cambridge University Press 1992
- [4] J. M. McDonough, *Lectures in Elementary Fluid Mechanics*. Departments of Mechanical Engineering and Mathematics University of Kentucky, Lexington
- [5] Batchelor, G. K., *An Introduction to Fluid Dynamics*. Cambridge University Press 1967
- [6] Allen E. Fuhs, Joseph. A. Schetz, *Handbook of Fluid Dynamics and Fluid Machinery*. Wiley-Interscience 1996
- [7] Hendrik C. Kuhlmann, *Lectures in Numerische Methoden der Strömungs- und Wärmetechnik*. Institut für Strömungsmechanik und Wärmeübertragung Technische Universität Wien
- [8] Herbert Oertel, *Prandtl-Führer durch die Strömungslehre*. Vieweg+Teubner Verlag 2008
- [9] V.Yakhot , S.A. Orszag, S. Thangam, T.B. Gatski and C.G. Speziale, *Development of turbulence models for shear flows by a double expansion technique*, Physics of Fluids A (ISSN 0899-8213), vol. 4, no. 7, July 1992
- [10] David C. Wilcox, *Turbulence Modeling for CFD*. 1993, 1994 DCW Industries, Inc.
- [11] Joel H. Ferziger and Milovan Peric, *Numerische Strömungsmechanik*. Springer- Verlag 2008

-
- [12] Bruno Eck, *Technische Strömungslehre*. Springer-Verlag 1991
- [13] *GAMBIT Modeling Guide*. Fluent, Inc. 2001
- [14] *FLUENT User's Guide*. Fluent, Inc. 2003
- [15] Ch. Reichl, W. Tilser, M. Böck, H. Lang, K. Haindl, F. Reining, M. Opitz, *Experimental and numerical analysis of the generation of a turbulent flow field in a free stream jet and its correlation to acoustic radiation and wall pressure fluctuations* DAGA 2008, 10.-13. March, 2008, Dresden, Deutschland
- [16] Ch. Reichl, M. Böck, W. Tilser, H. Lang, K. Haindl, F. Reining, M. Opitz, *On the correlation of the acoustic signal of microphones mounted on a flat plate to the turbulence of an impinging jet*. Acoustics'08 Paris, 29.06.-04.07.2008, Paris
- [17] Ch. Reichl, M. Böck, W. Tilser, H. Kühnelt, K. Haindl, M. Opitz, *Spectral Comparison of Numerical Simulation and Experimental Data of Turbulent Impinging Jets*. CMFF'09 Budapest, Hungary, September 9-12, 2009
- [18] Ch. Reichl, M. Böck, W. Tilser, H. Kühnelt, K. Haindl, M. Opitz, *Numerical Prediction and Experimental Characterization of Turbulent Flow Fields and Acoustic Perturbations of HVAC Components*. VENT 2009 ETH Zürich, October 18-21, 2009

Experimental and numerical analysis of the generation of a turbulent flow field in a free stream jet and its correlation to acoustic radiation and wall pressure fluctuations

Christoph Reichl¹, W. Tilšer^{1,2}, Michelle Böck^{1,2}, H. Lang¹, K. Haindl³, F. Reining³, M. Opitz³

¹ *arsenal research – Austrian Research Centers, Business Field Sustainable Energy Systems*

² *Technical University of Vienna, Institute of Solid State Physics*

³ *AKG Acoustics GmbH*

Email: christoph.reichl@arsenal.ac.at

Introduction

A turbulent circular free stream jet is generated using an axial symmetric fan driven by a brushless actuator with variable frequency leading to typical core-velocities of around 10 m/s ($Re = 99000$). The flow is propagated through a pipe (radius = 80.5 cm) system significantly damping the noise from the fan. Turbulence is generated using different sets of turbulence generators [2, 3, 4] in the tunnel (length approx. 3 m) consisting of meshes, rods, blades and spikes. The turbulent flow field downstream of the pipe outlet is measured using two-axis hot wire anemometry [1] with a temporal resolution of 48 kHz. The CTA probe is positioned using an automated three-axis traversing system. The turbulent jet impinges on a wall in the distance of 0.55 m from the pipe outlet. 12 Microphones are positioned on a flat plate mounted on the wall in the center-line of the jet. CFD (computational fluid dynamics) calculations are performed for the different turbulence generators and compared to the CTA signals. An important aspect of the work is the simultaneous recording of both the CTA- and the microphone signals. This allows for the calculation of correlation patterns between turbulence and the acoustic signals. The generation of free stream turbulence in a controlled way and its correlation to downstream pressure fluctuations is the primary aim of the work.

Numerical Simulation

The numerical analysis have been performed on a hybrid mesh consisting of tetrahedral cells in the region of the turbulence generators (see figure 3) and a prismatic / hexahedral mesh in the up- and downstream area. Mesh sizes of 2 mm at the turbulence generator core lead to typical cell counts of 3 million cells). Best results have been achieved by applying a turbulent velocity profile at the tube inlet and fixing the turbulent kinetic intensity to a value of 2.6 %. The fluid leaves the calculation area through the cylindrical surface and its base plane (see figure 1. The jet impinges on the opposite circular area of the cylinder, which is defined as a hard wall. Steady CFD calculations leading to acceptable low numeric residuals were not possible for all turbulence generators. Sharp blades caused very high fluctuating fields, which could not be captured by a steady solver. Comparing experimental and numerical results, the RNG formulation of the $k-\epsilon$ model gave best agreement. The differences have been found to be most pronounced in the near wall region at the microphone plate. Figure 2 shows the turbulent kinetic energy on the analysis plane for a turbulence generator with 4 spikes.

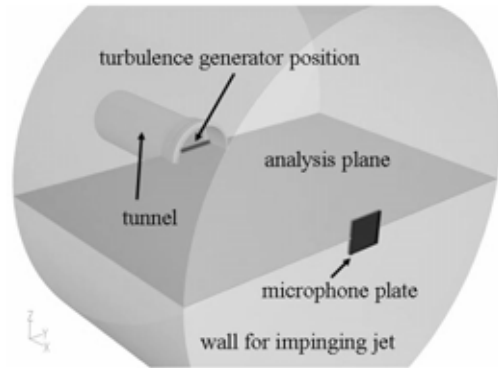


Figure 1: Geometry for the CFD simulation. A circular jet impinges on a microphone plate mounted on a wall. Turbulence generators can be applied in the outlet region of the tunnel.



Figure 2: Turbulent kinetic energy [m^2/s^2] for a turbulent generator with 4 spikes. The simulations are performed using a steady $k\epsilon$ -RNG model (grey scale range from 0 to 1).

Experimental Results

Signals from the 2-axis CTA (constant temperature anemometer) have been recorded simultaneously with 12 microphone signals with a sampling rate of 48 kHz. The data were acquired in the analysis plane on 492 points (streamwise tunnel direction x : 12 points, perpendicular crosswise direction $+y$: 41 points). All signals (CTA, microphone) have been scaled by their corresponding calibration values. For the spectral analysis they have been further numerically filtered (low pass filter 20 kHz), DC subtracted and Fourier transformed.

As an example, figure 4 compares two signals for 6 different turbulence generator setups: (1) the spectra of the CTA measurement 6 mm in front of the microphone plate and (2) the spectra of one of the microphone signals.

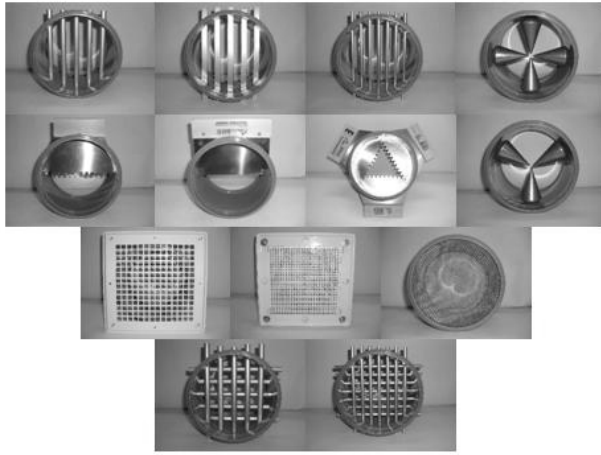


Figure 2: Different turbulence generators consisting of rods, blades, spikes and meshes. They can be mounted on top of the tunnel outlet.

All three turbulence generators (5 circular rods with diameter 12 mm, 5 quadratic rods with 12 mm side length and 7 circular rods with 8 mm diameter) were designed to have the same amount of obstruction.

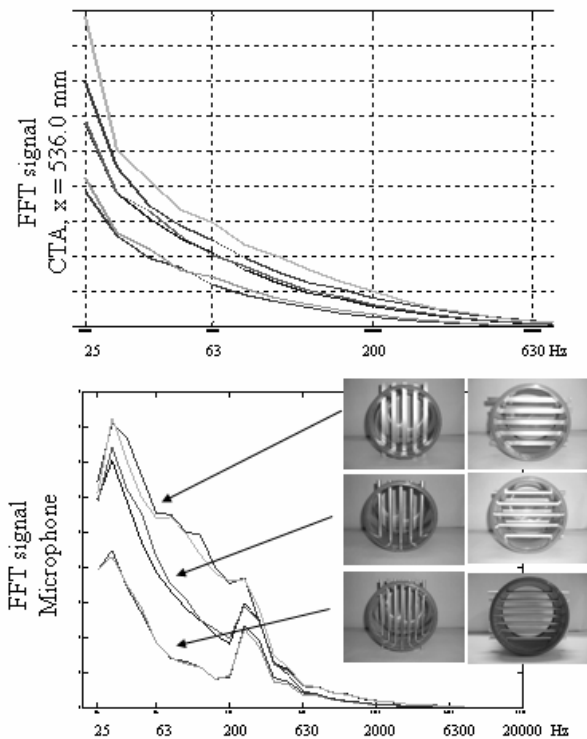


Figure 4: Comparison between frequency spectra of CTA signal (upper figure) 6 mm in front of microphone plate and microphone spectra (lower figure) for 6 different turbulence generator flow setups.

The microphone signals (lower figure 4) are clearly separated and show a peak around 250 Hz which is not observed in the CTA signals (upper figure 4). The reason for this can, however, not be found in the turbulence generator, as the peak persists, when no turbulence generator is present.

Conclusions & Outlook

Steady CFD simulations can give trends but are not ideally suited for quantitative analysis as they are not able to capture the inherent transient flow patterns. The RNG formulation of the k- ϵ model compared best to the experimental data (streamwise and crosswise velocity, turbulent kinetic energy). Differences in the models are most pronounced in the stagnation area of the impinging jet at the wall. For some turbulence generators (blades), a steady solution could not be achieved.

Correlations between turbulent velocity fields and microphone signals have been investigated for 11 different turbulence generators. Larger turbulence coincides with larger pressure fluctuations, the full frequency behaviour, however, could not always be reproduced. The reasons may lie in additional acoustic incoming waves, which can be attributed to dipolar and quadrupolar sound sources as well as vibrations of the turbulent generators.

Transient CFD simulations (DES) will be employed to provide frequency spectra for comparison to the experimental data. Furthermore, the correlation between simulated local velocity fluctuations and pressure fluctuations at the wall can be investigated. These results will also be compared to the experimental correlation, as CTA and microphone signals have been recorded simultaneously. The 12 microphone signals also allow for spatial correlation analysis.

References

- [1] Bruun, H. H.: Hot-Wire Anemometry: Principles and Signal Analysis, Publisher: Oxford University Press, USA (June 8, 1995), ISBN: 0198563426
- [2] Counihan, J.: An improved method of simulating an atmospheric boundary layer in a wind tunnel, J. Fluid Mechanics, vol. 3, pp. 197-214, 1969.
- [3] Guimaraes, J. H. D., dos Santos, S. J. F., Su, J., Silva Freire, A. P.: Large artificially generated turbulent boundary layers for the study of atmospheric flows, Proceedings for the 15th Brazilian Congress of Mechanical Engineering (COBEM99), Aguas de Lindoia, 1999
- [4] Hunt, J. C. R., Fernholz, H.: Wind-tunnel simulation of the atmospheric boundary layer: a report on Euromech 50, J. Fluid Mechanics, vol. 70, pp. 543-559, 1975.
- [5] Jovanovic, J.: The Statistical Dynamics of Turbulence, ISBN 3-540-20336-2 Springer Verlag Berlin Heidelberg New York, 2002
- [6] Ramezani, A., Shirvani, H., Mirzaee, I.: Heat transfer modelling of slot jet impinging on an inclined plate, Heat Transfer VIII, B. Sundén, C. A. Brebbia & A. Mendes (Editors)



SPECTRAL COMPARISON OF NUMERICAL SIMULATION AND EXPERIMENTAL DATA OF TURBULENT IMPINGING JETS

Christoph REICHL¹, Michelle BÖCK^{1,2}, Wolfgang TILŠER^{1,3}, Helmut
KÜHNELT⁴, Klaus HAINDL⁵, Martin OPITZ⁶

¹ Corresponding Author. Austrian Institute of Technology, Energy Department, Sustainable Thermal Energy Systems, Giefinggasse 2, A-1210 Vienna, Austria, Tel.: +43 (0) 50550 – 6605, Fax: +43 (0) 50550 – 6679, E-mail: christoph.reichl@ait.ac.at

² Technical University of Vienna, Institut für Solid State Physics, E-mail: michelle.boeck@ait.ac.at

³ Technical University of Vienna, Institut für Solid State Physics, E-mail: wolfgang.tilser@ait.ac.at

⁴ Austrian Institute of Technology, Mobility Department, E-mail: helmut.kuehnelt@ait.ac.at

⁵ AKG Acoustics GMBH, E-mail: haindlk@akg.com

⁶ AKG Acoustics GMBH, E-mail: opitzm@akg.com

ABSTRACT

A turbulent circular pipe-flow with typical core-velocities of around 10 m/s is generated by an axial symmetric fan. After leaving the cylindrical tube, the generated separating jet impinges on a flat plate. Turbulence is generated using different sets of turbulence generators at the pipe outlet consisting of rods, cubes and spikes. To extract the inlet boundary conditions for the CFD calculations, turbulent velocity profiles have been measured in the pipe using two-axis constant temperature anemometry (CTA). The turbulent flow field downstream of the pipe outlet is also measured using two-axis hot wire anemometry. The CTA probe is positioned using an automated three-axis traversing system recording the turbulent velocities on 492 points downstream of the pipe outlet.

CFD calculations are performed for the different turbulence generators using Detached Eddy Simulation (DES) to generate the base for the extraction of fluctuating velocity time series. The spectral evaluation of the data is analysed in 1/3 terz band representations via FFT. The spectral content of the time series is compared with the experimental values.

This contribution explores the robustness of present transient turbulence modelling approaches. Based on experimental and numerical methods free stream turbulence is generated in a well defined way and spectrally characterized.

Computational Fluid Dynamics (CFD), detached eddy simulation (DES), impinging jet, RANS, turbulence, turbulence generators

NOMENCLATURE

<i>CFD</i>	[-]	Computational Fluid Dynamics
<i>CTA</i>	[-]	Const. Temperature Anemometry
<i>DES</i>	[-]	Detached Eddy Simulation
<i>FFT</i>	[-]	Fast Fourier Transformation
<i>RANS</i>	[-]	Reynolds-averaged Navier-Stokes
<i>rms</i>	[-]	root mean square
<i>RNG</i>	[-]	Re-Normalisation Group

1. INTRODUCTION

A turbulent circular free stream jet is generated using an axial symmetric fan driven by a brushless actuator with variable frequency leading to typical core-velocities of around 10 m/s ($Re = 99000$). The flow is propagated through a pipe (radius = 80.5 mm). Turbulence is generated using different sets of turbulence generators [2, 3, 4] in the tunnel consisting of rods, blades and spikes. The length of the tunnel is approx. 2.5 m. The turbulent flow field downstream of the pipe outlet is measured using two-axis hot wire anemometry [1] with a temporal resolution of 48 kHz. The CTA probe is positioned using an automated three-axis traversing system. The turbulent jet impinges on a wall in the distance of 0.55 m from the pipe outlet. Computational fluid dynamics (CFD) calculations are performed for the different turbulence generators and compared to the CTA signals.

2. NUMERICAL SIMULATION

2.1. Geometry Definition

The geometric definition is shown in figure 1. After entering the simulation area at the tube inlet and crossing the turbulence generators, the fluid leaves the calculation area through the cylindrical surface and its base plane. The jet impinges on the

opposite circular area of the cylinder, which is defined as a hard wall.

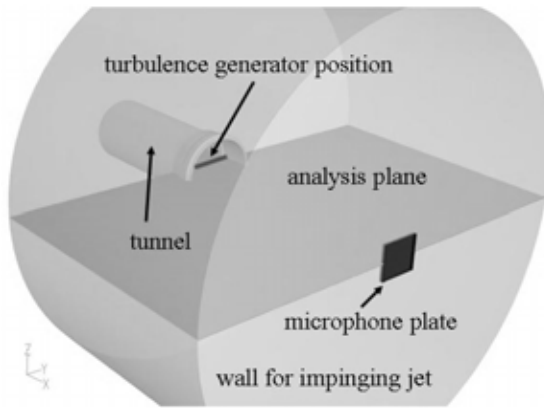


Figure 1. Geometry for the CFD simulation. A circular jet impinges on a microphone plate mounted on a hard wall. Turbulence generators can be applied in the outlet region of the tunnel. 12 different evaluation lines L01-L12 are defined in the area between tube outlet and plate. Their x-axis positions are given in table 1. Different turbulence generators are summarized in figure 3. The empty tube section (no turbulence generator) is called TG00.

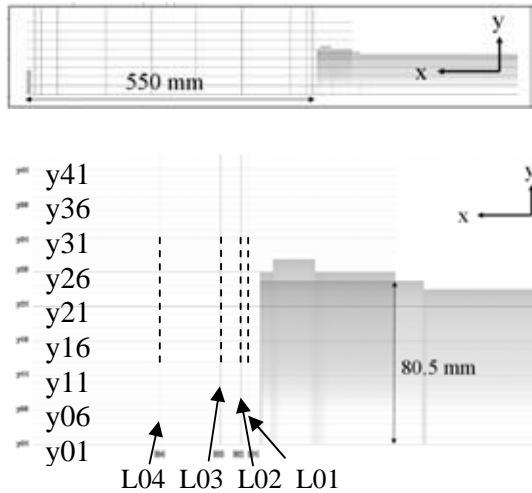


Figure 2. Definition of the postprocessing lines L01-L12.

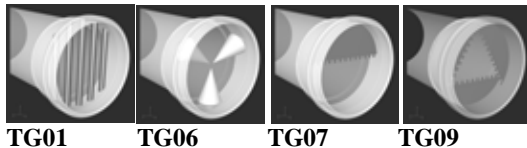


Figure 3. Different turbulence generators consisting of rods, spikes and blades. They can be mounted on top of the tunnel outlet.

Table 1. x-coordinates of the analysis planes

linename	x-axis position [mm]	linename	x-axis position [mm]
L01y	6.00	L07y	312.74
L02y	9.40	L08y	400.10
L03y	19.59	L09y	491.83
L04y	50.17	L10y	522.41
L05y	141.90	L11y	532.60
L06y	229.26	L12y	536.00

2.2 Mesh Definition

The numerical analysis have been performed on a hybrid mesh consisting of tetrahedral cells in the region of the turbulence generators (see figure 4) and a prismatic / hexahedral mesh in the up- and downstream area. Mesh sizes of 1 mm at the turbulence generator core and 12 mm at the boundaries lead to typical cell counts of 5 million cells.

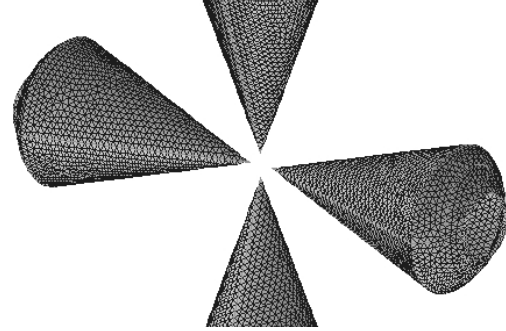


Figure 4. Mesh resolution on the spike surfaces of TG05.

2.3. Simulation Method

Results of steady RANS simulations have been calculated before [5] giving best results using the RNG formulation of the k- ϵ model. In publication [5] additional turbulence generators have been analyzed as well. Especially the sharp blades caused very high fluctuating fields, which could not be captured by a steady solver. The present paper focuses on five turbulence generators showing different spectral data. The mean velocity inlet boundary profiles were extracted from the experimental CTA data. The turbulence boundary condition was defined using the hydraulic diameter of 152.59 mm and a turbulence intensity of 5%. For the simulations the commercial Navier Stokes solver Fluent [6] was used applying the Detached Eddy Simulation with vorticity based production terms. Second order schemes were used in space and time.

Using a time step of 100 μ s around 5000 time steps were necessary to reach quasistatic behaviour of the flow field. An additional amount of 5000 time steps have been calculated and recorded to perform the steps for the spectral analysis.

2.4. Mean Velocities and Fluctuations

Figure 5 gives the mean and rms values of the velocity magnitude for the five turbulence generators. Results are given on planes with fixed $y=0$ (TGxx-y) and $z=0$ (TGxx-z) coordinates.

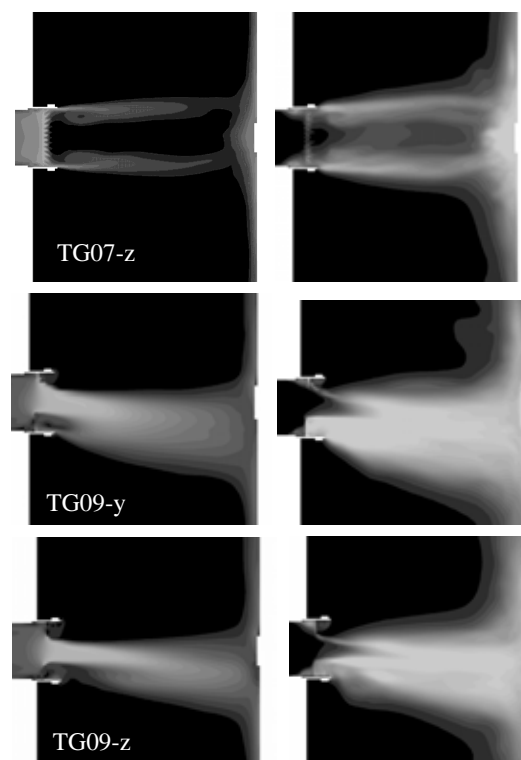
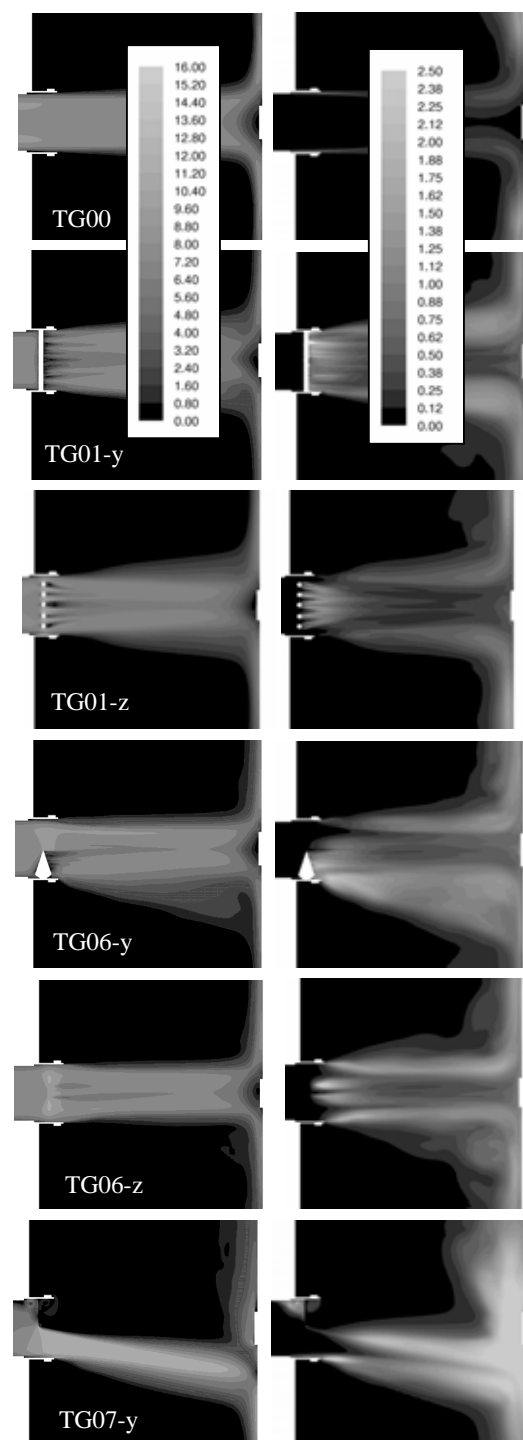
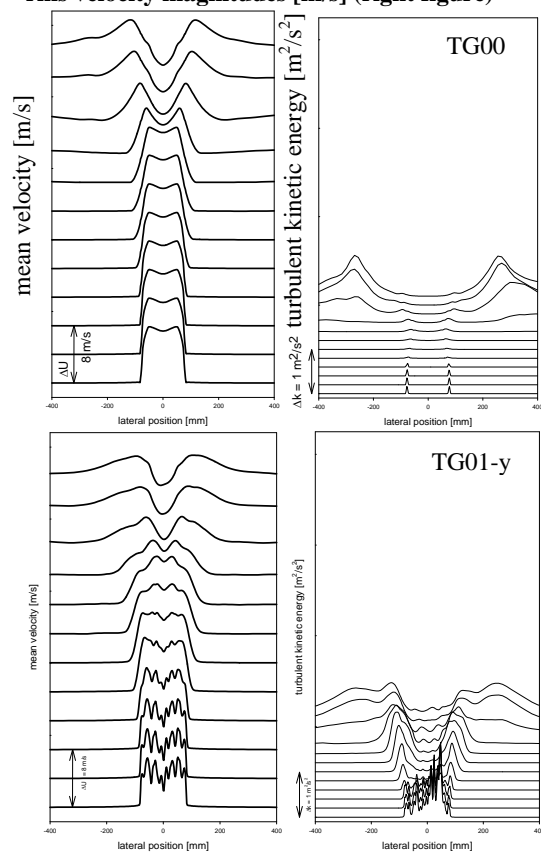


Figure 5. Mean velocities [m/s] (left figure) and rms velocity magnitudes [m/s] (right figure)



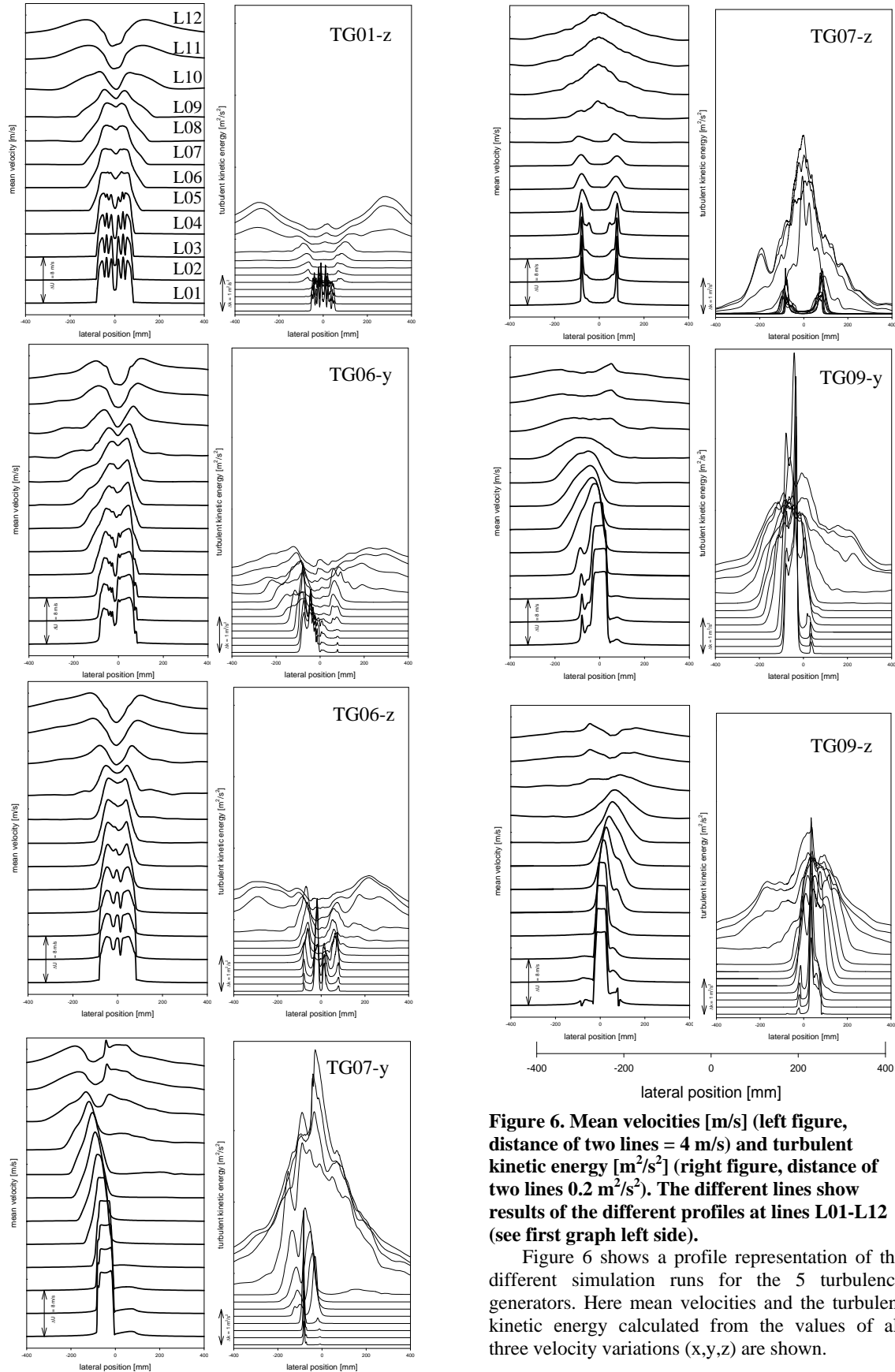


Figure 6. Mean velocities [m/s] (left figure, distance of two lines = 4 m/s) and turbulent kinetic energy [m²/s²] (right figure, distance of two lines 0.2 m²/s²). The different lines show results of the different profiles at lines L01-L12 (see first graph left side).

Figure 6 shows a profile representation of the different simulation runs for the 5 turbulence generators. Here mean velocities and the turbulent kinetic energy calculated from the values of all three velocity variations (x,y,z) are shown.

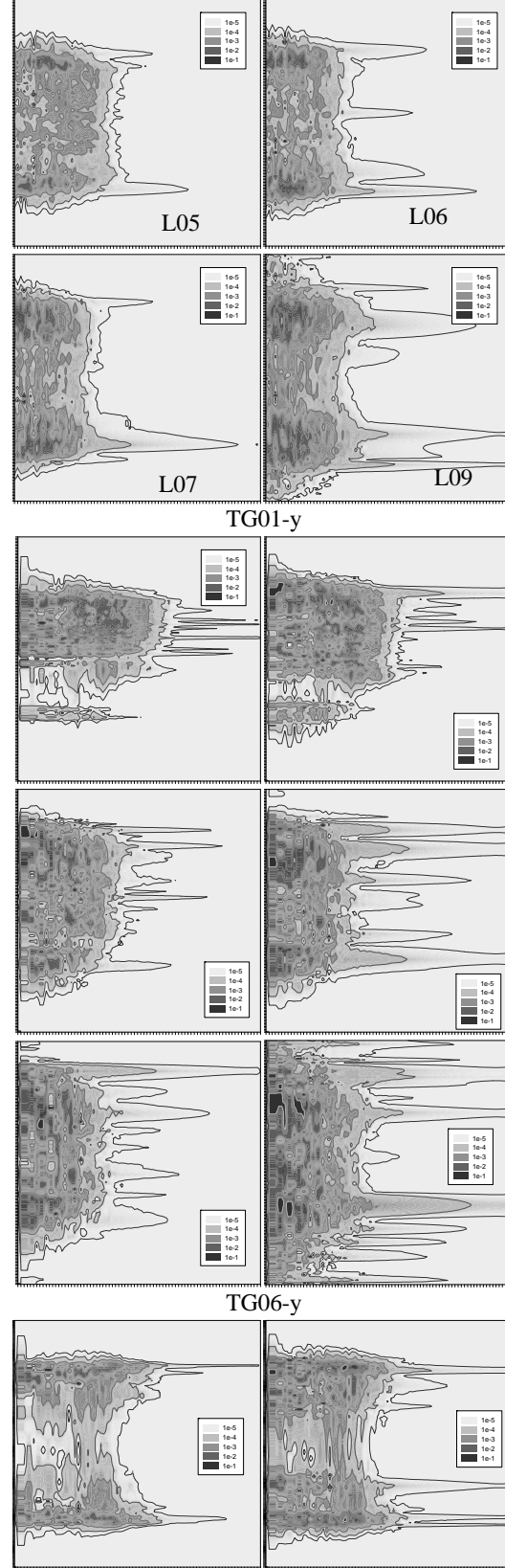
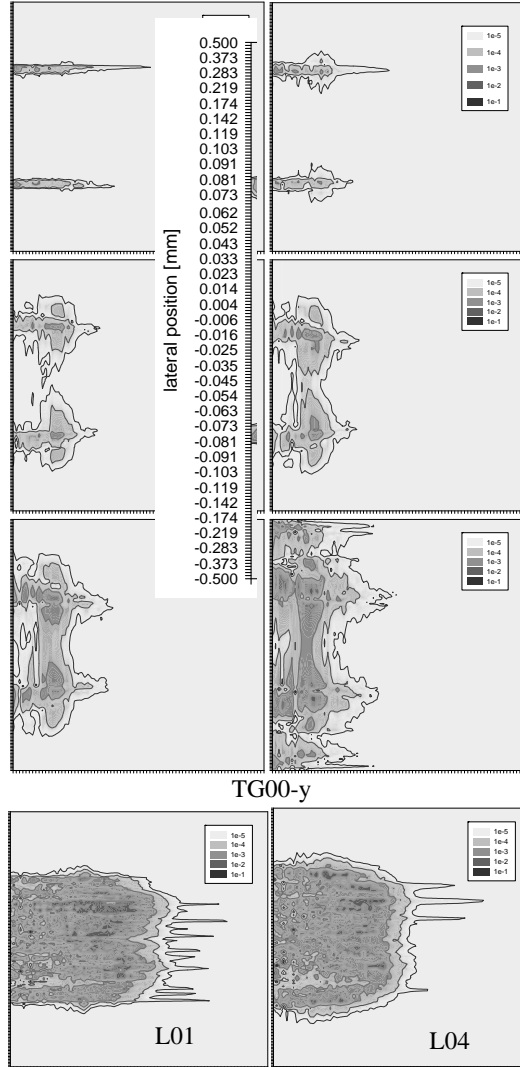
3. SPECTRAL ANALYSIS

Velocity fluctuations are available from the CTA measurements as well as from the numerical DES simulations. This part of the paper gives details for the data processing and shows the corresponding FFT spectra.

3.1 Simulation Results

With the purpose of a spectral analysis, the x-, y- and z-velocities on twelve evaluation lines (L01 – L12) have been recorded for about 5000 time steps.

Figure 7 and 8 show the spectral normalized, absolute squared value of the variance of the mean velocity, which is multiplied by a factor of two to account for the positive frequency space. FFT signals are displayed in a logarithmic scale with a reference value set to $1 \text{ m}^2/\text{s}^2$. Integrating over the frequency space yields the corresponding turbulent kinetic energy.



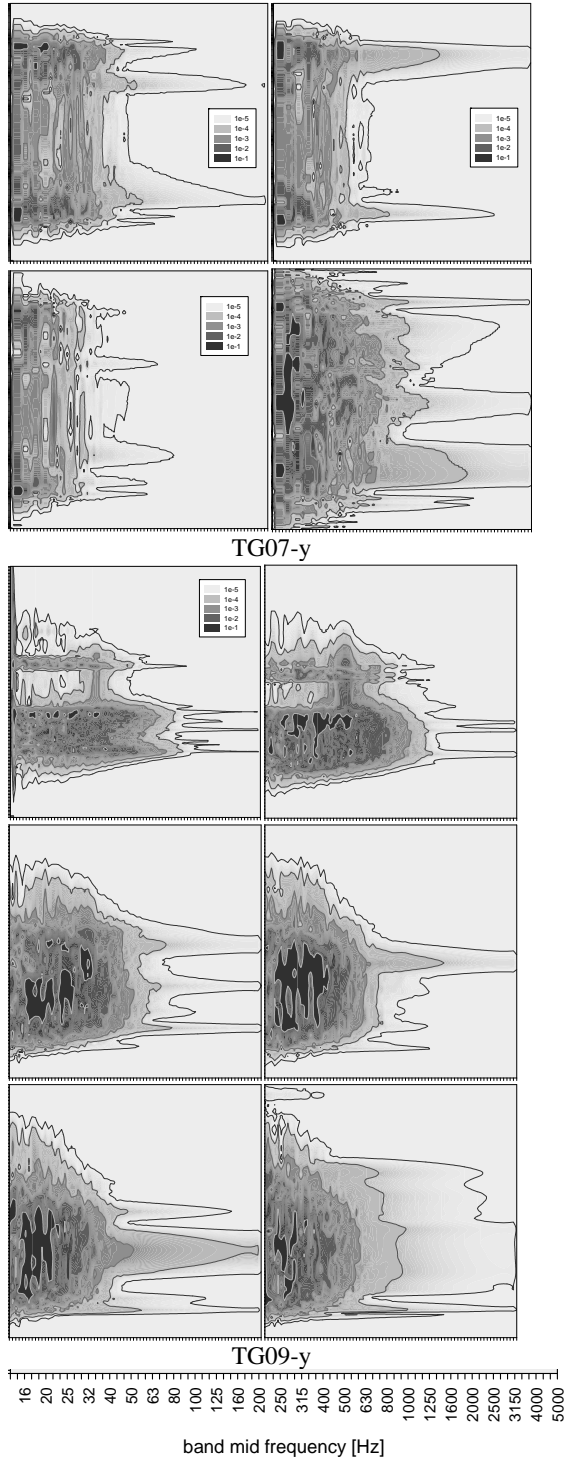
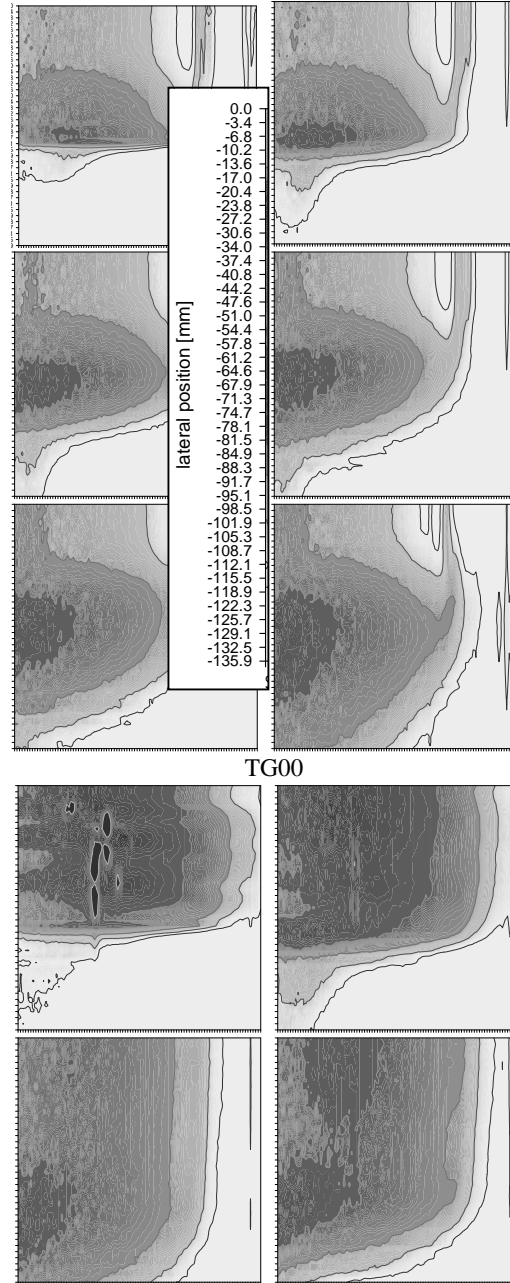


Figure 7. Frequency spectra at different lines (upper graphs L01, L04, mid graphs L05, L06, lower graphs L07, L09) for different turbulence generators TGxx. The grey scale represents the variance of the mean velocity [m²/s²]. The y-axis is nonlinear representing the nonlinear mesh.

3.2. Experimental Results

Signals from the 2-axis CTA have been recorded with a sampling rate of 48 kHz. The data was acquired in an analysis plane on 492 points (streamwise tunnel direction x: 12 points, perpendicular crosswise direction +y: 41 points). All signals have been scaled by their corresponding calibration values. The spectral analysis was carried out after numerically filtering (low pass filter 20 kHz), DC subtraction and Fourier transformation.



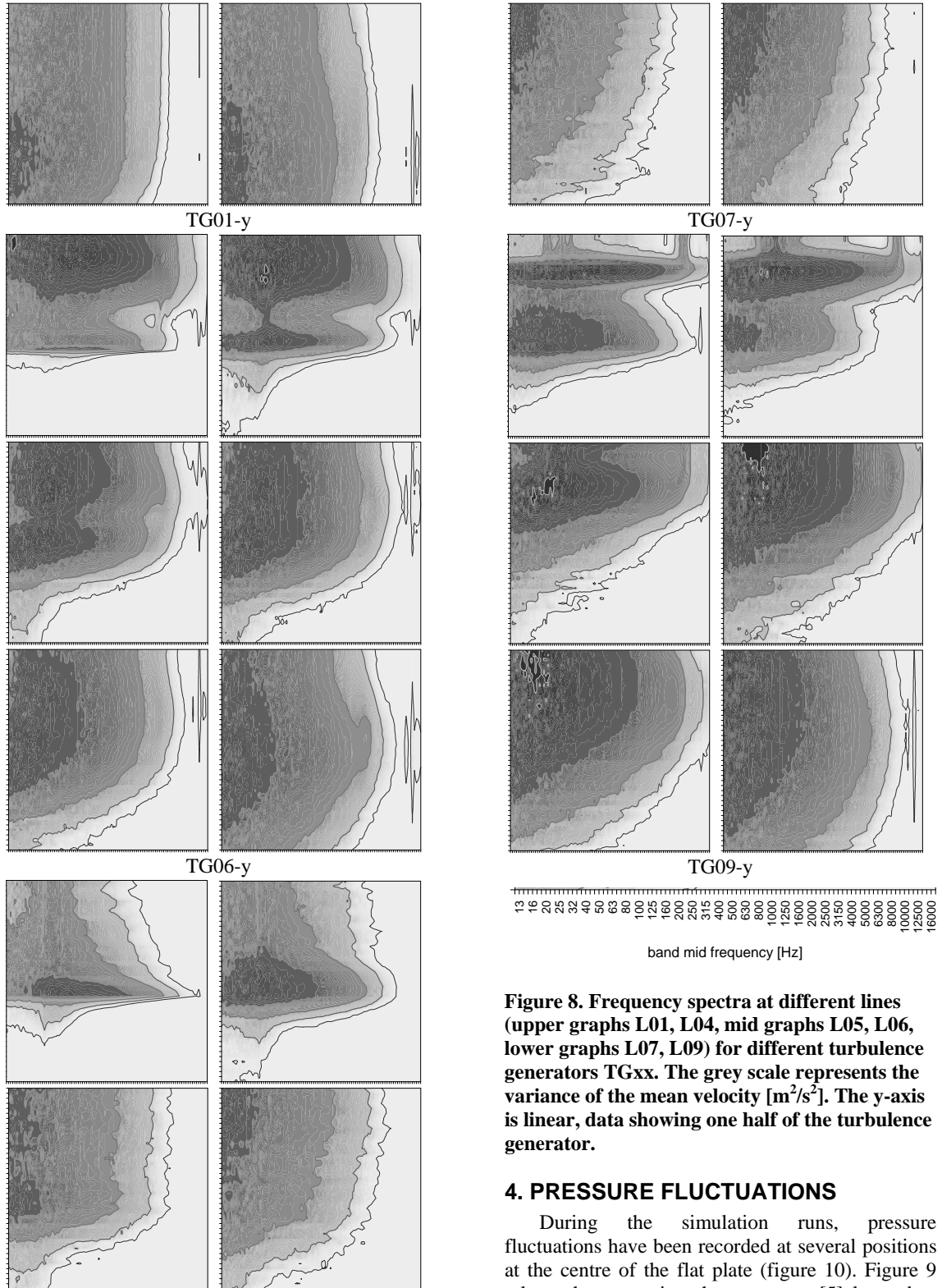


Figure 8. Frequency spectra at different lines (upper graphs L01, L04, mid graphs L05, L06, lower graphs L07, L09) for different turbulence generators TGxx. The grey scale represents the variance of the mean velocity $[\text{m}^2/\text{s}^2]$. The y-axis is linear, data showing one half of the turbulence generator.

4. PRESSURE FLUCTUATIONS

During the simulation runs, pressure fluctuations have been recorded at several positions at the centre of the flat plate (figure 10). Figure 9 relates them to microphone spectra [5] located at the same position.

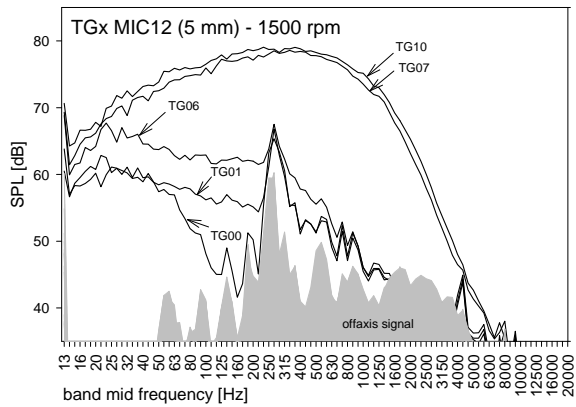


Figure 9. Comparison of the frequency spectra of the microphone MIC12 for the different turbulence generators (TGx). The signal was recorded at the center of the plate ($y \sim 1\text{cm}$, $z = 0$), where the turbulent jet impinges on the microphone plate. The gray area is the maximum signal of the acoustic offset measurement for the different TGx [5]. The reference pressure for the logarithmic scale was set to 20 μPa .

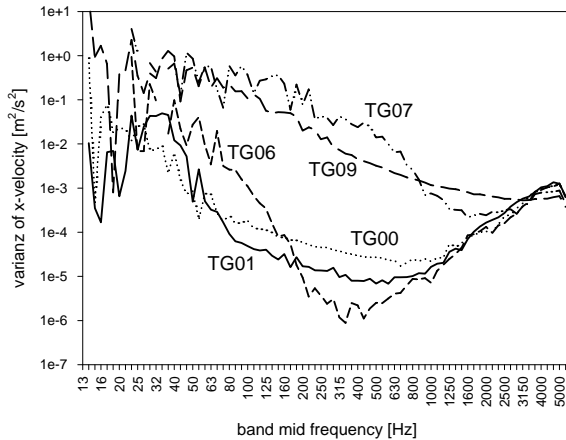


Figure 10. Comparison of the frequency spectra of the pressure fluctuations for the different turbulence generators (TGx) from the DES. TG10 and TG07 reach the highest and broadest spectra in the simulation as well as the experiment. The simulation results drop at lower frequency values than their experimental counterparts. This can be attributed to insufficient mesh resolution in the propagation region.

5. SUMMARY

Comparing the spectra from the DES (figure 7, mind the nonlinear y-axis, which is more dense in the shear layer) with the spectra from the experimental data (figure 8, only one half of the tube was scanned) the following results can be extracted.

The prominent features of the spatial frequency behaviour are well captured (e.g. the position of the

shear layers, the separation and the combination of the turbulent areas). However, the representation of all details of the spectra is limited. This can be partly attributed to the constraints of the computing power and cell size. Using a cell amount of 5 million cells, one timestep needs approximately 6 min real time, leading to calculation times of 40 days on 4 CPUs of a 3.2 GHz Linux cluster.

Due to the minimum cell side length of 1 mm at the turbulence generating surfaces and a mean value of around 5 mm cell side length in the turbulent area, occurring lower mesh densities prevent accurate propagation of higher frequencies, which can be seen in the lower frequency content of the numerical based spectra (fig. 7) compared to the experimental data (fig. 8).

The experimental spectra of TG00 show a higher turbulence level between the shear layers as compared to the simulation data.

Future investigations will, thus, be devoted to different mesh strategies and the implementation of stronger fluctuating boundary conditions to overcome the present limitations.

ACKNOWLEDGEMENTS

This work has been supported by the Austrian Research Promotion Agency (FFG) under “Bridge” contract No. 813008.

REFERENCES

- [1] Bruun, H. H., 1995, “Hot-Wire Anemometry: Principles and Signal Analysis”, Publisher: *Oxford University Press*, USA (June 8, ISBN: 0198563426
- [2] Counihan, J., 1969, “An improved method of simulating an atmospheric boundary layer in a wind tunnel”, *J. Fluid Mechanics*, Vol. 3, pp. 197-214
- [3] Guimaraes, J. H. D., dos Santos, S. J. F., Su, J., Silva Freire, A. P., 1999, “Large artificially generated turbulent boundary layers for the study of atmospheric flows”, *Proceedings for the 15th Brazilian Congress of Mechanical Engineering (COBEM99)*, Aguas de Lindoia
- [4] Hunt, J. C. R., Fernholz, H., 1975, “Wind-tunnel simulation of the atmospheric boundary layer”: a report on Euromech 50, *J. Fluid Mechanics*, Vol. 70, pp. 543-559
- [5] Reichl, Ch., Böck, M., Tilser, W., Lang, H., Haindl, K., Reining, F., Opitz, M., 2008, „On the correlation of the acoustic signal of microphones mounted on a flat plate to the turbulence of an impinging jet”, *proceedings of the Acoustics'08 Paris*, 29.06.-04.07., Paris
- [6] Fluent.Inc, ANSYS, Commercial CFD Navier Stokes Solver. Version 6.2.16, double precision, 64bit.

A turbulent circular free stream jet is generated using an axial symmetric fan driven by a brushless actuator with variable frequency leading to typical core-velocities of around 10 m/s ($Re = 99000$). The flow is propagated through a pipe system significantly damping the noise from the fan. Turbulence is generated using different sets of turbulence generators in the pipe consisting of meshes, rods, cubes and spikes. The turbulent flow field downstream of the pipe outlet is measured using two-axis hot wire anemometry with a temporal resolution of a minimum of 48 kHz. The CTA probe is positioned using an automated three-axis traversing system. Microphones located at freely adjustable positions are used to capture the acoustic radiation and the wall pressure fluctuations. CFD calculations are performed for the different turbulence generators and compared to the acoustic and CTA signals. An important aspect of the work is the simultaneous recording of both the CTA- and the acoustic signals in the experimental and numerical approach. This allows for the calculation of correlation patterns between turbulence and the acoustic signals. The generation of free stream turbulence in a controlled way and its correlation to downstream pressure fluctuations is the primary aim of the work.

1 Introduction

A turbulent circular free stream jet is generated using an axial symmetric fan driven by a brushless actuator with variable frequency leading to typical core-velocities of around 10 m/s ($Re = 99000$). The flow is propagated through a pipe (radius = 80.5 mm). Turbulence is generated using different sets of turbulence generators [2, 3, 4] in the tunnel (length approx. 2.5 m) consisting of meshes, rods, blades and spikes. The turbulent flow field downstream of the pipe outlet is measured using two-axis hot wire anemometry [1] with a temporal resolution of 48 kHz. The CTA probe is positioned using an automated three-axis traversing system. The turbulent jet impinges on a wall in the distance of 0.55 m from the pipe outlet. 12 Microphones are positioned on a flat plate mounted on the wall in the center-line of the jet. CFD (computational fluid dynamics) calculations are performed for the different turbulence generators and compared to the CTA signals. An important aspect of the work is the simultaneous recording of both the CTA- and the microphone signals. This allows for the calculation of correlation patterns between turbulence and the acoustic signals. The generation of free stream turbulence in a controlled way and its correlation to downstream pressure fluctuations is the primary aim of the work.

2 Numerical Simulation

The numerical analysis have been performed on a hybrid mesh consisting of tetrahedral cells in the region of the turbulence generators (see figure 2) and a prismatic / hexahedral mesh in the up- and downstream area. Mesh sizes of 2 mm at the turbulence generator core lead to typical cell counts of 3 million cells). Best results have been achieved by applying a turbulent velocity profile at the tube inlet and fixing the turbulent kinetic intensity to a value of 2.6 %. The fluid leaves the calculation area through the cylindrical surface and its base plane (see figure 2). The jet impinges on the opposite circular area of the cylinder, which is defined as a hard wall. Steady CFD calculations leading to acceptable low numeric residuals were not possible for all turbulence generators. Sharp blades caused very high fluctuating fields, which could not be captured by a steady solver. Comparing experimental and numerical

results, the RNG formulation of the k- ϵ model gave best agreement.

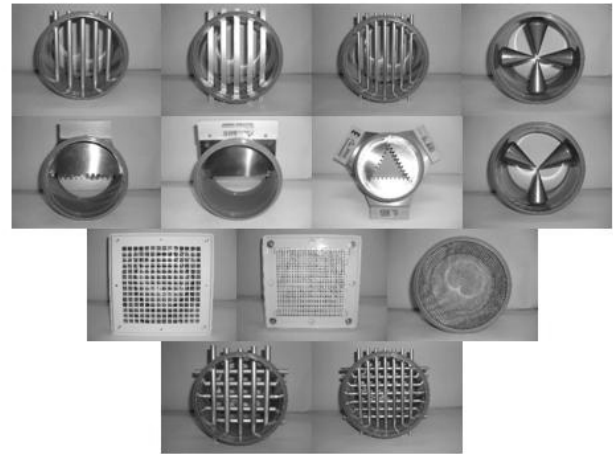


Fig.1 Different turbulence generators consisting of rods, blades, spikes and meshes. They can be mounted on top of the tunnel outlet. First row: TG01, TG08, TG02, TG05; Second row: TG07, TG10, TG09, TG06; Third row: TG11, TG13, TG12; Fourth Row: TG04, TG03

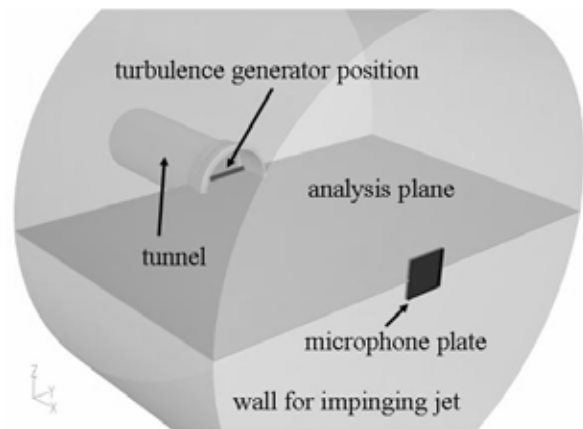


Fig.2 Geometry for the CFD simulation. A circular jet impinges on a microphone plate mounted on a wall. Turbulence generators can be applied in the outlet region of the tunnel.

The differences have been found to be most pronounced in the near wall region at the microphone plate. Figure 3

shows the turbulent kinetic energy on the analysis plane for a turbulence generator with 4 spikes (TG05).

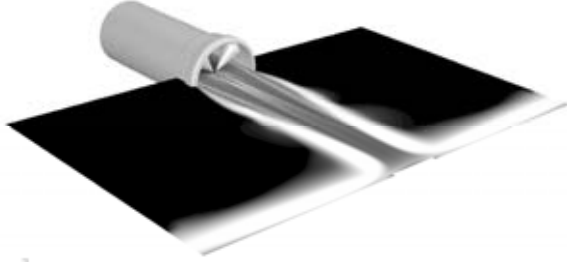
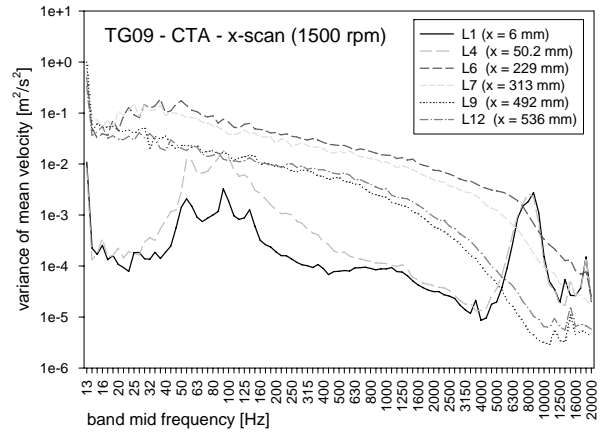
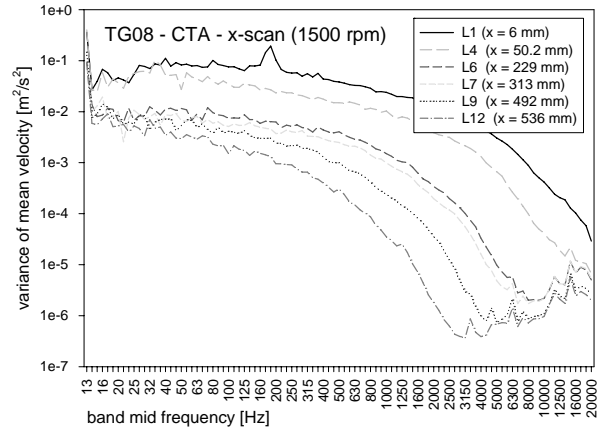
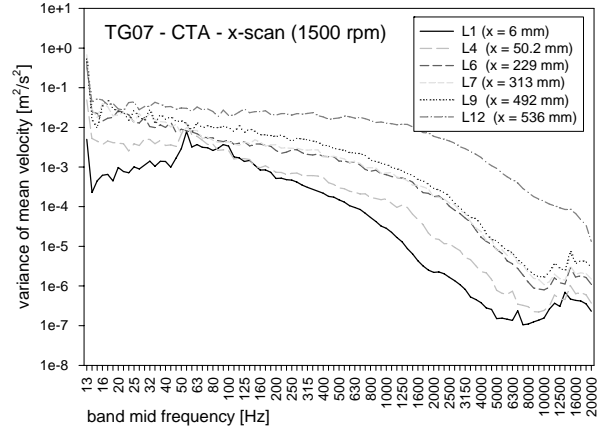
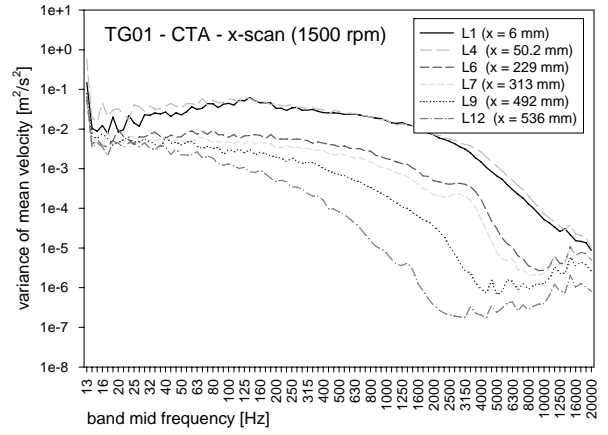
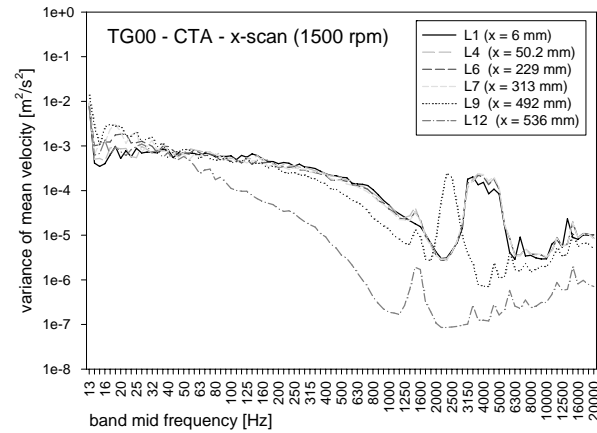


Fig.3 Turbulent kinetic energy [m^2/s^2] for a turbulent generator with 4 spikes. The simulations are performed using a steady $k\epsilon$ -RNG model (grey scale range from 0 to 1).

3 Experimental Results

Signals from the 2-axis CTA (constant temperature anemometer) have been recorded simultaneously with 12 microphone signals with a sampling rate of 48 kHz. The data were acquired in the analysis plane on 492 points (streamwise tunnel direction x : 12 points, perpendicular crosswise direction $+y$: 41 points). All signals (CTA, microphone) have been scaled by their corresponding calibration values. For the spectral analysis they have been further numerically filtered (low pass filter 20 kHz), DC subtracted and Fourier transformed. In the figures always the normalized, absolute squared value, which is multiplied by a factor of two to account for the positive frequency space, is shown. CTA and acoustic FFT signals are displayed in a logarithmic scale, for acoustic signals, the sound pressure level was calculated using a reference pressure of 20 μPa , for CTA signals the reference value was set to 1 m^2/s^2 . Figure 4 gives an overview of the evolvement of turbulent velocity field for different x -positions. The data was recorded in the center ($y=z=0$ m) of the jet directly pointing towards the microphone plate.



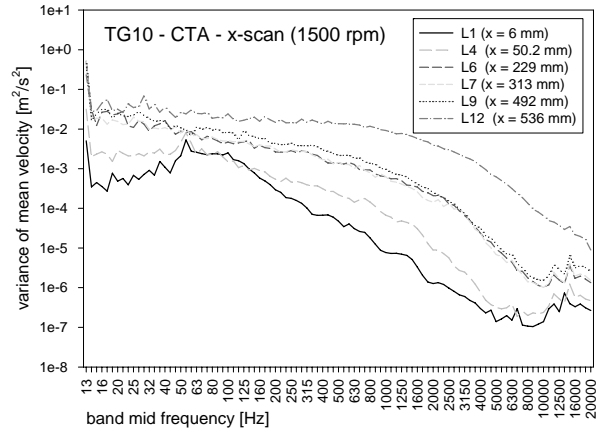


Fig.4 Development of the turbulent flow field of different turbulence generators, showing the variance of the mean velocity based on the CTA signal. The area below the different curves correspond to the variance of the mean velocity.

Different spatial evolution of the frequency distributions can be observed applying different turbulence generators. Often some spectral peaks can be found between 50 Hz and 160 Hz in the direct vicinity of the turbulence generator (L1). The spectra then generally start a deep slope down in sound pressure level from around 1000 Hz towards higher frequencies.

Acoustic measurements for all turbulence generators were performed downstream of the tube outlet (distance 55.5 cm) directly on the plate and offaxis (angle of 60° to the x-axis). Figure 5 shows the offaxis acoustic signal for a fan rotation frequency of 1500 rpm. The largest contribution lies in the 250 Hz range, almost no contribution can be seen in the lower frequency range. The signal is almost independent from the turbulence generator placed in the tube and comes primarily from the sound radiation of the fan.

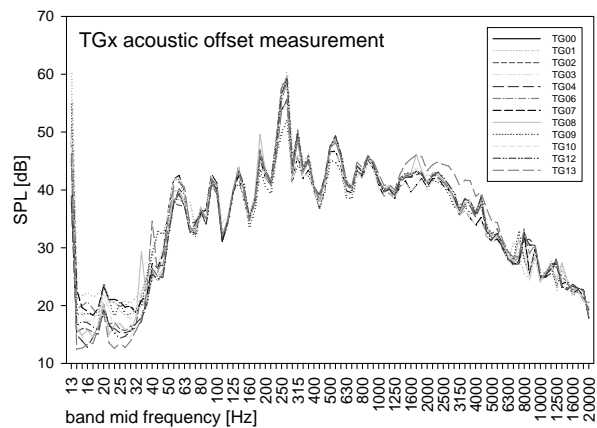


Fig.5 Acoustic measurements downstream of the tube outlet (distance 55.5 cm) and offaxis (angle of 30° to the x-axis). The fan speed was fixed to 1500 rpm.

Figure 6 – 8 compare parts of the recorded time-series of CTA and microphone signal. Periods of fast and slow fluctuations correlate (see fig. 8), an exact match (even considering a slight offset due to time shift between CTA and MIC position) of the waves cannot be seen. The signals of the microphones MIC10 and MIC12 which are horizontally separated by about 2 cm are shown in fig. 8.

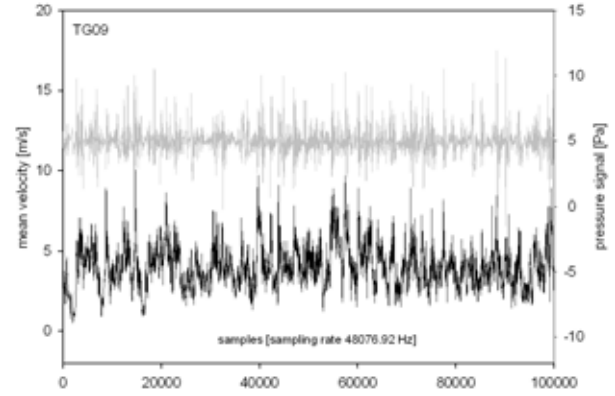


Fig.6 Comparison of the simultaneous recorded signals of the microphone MIC12 and the CTA positioned 5mm in front of the microphone for turbulence generator TG09. The gray curve corresponds to the microphone signal (right axis), the black curve to the mean velocity of the CTA (left axis).

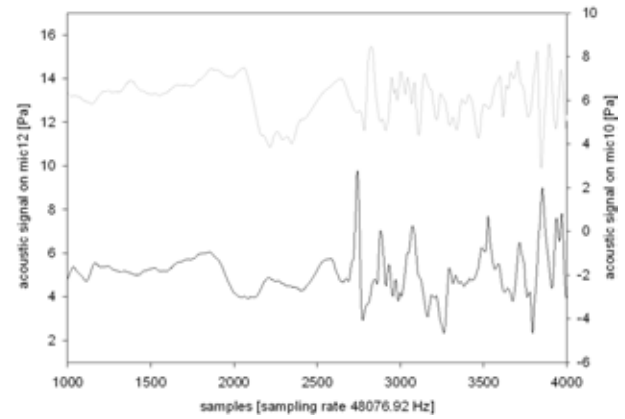


Fig.7 Simultaneous recording of the pressure signal at two microphones on the plate in the impinging jet range. The distance of the two microphones in y-direction is about 2cm. Showing overall similar behaviour (fast and slow fluctuations), the two curves are not matching, showing differing local pressure fluctuations at different positions on the plate.

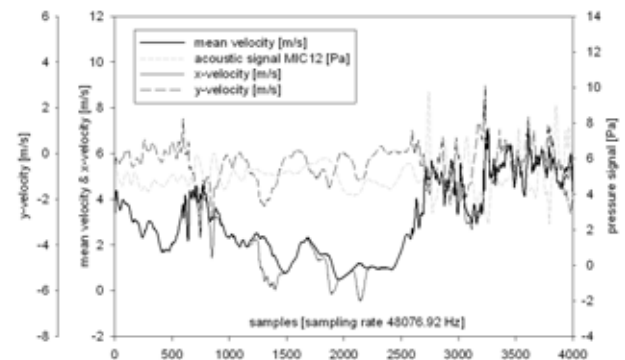


Fig.8 Comparison of the simultaneous recorded signals of the microphone MIC12 and the CTA positioned 5mm in front of the microphone (turbulence generator TG09). Shown are the mean velocity, the x- and the y-velocity components.

To analyse the correlation between microphone signal on the plate (MIC 12) and the CTA signal 5mm in front of the microphone, fig. 10 and fig. 11 show overviews of the frequency spectra for different turbulence generators.

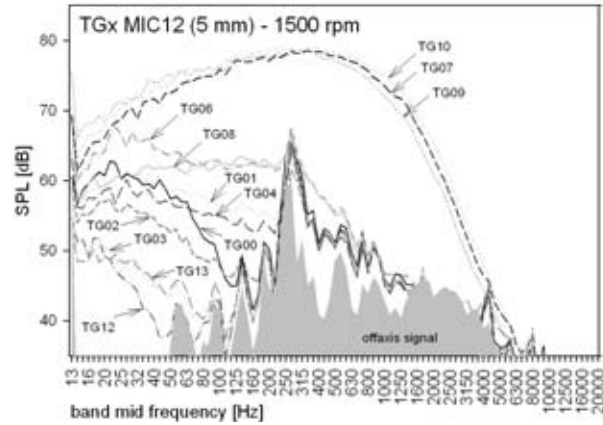


Fig.9 Comparison of the frequency spectra of the microphone MIC12 for the different turbulence generators (TGx). The signal was recorded at the center of the plate ($y \sim 1\text{cm}$, $z = 0$), where the turbulent jet impinges on the microphone plate. The gray area is the maximum signal of the acoustic offset measurement for the different TGx.

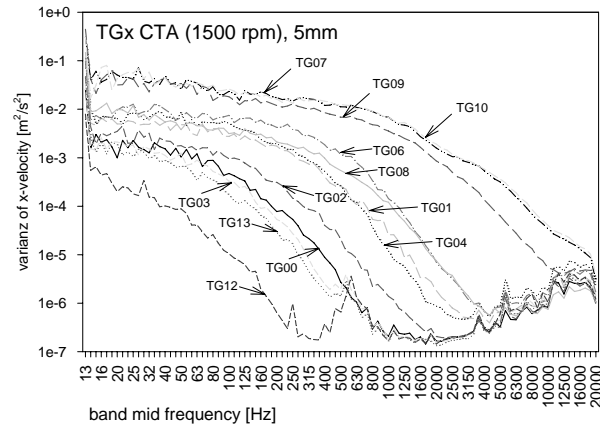


Fig.10 Comparison of frequency spectra of the CTA signal (mean velocity) for the different turbulence generators (TGx). The signal was recorded 5mm in front of the microphone MIC12, where the turbulent jet impinges on the microphone plate.

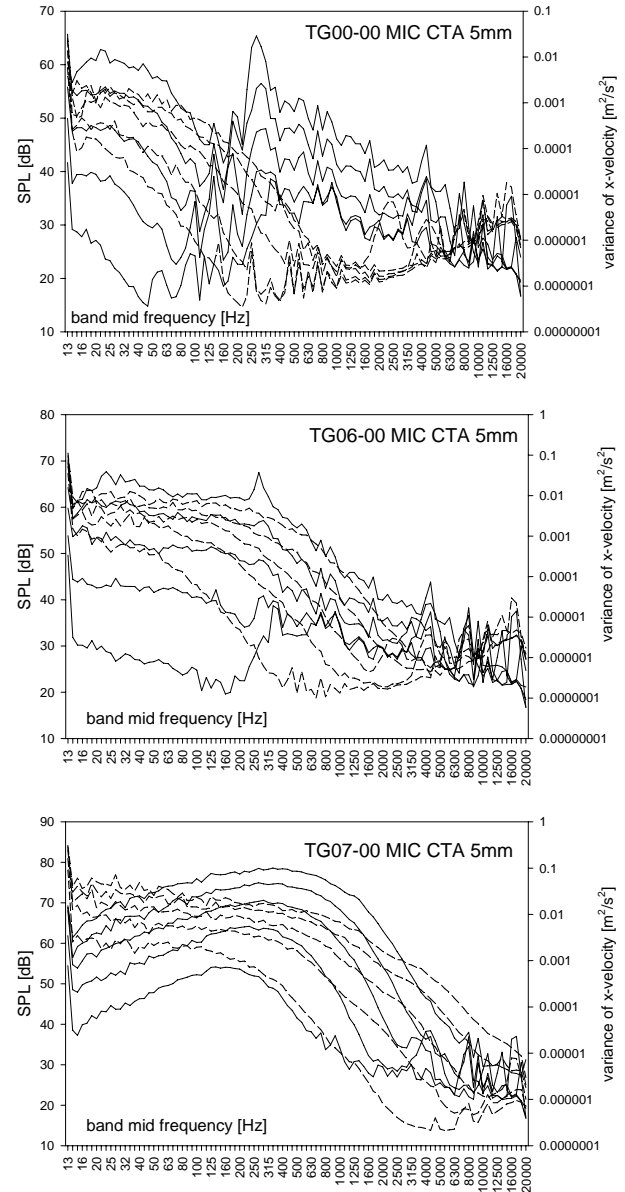
The microphone signals (fig. 9) clearly show large frequency content in the range up to 200 Hz, where no sound contribution from the fan (grey area) is present. The CTA signals (see fig. 10) show their large spectra content in this low frequency range. Comparing the different turbulence generators, a good agreement in the power and in the width of the spectra can be found.

For some turbulence generators (TG07, TG09, TG10) an even broader (and higher) spectrum is observed completely masking the fan noise (which is also directly propagating through the tube towards the microphone plate). Only part of this frequency range can be seen in the CTA signal and thus be attributed to the local velocity fluctuations at the plate.

Fig. 11 compares frequency spectra of the microphones on the plate (MIC 12) with the local x-velocity fluctuations 5mm in front of the microphone for different turbulence generators TGx.

For each generator TGx, microphone and CTA signals for 5 different rotation frequencies (500, 750, 1000, 1250 and 1500 rpm) of the fan have been measured.

If no turbulence generator is inserted into the tube (TG00) and for some “quiet” turbulence generators the noise from the fan can readily be seen in the spectra.



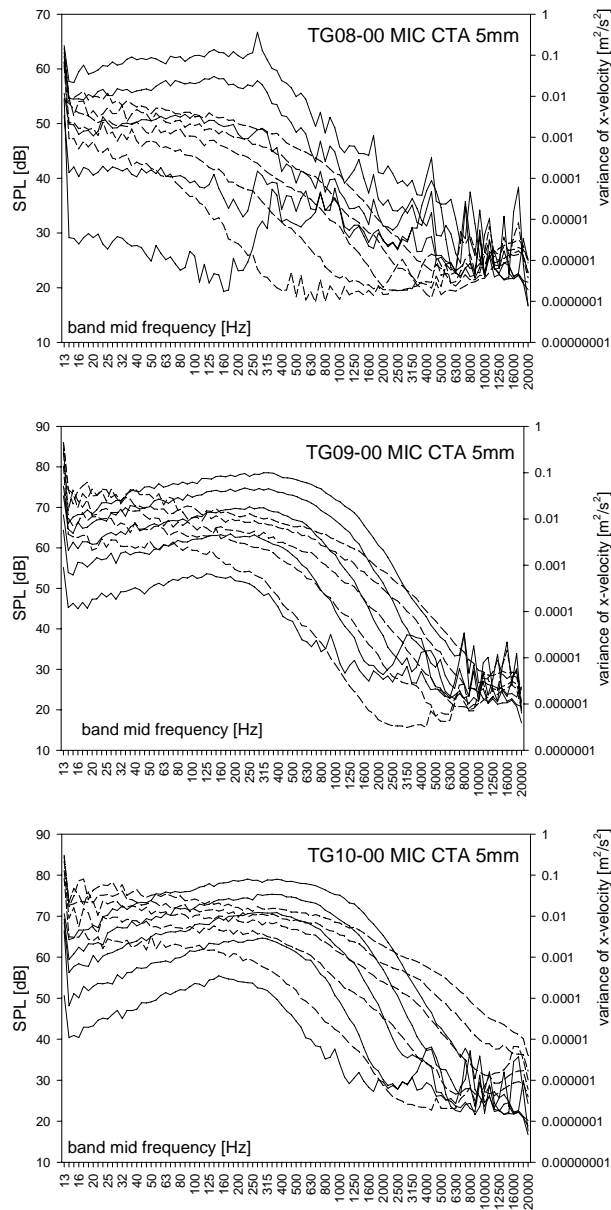


Fig.11 Comparison of the frequency spectra of the microphone signals (bold lines, MIC 12) to the CTA spectra (dashed lines) for different turbulence generators TGx. The CTA signal was recorded 5mm in front of the microphone MIC12, where the turbulent jet impinges on the microphone plate. The five different sets correspond to the fan speed frequencies of 500, 750, 1000, 1250 and 1500 rpm.

5 Conclusion

Steady CFD simulations can give trends but are not ideally suited for quantitative analysis as they are not able to capture the inherent transient flow patterns. The RNG formulation of the $k-\epsilon$ model compared best to the experimental data (streamwise and crosswise velocity, turbulent kinetic energy). Differences in the models are most pronounced in the stagnation area of the impinging jet at the wall. For some turbulence generators (blades), a steady solution could not be achieved.

Correlations between turbulent velocity fields and microphone signals have been investigated for different turbulence generators. Larger turbulence coincides with larger pressure fluctuations, the full frequency behaviour, however, could not always be reproduced. The reasons may lie in additional acoustic incoming waves, which can be attributed to dipolar and quadrupolar sound sources as well as vibrations of the turbulent generators.

Broader CTA spectra, however, coincide well with broader signals at the microphones.

Transient CFD simulations (DES) will be employed to provide frequency spectra for comparison to the experimental data. Furthermore, the correlation between simulated local velocity fluctuations and pressure fluctuations at the wall can be investigated. These results will also be compared to the experimental correlation, as CTA and microphone signals have been recorded simultaneously. The 12 microphone signals also allow for spatial correlation analysis.

Acknowledgements

We want to express our gratitude to the Austrian Science Foundation (FFG) supporting this work in the framework of the Bridge project TUNICA.

References

- [1] Bruun, H. H., "Hot-Wire Anemometry: Principles and Signal Analysis", Publisher: Oxford University Press, USA (June 8, 1995), ISBN: 0198563426
- [2] Counihan, J., "An improved method of simulating an atmospheric boundary layer in a wind tunnel", *J. Fluid Mechanics*, vol. 3, pp. 197-214, 1969.
- [3] Guimaraes, J. H. D., dos Santos, S. J. F., Su, J., Silva Freire, A. P., "Large artificially generated turbulent boundary layers for the study of atmospheric flows", *Proceedings of the 15th Brazilian Congress of Mechanical Engineering (COBEM99)*, Aguas de Lindoia, 1999
- [4] Hunt, J. C. R., Fernholz, H., "Wind-tunnel simulation of the atmospheric boundary layer": a report on Euromech 50, *J. Fluid Mechanics*, vol. 70, pp. 543-559, 1975.
- [5] Jovanovic, J., "The Statistical Dynamics of Turbulence", ISBN 3-540-20336-2 Springer Verlag Berlin Heidelberg New York, 2002
- [6] Ramezanpour, A., Shirvani, H., Mirzaee, I., "Heat transfer modelling of slot jet impinging on an inclined plate", *Heat Transfer VIII*, B. Sundén, C. A. Brebbia & A. Mendes (Editors)

Numerical Prediction and Experimental Characterization of Turbulent Flow Fields and Acoustic Perturbations of HVAC Components

Christoph Reichl¹, Michelle Böck^{1,2}, Wolfgang Tilšer^{1,2}, Helmut Kühnelt¹, Klaus Haindl³ and Martin Opitz³

¹Austrian Institute of Technology, Vienna, Austria

²Technical University of Vienna, Vienna, Austria

³AKG Acoustics GMBH, Vienna, Austria

Abstract

Turbulent flow fields are commonly present in HVAC ventilation systems. Especially outlet nozzle designs have a strong impact on turbulence and acoustic radiation in the emerging jets. It is highly desirable to model these turbulent flows and to characterize the spectral content of the pressure perturbations. For this purpose, a turbulent circular pipe-flow with typical core-velocities of around 10 m/s ($Re = 99000$) has been generated by an axial symmetric fan. Turbulence is generated using different sets of turbulence generators at the pipe outlet consisting of meshes, rods, cubes and spikes. The turbulent flow field downstream of the pipe outlet is measured using two-axis hot wire anemometry with a temporal resolution of 48 kHz. The CTA probe is positioned using an automated three-axis traversing system recording the turbulent velocities on 492 points downstream of the pipe outlet. A set of 12 microphones is used to capture wall pressure fluctuations and off axis sound fields. To extract the inlet boundary conditions for the CFD calculations, turbulent velocity profiles have been measured in the pipe using two-axis CTA. The development and stability of the simulated pipe flow is checked by comparing the numerical data to a second CTA data set further downstream in the pipe. CFD calculations are performed for the different turbulence generators using several numerical approaches: First, steady RANS simulations including standard k-epsilon, k-omega and non-isotropic turbulence models show the overall behaviour of the studied flow types. Second, unsteady DES has been carried out to generate the base for the extraction of fluctuating velocity and pressure time series. The spectral evaluation of the data is performed using Fourier Transformation and analysed in 1/3 terz band representations. The spectral content of the time series for the different HVAC jets is finally compared to the experimental values.

Key words: HVAC components, nozzles, acoustics, RANS, DES, CFD, CTA measurements

1. Introduction

Pressure fluctuations and velocity perturbations are commonly found in the wake of turbulent jets, which are generated by HVAC duct outlets. In this work turbulent jets in the low-velocity region of around 10 m/s are generated using turbulence generators [3, and references herein]. Turbulent flow fields are - in addition to the propagated fan noise - often the source of aero-acoustic noise. If pressure fluctuations and velocity fluctuations are known, the acoustic behaviour of jets can be characterized [2, 4]. This paper aims in analyzing the velocity and pressure fluctuations in impinging jets and compares simulation results to experimental investigations using two-axis hot wire anemometry [1].

2. Numerical Simulation

2.1. Geometry Definition

The geometry of the calculation domain is shown in figure 1. The calculation domain is an imaginary cylinder having a tube for the incoming fluid attached on one side and an impermeable wall for the impinging jet on the other. The fluid enters the domain at the tube inlet to pass through a turbulence generator (figure 3) and leaves it through the rest of surface except for the wall.

12 different evaluation lines L01-L12 are defined in the area between tube outlet and plate (see figure 2). Their x-axis positions are 6.00, 9.40, 19.59, 50.17, 141.90, 229.26, 312.74, 400.10, 491.83, 522.41, 532.60 and 536.00 mm. Different turbulence

generators are summarized in figure 3. The empty tube section (no turbulence generator) is TG00.

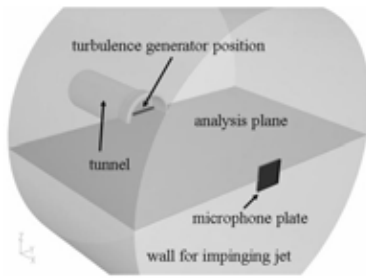


Figure 1. Geometry: A circular jet impinges on a plate mounted on a hard wall. Turbulence generators can be applied in the outlet region of the tunnel.

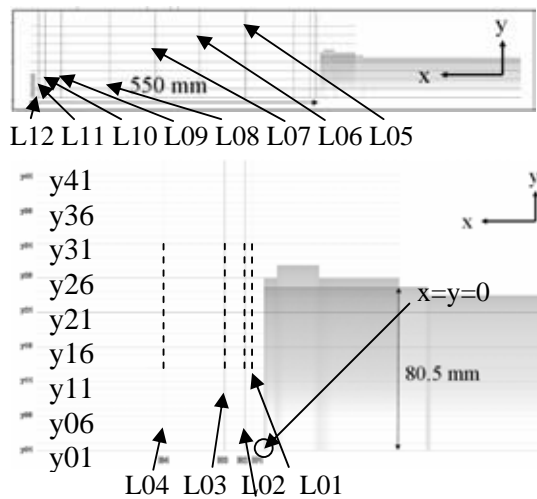


Figure 2. Definition of the postprocessing lines L01-L12.

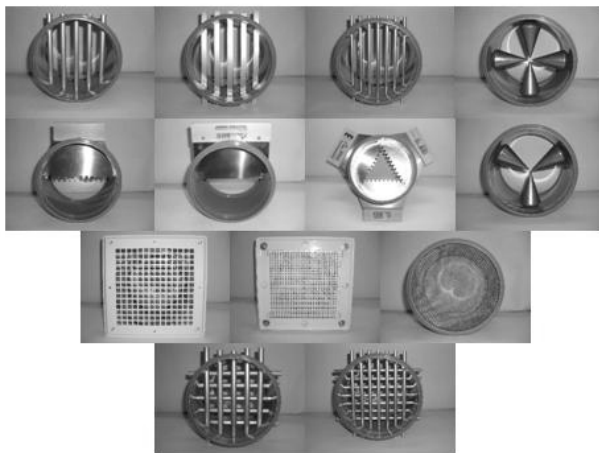


Figure 3. Different turbulence generators consisting of rods, blades, spikes and meshes. They can be mounted on top of the tunnel outlet. First row: TG01, TG08, TG02, TG05; Second row: TG07, TG10, TG09, TG06; Third row: TG11, TG13, TG12; Fourth Row: TG04, TG03

2.2. Mesh Definition

The numerical analysis have been performed on a hybrid mesh consisting of tetrahedral cells in the region of the turbulence generators (see figure 4) and a prismatic / hexahedral mesh in the up- and downstream area. Mesh sizes of 1 mm at the turbulence generator core and 12 mm at the boundaries lead to typical cell counts of 5 million cells.

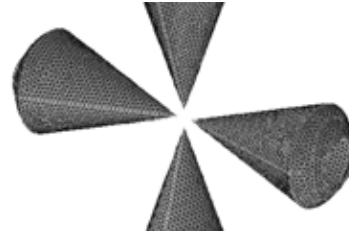


Figure 4. Mesh resolution on the spike surfaces of TG05.

2.3. Simulation Method

Results of steady RANS simulations have been calculated previously [3] giving best results for the RNG formulation of the $k-\epsilon$ model. In publication [3] additional turbulence generators have been analyzed as well. Especially the sharp blades caused very high fluctuating fields, which could not be captured by a steady solver. The mean velocity inlet boundary profiles were extracted from the experimental CTA data. The turbulence boundary condition was defined using the hydraulic diameter of 152.59 mm and a turbulence intensity of 5%. For the simulations the commercial Navier Stokes solver Fluent was used applying the Detached Eddy Simulation with vorticity based production terms. Second order schemes were used in space and time using the segregated implicit solver. Using a time step of 100 μ s around 5000 time steps were necessary to reach quasistatic behaviour of the flow field. An additional amount of 5000 time steps have been calculated and recorded to perform the steps for the spectral analysis.

2.4. Mean Velocities and Velocity Fluctuations

Mean values of the velocity magnitude for different turbulence generators are given on the plane $y=0$ (see figure 5) in a profile representations for selected turbulence generators. The different evaluation lines (L01 – L12) are separated and shifted by 4 m/s. Figure 6 shows profile representations of the turbulent kinetic energy of the DES simulations using different turbulence generators. The turbulent kinetic energy is calculated from the values of all three velocity variations (x, y, z). The different lines are separated and shifted by a value of 0.2 m^2/s^2 .

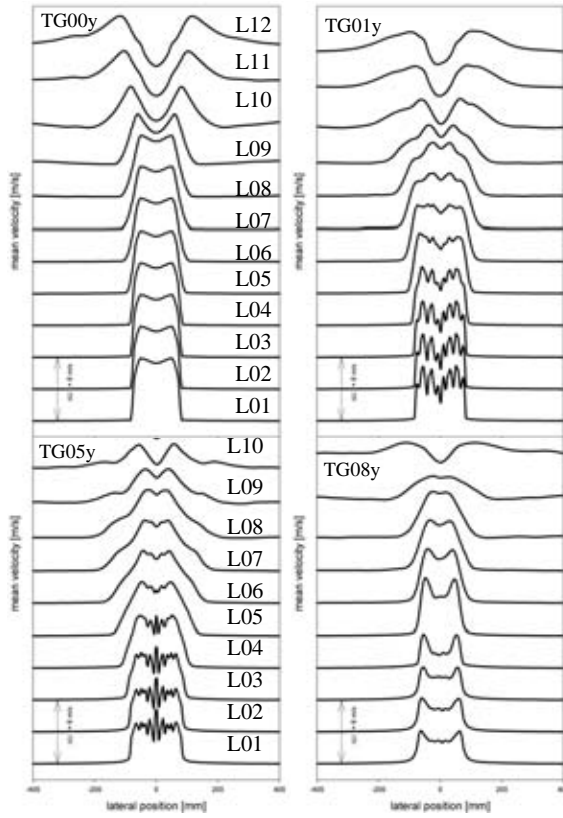


Figure 5. Mean velocities [m/s] (distance of two lines = 4 m/s. The different lines show results of the different profiles at lines L01-L12.

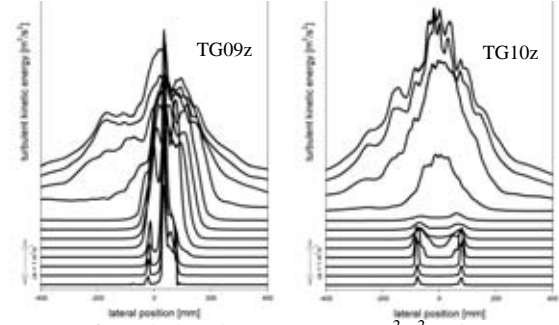
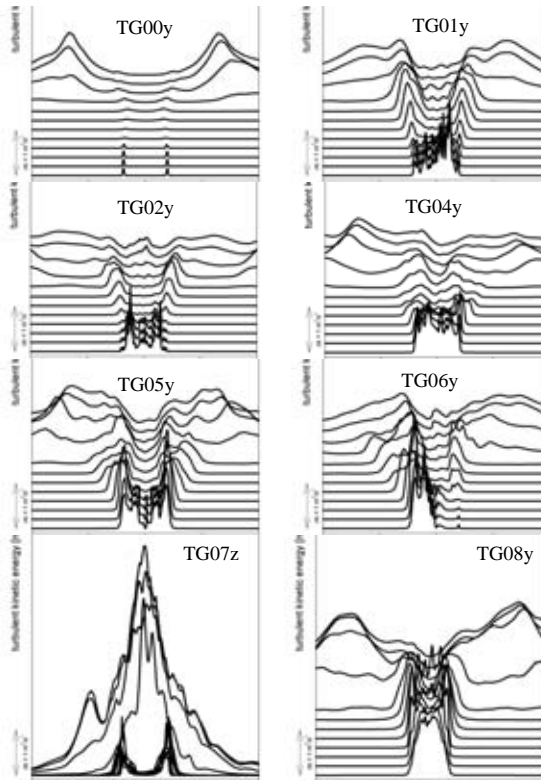


Figure 6. Turbulent kinetic energy [m^2/s^2] (distance of two lines = $0.2 \text{ m}^2/\text{s}^2$).

2.5. Pressure Fluctuations

Pressure fluctuations have been recorded during the transient DES and are presented in figure 7.

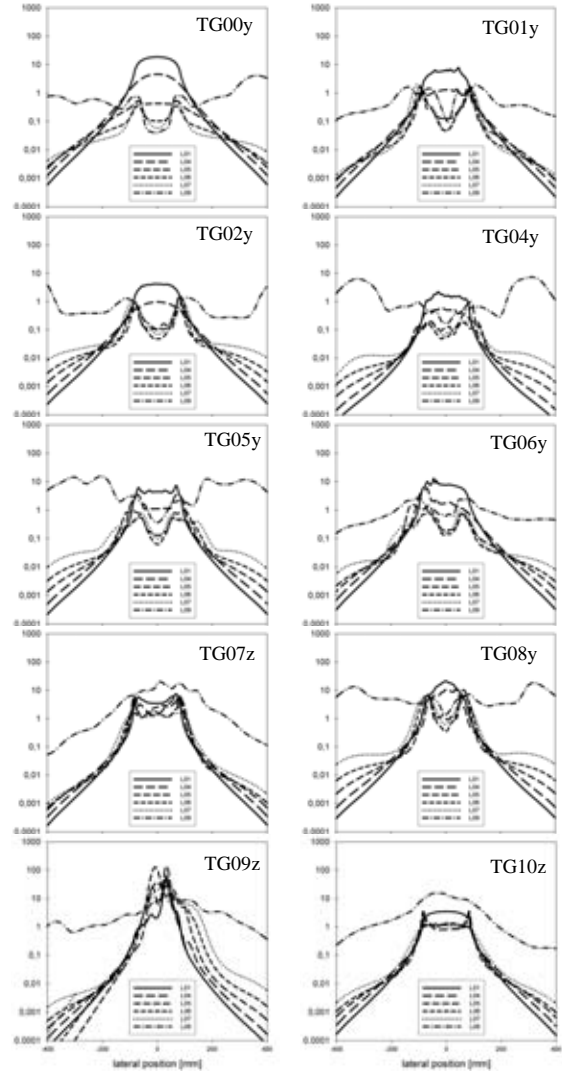


Figure 7. varianz of static pressure [Pa^2] on 6 evaluation lines L01, L04, L05, L06, L07 and L09 from top to bottom. The y-axis is given in a logarithmic representation.

3. Spectral Analysis

3.1. Pressure Fluctuations (DES Simulation)

The transient static pressure has been recorded on twelve evaluation lines (L01 – L12) for about 5000 time steps after the simulation has reached a quasi-periodic state. Figure 8 shows the spectral normalized, absolute squared value of the static pressure, which is multiplied by a factor of two to account for the positive frequency space. FFT signals are displayed in a logarithmic scale with a reference value set to $1 \text{ m}^2/\text{s}^2$.

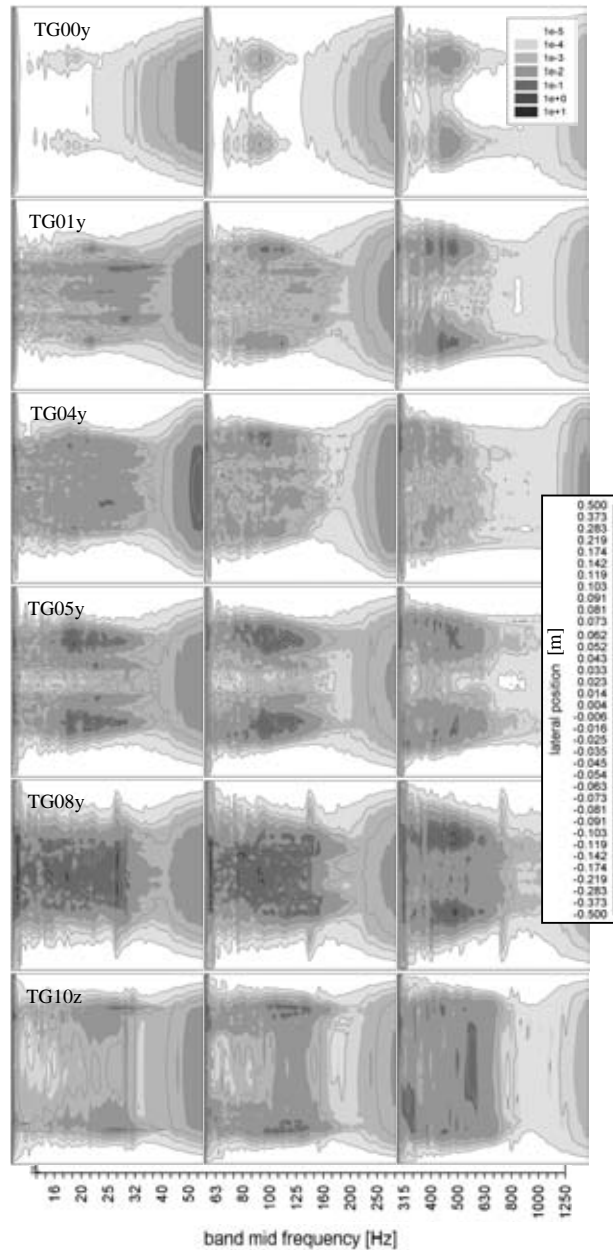


Figure 8. Spectral representation of the pressure fluctuations $[\text{Pa}^2]$ for different turbulence generators (left L01, mid L04, right L05).

3.2. Velocity Fluctuations (DES Simulation)

Figure 9 (simulation) and 10 (experiment) show the spectral normalized, absolute squared value of the mean velocity (multiplied by a factor of two, see section 3.1). FFT signals are displayed in a logarithmic scale with a reference value set to $1 \text{ m}^2/\text{s}^2$. Integrating over the frequency space yields the corresponding turbulent kinetic energy.

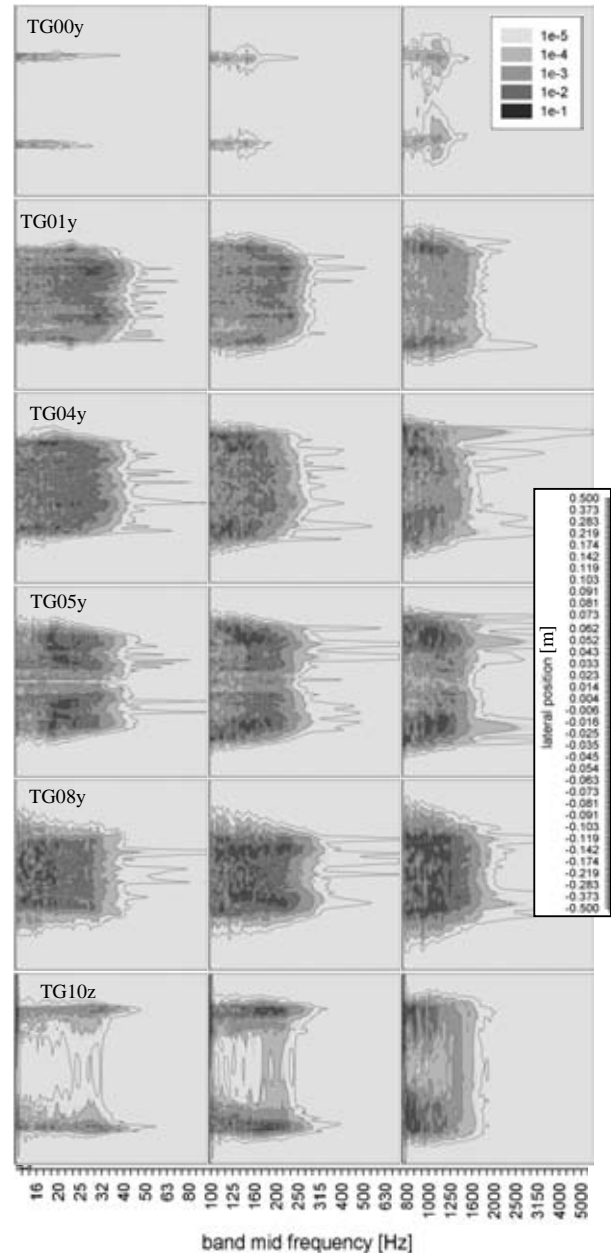


Figure 9. Frequency spectra at different lines (left L01, mid L04, right L05) for different turbulence generators TGxx. The grey scale represents the variance of the mean velocity $[\text{m}^2/\text{s}^2]$. The y-axis is nonlinear representing the nonlinear mesh. The band mid frequency axis numbers are shown enlarged and are valid for all three figures in a row.

3.3. Velocity Fluctuations (CTA)

Signals from the 2-axis CTA have been recorded with a sampling rate of 48 kHz. The data was acquired in an analysis plane on 492 points (streamwise tunnel direction x: 12 points, perpendicular crosswise direction +y: 41 points). All signals have been scaled by their corresponding calibration values. The spectral analysis was carried out after numerically filtering (low pass filter 20 kHz), DC subtraction and Fourier transformation (see figure 10).

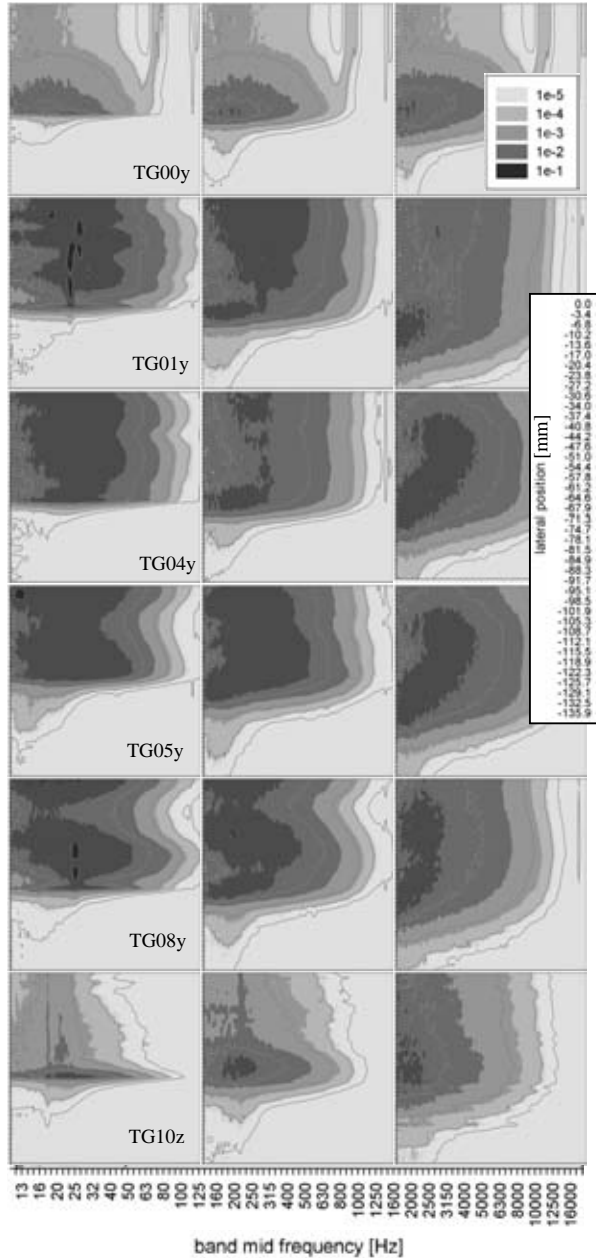


Figure 10. Frequency spectra at different lines (left L01, mid L04, right L05). The grey scale represents the variance of the mean velocity [m^2/s^2]. The y-axis is linear.

3.4. Near wall pressure fluctuations

During the simulation runs, pressure fluctuations have additionally been recorded at several positions at the centre of the flat plate, where the turbulent jet impinges ($y \sim 1cm, z = 0$, see figure 11). The wall is located 550 mm downstream of the tube outlet. For comparison the plate was also moved upstream to a wall-tube outlet distance of 140 mm.

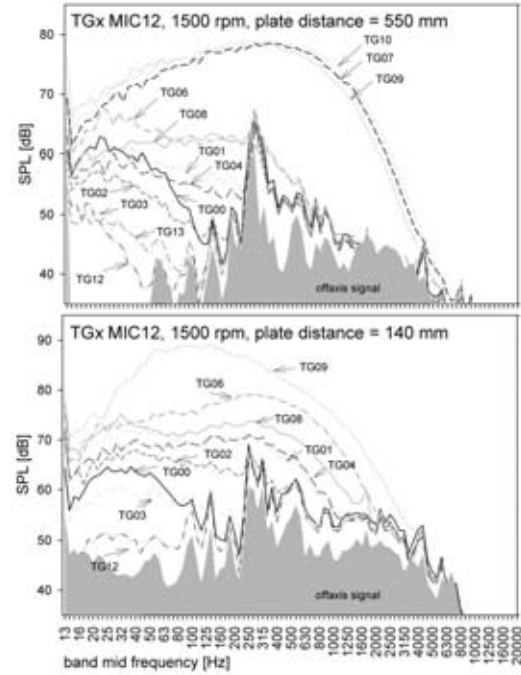


Figure 11. Comparison of the **measured** frequency spectra of the microphone MIC12 for different turbulence generators. The gray area is the maximum signal of the acoustic offset measurement for the different TGx [3].

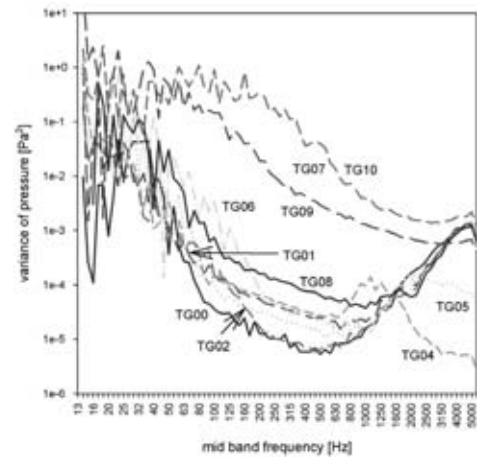


Figure 12. Comparison of the **calculated** frequency spectra of the pressure fluctuations for the different turbulence generators from the DES results.

3.5. Near wall velocity fluctuations

Frequency spectra of the CTA signal are compared for the different turbulence generators in figure 13. The wall plate distance was set to 550 mm and 140 mm. For both cases, the CTA probe was positioned 5 mm direct in front of the plate, in the 140 mm case CTA measurements have also been performed with the CTA in the middle between tube and plate.

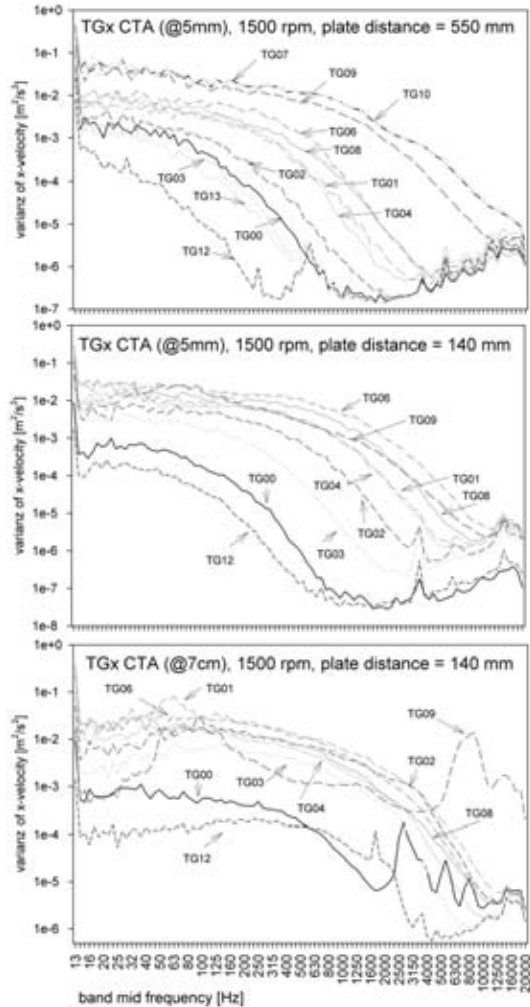


Figure 13. Frequency spectra of the CTA signals.

4. Conclusions

Correlations between near wall turbulent velocity fields (figure 13) and microphone signals (figure 11) can be experimentally established for different turbulence generators. While larger turbulence coincides with larger pressure fluctuations, the full frequency behaviour, however, could not always be reproduced. The reasons may lie in additional acoustic incoming waves, which can be attributed to dipolar and quadrupolar sound sources as well as vibrations of the turbulent generators. Higher and broader CTA spectra, however, coincide well with

broader signals at the microphones. These trends can also be reproduced by the DES simulated spectra of the pressure fluctuations (figure 12). The simulation results underpredict their experimental counterparts at lower frequency values.

Comparing the velocity spectra from the DES (figure 9, mind the nonlinear y-axis, which is more dense in the shear layer) with the spectra from the experimental data (figure 10, only one half of the tube was scanned) the following results can be extracted: The prominent features of the spatial frequency behaviour are well captured (e.g. the position of the shear layers, the separation and the combination of the turbulent areas). However, the representation of all details of the spectra is limited. This can be partly attributed to the constraints of the computing power and cell size.

Due to the minimum cell side length of 1 mm at the turbulence generating surfaces and a mean value of around 5 mm cell side length in the turbulent area, higher frequencies cannot be propagated well, which can be seen in the lower frequency content of the numerical based spectra compared to the experimental data.

The experimental spectra of TG00 show a higher turbulence level between the shear layers as compared to the simulation data.

Future investigations will, thus, be devoted to different mesh strategies and the implementation of stronger fluctuating boundary conditions to overcome the present limitations.

References

- [1] Bruun H.: (1995). "Hot-Wire Anemometry: Principles and Signal Analysis", Publisher: Oxford University Press, USA (June 8, 1995), ISBN: 0198563426
- [2] Lighthill M. J.: (1952). On sound generated aerodynamically – I. General Theory, *proceedings of the Royal Society of London, Series A*, Vol. 211, pp. 564-587
- [3] Reichl Ch., Böck M. Tilser W., Lang H., Haindl K., Reining F. and Opitz M.: (2008). „On the correlation of the acoustic signal of microphones mounted on a flat plate to the turbulence of an impinging jet”, *proceedings of the Acoustics'08 Paris*, 29.06.-04.07., Paris
- [4] Reichl Ch., Lang H., Krenn Ch. and Mann M.: (2005). Aero-Acoustic Comfort Characterization of Ventilation Nozzles using Transient and Steady CFD Simulations, NAFEMS Word Congress, 17.-20. Mai 2005, Malta.

This work has been supported by the Austrian Research Promotion Agency (FFG) under "Bridge" contract No. 813008.